Scanning ion conductance microscopy: Modelling and approaches to studying peptide secretion

Samantha Juoh Li Del Linz

2011

A thesis submitted to UCL for the Degree of Doctor of Philosophy

Neuroscience, Physiology and Pharmacology

UCL

Gower Street

London, WC1E 6BT

Declaration

I, Samantha Juoh Li Del Linz confirm that the work presented in this thesis is my own. Where information has been derived from other sources, I confirm that this has been indicated in the thesis.

Abstract

Scanning ion conductance microscopy (SICM) offers a number of benefits for both imaging and recording from biological samples. However, several fundamental issues concerning this technique, including the image resolution, remain to be clearly understood. In this thesis a model of SICM has been developed to address these issues. This model is quite general and can accommodate arbitrary geometries for both the probe and the sample surface. Model simulations using simple geometries are in good agreement with known analytical solutions and experimental data. The simulations have therefore been extended to examine a number of imaging issues, including the lateral resolution of SICM in response to a surface 'step' and to a pair of adjacent objects. The probe's interactions with features that are smaller than, or comparable to, the size of the probe tip have also been investigated. Further, the scanning of sloped objects has also been examined. The results of these simulations suggest some important considerations for scanning. The potential for extending the biological uses of SICM has also been examined in the area of protein/peptide secretion. It is demonstrated that SICM can be used to image secretory events from the Weibel-Palade bodies in endothelial cells. Further, to explore similar issues, on a smaller scale, the use of SICM to study neuropeptide Y (NPY) secretion has been examined. To this end a new preprohormone construct of NPY, which allows visualisation of the location of secretory events, has been tested. This construct contains a region coding for the pH-sensitive ecliptic pHluorin, and is shown to be capable of reporting fusion events, without major disruption of the kinetics of secretion. Experiments using this construct in conjunction with SICM are described and the potential for using SICM to provide insight into peptide secretion is discussed.

Acknowledgments

I am indebted to my supervisor Dr. Guy W. J. Moss for his encouragement and guidance. I am also grateful to Dr. F. Annibal Fernández and Dr. Eero J. Willman for their part in the SICM modelling project and in particular to Dr. Eero J. Willman for the Laplace solver code. I would like to thank Dr. Matthew D. Whim and Dr. Tom Carter for the opportunity to work in their laboratories and for many useful conversations. I would also like to thank Dr. David C. H. Benton for teaching me many useful techniques and for all his help in the peptide secretion project. Dr. Simon A. Hughes and Mr. Matthew Caldwell have also been generous in offering their advice on practical aspects of SICM and in sharing their reference scanning data.

On a more personal note I would like to thank everyone in the lab: Alan, David, Guy, Matthew and Simon, for their practical and moral support. I would also like to thank the other CoMPLEX students for helping me to stay sane, in particular: Alex, Dave and Lisa. Finally I would like to thank my family for all their support. In particular I am grateful to Paolo for his understanding and patience while I've been writing this thesis; I'll do my best to return the favour.

Contents

List of figures and tables

Chapter 1: Introduction

This thesis is concerned with developing the theory and uses of scanning ion conductance microscopy (SICM), with particular reference to applications in peptide secretion. SICM is a relatively new technology and before embarking on the development of additional imaging methods it is perhaps worth considering what criteria such imaging technologies should meet in an ideal situation. First, in order to observe dynamic processes, biological samples must be kept alive and functioning normally for the duration of the experiment, so an ideal imaging technology does not require fixed samples. Indeed, typically, good imaging will require a system that can operate while a sample is bathed in a physiological salt solution and is operating at normal biological temperatures and pressures. Second, so as not to disrupt biological processes by the act of measuring, the ideal technique should be non-invasive. Clearly, in addition to the above requirements, the images must be gathered with sufficient precision to resolve features of a size that is comparable to, or smaller than, the elements of interest. A further challenge is the speed of imaging, as this must be fast enough to follow the process under examination. Given the very diverse nature of biological measurements it is also unlikely that a single imaging technique will be sufficient for all purposes. Therefore, one might add an additional requirement, namely that imaging systems for one type of measurement should be compatible for use with other imaging techniques. To try to meet this diverse set of needs, new types of imaging technology continue to be developed and increasingly scanning probe technologies are becoming prominent. SICM is one of these scanning probe technologies and because it can meet a number of the above criteria it is of considerable interest.

1.1 Scanning probe techniques

In recent years, scanning probe microscopies have started to become more important in the study of biology, not just for imaging, but also for measuring function (for reviews see, for example: Müller, 2008; Francis et al., 2010; Amemiya et al., 2006; Klenerman and Korchev, 2006). These techniques typically measure a property of the sample at each point as the probe scans in a raster fashion (or the sample is moved in the x,y plane) so as to build a ‘map’ of the sample surface. The movement of the probe is usually controlled by a piezoelectric to allow a very high level of accuracy. Some of the most important of these techniques are briefly discussed below.

Atomic force microscopy

One of the most useful of the scanning probe techniques in a biological setting is atomic force microscopy (AFM). AFM was first developed by Binnig and co-workers in 1986 (Binnig et al., 1986) and uses the force interactions of a very sharp probe with the surface to map out the sample topography. This technique has been widely used and a number of different scan modes developed. The simplest form of scan mode is contact mode. In contact mode, a constant force is maintained between the probe and the sample by adjusting the sample height. This height information is used to build up a topographical map of the sample surface. However, since this involves a force being applied to the sample there may be sample (and probe) deformations that interfere with the biological system being measured. To reduce this problem tapping mode was developed. Tapping mode uses a probe oscillated at resonant frequency, which contacts the surface only at the lower points of its oscillation (Hansma et al., 1994; Putman et al., 1994). The frequency of these oscillations is modified by the presence of the surface and thus may be used to determine the probe-sample separation. Early estimates of the resolution of tapping mode suggested 1.1 – 1.5 nm lateral resolution (Möller et al., 1999). With careful choice of scanning protocols (Casuso and Scheuring, 2010) and tip and sample preparation (Czajkowsky and Shao, 2002; Müller and Engel, 2008) it has therefore been possible to image cell membranes in the form of supported lipid bilayers with a lateral resolution down to 1 nm or less and vertical resolution of 0.1 – 0.2 nm (Müller and Engel, 2007).

More sophisticated scan modes have also been developed. Many of these use functionalised tips to allow a wide range of surface properties to be investigated, such as electrochemical interactions and ion conductance (e.g. Frederix et al., 2005; Gerber and Lang, 2006; Müller and Dufrêne, 2008). In addition, a different mode of operation, single molecule force spectroscopy (SMFS), allows the examination of the intra- and inter- molecular forces on proteins, via protein unfolding and relaxation (e.g. Rief et al., 1997a,b; Rief et al., 1999). In this technique a single membrane protein, adhered to the AFM probe may be unfolded by retracting the probe, thus allowing a characteristic force-distance curve to be measured. This force-distance curve allows information about the protein secondary structure to be inferred from the distinct steps observed (Müller et al., 1999; Oesterhelt et al., 2000). Similarly, folding properties may be examined by allowing partial refolding of the protein before repeating the unfolding process, allowing the stability of different conformational states to be investigated. The

unfolding pathway thus observed is found to be variable with the likelihood of unfolding via a particular pathway dependent on the environment of the protein (e.g. Janovjak et al., 2003; Sapra et al., 2006; Park et al., 2007).

In a similar way, with a ligand attached to the tip, SMFS may also be used to investigate ligand-receptor binding interactions (e.g. Moy et al., 1994). In this format a single ligand molecule is attached to the tip via some spacer and allowed to bind with its receptor before the tip is retracted. This technique has also been expanded as "molecular recognition imaging mode" (Hinterdorfer et al., 1996; Dufrêne and Hinterdorfer, 2008), which allows a topographical map of a surface and the location of particular proteins to be obtained simultaneously. Another expansion of SMFS is dynamic single molecule force spectroscopy (DSMFS). In this technique the force applied over time is varied allowing an "energy-landscape" to be determined which gives information about such properties as the unfolding distance before each stable state, the energy barrier to unfolding and the lifetime of each state (Evans, 1998). This has been used to investigate questions such as which protein subunits are affected on drug binding (e.g. Kedrov et al., 2005; Kedrov et al., 2008), and which amino-acids in a ligand are important for binding (e.g. Ganchev et al., 2004).

AFM is thus a versatile technique that allows high resolution imaging of cellular membranes and may also be used as a tool for the nanoscale manipulation of membrane proteins.

Ultra Microelectrode Techniques

Scanning electrochemical microscopy (SECM) is a scanning probe technology that forms part of a range of related techniques called ultra microelectrode (UME) techniques. UME techniques utilise electrical properties, such as the current at the probe tip, due to redox reactions to generate their signals. SECM was developed in the 1980's by Bard and co-workers (Bard et al., 1989) and typically uses probes of ≤ 25 μm tip diameter. Several different modes of operation exist which allow different properties to be measured. Many of these involve the use of SECM as a scanning probe technique that creates a “functional map” of the sample surface. These techniques are often performed with small probes with the sample bathed in a redox-mediator and allow the use of SECM for topographical surface mapping or to map the chemical reactivity of a surface. There are known theoretical models of how UME currents change as a probe approaches a surface when that surface is bathed in a particular

redox-active species. Experimentally, comparison with these models allows determination of the probe-surface separation. Similarly deviations from this behaviour can be used to detect the presence of local redox-active species.

There are several challenges in studying living biological samples with SECM. One such challenge in topographical measurement is the choice of probe. When using constant height mode large tip sizes limit resolution, but small tips lead to limits on the height variation which may be measured without crashing. Different scan modes have therefore been developed to compensate for this including constant-distance imaging modes based on negative-feedback (e.g. Fan and Bard, 1999), tip-position modulation (e.g. Wipf and Bard, 1992) and shear-force (e.g. Pitta Bauermann et al., 2004). Another complication of SECM is the need of a redox-mediator in several of the scan modes used for imaging. Care must be taken in choosing the redox-mediator since some of those commonly used for SECM of non-living samples may be toxic for biological specimens, and thus unsuitable for either the determination of surface topography or the location of biological processes under investigation.

One of the strengths of SECM is the ability to examine biologically important redox processes. A number of experiments of this type have been performed using the tip generation-collection mode, which typically does not require a redox-mediator in the bathing solution since the redox active species is generated by the biological sample. There have been some notable uses of SECM in this type of experiment. For example, respiration has been studied, in systems ranging from plant specimens and bacteria to mammalian cells (for example, Lee et al., 1990; Holt and Bard, 2005; Feng et al., 2003). Topographical measurements have also been made of biological samples including single mammalian cells (Liebetrau et al., 2003). There is also promising work to simultaneously acquire high resolution topographical and reactivity maps of surfaces, (although this has not yet been used on biological samples; Laforge et al., 2009).

SECM therefore again shows great potential for applying scanning probe techniques to investigate biological systems. The wide range of operating modes and the possibility to work in combination with other related techniques and optical microscopy makes this a versatile biological tool.

Ultra microelectrode techniques are not used exclusively in scanning mode and technologies relating to SECM, such as amperometry and cyclic voltammetry are also widely applied (see Wang et al., 2009; Amemiya et al., 2006; for reviews of biological applications of UME techniques). Amperometry is a method in which the probe is held

at a fixed potential close to a region of interest, such as a secreting cell. The presence of redox active species, such as secreted catecholamines, can then be detected from currents generated due to redox reactions at the tip surface. Amperometry has been very extensively utilised in biology because it can be used to follow the secretion of signalling molecules such as dopamine and also because it offers a high level of temporal resolution (sub-ms for the best probes). In cyclic voltammetry, a variant on this theme, the probe potential is changed in a "triangular" fashion, starting at a low potential and steadily increasing with time before reaching a peak and ramping back down to the starting point. Often there is a rest time between each step to aide with the identification and concentration estimates of the reactive species to be determined. As mentioned above, these techniques have been extensively used to investigate biological processes such as exocytosis (e.g. Chow et al., 1992; Schroeder et al., 1992; Zhou et al., 1996; Mosahrov et al., 2003; Camacho et al., 2006), often in combination with each other or with patch-clamp techniques, such as membrane capacitance measurements (e.g. patch amperometry; Albilos et al., 1997).

Scanning Ion Conductance Microscopy

The scanning probe technique that is the subject of this thesis is scanning ion conductance microscopy (SICM). This technique offers surface detection by measuring changes in resistance that can be seen when a conducting probe is brought close to an insulating surface in a conducting solution. SICM was first developed by Hansma and co-workers (Hansma et al., 1989) and was later extended to use on biological samples in physiological solutions by Korchev and co-workers (Korchev et al., 1997a, Korchev et al., 1997b). A brief explanation of the operation of SICM is outlined below.

Operation of SICM

The operation of SICM is as outlined in Fig. 1.1a. The SICM probe comprises a hollow glass tube pulled to a very fine aperture at the tip. This probe is filled with an electrolyte solution and a wire electrode is inserted at the top. The sample to be imaged is placed in a bath filled with electrolyte and a ground electrode is placed in the bath solution. When a potential difference is applied between the probe and ground electrodes an ion current will flow. As the probe is brought very close to an insulating surface (such as the cell membrane, to a reasonable approximation), the current flowing between the electrodes will reduce as the flow of ions becomes partially occluded (Fig. 1.1c).

The SICM system can be idealised as a pair of resistors in series as shown in Fig. 1.1b. As can be seen from Eq. 1 the probe current depends on both the probe resistance R_p and the access resistance R_{ac}.

$$I = \frac{V}{R_p + R_{ac}} \qquad \text{Equation 1.1}$$

The applied voltage, V, and R_p are constant, whilst R_{ac} is dependent on the distance between the probe and surface. When the probe is far from the surface R_{ac} is negligible and the current reaches a steady maximal value, I_s, the infinity current. However, as the probe is brought close to the surface R_{ac} becomes significant and its value is directly related to the separation between the probe and the surface. Thus, SICM uses the variations in R_{ac} as a proximity detector.

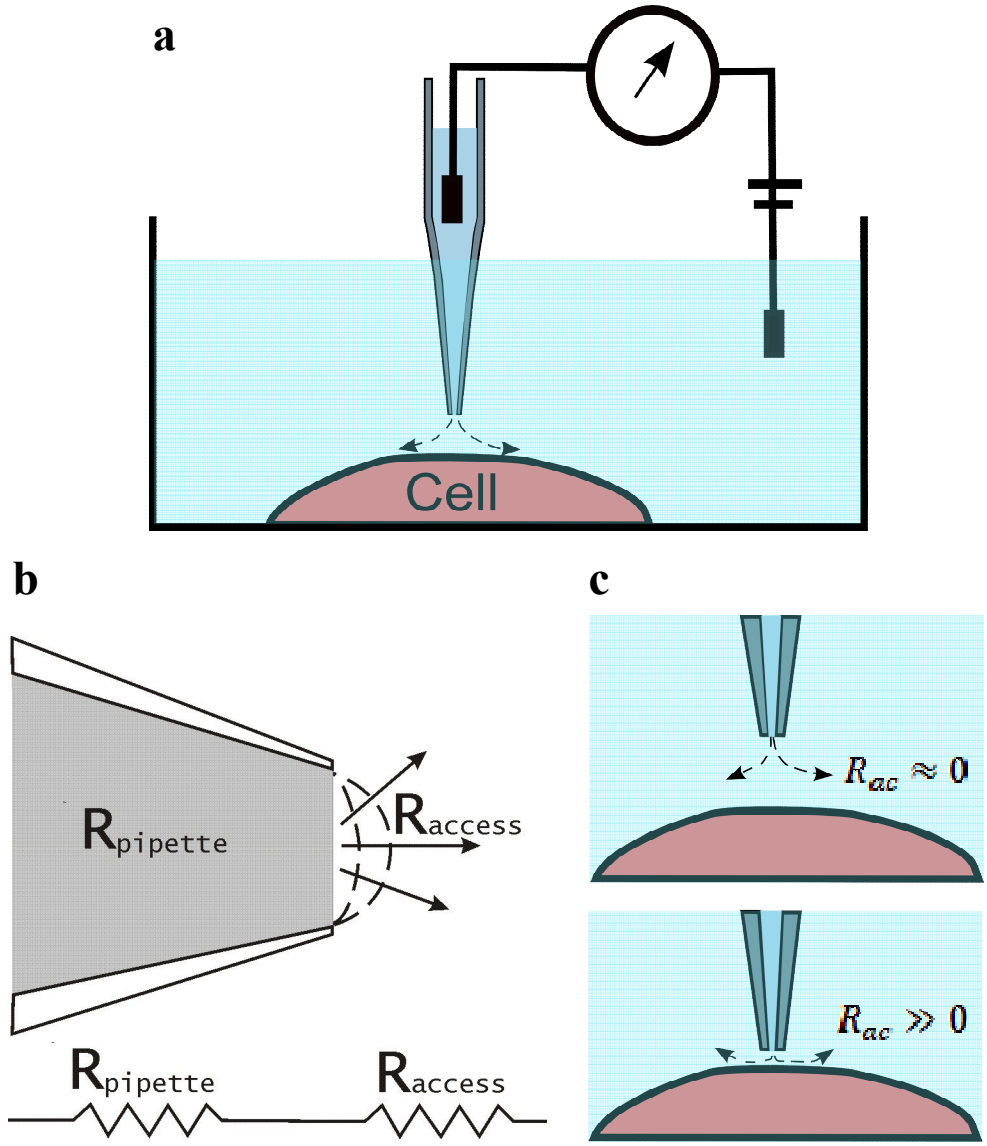

Figure 1.1 Principle of operation for the scanning ion conductance microscope.
a) The SICM probe is a nanopipette filled with electrolyte and a wire electrode. This probe is submerged in an electrolyte bath which contains a second electrode. A potential difference is applied between the electrodes and the current flowing through the pipette is measured. b) The pipette may be considered as two resistors connected in series. With the constant resistance due to the pipette R_p and the access resistance R_{ac} which is due to the resistance to current flow at the pipette tip. c) When the pipette is far from an insulating surface R_{ac} is negligible but as the pipette is brought very close to the surface R_{ac} becomes significant and is dependent on the distance between the probe and surface.

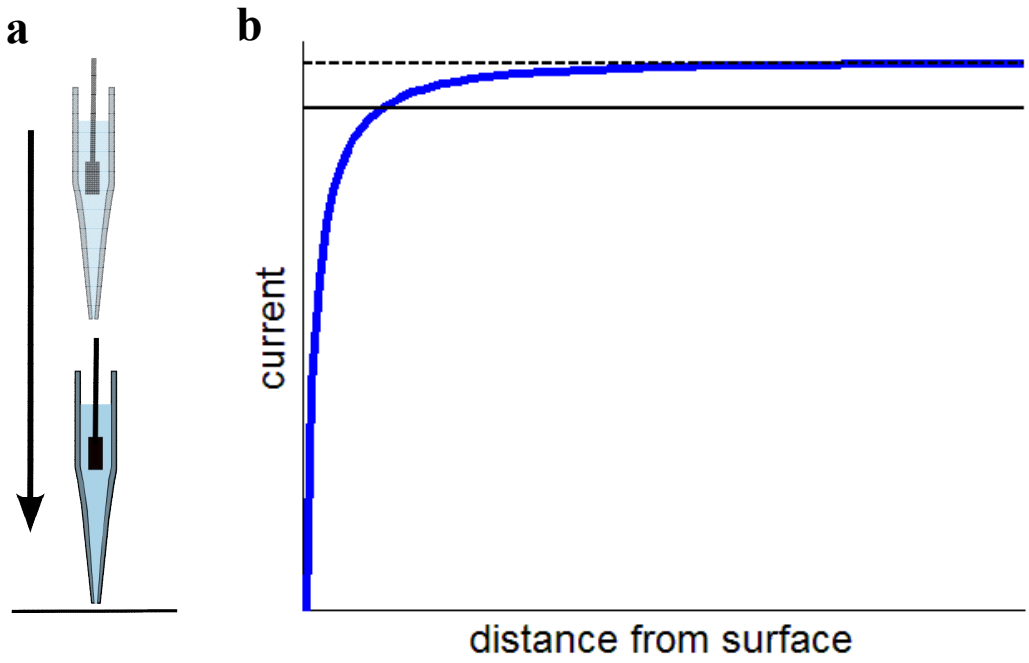

Figure 1.2 The approach curve.
To establish an approach curve the SICM probe is held far from the surface. The current flowing through the pipette at this point is at its maximal value and is the so called infinity current I_s. The probe is then lowered towards the surface and the current – distance relationship thus found is called the approach curve. An example approach curve is shown in panel b, where the solid blue line represents the probe current and the dashed black line shows I_s. The solid black line shows the set point current, I_{sp}, for a 1 % set point.

In practice surface detection is based upon the approach curve, which relates the probe current to the separation between the probe and the surface. The probe current is measured far from the surface to establish I_s and then as the probe is lowered close to the surface, the regime where R_{ac} dominates is reached and the current reduces in a non-linear fashion Fig. 1.2. Experimentally, a percentage set point is chosen, typically between 0.1 – 1 %, and when the probe current reaches this reduced value compared to I_s (I_{sp}), the surface is considered to be detected and the z-piezo position is recorded. The probe is then moved to the next measurement position. This procedure may then be repeated at different x,y positions to build up a topographical map of the sample.

Uses of SICM

One of the strengths of the SICM technique is that in the ideal case no deforming force will be applied to the sample. As mentioned earlier, SICM may also be readily combined with other techniques such as optical microscopy (Shevchuk et al., 2001) and confocal microscopy (Gorelik et al., 2002; Shevchuk et al., 2008a,b). The

combined confocal microscopy technique can be applied using a confocal spot which is aligned relative to the SICM probe tip. Thus, as a topographical scan is performed, a confocal image of surface fluorescence may be obtained simultaneously (Gorelik et al., 2002). The SICM probe may also optionally be used in more active ways. Such applications include using a SICM probe for nano-manipulation such as nano-writing, where individual charged molecules are deposited via the pipette tip (Ying et al., 2002; Ying et al., 2004). A related application is to iontophoretically deliver a stimulus locally at well defined parts of the cell surface (Piper et al., 2008). Pressure application via the scanning tip has also been used to allow force mapping of the cell surface, and has thus allowed some of the mechanical properties of the cell membrane and cytoskeleton to be observed (Sánchez et al., 2008). In addition the probe used in SICM is similar to an electrophysiological probe and may be used to make electrical recordings of the cell membrane. Due to the typical size of an SICM probe (~ 100 nm tip diameter and 100 - 200 MΩ resistance, comparable to what is often referred to as a "sharp electrode" in electrophysiology) cell-attached patch-clamp recordings may be made, but whole-cell patch-clamp recordings are not usually achievable. Nevertheless, a cell may first be scanned to produce a topographical map of the cell membrane and then patched in a specified area in a process known as "smart" patch-clamping (Korchev et al., 2000). This has been used to map functional ion channels, such as the ATP-regulated K^+ channels in cardiomyoctyes (Korchev et al., 2000).

Additionally, some work has been done to follow both endocytosis (Shevchuk et al., 2008a) and exocytosis via SICM (Shin and Gillis, 2006). Shin and Gillis showed that depressions appeared in bovine chromaffin cells after stimulation with high K^+ (Shin and Gillis, 2006), suggesting that the fusion of dense core granules is detectable via SICM. Endocytosis at clathrin-coated pits has also been reported using SICM combined with surface confocal microscopy (Shevchuk et al., 2008a). Transient depressions in the plasma membrane were recorded which were co-localised with either markers of clathrin-coated pits or of caveolae. However the temporal resolution of these scans was insufficient to allow the dynamics of endocytosis to be observed. These results indicate that SICM may be a useful tool in studying secretion. In particular I propose in this thesis to examine the use of SICM for studying neuropeptide secretion.

1.2 Overview of Neuropeptides

Neuropeptide production

Neuropeptides are signalling molecules that play important roles in regulating many physiological processes, including higher order behaviours such as eating and sleeping (e.g. Kalra et al., 1999; Tsujino and Sakuri, 2009). Peptides begin their life as part of a preprohormone. Multiple, distinct neuropeptides (as well as non-functional peptide products) may be coded for in the same preprohormone with the sequences of each peptide product usually separated by a di-basic cleavage signal (Fig. 1.3). The preprohormone can contain one or more nascent copies of each of its active neuropeptide products.

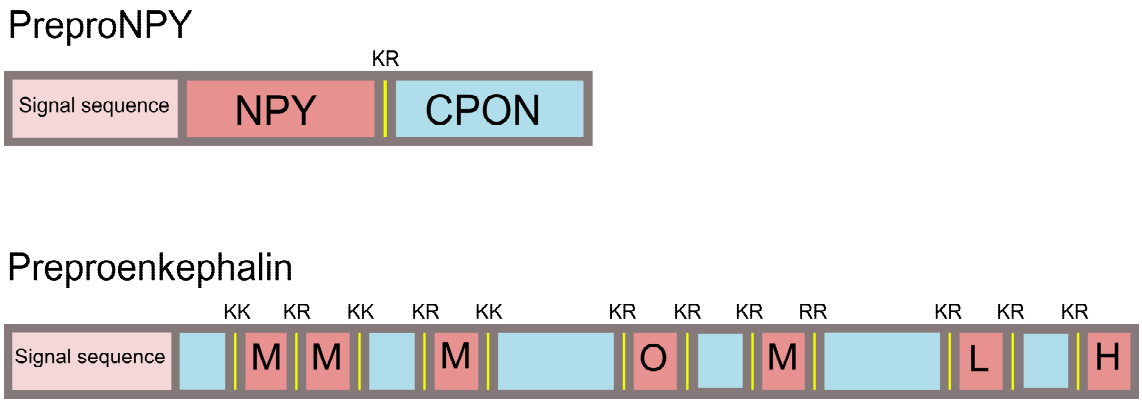

Figure 1.3 A schematic illustration of preprohormone structures
The precursor of NPY, preproNPY, encodes just a single copy of the active neuropeptide Y. In addition the non-functional peptide product CPON is also encoded. In contrast, preproenkephalin (one of the precursors for the peptides that are active at opioid receptors) encodes four copies of Met-enkephalin (M), in addition to one copy of Leu-enkephalin (L), and one copy each of the similar opioid peptides Met-enkephalin-Arg-Gly-Leu (O) and Met-enkephalin-Arg-Phe (H). All preprohormones contain a signal sequence that is essential for directing their peptides to the endoplasmic reticulum. Dibasic residues such as Lys-Arg (KR), Arg-Arg (RR) or Lys-Lys (KK) encode the cleavage sites between peptide products that are cleaved by prohormone convertase enzymes.

Preprohormones are synthesised in the soma and include a signal sequence that directs prohormone translation and entry into the endoplasmic reticulum (ER). Inside the ER the signal sequence is removed by signal endopeptidase. Some protein folding may also occur here. The inactive prohormone then enters the Golgi complex and in the trans-Golgi, sections of membrane bud off to form the basis of the large dense core vesicles (LDCVs) that undergo secretion in the regulated secretory pathway. There is considerable debate about the mechanism(s) by which peptides enter the regulated

secretory pathway, rather than the constitutive pathway see for example Dannies, (1999) and Sobota et al., (2006). It has been suggested that peptides contain a sorting signal (e.g. Cool et al., 1995; Loh et al., 1997) but in the case of the NPY preprohormone, it has been shown that a signal sequence alone appears to be sufficient to direct the green fluorescent protein (GFP) into the regulated secretory pathway (El Meskini et al., 2001). This property is very useful when constructing artificial preprohormones.

Peptide processing

Inactive prohormone precursors are cleaved by prohormone convertases acting mostly at di-basic residue signals, although mono- or tri- basics may sometimes also be cleaved. Following cleavage a number of additional post-translational processing steps may also occur, such as C-terminal amidation. This additional processing is often important for activity, as is the case for FMRFamide (Green and Cottrell, 1999; Payza, 1987). Whether cleavage takes place before or after the budding of the LDCV or starts in the *trans*-Golgi network and continues inside the LDCV is still a matter of debate (Dannies, 1999).

Peptide release

LDCVs are trafficked to the cell membrane via microtubules and a variety of motor molecules may be involved. Unlike the small synaptic vesicles that contain transmitters such as GABA and glutamate, LDCVs are not necessarily released from the synapse. In fact, neurones can release peptides not only from synapses, but also from the cell body and the cell dendrites (Orci et al., 1988). Indeed, it may even be that dendritic release is the major form of release for some neurons (Ludwig and Leng, 2006).

Peptide release is a process which has been shown to be dependent on Ca2+ and on stimulation frequency (see for review for example Burgoyne and Morgan, 2003; Sudhof, 2004; Scalettar 2006). Most peptide exocytosis is triggered by Ca2+ and is highly dependent on Ca2+ concentration (e.g. Heinemann et al., 1993; Voets et al., 1999). Several studies have been performed to investigate the dependence of peptide release on the type and frequency of stimulation. Some early studies were performed on specialised neuroendocrine cells by measuring the total amount of peptide released, or some other downstream marker, upon electrical stimulation. These studies showed that for many peptides the total amount of peptide released increased with increasing

frequency up to some maximal value before reducing with frequencies above this value (e.g. Gainer et al., 1986; Bicknell, 1988). The patterning of stimulation was also found to be important. For several peptides and cell types it was found that bursts of high frequency stimulation evoke greater overall peptide release than continuous stimulation at the same average frequency e.g. vasoactive intestinal peptide (Andersson et al., 1982), NPY (Lundberg et al., 1986 and 1989), vasopresin (Muschol and Salzberg, 2000) and leuteinizing hormone releasing hormone (Peng and Horn, 1991); whilst for others e.g. oxytocin (Muschol and Salzberg, 2000) the converse is true. There is also evidence that the basis of the frequency dependence of peptide secretion may be due to increased internal Ca2+ concentration after a build up during successive action potentials (e.g. Jackson et al., 1991; Stuenkel and Nordmann, 1993; Muschol and Salzberg, 2000).

Further studies using changes in membrane capacitance to follow LDCV fusion, and thus with much higher temporal resolution than by measuring secreted peptides, identified three distinct phases of secretion: fast, slow and sustained (e.g. Neher and Zucker 1993; Heinemann et al., 1994; Horrigan and Bookman, 1994; Eliasson et al., 1997; Voets et al., 1999; Sorensen 2004; Marengo, 2005; Ge et al., 2006). Both the fast and slow phases are completed within 100 ms to a few seconds, whereas the sustained phase may last for 10s of seconds to many minutes. These phases are thought to correspond to different pools of LDCVs which may be physically or functionally distinct e.g. by location or age (Duncan et al 2003; Wiegand et al 2003). Horrigan and Bookman (1994) and others classified these vesicle pools as, the immediately releasable pool (IRP), which are docked with the plasma membrane and are fully release competent, the readily releasable pool (RRP), which are close to the plasma membrane but are undocked and may still require further processing to become release competent and the reserve or refractory pool which may be far from the plasma membrane and/or unprimed (e.g. Neher and Zucker 1993, Parsons et al 1995; Eliasson et al 1997; Xu et al 1999).

Peptide secretion from neuroendocrine and endocrine cells typically follows a slower time course than the secretion of small synaptic transmitters but shares much of the same release machinery. In general the fusion between two phospholipid membranes is brought about by several conserved elements. The fusion between the membrane of the LDCV and the cell plasma membrane is thought to involve essentially the same proteins as for the fusion of small synaptic vesicles but may differ in the exact subtypes and time course of docking and priming (e.g. Pang and Sudhof, 2010). A set of six

proteins comprises the fusion machinery in these systems (for reviews see for example: Rizo et al, 2006; Gustavsson and Han 2009; Sorensen, 2009; Sudhof and Rothman 2009; Pang and Sudhof 2010) and their functions are briefly outlined below. The core of the fusion machinery is: the Ca2+ sensor (synaptotagmin) with an ancillary protein (complexin), an SM protein (typically Munc18-1), two plasma membrane associated t-SNARE proteins (typically syntaxin and SNAP-25) and the vesicle associated v-SNARE (e.g. VAMP2/synaptobrevin). The v-SNAREs and t-SNAREs form the trans-SNARE complex (or SNARE-pin), which is a stable bundle of four helices, three on the target membrane side, one from syntaxin and two from SNAP-25, and one from the vesicle membrane side from VAMP2/synaptobrevin. The C-terminal domains of VAMP2/synaptobrevin and syntaxin are located in the vesicle and target membranes respectively. Therefore as the trans-SNARE complex forms (catalysed by the SM protein) the two fusing membranes are brought close together, in the 'docked' state. The Ca2+ sensor forms a complex with the ancillary protein complexin. Complexin acts as a grapple and binds the t-SNAREs and v-SNAREs and synaptotagmin and simultaneously brings these proteins together while also preventing membrane fusion until synaptotagmin is Ca2+-bound, in the 'primed' state. Membrane fusion is therefore both catalysed and clamped by the synaptotagmin/complexin complex. Once the Ca2+ sensor is Ca2+ bound the complexin clamp is removed, thus allowing the trans-SNARE complex to zipper further towards the energetically favourable cis-SNARE complex, generating part of the force needed to form the fusion pore. The LDCV and plasma membranes may then fuse under the force generated by the zippering SNAREs. Several SNARE-pins may be required for the fusion of a single granule.

Details about the mechanisms of peptide release are also controversial. Several different modes of release have been observed. This can range from full fusion where the dense core granule membrane fuses with the plasma membrane, releasing all of its contents, to more complicated modes such as kiss-and-run. In kiss-and-run vesicle fusion a transient fusion pore is established between the vesicle and the plasma membranes which subsequently closes without full fusion and may go through several such cycles or even ultimately take part in full fusion. Kiss-and-run fusion in dense core granules may allow the differential release of cargo molecules with the fusion pore sufficiently large to allow the passage of small species such as ATP, GABA and catecholamines, (Chen et al., 2005; Obermuller et al., 2005; MacDonald et al., 2006; Eliasson et al., 2008; Vardjan et al., 2007a,b) but small enough to either block the

passage of larger molecules such as peptides or to lead to slower release (Barg et al., 2002a; Perrais et al., 2004; Stenovec et al., 2004; Salio et al., 2006). However there is conflicting evidence on whether neuropeptides may be released via the fusion pore. Tsuboi and Rutter observed the release of fluorescently-tagged peptide without the subsequent transfer of vesicle membrane proteins into the plasma membrane, suggesting that the vesicle membrane remained intact after release (Tsuboi and Rutter, 2003). Conversely, Barg and co-workers did not observe the release of peptides via the fusion pore but only after full fusion events (Barg et al., 2002a). Additionally, several studies have shown other release modes such as kiss-and-glide, where the vesicle is seen to move after the fusion pore is established (Tsuboi et al., 2000) and prolonged 'kissing' where a long-lived fusion pore is observed (Chen et al., 2005). It has also been shown that the fusion pore may initially form with sub-nanometre dimensions, such that very small species such as protons may cross, and only subsequently may widen partially to allow some cargo release (Stenovec et al., 2004; Vardjan et al., 2007a). Further, the fusion pore has been shown to be regulated by G-protein coupled receptor pathways which, when active, moderate the quantal size of release and may promote kiss-and-run release by reducing the open time of the fusion pore (Chen et al., 2005). A further complexity in understanding secretion is the fate of granule cargo after release. Recent studies have provided evidence of granule fusion without rapid de-granulation, leading to stable deposits on the cell surface (de Wit et al., 2009). It has been suggested that this is due to an interaction between the cargo and the vesicle matrix and seems highly dependent on the cargo.

The predominant mode of exocytosis may also be Ca2+ dependent with changes in intracellular Ca2+ concentration leading to transitions between different modes of release (e.g. Ales et al., 1999; Elhamadi et al., 2006; Xia et al 2009). The details of these finding have been controversial with differences in species and experimental conditions leading to opposing observations in some cases. For example in rat chromaffin cells, in conditions to monitor spontaneous release, raising external Ca2+ concentration leads to a transition from full fusion to kiss-and-run (Ales et al., 1999). Conversely in bovine chromaffin cells, under physiological-like electrical stimulation, raising internal Ca2+ concentration shifts the mode of exocytosis from kiss-and-run to full fusion (Elhamadi et al., 2006). Similarly in neurones high frequency stimulation has been seen to promote kiss-and-run rather than full fusion from LDCVs (Xia et al 2009). Thus the mode of

exocytosis may be seen to be dynamic and to depend on a variety of factors including Ca2+.

Neuropeptide Y

In this thesis preproneuropeptide Y (NPY) was used as model system to examine peptide secretion. NPY is an amidated 36 amino acid peptide (Tatemoto et al., 1982) and is one of the most common peptides in both the central and peripheral nervous systems and is also present in non-neuronal locations. It has been shown to have a wide variety of functions and there are several NPY receptors (Y-Rs). These receptors bind not only NPY but also other peptides in the NPY hormone family (PYY and PP) with differing affinities. In mammals five Y-R subtypes have been identified which have been split into three families based on sequence homology. The Y1-R family has three members, Y1-R, Y4-R and Y6-R, and the other families Y2-R and Y5-R each have a single member. Y1-R is seen to act predominantly postsynaptically, while Y2-R mostly acts presynaptically by suppressing neurotransmitter release (Lindner et al., 2008). Y5-R is expressed predominantly in the CNS rather than the periphery (in contrast to Y1-R, Y2-R and Y4-R).

NPY appears to have different functions in different systems some examples of which are summarised below. In the hypothalamus, NPY plays a role in the circadian timing system via Y2-Rs during the day and Y5-Rs during the night (Yannielli and Harrington, 2001). Also in this region NPY takes part in appetite regulation with evidence from pharmacological and behavioural studies showing increased food intake in response to direct NPY application (Clark et al., 1984, Stanley and Leibowitz, 1985). This role in feeding behaviour and energy balance has been widely studied, with evidence pointing to Y5-R as the mediator of the NPY feeding response (Berglund et al., 2003).

In the cardio-vascular system NPY is expressed in perivascular sympathetic fibres and co-exists with nor-epinephrine where it innervates the muscle of the heart, spleen and vas deferens (Lundberg et al., 1990). In these systems NPY shows a vasoconstrictive effect, either directly, mainly through the action of postsynaptic Y1-Rs, or indirectly by potentiating nor-epinephrine-induced vasoconstriction (e.g. Wahlestedt et al., 1985). (However, it is worth noting that pre-synaptically NPY inhibits the release of nor-epinephrine; Lundberg and Stjarne, 1984). NPY may also have an analgesic effect via the dorsal horn neurons (Hökfelt et al., 1998). In addition, NPY in the

hippocampus has been suggested to play a role in epilepsy and prion disease. In this region NPY is expressed in GABA-ergic interneurons and this expression increases in response to seizures (e.g. Gruber et al., 1994). This and other evidence has led to the theory that NPY may have a post-seizure neuro-protective effect that is mediated via Y5-Rs (e.g. Marsh et al., 1999). Thus it can be seen that NPY plays a wide variety of roles and therefore makes an ideal candidate for study. It should also be noted that the work in this project need not be specific to NPY but could in principle be applied to any neuropeptide with a known preprohormone sequence.

1.3 Possible Applications of SICM to Study Peptide Secretion

There are a number of ways in which SICM could potentially be used to examine neuropeptide secretion. As discussed above previous work has shown that SICM may be used to study endo- and exo- cytosis (Shevchuk et al., 2008a, Shin and Gillis, 2006) and that evidence supporting the idea that pits left by the fusion of a single dense core granule has been observed (Shin and Gillis, 2006). SICM may also be useful in investigating the fate of granule contents after secretion. The work of de Wit and co-workers (de Wit et al., 2009) suggests that under certain conditions the granule contents stay adhered to the cell surface for some time after secretion. Scanning could be used to detect the presence of these adhered cargoes with minimal application of force. Furthermore the use of SICM in combination with fluorescent-tagging, especially with the pH sensitive GFP pHluorin, could allow the mode of secretion to be investigated. Several of the different release modes currently identified, such as full fusion with subsequent cargo diffusion or retention, "kiss-and-run", "kiss-and-glide" and "prolonged kissing", should be distinguishable using this combined approach. An alternative way in which SICM could be used to investigate neuropeptide secretion would be to map ion channels near release sites, via SICM “smart” patch-clamp. This would build on previous work on the regulation of exo- and endo- cytosis by ion-channels and G-protein coupled receptors (e.g. Artalejo et al., 1994; Albilos et al., 2000; Teschemacher and Seward, 2000; Fulop and Smith, 2006; Bauer et al., 2007) including the tight coupling between the location of Ca^{2+}-activated ion channels and dense core granule release sites in insulin secreting cells (Barg et al., 2002b). It would therefore be interesting to map the functional ion channels near to release sites with other cells and cargoes. The SICM probe could also be used to iontophoretically deliver stimulants to microdomains of the cell and in this way to study the factors which influence release

from different parts of the cell. Another exciting possibility would be to image the fusion pore directly. However current estimates of the size of the fusion pore in the low nanometre range (Albillos et al., 1997, Jorgacevski et al., 2010) may prove to be beyond the lateral resolution of SICM.

The subject of my work has been to try to extend the use of SICM towards the study of neuropeptide secretion. The theoretical background of SICM has not been fully explored, leaving scope for some features of scanning to be better defined. In particular the lateral resolution of a scan and its dependence on the exact geometry of the probe remain to be elucidated. Some estimates of the lateral resolution of SICM have recently been made, indeed some during the work presented in this thesis (e.g. Adenle and Fitzgerald, 2005; Bae and Butler, 2008; Edwards et al., 2009; Rheinlaender and Schäffer 2009). However, a number of important issues remained unresolved. I have therefore set out to model SICM and use this model to investigate the lateral scan resolution and the effect of probe geometry on scanning. I will use the results of this model to discuss how best to use SICM to study neuropeptide secretion and also present work towards the practical implementation of this scheme.

In this thesis I aim to investigate the mode of neuropeptide release and the fate of LDCV cargoes both during and immediately after LDCV fusion under different conditions. To do this I will use a combination of experimental techniques including FMRFamide-tagging, pHluorin based optical detection and SICM.

Chapter 2: Methods

2.1 Production of Plasmid Constructs

Overview of cDNA Construct Manufacture

Plasmid constructs were built by ligating appropriate cDNA fragments together. These DNA fragments were amplified by PCR to introduce the desired restriction enzyme cleavage sites at both the 3' and 5' ends. The expected size of the PCR product was verified through gel electrophoresis and fragments of the correct length were then removed and recovered through DNA gel clean-up. Restriction enzymes can cleave poorly near the ends of linear PCR products, so these products were not cut directly. Instead, they were ligated into a specialised vector for subcloning PCR products (pPCR Script Amp, Stratagene, CA, USA), and transformed using XL10-Gold competent cells (Stratagene). The resulting colonies were blue-white screened (to identify colonies with a plasmid carrying the insert) and these colonies were then cultured overnight before miniprepping to recover the plasmid DNA. A digest was then carried out on the purified plasmids with the appropriate 3' and 5' restriction enzymes so that the presence of the desired fragments could be confirmed by gel electrophoresis. If the gel gave the expected results this was good evidence that the plasmid contained the desired insert. The insert sequence was then verified by sequencing. Once the correct sequence had been confirmed a digest was performed on both the sequenced plasmid DNA and a suitable mammalian expression vector using the same restriction enzymes cleaving at the 3' and 5' ends of the insert DNA. Gel-electrophoresis was performed, the DNA was recovered, and a ligation was set up to join the plasmid and the insert DNA. This ligation was then transformed using JM109 *E. coli* competent cells. Single colonies were then cultured and miniprepped to recover the plasmid DNA. A digest was then performed and a gel was run to check both the plasmid and insert DNA were present. The DNA was then sequenced to confirm that the joins with the vector DNA were correct. Once a suitable plasmid had been constructed and the sequence confirmed, a larger scale, midiprep, purification was performed to obtain DNA suitable for transfection of cells.

The sections below outline the typical experimental procedures.

Polymerase Chain Reaction (PCR)

Reaction mixtures were made up as follows in a 0.2 ml PCR tube (Sarstedt, Leicester, UK); ~10 ng of template DNA, 2.5 µl of 10 µM forward and reverse primers (Eurofins MWG Operon, London, UK), 1 µl of 25 mM dNTPs (New England Biolabs (UK) Ltd, Hertfordshire., UK), 10 µl of 5× Phusion HF Buffer with 7.5 mM $MgCl_2$ (Finnzymes, Espoo, Finland) and deionised H_2O (Milli-Q, Millipore) up to a final volume of 49.5 µl. The "hot-start" PCR method was used, so the reactions were brought up to 96 ºC before 0.5 µl of 2 U/µl Phusion DNA Polymerase (Finnzymes) was added. The reactions were then run in a thermal cycler (2720, Applied Biosystems, Warrington, UK) using the following conditions: 35 cycles of 95 ºC for 40 s, 58 ºC for 40 s and 72 ºC for 60 s then a final elongation step of 72 ºC for 10 min.

Gel Electrophoresis

A 2 % (weight / volume) agarose gel, was made by combining agarose (Fisher BioReagents, Leicestershire, UK) and 1× TAE buffer (40 mM Tris base, 5 mM sodium acetate, 1 mM EDTA). This mixture was heated until the agarose had melted. Just before the mixture set, ethidium bromide solution (10 mg/ml, Promega UK, Southampton, UK) was added to a final concentration of 0.7 µg/ml. The mixture was then cast in a mould to give 8, 15 or 20 wells.

Gel PCR products or restriction enzyme digests, were prepared for electrophoresis by adding 5 µl of 6× loading buffer to 20 µl of sample. The loading buffer contained bromophenol blue which is a dye that runs ahead of DNA fragments to indicate the progress of the gel. A reference sample was also prepared containing 2 µl of 1 kb ladder (Invitrogen Ltd, Paisley, UK), which is formed of double-stranded DNA of various standard lengths in order to give bands of known size.

The set gel was then placed in an electrophoresis tank between positive and negative electrodes and covered with 1× TAE. The samples were each loaded into a well. The gel was then run by applying a constant voltage between the electrodes using a Power-Pac 300 (Bio-Rad Laboratories Ltd, Hertfordshire, UK). Typical running conditions were 100 V for 40 minutes.

The gel was then removed from the electrophoresis chamber and a placed on a gel box where a UV light source was used to illuminate the ethidium bromide-stained DNA bands in the gel. A CCD camera was used to capture this image for analysis and

record keeping. The length of DNA fragments in each sample was estimated by comparison to the reference lane.

Gel Clean-Up

DNA bands in agarose gels from either PCRs or enzyme digests were visualised by illuminating with a UV light source and were then removed by cutting with a razor blade. These samples were then purified using the Wizard® SV Gel and PCR Clean-Up System (Promega) following the manufacturer's instructions. Briefly, each sample was dissolved in 1 µl of membrane binding solution (4.5 M guanidine isothiocyanate) per mg of gel, by vortexing and incubating at 50-65 ºC for approximately 15 minutes. The dissolved sample was transferred to a minicolumn and left to incubate at room temperature (typically 20-25 ºC) for 1 minute to allow binding to the column substrate. The minicolumn was then centrifuged at 16000 × g for 1 minute, (5415C microcentrifuge, Eppendorf UK Ltd, Cambridge, UK), and the flow-through discarded. The DNA was then washed by adding 700 µl of membrane wash solution (10 mM potassium acetate (pH 5.0), 80 % ethanol, 16.7 µM EDTA (pH 8.0)) to the column and centrifuging at 16000 x g for 1 minute. The DNA was then washed a second time by applying 500 µl of membrane wash solution and centrifuging at 16000 x g for 5 minutes. The minicolumn was then transferred to a 1.5 ml microcentrifuge tube. 50 µl of nuclease-free water was added to the minicolumn and incubated at room temperature for 1 minute. To elute the DNA, the minicolumn was then centrifuged at 16000 x g for 1 minute.

Insertion of Blunt-Ended PCR Products into pPCR-Script or pTarget

Restriction enzymes can cleave poorly near the ends of linear PCR products. The recovered PCR product was therefore ligated into a specialised vector for cloning PCR products; either pTarget or pPCR-Script Amp (Stratagene).

For pPCR-Script Amp the procedure was as follows. A 10 µl reaction was set up to contain 1 µl of 10 ng/µl cloning vector, 1 µl of 10× reaction buffer, 0.5 µl of 10 mM rATP, 1 µl of 5 U/µl SrfI restriction enzyme, 1 µl of 4 U/µl T4 DNA ligase, and ~400-1000 ng of recovered PCR product (to give an insert:vector ratio of 40:1-100:1). Any remaining volume was made up with deionised H_2O (Milli-Q). All reactions were performed in 0.2 ml PCR tubes. The ligation reaction was then incubated at room

temperature for 1 hour before being heat-inactivated by incubating at 65 ºC for 10 minutes.

For pTarget, blunt-ended PCR products were introduced by first creating 'A' overhangs on the 3' end of the leading strand and the 5' end of the complementary strand of the insert. To introduce these overhangs an 'A'-tailing reaction was carried out as follows; 1 µl of Taq 10× reaction buffer, 1 µl of 2 mM dATP, 1 µl of 5 U/µl Taq DNA polymerase (Promega) and 7 µl of insert DNA were added to a 0.2 ml microcentrifuge tube (Sarstedt). The reaction was mixed and then incubated at 70 ºC for 30 minutes.

The 'A'-tailed insert DNA was then ligated into pTarget by the following method. 1 µl of T4 DNA ligase 10 reaction buffer, 1 µl of pTarget vector, sufficient 'A'-tailed insert DNA to give a 3:1 insert:vector molar ratio, 1 µl of 3 U/µl T4 DNA ligase and deionised H_2O (Milli-Q) up to a final volume of 10 µl were mixed in a 0.5 ml tube (Sarstedt). The reaction was then incubated at 4 °C overnight.

Overview of Transformation

A transformation reaction involves the incorporation of plasmid DNA into a bacterial host cell and consequently allows the amplification of the plasmid DNA. The plasmid contains an appropriate origin of replication such that it will be copied and passed on to the daughter cells. It also carries a gene to provide resistance to an antibiotic so that bacterial colonies containing the plasmid may be selected for. After transformation the cells are grown on selective media containing the antibiotic to maintain selection pressure.

Transformation of simple ligation reactions and the ligation of inserts into pTarget were carried out using JM109 - *E. Coli* competent cells (Promega), while blunt-ended PCR products ligated into pPCR-Script or pCMV-Script were transformed using XL10-Gold Ultracompetent cells (Stratagene).

Transformation using XL10-Gold

40 µl of XL10-Gold Ultracompetent cells (Stratagene) and 1.6 µl of β-mercaptoethanol were mixed on ice in a chilled 14 ml tube (BD Falcon 2059, BD Biosciences, Oxford, UK). The reaction was then incubated on ice for 10 minutes. 2 µl of ligation reaction was added, swirled gently to mix, and the reaction incubated on ice

for a further 30 minutes. The reaction was then heat-shocked at 42 ºC for 30 s and returned to ice for 2 minutes. 0.45 ml of SOC media, heated to 42 ºC, was then added and the cells were incubated in a shaking-incubator at 37 ºC for 1 hour. 200 µl of the reaction was then plated on an LB agar plate inoculated with 20 µg/ml ampicillin. Plates were treated by applying 4 µl of 200 mg/ml IPTG and 16 µl of 20 mg/ml X-Gal (Promega) to allow blue-white screening. The plate was then incubated overnight in a 37 ºC oven. Colonies containing plasmid within the polylinker insert appeared white.

Transformation using JM109 *E. coli* Competent Cells

100 µl of JM109 cells *E. Coli* Competent Cells (Promega) and 1-50 ng of the ligation reaction were mixed on ice in a chilled 14 ml tube (BD Falcon 2059, BD Biosciences). The mixture was incubated on ice for 10 minutes and then heat-shocked in a water bath at 42 ºC for 45-50 s. The reaction was immediately returned to ice for a further 2 minutes. 1 ml of SOC media, chilled to 4 ºC, was then added. The reaction was cultured for 1 hour at 37 ºC in a shaking-incubator. The reaction was then plated on LB agar plates which had been inoculated with 20 µg/ml ampicillin. 100 µl of the reaction was spread on one plate while the rest of the reaction was centrifuged (at 16000 x g for 1 minute), resuspended in 100 µl of media and plated on a second LB agar plate. The plates were then inverted and incubated overnight in a 37 ºC oven.

DNA purification by Miniprep

A single bacterial colony was picked from a plated transformation reaction using the following method. A pipette tip was passed through a flame to sterilise and seal the end. This was then pressed onto an isolated colony and the whole tip transferred to a 14 ml tube (BD Falcon 2059, BD Biosciences) containing 3 ml of LB media inoculated with 20 µg/ml ampicillin. This tube was then cultured overnight in a shaking-incubator at 37 ºC.

Minipreps were carried out using Wizard® *Plus* SV Minipreps DNA Purification System (Promega) according to the manufacturer's instructions. Briefly, 1.3 ml of overnight culture was placed in a 1.5 ml microcentrifuge (Sarstedt) tube and centrifuged at 16000 x g for 5 minutes to pellet the bacteria. The supernatant was removed and the pellet resuspended in 250 µl of cell resuspension solution (50 mM Tris-HCl (pH 7.5), 10 mM EDTA, 100 µg/ml RNAase A) by vortexing. 250 µl of cell lysis solution (0.2 M NaOH, 1 % SDS) was added and the contents were mixed by

inversion. 10 µl of alkaline protease solution was then added, the contents were mixed by inversion and left to incubate at room temperature for 5 minutes. 350 µl of neutralization solution (4.09 M guanidine hydrochloride, 0.759 M potassium acetate, 2.12 M glacial acetic acid) was added and inverted to mix. At this stage unwanted products formed a white precipitate. The reaction was then centrifuged for 10 minutes to pellet these products.

The cleared lysate containing the plasmid DNA was then transferred to a Wizard® *Plus* SV minicolumn to bind the plasmid DNA. The minicolumn was then centrifuged at 16000 x g for 1 minute and the flow-through discarded. 750 µl of column wash solution (60 mM potassium acetate, 8.3 mM Tris-HCl (pH 7.5), 0.04 mM EDTA (pH 8.0), 60 % ethanol) was then added to the minicolumn and the column was centrifuged for 1 minute at 16000 x g. The flow-through was discarded and the wash process repeated with 250 µl of column wash solution, centrifuging at 16000 x g for 2 minutes. The minicolumn was then transferred to a 1.5 ml microcentrifuge tube and 100 µl of nuclease-free water added to the column to elute the plasmid DNA. The column was then centrifuged at 16000 x g for 1 minute and the eluted plasmid was stored at -20 ºC until further use.

Determination of DNA Concentration by Absorption Spectrometry

DNA absorbs maximally at 260 nm. This may be used to estimate the amount of DNA contained in a sample. Proteins show maximum absorbance at 280 nm but also have overlap at 260 nm. Contamination of the DNA by proteins could therefore skew estimates based only on absorbance at 260 nm. Consequently, the ratio of absorbance at 260/280 nm was used to check the purity of the DNA. The absorbance at 260 nm may then be used to determine the concentration of DNA (provided there were low contaminant levels).

A SmartSpec™ 3000 spectrophotometer (Bio-Rad) was used to measure absorbance. A background absorbance reading was taken using a cuvette containing 500 µl of deionised H_2O (Milli-Q). 10 µl of the sample was added to the same cuvette, mixed and the absorbance was re-measured.

Sequencing

Sequencing reactions were carried out using an ABI Prism Big Dye Terminator Cycle Sequencing Ready Reaction Kit v 3.1 (Applied Biosystems). For each reaction

100-250 ng of double stranded template DNA, 1 µl of 1.6 µM primer, 2 µl of Terminator Ready Reaction Mix, 2 µl of reaction buffer and deionised H_2O (Milli-Q) up to a final volume of 10 µl were mixed in a 0.2 ml PCR tube. The reaction was then run in a thermal cycler (Applied Biosystems, 2720) for 25 cycles of 96 ºC for 30 s, 50 ºC for 15 s and 60 ºC for 240 s.

The DNA was then precipitated. The precipitation solution was prepared by adding 2 µl of 3 M NaO-acetate (pH 5.2) and 50 µl 95 % ethanol to the sequencing reaction and incubating at room temperature for 15 minutes. The DNA was then pelleted by centrifuging at 16000 x g for 20 minutes. The pellet was washed by adding 250 µl of 70 % ethanol and centrifuging at 16000 x g for 5 minutes. The supernatant was then aspirated away and the pellet air-dried. The sample was then sent for sequencing at the departmental sequencing facility. This facility used a 3100-Avant Genetic Analyzer from Applied Biosystems.

Restriction Enzyme Digest

20 µl reaction volume digests were carried out in 0.5 ml PCR tubes (Sarstedt) with the following reaction mix; 1 µl of the restriction enzyme (typically 10 U/µl), 2 µl of 10× reaction buffer, 1-15 µg of the DNA to be digested and deionised H_2O (Milli-Q) up to the final volume. The reaction was gently mixed and then incubated for 2-2.5 hours in a water bath at the appropriate temperature. For the enzymes used, incubation temperatures were either 37 ºC or 25 ºC. 'Double digests' were carried out if the buffer type and incubation temperature were the same for both enzymes in the digest. This was achieved by modifying the above reaction mix by adding 1 µl of the second restriction enzyme and reducing the amount of H_2O. All enzymes and reaction buffers were obtained from either Promega or New England Biolabs (NEB).

Precipitation of DNA

Precipitation allowed DNA to be recovered between digests with different restriction enzymes. A DNA-containing sample was precipitated by adding 10 % of the sample volume of 3 M sodium acetate (pH 5.2) and 2 volumes of 100 % ethanol. The reaction was then incubated on ice for 30 minutes to allow precipitation of the DNA. The reaction was then centrifuged at 16000 x g for 15 minutes to pellet the DNA. Immediately after centrifugation, the supernatant was aspirated. The DNA pellet was then washed in 200 µl of 70 % ethanol. The DNA pellet was then air dried until the

ethanol was completely evaporated. The DNA was then re-suspended in the required volume of deionised H_2O (Milli-Q).

Ligation

To join "sticky-ended" insert DNA into a plasmid vector a 20 µl reaction volume was used. This was composed of 1 µl T4 DNA ligase (400 U/µl), 2 µl T4 DNA ligase 10× reaction buffer (with 10 mM ATP) (NEB) and a total of 17 µl comprising insert and plasmid vector DNA and deionised H_2O (Milli-Q). Plasmid and insert quantity varied between 30-50 % and 50-70 % respectively. Reactions were mixed in a 0.5 ml PCR tube and then incubated at 4 ºC overnight.

Purification of DNA by Midiprep

Midiprep purification was used to prepare plasmid constructs for transfection. A single bacterial colony was picked from a plated transformation reaction as outlined in section above. The colony was grown in liquid culture (5 ml) for 8 hours at 37 ºC in a shaking-incubator (220 rpm). 5 µl of this culture was transferred to a flask containing 35 ml of LB/amp media. The flask was then loosely covered and placed in a shaking-incubator at 37 ºC for 12-16 hours. The entire 35 ml culture was transferred to a 35 ml centrifuge tube (Nalgene, Thermo Fisher Scientific, Roskilde, Denmark) and centrifuged in a Beckman J2-M1 centrifuge (Beckman Coulter (UK) Ltd, High Wycombe, UK) at 5000 xg for 10 minutes, to pellet the bacteria. The supernatant was then treated with bleach and discarded.

The midiprep was carried out using the Mobius™ 200 Plasmid Kit (Novagen) according to the manufacturer's instructions. Briefly the bacterial pellet was resuspended in 2.1 ml of bacterial resuspension buffer (with added RNase A). 2.1 ml of bacterial lysis buffer was added and swirled to mix. The reaction was incubated at room temperature for 5 minutes. 2.1 ml of chilled neutralization buffer was added and the tube was inverted to mix. The mixture was then incubated (on ice) for 5 minutes. Genomic DNA and many other unwanted products precipitate during this incubation. The mixture was then centrifuged at 10000 × g for 4 minutes to pellet these products. The cleared lysate was decanted onto the Mobius 200 filter unit and the flow-through was collected in a 15 ml conical tube. The Mobius 200 column was prepared by adding 5 ml of equilibration buffer which was allowed to flow through the column under gravity. The filtered lysate was then added to the column and also allowed to flow

through under gravity to permit plasmid binding to the column. The column was then washed by adding 5 ml of wash solution (also allowed to flow through under gravity) and finally 2 ml of elution buffer was added to the column and the eluted plasmid DNA collected in a clean microcentrifuge tube.

1 ml of the eluted sample was transferred to each of two 2 ml microcentrifuge tubes (Sarstedt). The eluted plasmid was then precipitated by adding 0.7 ml of isopropanol to each tube. The tubes were centrifuged at 16000 x g for 15 minutes. The supernatant was decanted and each pellet was washed by adding 1 ml of 70 % ethanol. The tubes were then centrifuged for a further 10 minutes, the supernatant was then discarded and the pellets were air-dried. Once the tubes were completely dry the pellets were resuspended and combined in a total volume of 200 µl of 1×TE buffer (10 mM Tris-HCl, 1 mM EDTA).

2.2 Genetically Modified constructs

pNPY-GFP constructs

The construct pNPY-seGFP had previously been made, by the author, by the construction of an artificial pre-prohormone containing NPY, the pH-sensitive GFP super ecliptic pHluorin (seGFP) (Miesenböck et al., 1998), CPON, and a double FMRFamide tag, all separated by di-basic cleavage signals (NPY-seGFP), and subcloning this artificial gene into pcDNA 3.1 (+) zeo (Fig. 2.1) (Lee, 2006). Other fluorescently labelled versions of the pNPY-FMRFamide construct were also made with the seGFP exchanged for a different fluorescent protein in the same insertion position. In this way pNPY-EGFP and pNPY-monomeric dsRed were made.

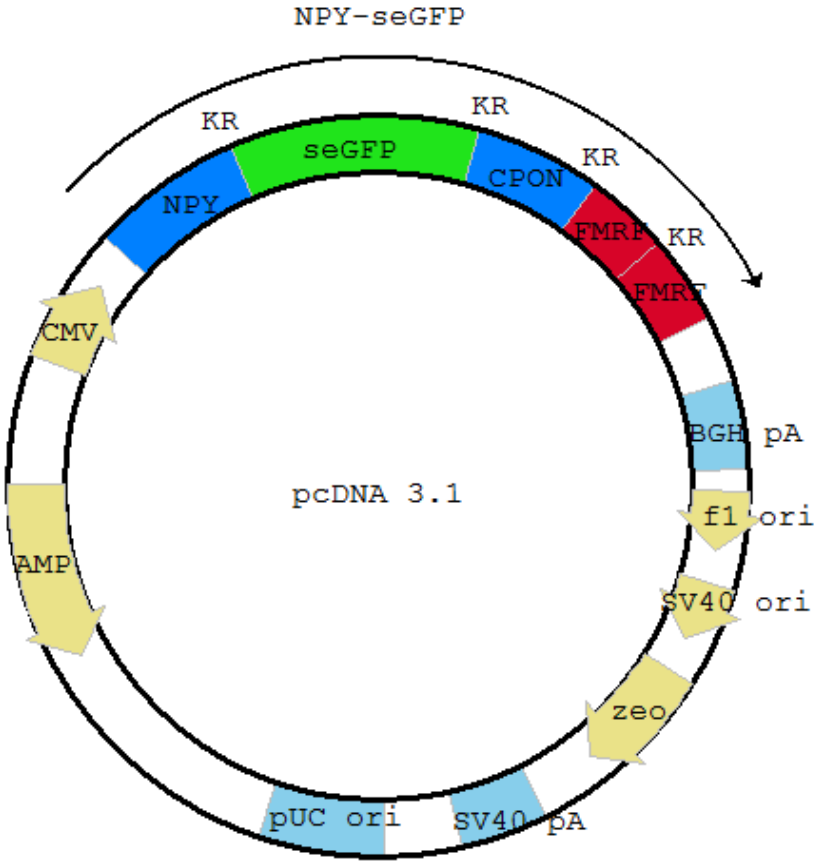

Figure 2.1 Map of pNPY-seGFP
The modified pre-prohormone NPY-seGFP is shown by the arrow. Elements within the pre-prohormone are separated by di-basic carboxypeptidase recognition sites shown as KR. The pcDNA3.1+ backbone is also shown, where CMV indicates the CMV promoter sequence for mammalian cells, BGH pA is the BGH polyadenylation sequence, f1 ori is the f1 origin, SV40 ori is the SV40 early promoter and origin, zeo is the zeocyin resistance gene (ORF), SV40 pA is the early polyadenylation sequence, pUC ori is the pUC origin, AMP is the ampicillin resistance gene (ORF).

mCherry-tagged FMRFamide Channel

The fluorescent protein mCherry (Shu et al., 2006) was added to the FMRFamide channel FaNaCh as an N-terminal fusion product. This artificial gene was inserted into pcDNA 3.1 (+) zeo (Fig. 2.2), to make pmCherry-FaNaCh.

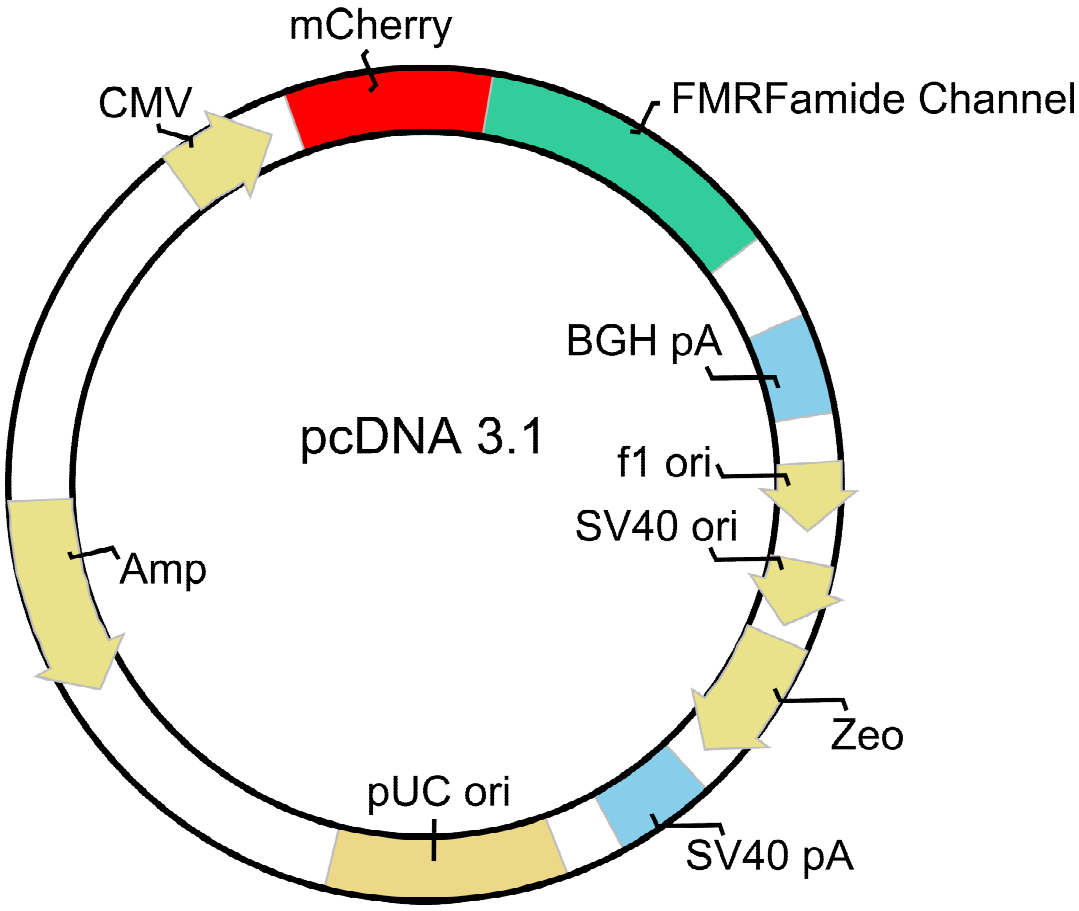

Figure 2.2 Map of pmCherry-FaNaCH
The FMRFamide channel FaNaCh was tagged by adding mCherry as an N-terminal fusion product. The pcDNA3.1+ backbone is also shown, where CMV indicates the CMV promoter sequence for mammalian cells, BGH pA is the BGH polyadenylation sequence, f1 ori is the f1 origin, SV40 ori is the SV40 early promoter and origin, zeo is the zeocyin resistance gene (ORF), SV40 pA is the early polyadenylation sequence, pUC ori is the pUC origin, AMP is the ampicillin resistance gene (ORF).

2.3 Culture and Transfection of Cells

Culture of AtT20s

AtT-20 D16v cells (derived from mouse anterior pituitary tumour) were grown in 50 ml plastic tissue culture flasks (Nunc, Thermo Fisher Scientific, Roskilde, Denmark) and maintained in 5 % CO_2 at 37 ºC in an Innova CO-170 incubator (New Brunswick Scientific (UK) Ltd, Hertfordshire, UK). AtT-20 growth medium was made using Dulbecco's modified Eagle's medium (DMEM) (Invitrogen, 41965) supplemented with 10 % foetal bovine serum (Invitrogen).

All manipulation of cells was carried out in a Class II microbiological safety cabinet (Walker Safety Cabinets Ltd, Derbyshire, UK). Cells were passaged every 3-4 days using the following method. Growth medium was discarded. The cells were washed in 10 ml of Hank's balanced salt solution (HBSS) (Invitrogen). The HBSS was then removed and replaced with 1 ml of 0.05% trypsin-EDTA (Invitrogen) for 1-2 minutes to lift them from the substrate. Once the cells had lifted, 10 ml of AtT-20 growth medium was added and the cell suspension was transferred to a 15 ml microcentrifuge tube (BD Falcon 2097, BD Biosciences) and centrifuged at 180 x g for 3 minutes in a microcentrifuge (Mistral 1000, MSE (UK) Ltd, London, UK) to pellet the cells. The supernatant was then discarded and the cells were resuspended in 10 ml of growth medium. This was then split by transferring 33 % to a new flask and adding growth medium to a final volume of 10 ml. Cells were also split at 33 % for plating onto 35 mm tissue culture dishes (BD Falcon 3001, BD Biosciences), in which case 1 ml of growth medium was added to each dish and 0.5 ml of cell suspension was added dropwise.

Transient Transfection of Cells

Lipofectamine 2000 (Invitrogen), was used for plasmid DNA transfection. The following protocol was used for cells cultured in a 35 mm diameter tissue culture dish. 50 µl of OptiMEM 1 (Invitrogen) was added to each of two microcentrifuge tubes (BD Falcon 2097). 3 µl of 1 µg/µl lipofectamine 2000 was added to the first tube and a total of 1.5 µg of plasmid construct DNA was added to the second. For an experiment with a non-fluorescently labelled NPY construct this was typically comprised of, 0.65 µg of the plasmid coding for the FMRFamide channel (pFaNaCh), 0.65 µg of FMRFamide-tagged NPY and 0.2 µg of cytosolically expressed GFP (QBI 25, Qbiogene, Cambridge,

UK). For experiments with NPY-seGFP this was typically comprised of 0.75 µg of pNPY-seGFP and 0.75 µg of pFaNaCh (or 0.75 µg of the mCherry-tagged channel construct). The microcentrifuge tubes were then incubated for 5 minutes at room temperature. The contents of the first tube were then transferred to the second and incubated for a further 20 minutes. The dish of cells was then removed from the incubator. The transfection solution was then added drop-wise and the dish re-covered and swirled gently to mix. The cells were then returned to the incubator overnight.

Preparation of Cells for Imaging

Glass bottomed 35 mm dishes were made by drilling holes in the bottom of 35 mm plastic tissue culture dishes and attaching grade 0 glass cover slips (VWR International Ltd, Leceistershire, UK or Deckglasër, Germany), which had first been washed in 100 % ethanol, to the bottom of each dish using sylgard (Dow Corning Europe, Belgium). The dishes were then incubated overnight at 60 ºC to cure the sylgard. Dishes were then washed in 70 % ethanol, dried and UV sterilised. Before use, the glass section of each dish was coated with 200 µl of 0.05 mg/ml poly-D-lysine (Sigma) (in water) by incubating overnight at room temperature, washing in sterile tissue culture water (Sigma) and air drying in a Class II hood. Other coatings were also tried such as poly-D-lysine (in borate buffer) at 0.1 mg/ml, poly-L-lysine (Sigma) (in borate buffer or water) at 0.1 mg/ml, poly-L-ornithine (Sigma) (in borate buffer) at 0.1 mg/ml, laminin (Sigma) at 0.1 mg/ml (in HBSS), gelatin at 1% (in water) and collagen at 6-10 µg/cm^2 of glass. AtT-20s were split, as described above, at 20 % and plated in a 250 µl suspension which just covered the surface of the cover slip. The dishes were then incubated for 4-6 hours at 37 ºC before flooding each dish with a further 1.5 ml of growth medium. Cells were then transfected after typically 24 hours as described above.

2.4 Imaging of Cells

Unless otherwise stated cells were imaged on a Zeiss Axiovert 200M microscope (Carl Zeiss Ltd, Hertfordshire, UK) using a Hamamatsu ORCA-ER Camera (Hamamatsu Photonics UK Ltd, Hertfordshire, UK) and controller and an Improvision Orbit (Improvision Ltd, Coventry, UK) control system. The light source was a Curtis ebq 100 arc lamp. The system was controlled by a PC running Improvision Volocity software. The filter sets used for illumination and collection were of wavelengths as outlined in Table 2.3.

Collected images were exported in the lossless bitmap format and converted to a stack for analysis using ImageJ (Abramoff et al., 2004). Lines or circular regions of interest (ROIs) were selected and measurements of either mean intensity or intensity profile along a line were made. These measurements were then repeated for each slice in the stack using ROIs at the same co-ordinates as on the first slice.

Channel	Excitation / nm	Emission / nm	Dichroic / nm
Green	450/50	510/50	480
YFP	500/20	535/30	515
CFP	436/20	480/40	455
Red	546/12	590 LP	580

Figure 2.3: Excitation and emission bands of filter sets for live cell imaging
All are band pass filters except where otherwise indicated.

Optical Test of Expression for NPY-seGFP

AtT-20 cells were transfected after 24 hours with 1.5 µg of pNPY-seGFP and prepared for imaging as describe above. Cells were imaged 24 hours post transfection. For imaging, the growth medium was exchanged for standard buffer (in mM: 137 NaCl, 5 KCl, 2 $CaCl_2$, 1 $MgCl_2$, 10 HEPES, 10 D-glucose titrated to pH 7.4 with NaOH). Fluorescence was excited and collected using the green filter set (Figure 2.3).

pH Challenge of NPY-seGFP

To determine if seGFP fluorescence changed intensity with changes in pH an NH_4Cl solution was used to break down the internal pH gradients of the cell. Cells were transfected and plated onto poly-D-lysine coated glass as described above. The NH_4Cl solution was made by replacing 50 mM NaCl with 50 mM NH_4Cl in the standard buffer which was then titrated to pH 8. Cells were first imaged in standard buffer and were then imaged after 30 s of perfusion with NH_4Cl solution before being returned to standard buffer.

Immunofluorescence

The localisation of the fluorescently-tagged NPY construct in transfected AtT20s was investigated using immunofluorescence. The colocalisation of the GFP tag with ACTH which is endogenously expressed in AtT20s was examined. AtT20s were grown on poly-D-lysine coated grade 0 cover slips (Deckglasër) in a similar way to that outlined above. Eight coated cover slips were placed in the bottom of a plastic 35 mm tissue culture dish. AtT20s were split at 20 % and 300 µl of cell suspension plated on each cover slip. These were then incubated at 37 ºC for 4-6 hours before flooding the dish with 2 ml of growth medium. After 24 hours each dish (containing eight cover slips) was transfected with 1.5 µg of NPY-EGFP (as described above).

At 48 hours post transfection cells were fixed by removing growth medium, washing with PBS and incubating in fixative (3% (w/v) PFA in PBS) for 15-20 minutes. Cells were then washed once in permeabilisation/quench solution (50 mM NH_4Cl, 0.2 % (w/v) saponin in PBS) and then incubated in permeabilisation/quench solution for 10-15 minutes. The permeabilisation/quench solution was then aspirated and replaced with blocking buffer (PGAS which contained 0.2 % (w/v) gelatin, 0.02 % (w/v) saponin, 0.02 % (w/v) NaN_3 in PBS) and incubated for 5 minutes. Primary antibody solution was prepared by diluting rabbit anti-ACTH antibody (Sigma) 1:300 in PGAS (sheep polyclonal anti-GFP (Biogenesis Ltd, Poole, UK) was also added at a 1:200 dilution to enhance the GFP signal). A 50 µl drop of antibody solution was placed onto parafilm and the cover slip placed cell side down onto it. The cells were incubated with the antibody in a humidified chamber for 30 min – 1 hour. The cover slips were then transferred to a 4-well plate and washed 4 times in 1 ml of PGAS solution. The secondary antibody, donkey Rhodamine-conjugated anti-rabbit antibody (Stratech Scientific Ltd, Newmarket, UK) was diluted 1:200 in PGAS (with donkey Cy-2-conjugated anti-sheep antibody (Stratech) at a 1:150 dilution for the enhanced GFP signal) and 50 µl of this solution was dotted onto parafilm. The cover slips were placed cell side down onto the antibody solution drop and incubated in a humidified chamber in the dark for 30 min – 1 hour. Cells were then transferred to a 4-well plate and washed 4 times in 1 ml of PGAS solution. Cells were then washed three times in 1 ml of PBS and twice in deionised H_2O (Milli-Q). Slides were prepared by labelling and adding a 5 µl drop of Mowiol antifade solution. The cover slips were then placed cell side down onto the Mowiol. Slides were stored in the dark for ~4 hours before viewing. This protocol was also performed on untransfected cells to act as a negative control. Images

were collected on a Leica TCS SP2 confocal microscope (Leica Microsystems (UK) Ltd, Bucks, UK).

Localisation of the FMRFamide receptor as expressed from pmCherry-FaNaCh

AtT20s were plated and co-transfected as outlined above with pmCherry-FaNaCh and pNPY-EGFP at a 1:1 ratio. Cells were imaged after 24 hours, in standard buffer, using an upright Zeiss 510 Meta laser-scanning confocal microscope (Zeiss, Oberkochen, Germany) with a Zeiss Achroplan 63X/0.95 NA objective. Green fluorescence was excited at 488 nm and emission collected from 505 – 530 nm, while red fluorescence was excited at 543 nm and emission collected > 560 nm. Dual colour confocal stacks with z-slices at 0.67 μm intervals through the cell were taken.

2.5 Patch-clamp Recording of Secretory Events

Electrophysiological experiments were performed using a patch clamp amplifier (EPC9, HEKA Elektronik Dr. Schulze GmbH, Germany). This was controlled and data were recorded using the Pulse (HEKA) acquisition software. The bath was formed of a 35 mm diameter plastic tissue culture dish in a purpose-made perspex holder. The bath was perfused with bath solution (in mM: 135 NaCl, 3 KCl, 2 $CaCl_2$, 1 $MgCl_2$, 10 HEPES, 11 D-glucose titrated to pH 7.3 with NaOH) leaving a bath volume of ~2 ml. The bath was placed on the stage of an inverted microscope (TE200 Eclipse, Nikon Instruments Europe B.V., Surrey, UK). Illumination for fluorescence visualisation was provided by a mercury lamp (Nikon) and was filtered using a Nikon B-2A filter set (excitation: 450-490 nm band-pass, dichroic mirror: 505 nm long-pass, emission: 515 nm long-pass). The microscope was mounted on an air table and surrounded by a Faraday cage. All metal within the cage was connected to a common earth. Pipettes were pulled from thin-walled borosilicate glass with an internal filament (GC150TF, Harvard) in a 2-stage vertical pipette puller (PC-10, Narishige International Ltd, London, UK). These were then coated with sylgard (Dow Corning) and polished using a microforge (MF-9, Narishige). The patch electrode consisted of a pipette which was backfilled with pipette solution (in mM: 120 Cs-acetate, 15 CsCl, 5 NaCl, 10 HEPES 4 MgATP, 0.3 NaGTP titrated to pH 7.2 with CsOH) filtered with a 0.2 μm filter (Nalgene), and placed in the pipette holder. The patch electrode was connected to the head stage of the patch amplifier by a silver chloride-coated wire. The bath electrode was formed from a silver chloride bead in a small bath solution-filled reservoir

connected to the head stage ground. This was, in turn, connected to the bath via an agar bridge.

AtT-20s were plated onto 35 mm plastic tissue culture dishes. After 24 hours cells were co-transfected with 0.65 µg of pNPY-seGFP, 0.65 µg of pFaNaCh (or mCherry-tagged FMRFamide channel) and 0.2 µg of QBI 25 (Qbiogene) which encodes cytosolically expressed GFP because the optical system used did not allow visualisation of NPY-seGFP fluorescence.

Whole cell recordings were made with a holding potential of –80 mV. Cells were stimulated by stepping from –80 mV to + 20 mV for 3 s before being returned to –80 mV. Alternatively a similar protocol with the same amplitude stimulation step for 25 ms at 5 Hz was used. These stimulation protocols followed that of Whim and Moss (Whim and Moss, 2001) and were expected to give a rapid inward current in response to FMRFamide release from a cell expressing both the FMRFamide tag and the FMRFamide channel (FaNaCh). In some experiments the function of the FaNaCh channel (as expressed from either pFaNaCh or pmCherry-FaNaCh) was tested by making a whole cell recording, holding at -80 mV, while extracellular solution was switched between bath solution and 200 nM FMRFamide solution.

Investigation of the effect of fluorescent-tagging on the time course of secretory events

As a further control the effect of fluorescent-tagging on the time course of secretory events was investigated. Three different versions of the NPY-construct were used: pNPY-2F which coded for non-amidated NPY-tagged with two copies of FMRFamide (as described in Whim, 2006), pNPY-seGFP or pNPY-Venus, a modification of pNPY-2F, which had been previously produced in Professor Matthew Whim's laboratory. pNPY-Venus coded for the YFP variant Venus attached to the C-terminus of NPY as a fusion product (Mitchell et al., 2008). AtT20s were plated onto 35 mm plastic tissue culture dishes and co-transfected after 24 hours with 0.65 µg of the NPY-construct under investigation, 0.65 µg of pFaNaCH and 0.2 µg of QBI. Cells were recorded from 24-72 hours post transfection. These experiments were primarily carried out in the laboratory of Professor Matthew Whim (Department of Biology, Penn State University, PA, USA) with supplementary experiments in UCL, using the apparatus outlined in the previous section.

Electrophysiological recordings were carried out in a similar way to that described above. The patch-clamp amplifier used was a MultiClamp 700A (Axon, Molecular Devices, CA, USA), digitised using a Digidata 1322A (Axon, Molecular Devices) the amplifier was controlled via a PC running the Multiclamp Commander 700 software (Axon, Molecular Devices). Data were acquired using Clampex version 9 (Axon, Molecular Devices). The bath and pipette solution used were as outlined in the previous section. Some recordings were made with pipette solution supplemented with 200 μM cyclic-AMP. The stimulation protocols used were as described in the previous section.

2.6 Combined optical and electrophysiological recording of NPY-seGFP

In order to follow peptide secretion optically a fast imaging system was needed. These experiments were therefore done in the laboratory of Dr Tom Carter (National Institute for Medical Research, UK) using his system which combined fast imaging with electrophysiological recording. AtT-20 cells were plated on glass in commercially available glass-bottomed dishes (MatTeK Corp., Ashland, USA) as for in-house-fashioned glass-bottomed dishes. Cells were co-transfected with pNPY-seGFP and either pmCherry-FaNach, or pFaNaCh + dsRedN1 (cytosolically expressed dsRed) and imaged in standard buffer after 24 – 72 hours. In later experiments cells were plated in in-house-fashioned dishes with various coatings. Cells were only imaged after a successful patch had been made in the whole cell configuration.

Whole cell recordings were made using an Axopatch 200B amplifier and headstage (Axon, Molecular devices). Imaging was performed using a fast acquisition system formed of an Olympus IX71 inverted fluorescence microscope, an Olympus U Plan S Apochromat 100X/1.40 NA objective, a fast wavelength switching monochromator (Cairn Research, Faversham, United Kingdom) and an Ixon EMCCD camera (Andor, Belfast, United Kingdom). Wavelength switching, image capture and electrophysiological recording and stimulation were synchronised using WinFluor software (Dr John Dempster, Strathclyde University, Glasgow, United Kingdom).

Acquired optical data, were averaged where desired to give 1 s intervals between frames in WinFluor. Averaged or raw data were then exported in a lossless format and analysed in ImageJ (Abramoff et al., 2004). Regions of interest were identified and the average pixel intensity found for all frames.

2.7 Scanning ion conductance microscopy

These experiments utilised an Ionscope scanning ion conductance microscope, mounted on a Nikon TE2000 optical microscope. The SICM was operated in hopping mode (Novak et al., 2009) with a set point of 0.4 – 1 %. Nanopipettes were pulled using thick-walled borosilicate glass (1.0 mm OD, 0.58 mm ID; Intracel Ltd, Hertfordshire, UK) on a P-2000 laser puller (Sutter Instrument Company, CA, USA). All pipettes were coated with ski wax (Mammut Sports Group, Switzerland, ToKo all-in-one hot wax) to reduce noise.

Primary human umbilical vein endothelial cells (HUVECs) were cultured and transfected by nucleofection by Dr Laura Knipe (NIMR) as previously described (Erent et al., 2007). Cells were transferred to standard buffer before scanning. Transfected cells were identified by fluorescence. SICM scans with a 1 % set-point were made before and after stimulation with 2 μM ionomycin. The loss of some VWF-EGFP from transfected cells after stimulation was confirmed by fluorescence.

In later experiments AtT-20 cells were plated on either plastic (nunc) or glass bottomed dishes and transfected with 0.8 μg of pNPY-seGFP and 0.2 μg of the cytosolic RFP pdsRed-N1 (Clontech-Takara Bio Europe, France) and prepared for imaging 24-48 hrs post transfection as describe in section 2.2. The growth medium was exchanged for standard buffer before scanning and standard buffer was also used as pipette filler. Transfected cells were scanned before and after stimulation with 10 μM ionomycin (Sigma) or 20 mM caffeine (Sigma). seGFP fluorescence images were also acquired, using a WAT-120N camera (Watec, Japan), before and after stimulation to monitor secretion.

2.8 Finite Element Model of SICM

An electrostatic model of SICM was developed and is described in detail in Chapter 3. This involved the numerical solution of the Laplace equation (Eq. 3.2, Chapter 3) using the finite element method (FEM). Boundary conditions were applied which approximated the system of an experimental SICM probe at some height above an insulating surface, submerged in a bath of conducting solution. This analysis was performed using Matlab (version R2008b, The Mathworks Inc., Cambridge, UK) and GiD (GiD version 9, International Centre for Numerical Methods in Engineering CIMNE, Barcelona, Spain).

In order to address arbitrary surfaces, Matlab was used to generate a batch file that specified the problem geometry and gave detailed meshing instructions. This batch file was then interpreted using GiD software and a 3D mesh was generated in the simulation volume. (Although many SICM problems can be solved in 2D, some require 3D capability, as described in Chapter 4. Consequently all simulations used an environment capable of 3D.)

Meshes were generated using an unstructured grid. Although structured (regular) meshing is adequate for relatively simple 2D problems, unstructured meshes are far more flexible and thus provide the most powerful approach when trying to cope with 3D geometries. Even so, some geometries could not be dealt with by GiD. In these cases, a similar, nearby pipette position was simulated, wherever possible.

All meshed geometries were then returned to Matlab for solving. Within Matlab, boundary conditions were applied and the FE method was applied to solve Laplace's equation for the potential ϕ (Eq.3.2, Chapter 3). For speed, the matrix manipulations were implemented using a Matlab MEX file extension written in C++. The system was solved by direct matrix inversion using the Gauss-Legendre method. The current flowing through the pipette was then calculated from the potentials in Matlab. The pipette resistance R_p was adjusted to compensate for the truncated pipette length used in the simulation and the current was rescaled based on this new resistance.

During each simulation the system was modelled with the pipette at a range of heights above the surface. This process was then repeated for a series of points in the x,y plane. Further calculations were then performed to allow a simulated height profile to be extracted. Further detail of these calculations is given in Chapter 3.3

The C++ and Matlab code for solving Laplace's equation and calculating the pipette current were written by Dr Eero Willman (Department of Electrical Engineering, UCL). The code to generate geometries and meshes and to control the flow of the model were written by the author. The code used in the model may be found in Appendix 1.

Chapter 3

Development and validation of a finite element method model of SICM

In this chapter a finite element approach is described and tested as a means of understanding SICM imaging in a more quantitative way.

3.1 Previous approaches to modelling SICM

There have been a number of previous attempts to model probe-surface interactions in SICM. One of the first of these was by Adenle and Fitzgerald (Adenle and Fitzgerald, 2005) and was based on finding an approximate expression for the probe current using a pre-existing model of the oxidative ion concentration at an inlaid disk microelectrode held at very negative potential (Bond et al., 1988). Using this model Adenle and Fitzgerald were able to simulate a number of different scan modes of SICM such as constant-distance, constant-current and distance-modulated SICM. Despite covering a number of scan modes, this work did not consider the recent, new scan regime of "hopping-mode" SICM (Novak et al., 2009). Hopping mode allows surfaces with large height changes to be mapped more effectively. In "hopping-mode" for each point scanned in the x,y plane the probe is first withdrawn to a safe height above the surface, then moved laterally before finally being lowered towards the sample until the current set-point is reached, and the z-piezo height recorded. This minimises crashes when laterally approaching tall objects and therefore allows better scanning of complicated structures such as neuronal processes. Adenle and Fitzgerald's model represented an interesting approach but it has not since been developed to investigate hopping mode SICM or to help understand some of the more essential properties of the scanning ion conductance microscope such as the lateral resolution of an SICM probe. In addition, the work of Adenle and Fitzgerald revealed some variation between experimental and simulated approach curves even with this simple model, suggesting that the approximation of ion current they chose may not be as accurate as needed for detailed analysis.

A number of reports have used finite element analysis either to examine SICM or to understand the behaviour of SICM-like probes. For example, Bae and Butler used a finite element approach to estimate membrane tension, stress, and strain under the tip of a microelectrode probe (Bae and Butler, 2008). Ying and co-workers (Ying et al., 2004) briefly examined a conical pipette (filled with buffer solution and with constant

ion current through the pipette) in a finite element model, applying boundary conditions to solve Poisson's equation. They used a 2D model of the pipette and only studied a position far from the sample surface where they examined variations in the electric field close to the pipette tip, both inside and outside. This simple model demonstrated that most variation in the electric field occurs inside the pipette close to the tip and that the field falls to zero very rapidly outside the tip.

The most recent works in modelling SICM were published after this project began, and are far more extensive than the previous studies. This work was carried out by Edwards and co-workers (Edwards et al., 2009) and Rheinlaender and Schäffer (Rheinlaender and Schäffer, 2009). Both of these studies also used the finite element method to model the SICM probe current and its relation to the position above a sample surface. The generality of this approach and the fact that it is based on the physical (electrostatic) properties of the system (and therefore does not rely on an assumed form of access resistance) make it attractive.

Edwards et al., used their model to look at both modulated and unmodulated scanning modes, but with an emphasis on the modulated scanning approach. Edwards and co-workers made some good initial progress in looking at the validity of their model and in examining two example surfaces. The first was a sharp square step, (elongated in 3D so it is approximately a 2D problem). For these simulations Edwards et al., attempted to estimate the broadness of the probe-current response to the step and attempts were made to validate the simulations with experimental data (although the relative sizes of the pipette and surface features they used were not ideal for this). Edwards et al., also examined probe interactions with an object that was smaller than the probe tip, as is done later in this thesis. Ultimately however, although the work of Edwards et al predicts some important scan profiles, it does not go on to resolve a number of other important issues. For example, it does not provide an exact estimate of lateral resolution. The work of Edwards et al., also has some limitations for practical applications in SICM. For instance, the values used in the simulations for some of the variables, such as the glass thickness, did not match well with those used experimentally for scanning. Furthermore, they chose a probe half-cone angle that is probably unrealistic.

Rheinlaender and Schäffer also recently presented a finite element method (FEM) model of SICM and based their analysis on a constant-height scan mode, with further calculations used to approximate a constant-current mode (based on the

assumption that the approach curves to different structures will have the same form and therefore need only to be shifted in height). They examined lateral resolution in a more quantitative way, both by examining the lateral distance taken to respond to a single object and also the ability to resolve a pair of objects. Their model was not experimentally validated but did allow them to define an "effective correlation transfer function" which described the inherent image distortion produced by an SICM scan that fitted the simulated data well. Their work offers quantitative measures of lateral resolution but may be limited by the lack of experimental validation, the possible inaccuracy due to the assumptions on which their constant-current mode is based and by only simulating objects which are both much shorter and narrower than the probe inner diameter. This last factor may lead to complications due to possible artefacts introduced when scanning objects smaller than the probe diameter and is examined later in this thesis.

Therefore, although the studies of Edwards and co-workers and of Rheinlaender and Schäffer provide excellent support for the FEM approach to modelling SICM, and make a number of important advances they leave open a number of questions. The work in this thesis will address these issues using a FEM model of SICM. As a starting point, some simple approaches to validate my FEM model are considered.

3.2 Finite element model of SICM

The simulations presented here are for an electrostatic model. In physics, the term ‘electrostatic’ is applied whenever there are no time-varying electric fields as is the case when a constant potential difference is applied to the electrodes in hopping mode SICM. The SICM probe, the sample surface, the bath and the bath electrode are all considered in the model.

In general any problem in electrostatics can be solved by finding a solution to Gauss' Law ($\nabla.\varepsilon_r \underline{E} = \rho_s / \varepsilon_0$) which is equivalent to Poisson’s equation for the potential, ϕ:

$$\nabla.(\varepsilon_r \nabla\phi) = -\frac{\rho_s}{\varepsilon_0} \qquad \text{Equation 3.1}$$

Where ρ_s is the space charge density, ε_0 is the dielectric constant and ε_r is the permittivity. In our case since there are no free charges this simplifies our problem to the Laplace equation:

$$\nabla.(\varepsilon_r \nabla\phi) = 0 \qquad \text{Equation 3.2}$$

If we solve this equation with the appropriate boundary conditions the potential field given will be that of our problem. We may also calculate the current flowing through the pipette using some simple relations. First the electric field may be calculated by:

$$\underline{E} = -\nabla\phi \qquad \text{Equation 3.3}$$

Then the current density J may be calculated from:

$$\underline{J} = \sigma \underline{E} = -\sigma\nabla\phi \qquad \text{Equation 3.4}$$

Where σ is the conductivity. The current flowing through the metal electrode (perpendicular to the surface) may then easily be calculated from the current density by:

$$I = \int_S \underline{J} \cdot d\underline{A} \qquad \text{Equation 3.5}$$

Where d$\underline{A}$ is a surface element of surface S. Similarly other properties of interest may be calculated once the potential solution is found.

In order to represent complicated probe and surface geometries it was decided to use a 3D model. As indicated earlier, in order to solve the Laplace equation for an arbitrary 3D system it is necessary to use a numerical solution method since the problem is not analytically tractable. Several numerical methods exist but the two which seem most useful for this type of problem are the finite difference method (FDM) and the finite element method (FEM). For both of these methods the simulation volume is "meshed", i.e. divided into subvolumes. Numerical approximations are then applied to solve the equations within each of these small subvolumes. FDM is based on the application of physical laws at a point whereas FEM is based on their application across a surface or volume. FDM is a useful method but is easiest to apply with the simulation space split up into a uniform mesh of grid points. This reliance on a uniform mesh makes it difficult to represent complicated surfaces and can prove very computationally expensive for large simulation volumes as the size of mesh elements is fixed. FEM may be used with conformal (non-uniform) meshes which more closely follow the geometrical boundaries of the system and also allow variable mesh element sizes which may reduce the computations needed by allowing larger mesh elements to be used in areas with little variation in electric field E. For these reasons, it was decided to use the finite element method to model SICM.

3.3 Details of the model used to simulate SICM

Overview of simulation procedure

As described above, the finite element method was chosen to model the potential changes (and hence changes in current flow) as a SICM probe approaches a surface with an arbitrary topography. An overview of the steps used in this model is described here and more detailed explanations are given later.

In order to address arbitrary surfaces, Matlab was used to generate a batch file that specified the problem geometry and gave detailed meshing instructions. This batch file was then interpreted using GiD software (CIMNE, Spain) and a 3D mesh was generated in the simulation volume. (Although many SICM problems can be solved in 2D, some require 3D capability, as described in Chapter 4. Consequently all simulations used an environment capable of 3D.)

Meshes were generated using an unstructured grid. Although structured (regular) meshing is adequate for relatively simple 2D problems, unstructured meshes are far more flexible and thus provide the most powerful approach when trying to cope with 3D geometries. Even so, some geometries could not be dealt with by GiD. In these cases, a similar, nearby pipette position was simulated, wherever possible.

All meshed geometries were then returned to Matlab for solving. Within Matlab, boundary conditions were applied and the FE method was applied to solve Laplace's equation for the potential ϕ (Eq.3.2). For speed, the matrix manipulations were implemented using a Matlab MEX file extension written in C++. The system was solved by direct matrix inversion using the Gauss-Legendre method. The current flowing through the pipette was then calculated from the potentials in Matlab. The pipette resistance R_p was adjusted to compensate for the truncated pipette length used in the simulation and the current was rescaled based on this new resistance.

During each simulation the system was modelled with the pipette at a range of heights above the surface. This process was then repeated for a series of points in the x,y plane as outlined in Figure 3.4. From these data an approach curve (pipette current vs. height above the surface) was produced at each of the specified positions in the x,y plane. Because SICM imaging operates by using a current set-point to estimate sample height, and it is not possible to know in advance where the set point will be reached, approach curves were interpolated. The height at which the set point was reached (i.e. a given current reduction compared to the current flowing when the pipette was far away

from the surface) was then calculated, thus allowing the returned height at that set-point to be found.

The C++ and Matlab code for solving Laplace's equation and calculating the pipette current were written by Dr Eero Willman (Department of Electrical Engineering, UCL). The code to generate geometries and meshes and to control the flow of the model were written by the author. The code used in the model may be found in Appendix 1.

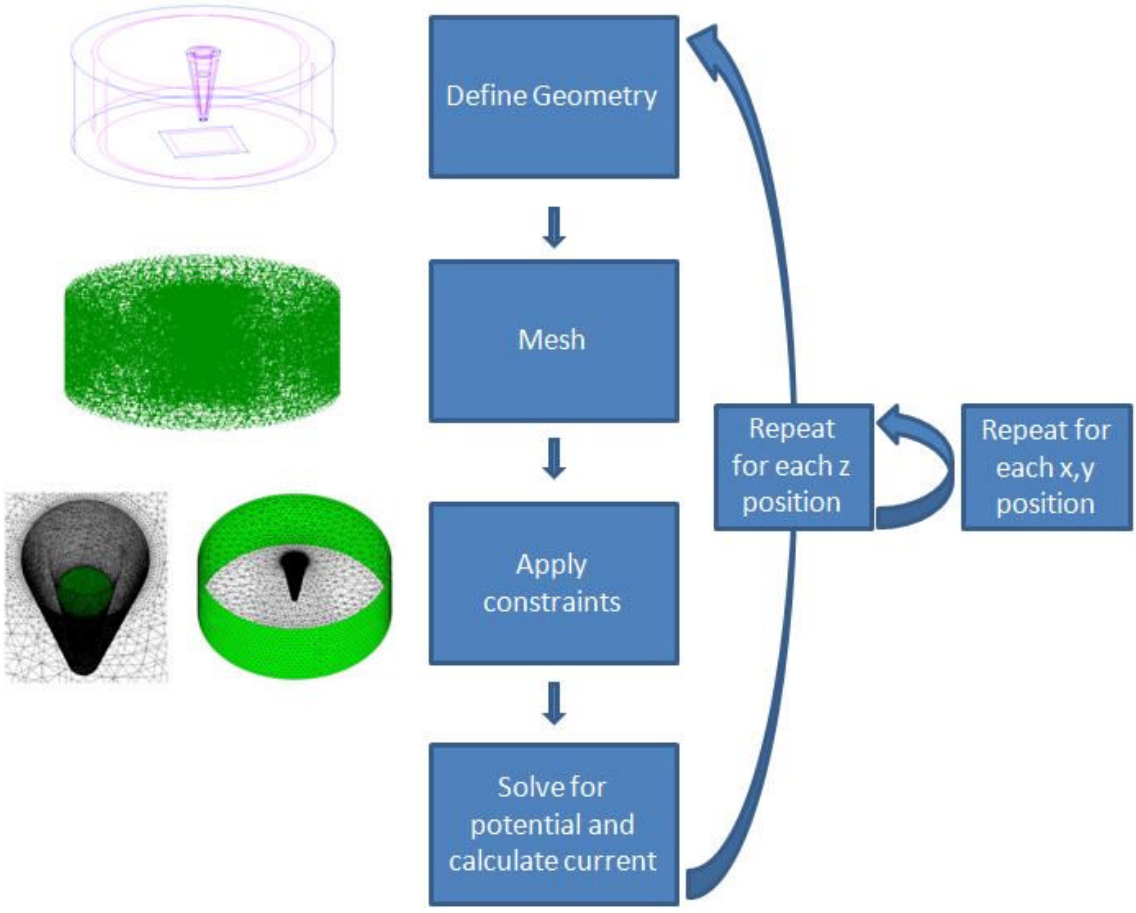

Figure 3.4 Overview of the steps involved in the modelling process
For each (*x*,*y*,*z*) position the problem geometry was defined, this geometry was then discretised using a mesh of 1D points, 2D triangles and 3D tetrahedra. Boundary conditions were assigned to surfaces, such as the pipette electrode, previously defined in the mesh. Volumes in the mesh were assigned to either the conducting solution or the pipette glass such that constraints could be applied at the boundary. Laplace's equation for the potential was then solved using the specified boundary conditions. The current flowing through the pipette was then calculated from the potential. For each *x*,*y* position a series of *z* positions were simulated.

Model geometry and boundary conditions

The pipette was typically modelled as a cone (Fig. 3.5a) of half angle 3 º since this is the cone angle estimated from SICM pipettes imaged by electron microscopy (Ying et al., 2004). All distances in the model were expressed in units of inner pipette radii (r). The outer diameter of the pipette was typically specified using an outer:inner ratio (OD:ID) of 1:0.58. This is the (OD:ID) of the glass capillaries used experimentally for pulling SICM probes in this laboratory (Intracell, Royston,UK). In the model it was thus assumed that this ratio stayed constant, when the glass is pulled, as seems to be the case experimentally (Corey and Stevens, 1983). The wire electrode inside the pipette was simulated as a conducting disc a fixed distance from the pipette mouth (Fig. 3.5b). This disc was given the Dirichlet boundary condition i.e. a constant potential $\phi = V_0$ was assigned to it. The ground electrode was simulated as a conducting ring around the simulation volume (Fig. 3.5c) to allow a smaller total simulation volume to be used without biasing any particular direction. The ground electrode was given the fixed potential of 0. The walls of the pipette were treated as a dielectric with the permittivity of borosilicate glass of $4.7\varepsilon_0$ (where ε_0 is the permittivity of free space). The inside of the pipette and the bath were treated as a conducting solution with conductivity 1.25 $\Omega^{-1}cm^{-1}$ (calculated as the inverse of the resistivity of Ringer's solution of 80 Ωcm (Hille, 1992). The potential solution was allowed to be discontinuous at the boundaries between the pipette wall and the conducting solution, such that current could not flow across the boundary but the behaviour of the electric field could be treated accurately. Therefore at the glass-liquid boundaries $d\phi/dn$, the rate of change of ϕ with respect to the surface normal n, was allowed to be discontinuous at this boundary and set to zero on the glass side and left free on the liquid side. The surface to be imaged was treated as an insulator and so took the Neumann boundary condition $d\phi/dn = 0$.

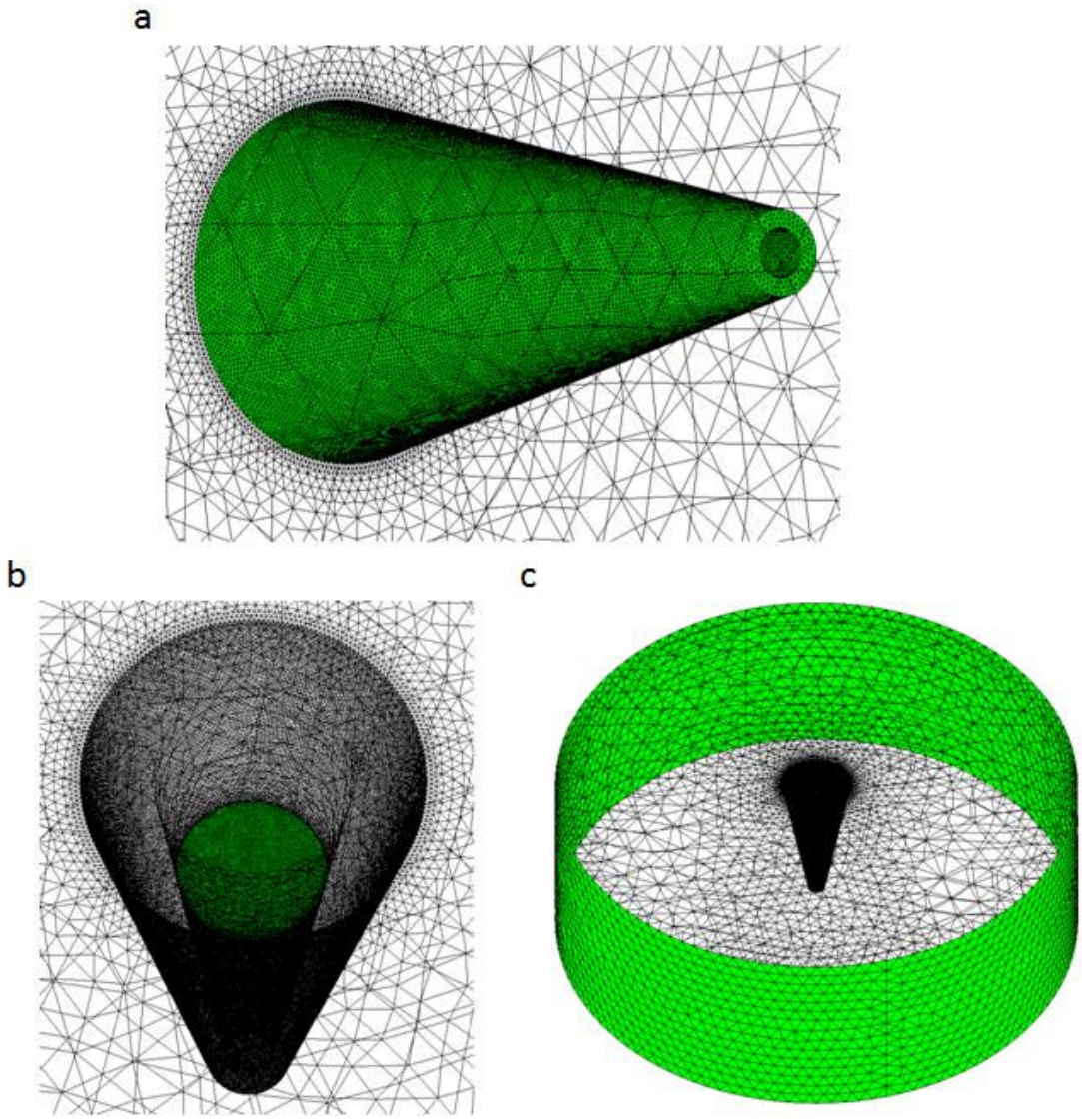

Figure 3.5 Geometry of the simulated pipette and ground electrode
The pipette was modelled as a cone of dielectric material with the geometry as in (a). The pipette electrode was modelled as a conducting disc a fixed distance from the pipette tip (b). The ground electrode was modelled as a circular sheet at the edge of the simulation volume (c).

Choice of mesh element sizes and total simulation volume

The FE method tends to become more accurate at finer mesh sizes, (unless for example, numerical rounding errors become increased disproportionately in attempting to find the solution). However, small grid sizes create very large data sets that dramatically reduce modelling speed. This quickly becomes a problem and even without such large data sets, typically, the simulation for each geometry reported in this thesis took 2-5 days to run. Therefore, a variable resolution mesh was used, with a finer

mesh in important areas such as the pipette electrode, the glass-liquid interface and the insulating surface (where there are likely to be more rapid changes in potential or more complex surfaces to be represented).

In order to check the accuracy of the simulations the maximum mesh element spacing in different parts of the mesh was varied. In particular the mesh size on the pipette electrode was investigated as the potential varied rapidly close to this electrode and the number of elements was also expected to affect the accuracy of the current calculation from the solved potential values. With this mesh size varying, a series of simulations were run to estimate the approach curve when the pipette interacts with a flat surface. There was no significant trend in the solutions found when the mesh size was varied over the range 0.01-0.2. Therefore, a maximum mesh element size of 0.1 units was used in all subsequent simulations (Figure 3.6).

The choice of the height and radius of the simulation volume was also investigated. In order to reduce the modelling time, the radius of the simulation volume was typically of the order 10r, whereas experimentally this value would be of the order 10^5r. It was therefore necessary to verify that the simulation volume chosen was large enough to give an appropriate separation between the pipette and the ground electrode. Similarly, the height used in the simulation was much less than that of the experimental situation. To validate the simulation volume height and radius chosen, the approach of a pipette to a flat surface was modelled as the simulation height was doubled (Figure 3.6b triangles) and as the simulation radius was doubled (Figure 3.6b squares). The approach curves thus generated were then compared to the standard conditions used (Figure 3.6b red points). No significant changes in the model solutions were found in either case. This suggested that the choice of simulation height of 35 units and simulation radius of 55 units were not affecting the calculated currents. As can be seen in Figure 3.9a most of the potential changes occur within the pipette with very rapid changes at the tip. Therefore it seems reasonable that the simulation volume used did not affect these currents.

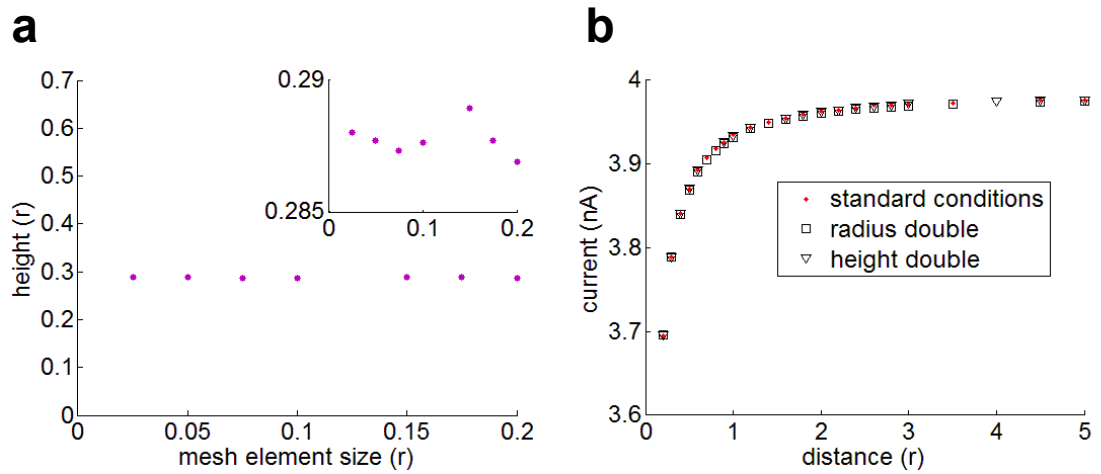

Figure 3.6 Validation of model mesh element size and total simulation volume
a) The maximum mesh element size on the pipette electrode was varied and the returned height at a 5 % set-point was measured. No trend was observed in the returned height below 0.2 units. b) Current-distance curves calculated in simulation volumes where the height of the simulation (triangles) and simulation diameter (squares) were doubled. These curves are shown along with the simulation height and diameter normally used (red points). These curves could, essentially, be superimposed and thus no significant difference was evident.

Data analysis

The response of the SICM will depend, not only on how the access resistance varies but also on the relative value of the pipette resistance (Eq. 3.38).

$$I = \frac{V_0}{R_p + R_{ac}} \qquad \text{Equation 3.38}$$

Where I is the probe current, V_0 is the applied probe potential, R_p is the probe series resistance and R_{ac} is the access resistance. Therefore, the short length of the pipette within the simulation volume may not provide an accurate estimate of the approach curve. However, as shown below, and in Fig 3.7 the resistance of a conical pipette, filled with a conducting solution can be easily calculated. In general the resistance of a conductor of length L and cross sectional area A of uniform resistivity ρ is:

$$R = \frac{\rho L}{A} \qquad \text{Equation 3.39}$$

For a conical pipette of geometry as shown in Fig. 3.7 the pipette resistance R_p is therefore:

$$R_p = \frac{\rho}{\pi \tan(\theta)}\left(\frac{1}{r} - \frac{1}{r_1}\right) \qquad \text{Equation 3.40}$$

In the limit $r_1 \gg r$, $R_p \rightarrow R_{plim}$:

$$R_{plim} \approx \frac{\rho}{\pi \tan(\theta) r} \qquad \text{Equation 3.41}$$

Therefore, for all simulations the pipette resistance was adjusted to account for the limited pipette length simulated (Fig. 3.7). The current was then rescaled based on the new R_p value, R_{plim}.

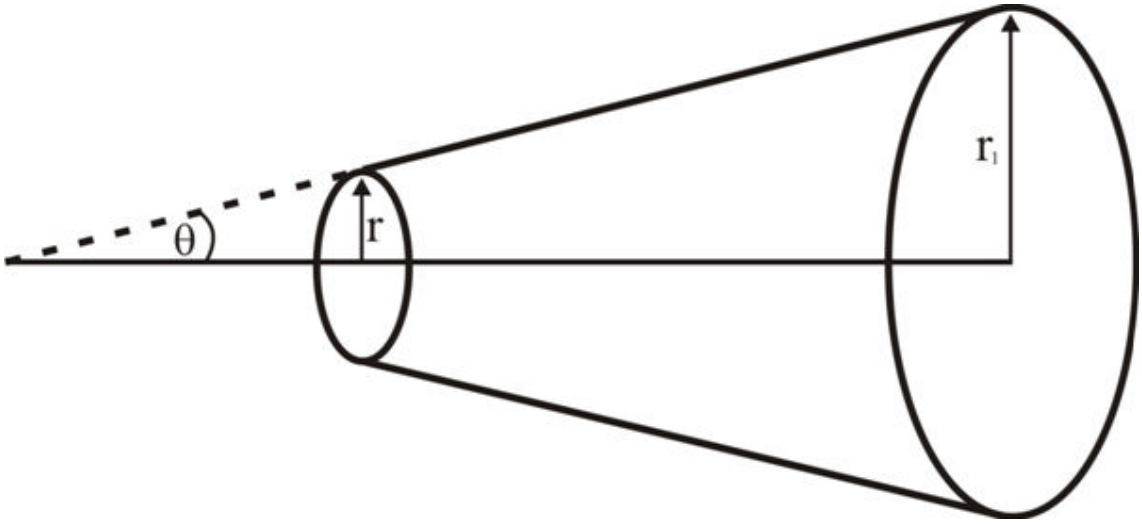

Figure 3.7 The resistance of a conducting cone may be calculated theoretically
For an experimental pipette, the tip radius r « r_1 the radius at the top of the pipette, thus the value of R_p will be given by R_{plim} (see text for definition). The value of R_p found in the simulation was therefore rescaled to R_{plim} and the current then also rescaled.

For each *x,y* position a series of simulations with the pipette a different distance from the surface were performed. For each *x,y* position an approach curve was produced (a plot of the current flowing through the pipette vs the distance between the pipette tip and surface). Given that SICM works by estimating heights at a given set point and that only a limited number of heights may be simulated, the simulation data needs to be interpolated to allow calculation of the returned height for an arbitrary percentage set point (*S*):

$$I_s = I_0\left(1 - \frac{S}{100\%}\right) \qquad \text{Equation 3.42}$$

Where I_s is the probe current at the set point and I_0 is the probe current when the probe is far from the surface. In addition, given that *S* is usually a small fraction (~1%) this interpolation needs to be quite accurate. Initial tests using simple linear interpolation proved that this method was inadequate for these purposes because there is a small amount of scatter in the simulation solutions due to rounding errors. Given the form of

Equation 3.38 and the similarity of Fig. 3.8 to a dose-response curve, an initial attempt was made to fit the data to a Hill function of the form shown in Equation 3.43 (where z is the height between the pipette tip and the surface and A_1-A_4 are constants):

$$I = \frac{A_1}{A_2 + \frac{A_3}{z^{A_4}}} \qquad \text{Equation 3.43}$$

Although this provided a superficially reasonable fit, it was not found to be adequate in many cases. By trial and error Equation 3.43 was extended to the form of Equation 3.44 and it was found that most curves could be fitted very well (i.e. showed no systematic deviation of residuals) with a function of this form:

$$I = \frac{A_1}{A_2 + \frac{A_3}{z^{A_4}} + \frac{A_5}{z^{A_6}}} \qquad \text{Equation 3.44}$$

This is illustrated in Fig. 3.8 where linear interpolation and fitting are compared over the critical range where the current varied from I_0 by 0 – 2.5%.

The fitting function was then used to determine the returned height for a given percentage set-point. I_0 the current far from the surface was taken as the fitted current value at a separation between the surface and probe tip of 10r since the current was seen to vary little above this height. The percentage change in I, was then analysed and the value of z at which $I = I_s$ gave the returned height at that set-point. When fitting a set of approach curves for different x,y positions, on the same surface, fits were only accepted if the values of I_0 varied by < 0.05 %. Fits were also tested for systematic deviations by plotting residuals (the difference between a fit and the simulated data). Fits with systematic deviations were rejected. Using Equation 3.44, it was possible to fit almost all curves without any obvious systematic deviations. However, in a few cases it was not possible to maintain this quality of fit over the entire approach curve. In these cases, fits were made only to the upper portion of the approach curve which will, in practice, be the essential region for determining sample heights during scanning. In such cases approach curves were only analysed for returned height within the well fitted region of the simulated data.

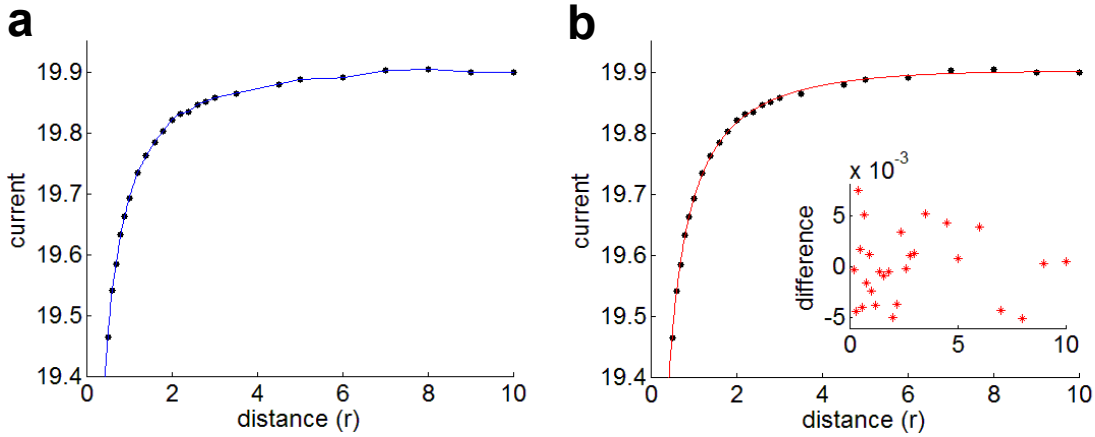

Figure 3.8 Interpolation of approach curves to allow analysis at arbitrary set points
Linear interpolation (a) gives rise to errors due to scatter in the simulated data, probably caused by rounding errors. Fitting with Equation 3.44 (b) gives a more accurate fit over the critical range of set-point from 0 – 2.5 %. A fit to Equation 3.44 was only accepted if no trend was seen in the residuals (inset).

3.4 Validation of the model

Although these simulations are designed to predict the pipette current in situations where analytical solutions are not available, there are some simple tests that can be done to provide confidence in the simulation. These are discussed below.

Variation of potential within the pipette shaft

Equation 3.40, used to predict the resistance of the pipette also provides a way to predict the potential changes within the pipette shaft. We may calculate the potential found at the tip V_{tip} of a pipette of length z, and resistance up to length z of $R(z)$ as:

$$V_{tip} = V_0 - IR(z) \qquad \text{Equation 3.45}$$

Substituting from Eq. 3.38 for the current I gives:

$$V_{tip} = V_0 - \frac{V_0 R(z)}{R_p + R_{ac}} \qquad \text{Equation 3.46}$$

Where R_p is the total pipette resistance and is calculated from Equation 3.40 and $R(z)$ also takes a similar form:

$$R(z) = \frac{\rho}{\pi \tan(\theta)}\left(\frac{1}{r(z)} - \frac{1}{r_1}\right) \qquad \text{Equation 3.47}$$

This was used to predict the potential down the shaft of a simulated conical pipette of three different half-cone angles. The value of R_{ac} chosen was that predicted for a circular pore by Hall (Hall, 1975, see below for further explanation). These theoretically predicted curves were then compared to simulated data for a pipette of the

specified half-cone angle far away from a flat surface. It can be seen that the potential change along the central axis of the pipette is non-linear and that much of the potential drop occurs at the tip for a conical pipette. Thus, visually, it can be seen that these solutions are qualitatively correct. A more accurate, quantitative prediction can be made by extracting the simulated potential values down the pipette and comparing them to the predictions of Eq. 3.46. This is done in Fig. 3.9b. As can be seen, the simulations (coloured points) give values that agree well with the expected analytical solution (coloured lines). The dotted line in Fig. 3.9b shows the effect on the analytical solution of using the access resistance value found in the simulation. This gives a very small difference in the predicted potential which increases with increasing half-cone angle (although this is still a small difference even at a 12˚ half cone angle), as might be expected as the pipette deviates further from a circular pore.

a

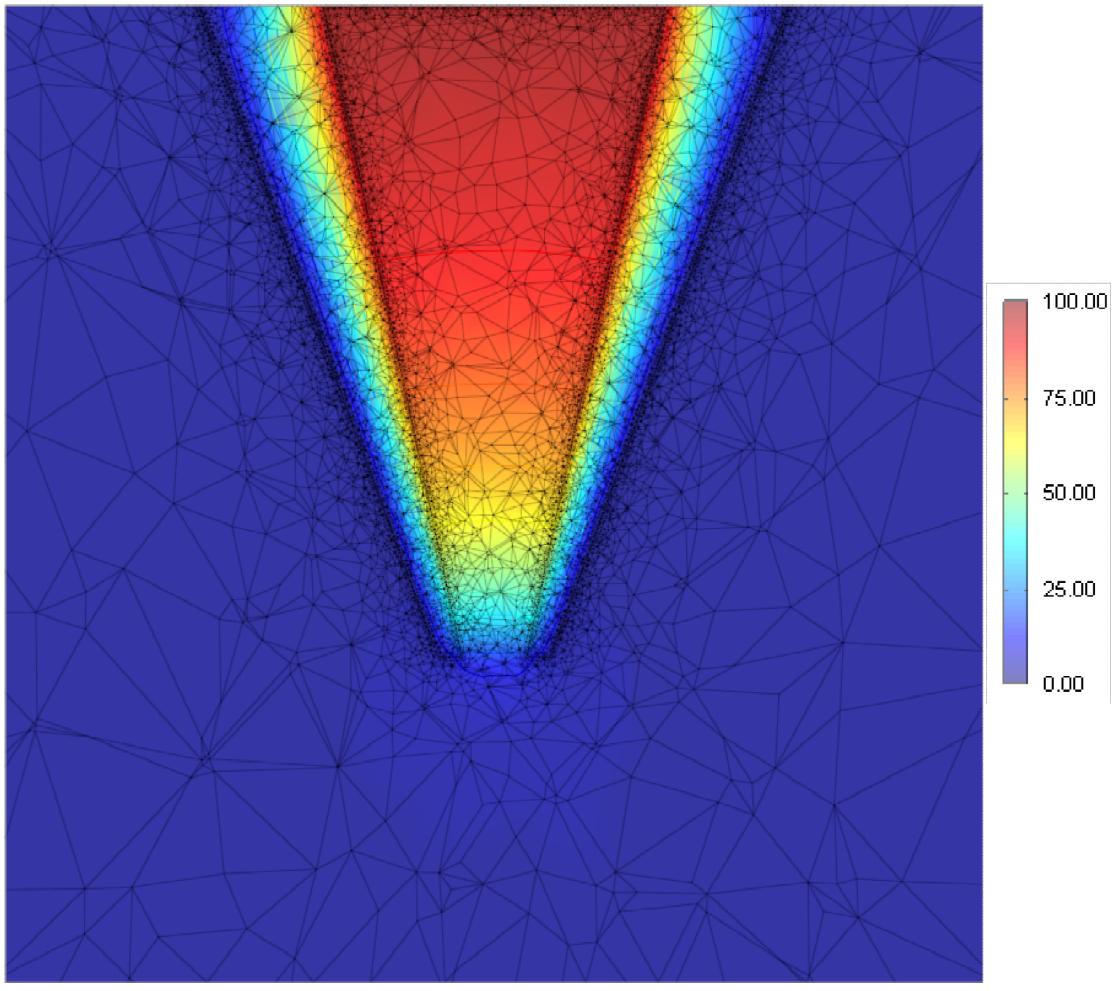

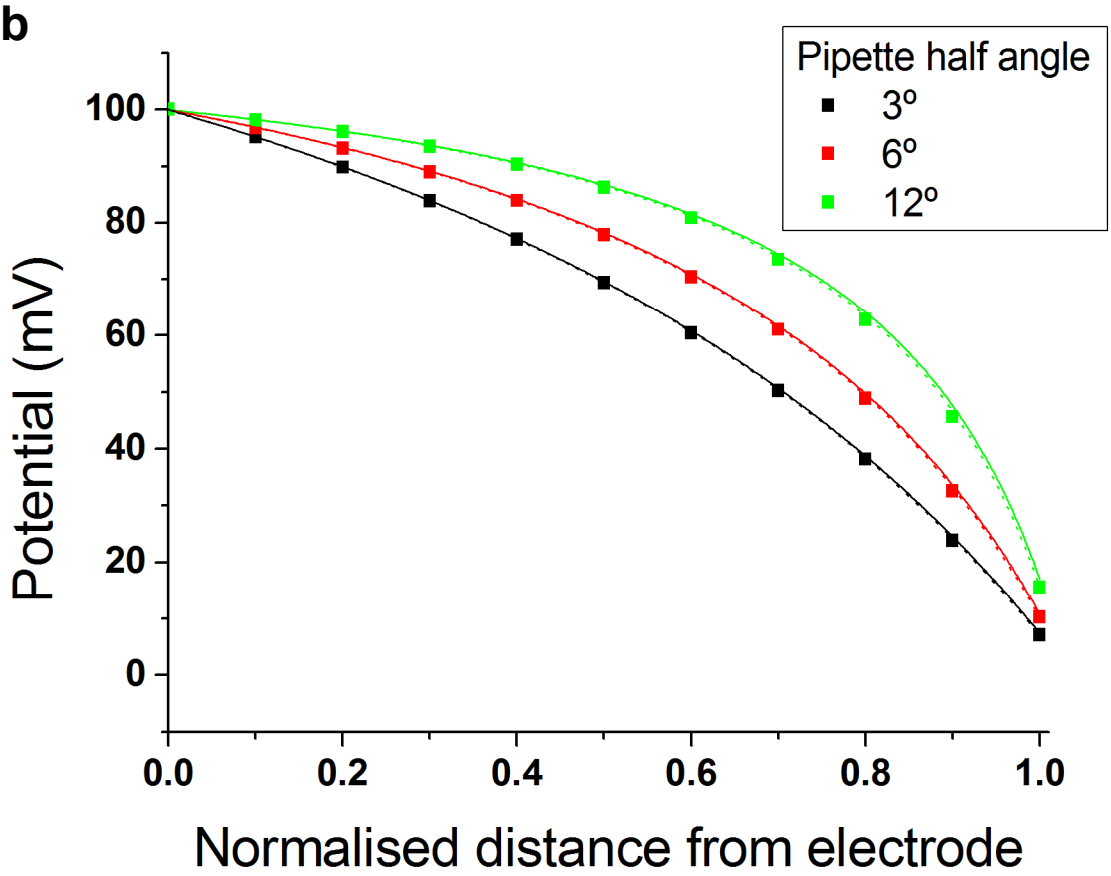

Figure 3.9 The potential within a conical pipette
a) (previous page) Shows the potential solution for a simulated conical pipette of half-angle 12 º. A pseudo-colour plot of the potential superimposed on the mesh for the pipette and surroundings is shown when the pipette is far from a flat surface. The potential is free to vary through the pipette glass but no current may flow across the glass-pipette boundaries. The pseudo-colour scale bar range is from 0 – 100 mV.
b) Shows a comparison of the simulated potential, sampled at different points along the pipette, (points) with the theoretical value as calculated by Equation 3.46 and using either the theoretical value of R_{ac} (Eq. 3.49) (solid lines) or the value of R_{ac} that could be calculated from the simulations (dotted lines). This was carried out for pipettes of half-cone angles 3 º (black), 6 º (red) and 12 º (green). The simulated data appear in good agreement with the prediction.

Variation of access resistance with glass thickness

Interest in ion channel research has led to two previously calculated estimates of the access resistance for a small circular pore in a biological membrane by different analytical approaches. These are of interest for comparison to our pipette access resistance in open solution. In the first case a calculation was made by assuming that the pore access resistance would be equal to that of the convergence resistance to a hemisphere (Hille, 1968). This estimate provided the value shown in Equation 3.48:

$$R_{ac} = \frac{\rho}{2\pi r} \qquad \text{Equation 3.48}$$

In the second case, a more accurate estimate was made using a result from electrostatics, calculated on the assumption that the mouth of the pore is an equipotential surface (Hall, 1975). In this case it was found that the access resistance was given by:

$$R_{ac} = \frac{\rho}{4r} \qquad \text{Equation 3.49}$$

It is reasonable to assume that the simulation data should provide an estimate of the access resistance that is close to these predicted values (particularly the second, more accurate, calculation). However, given that these access resistance calculations show a π/2-fold change in the calculated value when the region outside of the pore is included in the calculation, then the thickness of the glass may well influence the access resistance calculated from the simulation. Thus, a number of simulations were undertaken to address these issues. The results are shown in Fig. 3.10. The estimated access resistance does indeed vary with glass thickness, although the variation is quite small over the range of experimentally used glass thicknesses (typically OD:ID of 1:0.78 (1.28) to 1:0.5 (2.0)). The results from simulations given an asymptotic value of R_{ac} = 2.11 kΩ, which is within 6 % of the second, more accurate estimate of access resistance R_{ac} = 2.0 kΩ (assuming r = 100 nm and ρ = 80 Ωcm in both calculations). The small difference remaining may well be because the assumption about an equipotential surface does not apply exactly in our case (Fig 3.11).

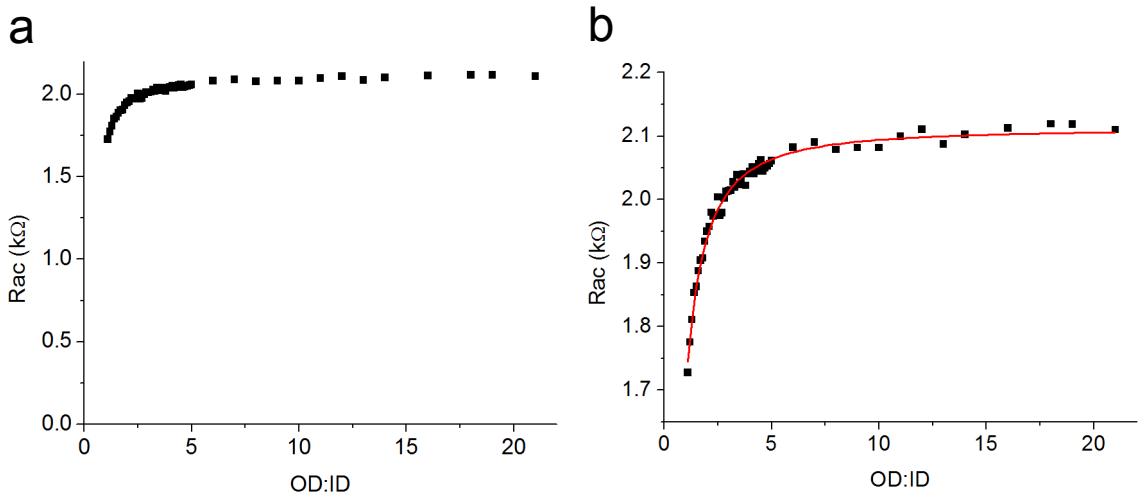

Figure 3.10 Variation of access resistance with probe glass thickness
a) The value of R_{ac} found in simulations with varying glass thicknesses (OD/ID). b) The same data as in a) on an expanded axis for R_{ac}. The red line shows a fit of these data to a Hill equation of the form: $R_{ac} = R_{\max}\frac{x^n}{A^n + x^n}$ where R_{max} is the asymptotic value of R_{ac} and A and n are constants. The fitted values of these parameters was R_{max} = 2.11±0.004, A = 0.37±0.02, n = 1.45±0.05.

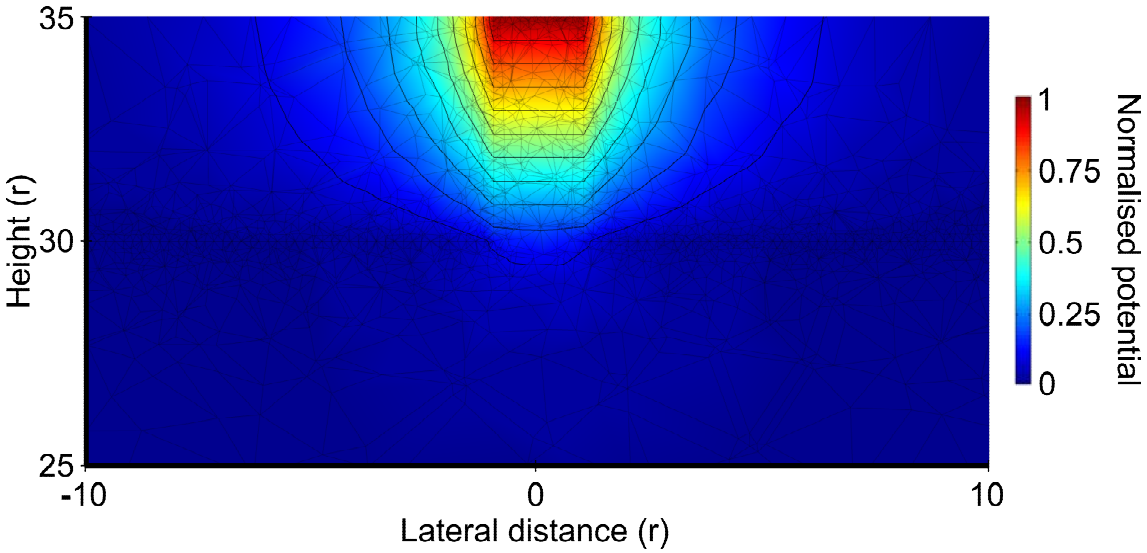

Figure 3.11 Variation of potential at the pipette mouth shown in close up
A pseudo-colour plot of the potential superimposed on the mesh for the pipette and surroundings when the pipette is far from a flat surface for an OD:ID = 22r is shown. The pipette tip is at height 30r. Equipotential lines are also shown. The potential across the pipette mouth is not an equipotential surface.

Approach to a flat surface: comparison with experimental data

Although an exact analytical solution for the pipette approaching a flat surface has not been found we may still compare the simulated approach curve with an experimental approach to a flat surface. For an approach to the flat surface of a petri dish the experimental approach curve (shown as current vs time for a constant fall rate in Fig. 3.12a) has a surprising shape. In the final stages of the approach before full current shutdown the gradient of the approach curve is significantly reduced. However, obtaining data for an SICM probe approaching a perfectly flat surface is very difficult. Further, making sure that the probe is exactly perpendicular to this surface is also difficult. Therefore, the more likely situation is that the probe tip will contact the surface before the pipette current reaches zero. If this happens the pipette will bend. Therefore, we need some way of telling whether contact has been made, and hence, which parts of the approach curve are useful. One observation that can help us is the steepness of the approach curve. All theoretical models predict that the approach curve becomes steeper as the probe nears the sample surface. If this sample is vibrating at all then the distance between the probe and the sample will be varying and hence the probe current will be varying. This variation in current will increase as the steepness of the curve increases. Thus, the current variance should continue to increase in proportion to the slope of the approach curve. Once it starts to deviate from this we have an indication that contact has

been made. These factors were examined by looking at the approach curve and the variance of the probe current (Fig. 3.12b) calculated from the experimental data. As can be seen, the variance initially varies linearly with incremental change in current ΔI but becomes non-linear with increasing ΔI. The linear part of this curve (Fig 3.12b inset) corresponds to probe heights above a certain value z_0. Thus, beyond this point the more scattered variance was taken to reflect probe tip deformation. The zero of probe-surface separation (x axis in Fig. 3.13) was therefore taken as between z_0 and the following step towards the surface.

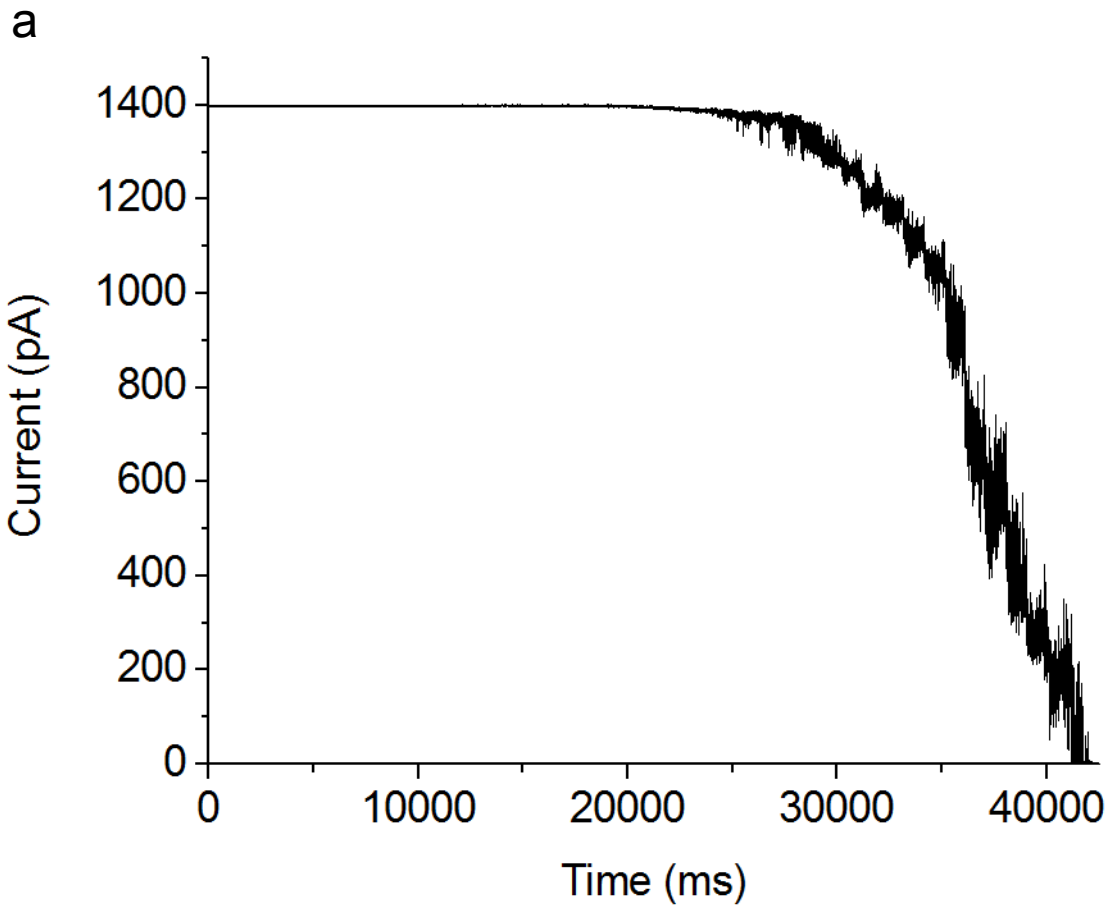

Figure 3.12 The experimental approach curve
a) An experimental approach curve to the flat surface of a petri dish is shown. In this experiment the bath and pipette were filled with the same physiological solution. The pipette had a resistance of 58 MΩ, far from the surface and a potential of 200 mV was applied. The probe was brought to the surface in steps at a rate of 5 nm per s so the time axis is representative of height. These data were acquired by Dr. Simon Hughes and Mr. Matthew Caldwell, UCL. b) (following page) The variance of the current within each z step was seen to increase as the probe surface separation was reduced. The variation of current variance with incremental change in probe current ΔI is shown for the full approach curve (shown in a). This variance was linearly dependent on ΔI for probe heights > z_0 (shown inset). The height between z_0 and the following step towards the surface was therefore taken as the zero of probe-surface separation.

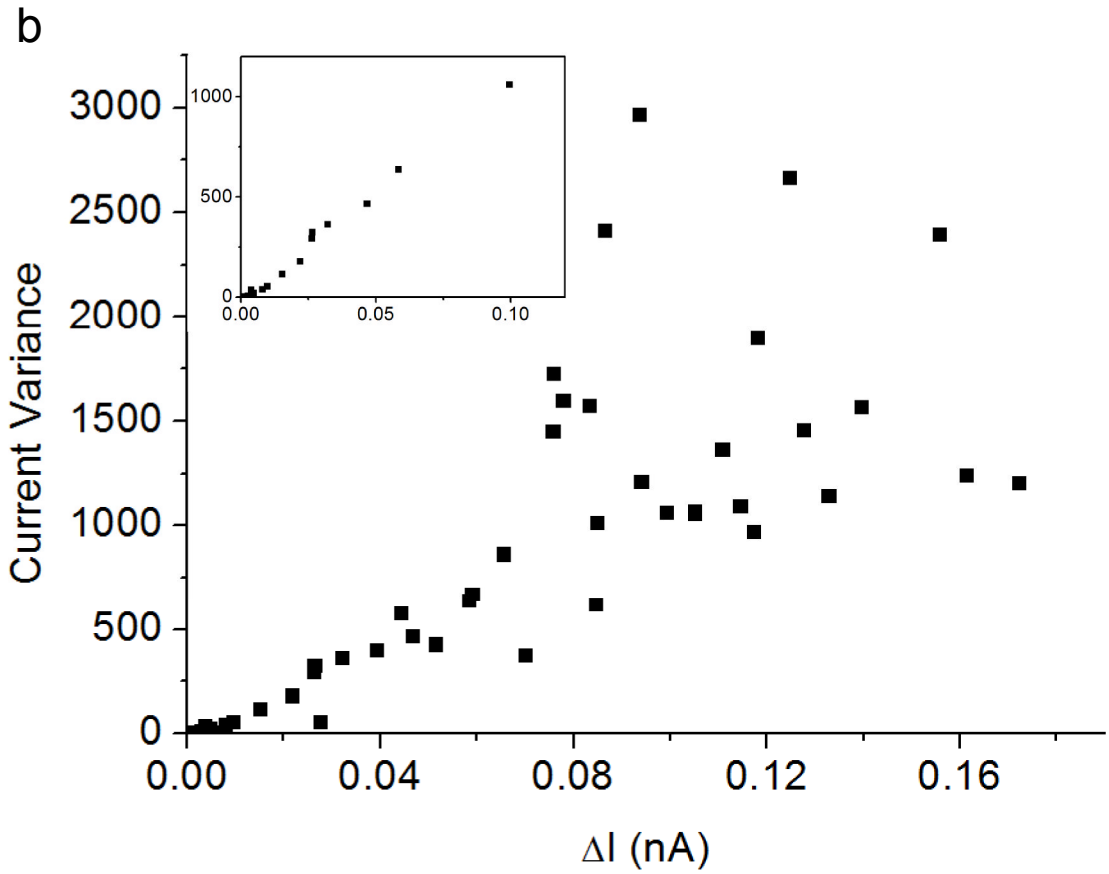

Due to the shape of the experimental approach curve and the probable causes of this, the simulated curve was only compared to the upper part of the experimental approach curve (for probe-surface separation > 0, determined as described above). The simulated currents were fitted to the experimental data by scaling these currents based on a corrected value of R_p for particular values of r (Fig. 3.13). The simulated approach curve was seen to be in agreement with the experimental curve for a value of r = 150 nm.

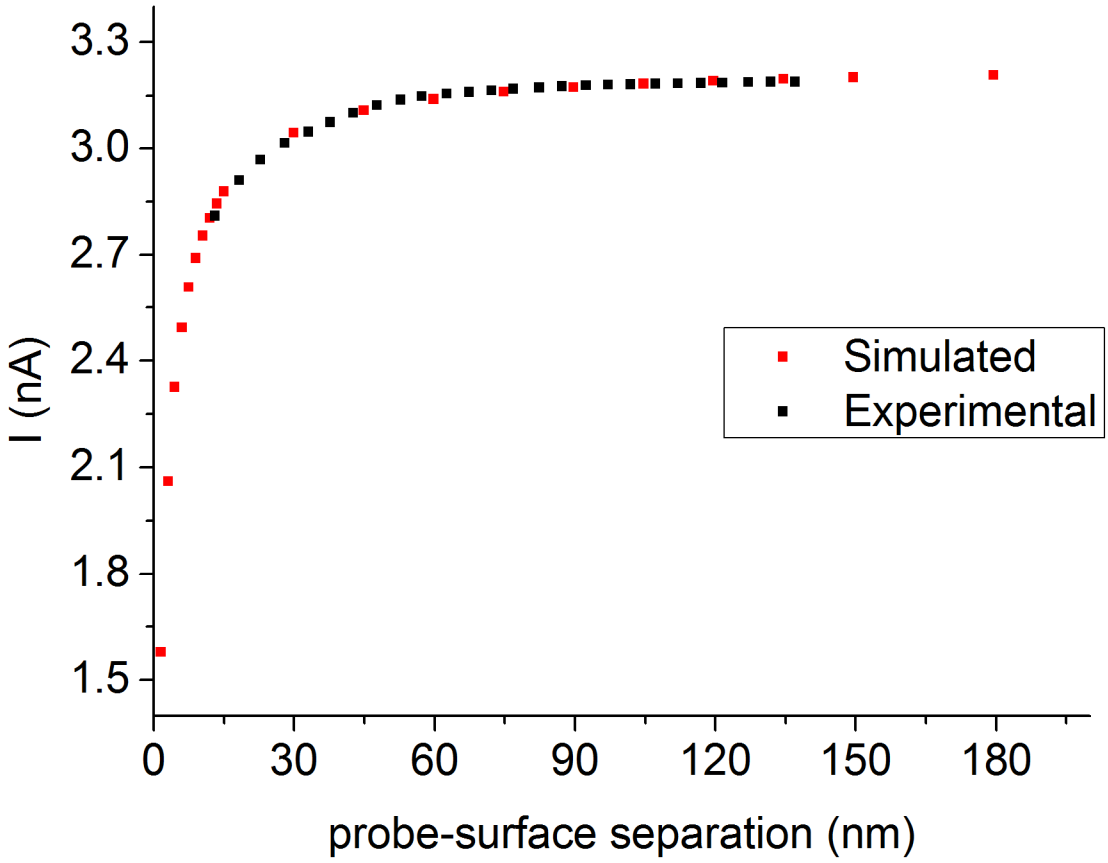

Figure 3.13 Comparison of the simulated and experimental approach curve
Simulations with the probe at several heights above a flat surface were simulated (red points) with the parameters described above and an applied potential of 200 mV. These data were fitted to the experimental approach curve (black points, averaged current data within each z step for data shown in Fig. 3.12, for probe-surface separation > 0) by adjusting the corrected value of R_p based on different values of r. The simulated points fit the experimental curve for a value of r = 150 nm.

Validity of the model

Taken together the findings presented in this chapter suggest that the FEM model presented here is capable of predicting SICM behaviour as it agrees with results derived both theoretically and experimentally. This model was therefore used to address questions about lateral scan resolution and the implications for scanning objects smaller than the probe tip and sloped objects. The results of this investigation are presented in the following chapter.

Chapter 4

Resolution, image fidelity and the working limits of scanning ion conductance microscopy

Introduction

In this chapter finite element modelling is used to examine the lateral resolution of the scanning ion conductance microscope. The related issue of image fidelity is also examined, particularly with respect to objects that are smaller than the size of the probe. Finally, simulations are presented which address some practical considerations for scanning.

4.1 Lateral resolution

It is not clear *a priori*, what the best way to define lateral resolution might be, or indeed, whether a single definition is appropriate. However, two tests of resolution that are useful in other areas of microscopy are (i) the system's response to a step and (ii) the ability to separate adjacent objects (Figure 4.1). Therefore, both types of situation were modelled to investigate lateral resolution. It should be noted that the spacing between a pair of objects is taken as the distance between the in-most edges (X in Fig. 4.1) and not the distance between the centres of the objects, since the objects have finite width.

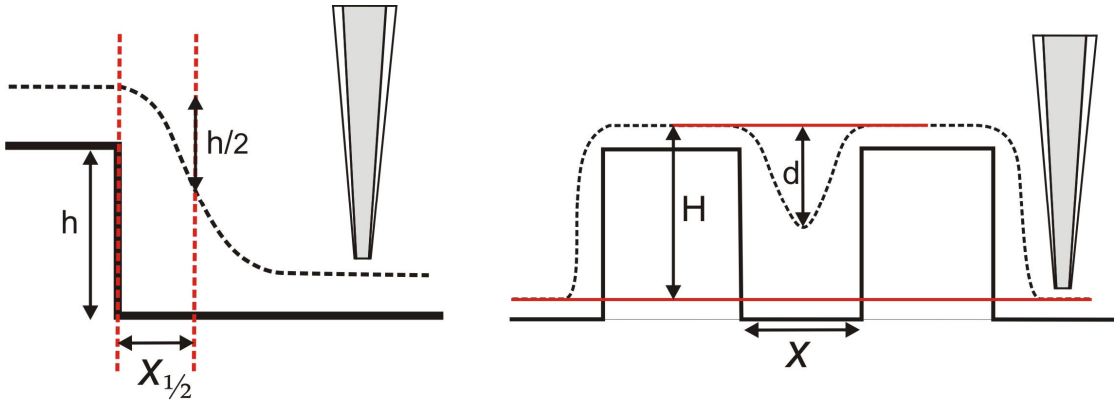

Figure 4.1 Two different measures of lateral resolution
First, the lateral distance taken for a 50 % reduction in the measured height of a single step (left-hand panel). Second, the ability to distinguish two peaks that are closely spaced (right-hand panel). For this second test the peaks were determined to be resolved when the height reduction between the two peaks, d, was positive. A percentage deflection δ(= d/H x100%) is also discussed in this chapter.

Response to a step

The probe response to a square step was first investigated by examining a square pedestal which was larger than the pipette tip in both the *x* direction (width = 7r) and the *y* direction (breadth = 30r) (Figure 4.2). Two different heights, 1r and 5r, were simulated in order to investigate whether the lateral resolution changes when objects are of comparable height to the pipette diameter.

For a step of height 1r a scan across the centre of the step (in the *x* direction) was simulated. Points were simulated at an *x*-position spacing of 0.5r. The line scan was only simulated to the centre of the step because solutions over the second half of the object must be identical (given the symmetrical nature of the problem geometry). (As a precautionary test of the software this approach was validated through simplified test simulations on problems with this symmetry (data not shown).) The FEM-calculated potentials are shown in the upper panel of Fig 4.3 in the case where the pipette is at position (0r,0r,1.01r) (where *x* and *y* coordinates are measured with respect to the centre of the step).

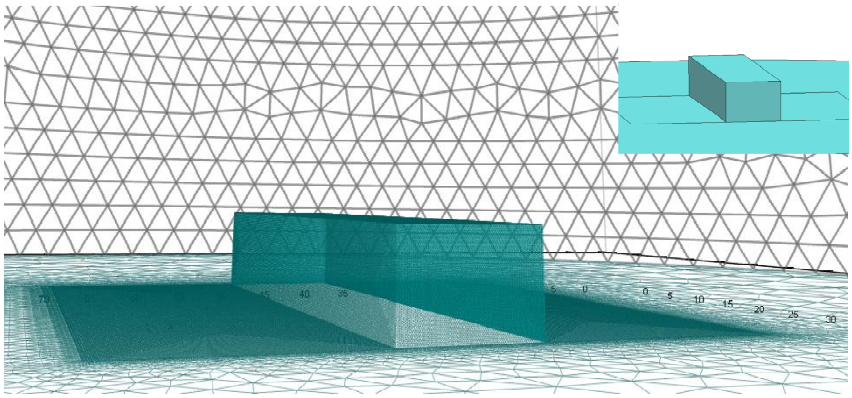

Figure 4.2 Mesh profile of the surface used to investigate the response of an SICM probe to a vertical step
An elongated step of varying heights was used to test the probe response. A view of an example surface mesh for this object is shown with the surface as specified in GiD shown inset.

The height profile returned from these data for a 1 % set point is also shown in Fig. 4.3 (lower panel). These returned heights were fitted to a logistic function of the form:

$$z = A1 + \frac{A2 - A1}{1 + 10^{(X_{1/2} - x)p}} \qquad \text{Equation 4.1}$$

The fitted value of $X_{1/2}$ was -0.62±0.06r (it should be noted that for fitting purposes the *x* origin was shifted to *x* = -3.5r from the leading edge of the step) giving a value of full

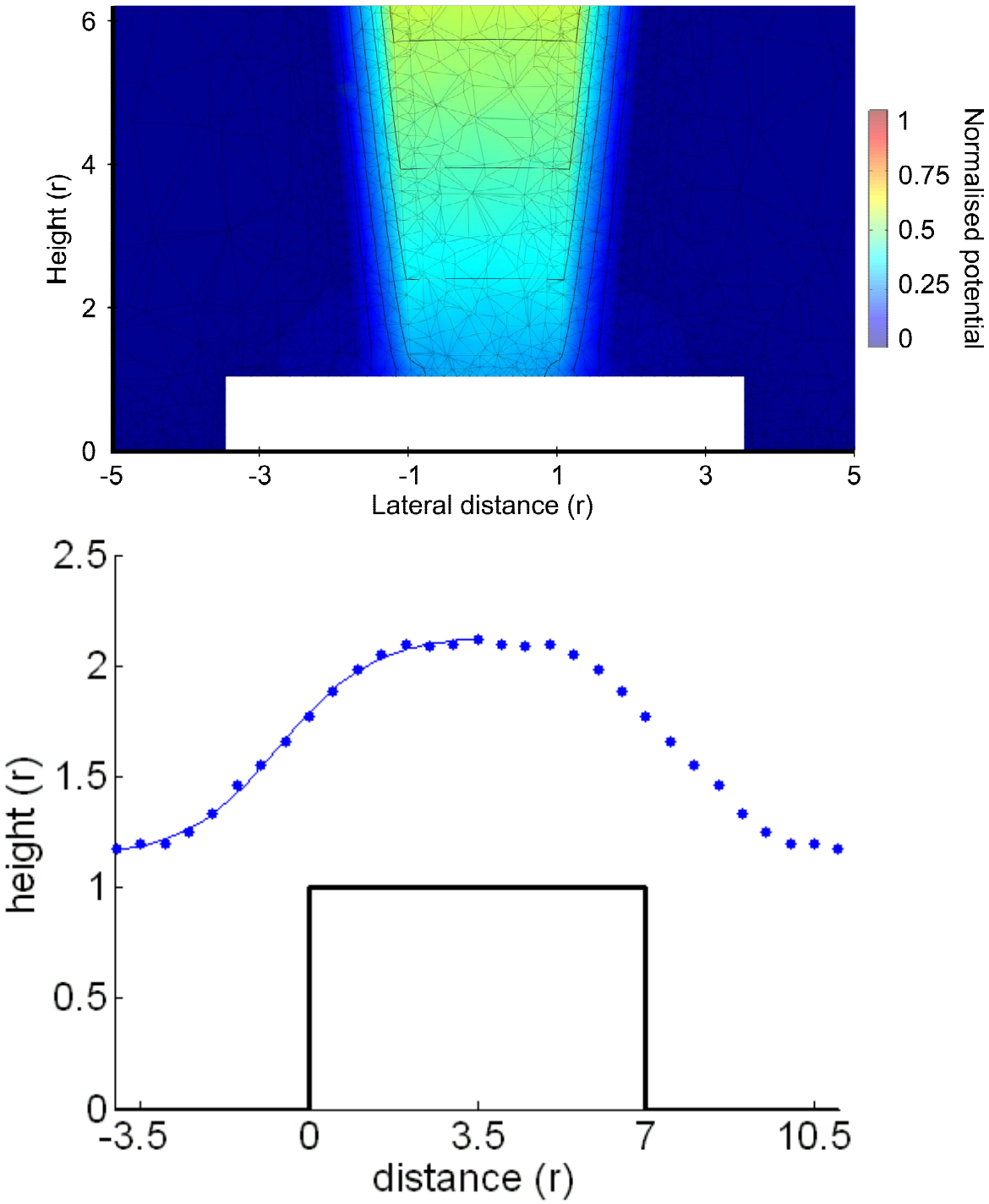

Figure 4.3 Response to a square step of 1r height
The upper panel shows the potential in the region close to the pipette tip for a single simulation with a surface-tip separation of 0.1r and the pipette centred on the step centre. Normalised potential is shown in pseudo-colour, equi-potential lines are shown as mid-weight lines and the mesh is shown as light-weight lines. The lower panel shows the detected heights found for a 1 % set point as the pipette was scanned laterally across the step (blue points). In this graph the x origin has been shifted to the step edge. Equation 4.1 was fitted to these (x-shifted) data (blue line). The fitted values of the free parameters were $A1$ = 1.14±0.02r, $A2$ = 2.14±0.01r, $X_{1/2}$ = -0.62±0.06r, and p = 0.441±0.028r^{-1}. The lateral distance required for a probe to go from 25 % to 75 % of the maximal step response was 2.17±0.14r.

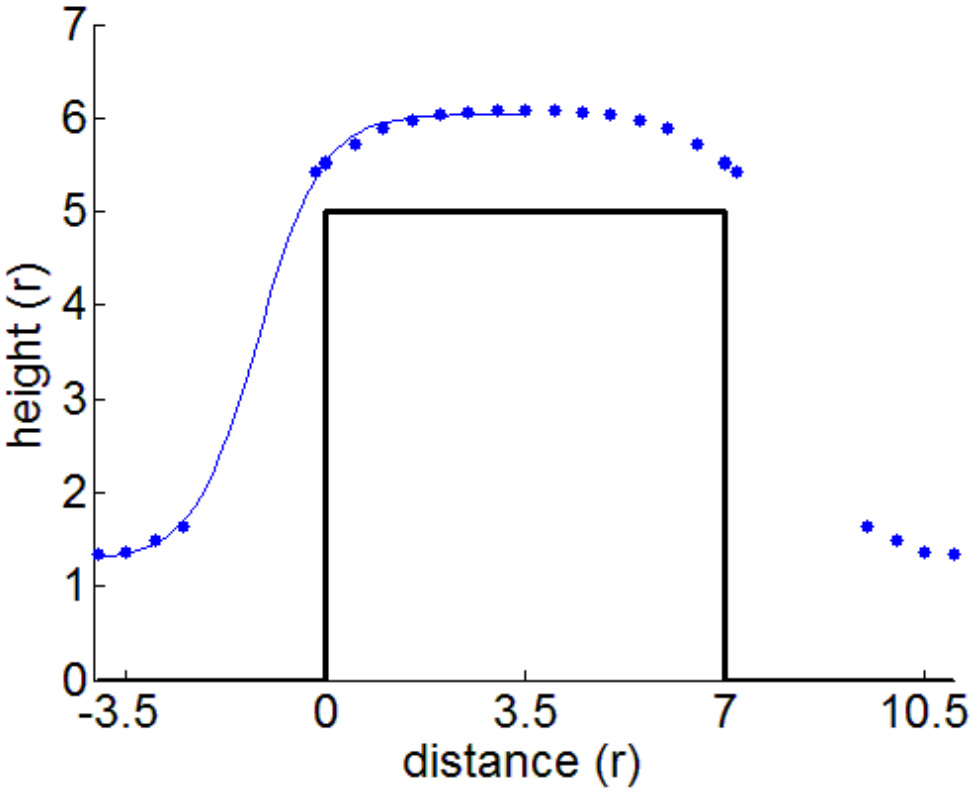

Figure 4.4 Response to a square step of 5r height
The detected heights found for a 1 % set point as the pipette was scanned laterally across the step (blue points) are shown. In this graph the *x*-axis origin has been shifted to the step edge. Eq. 4.1 was fitted to these data (blue line). The fitted values of the free parameters were $A1$ = 1.28±0.03r, $A2$ = 6.04±0.02r, p = 0.77±0.03r^{-1}, $X_{1/2}$ = -1.19±0.04r. The lateral distance required for a probe to go from 25 % to 75 % of the maximal response was 1.23±0.05r.

width at half maximum FWHM = 8.25±0.12r, for this feature of actual width 7r. The lateral distance required for a probe to go from 25 to 75 % of the maximal step response was 2.17±0.14r.

A similar procedure was followed to simulate a scan across the centre of a square step of height 5r. The predicted height profile obtained when scanning at a 1 % set point is also shown (Figure 4.4). As is evident from this figure, when a step of height 5r was used some points close to the edge of the pedestal were not analysable. This was mostly because the set point would not have been reached before the pipette would collide with the surface. However, at two additional positions within the simulated data sets the function used for fitting approach curves did not provide a satisfactory fit and these positions were also excluded. With the remaining points a scan profile was estimated and the logistic function of Equation 4.1 was fitted to the profile. Fitting the data provided an $X_{1/2}$ value of -1.19±0.04r. (and gave a value of FWHM = 9.38±0.09r).

(For fitting purposes the *x*-axis origin was shifted to x = -3.5r from the leading edge of the step). The 25 % to 75 % response distance was 1.23±0.05r. By comparing the results of fits shown in Figures 4.3 and 4.4 it can be seen that there is an interaction between the apparent lateral resolution of the probe and the height of the object that it is scanning. Thus, as estimated by the distance needed to reach 50% of the maximal height drop when crossing a step, the lateral resolution for an SICM probe when responding to a tall step is approximately 2.4r, while for objects of a height that is similar to the pipette radius this distance almost halves to approximately 1.3r. The implications of these findings are discussed later.

Distinguishing double peaks

The second measure of lateral resolution to be investigated was the distance at which two square pedestals could just be distinguished. For these simulations two elongated pedestals of width 2r and height 1r were simulated (Fig. 4.5) and the separation between them was varied. As with the earlier simulations, modelling was restricted to a 'scan' across the centre of these peaks. Peaks with spacings of 0.5r (Fig. 4.6), 1r (Fig. 4.7), 2r (Fig. 4.8) and 3r (Fig. 4.9) were investigated. This process was repeated for a set of peaks of height 5r (Fig. 4.10-13) and the data for both sets of simulations are summarised in Figure 4.14.

Two pedestals of height 1r, were found not to be distinguishable at separations of 0.5r and 1r but instead appeared as a single peak. This was reflected in a negative value of the height "reduction" between peaks (d as described in Fig. 4.1). For a

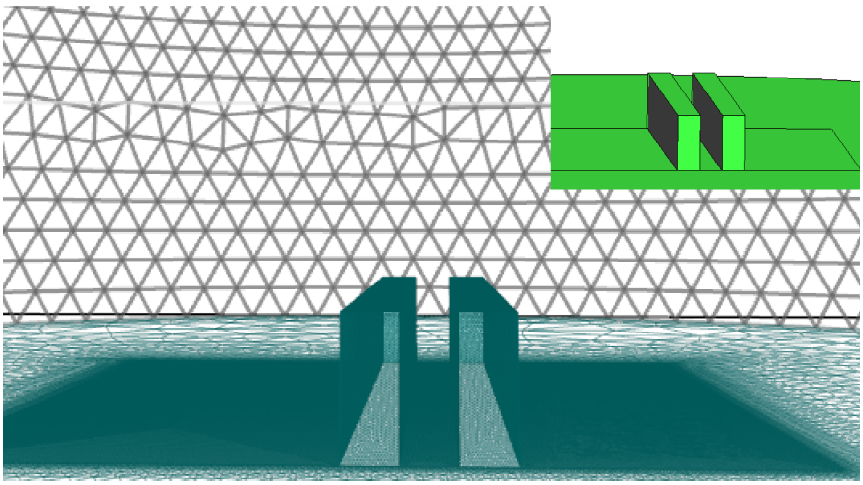

Figure 4.5 Mesh profile of the surface used to investigate the probe response to a pair of adjacent pedestals
A view of an example surface mesh for this object is shown along with the surface as specified in GiD (inset).

separation of 0.5 r d = -0.07r, while at a separation of 1r, d = -0.04r. However, for a spacing of 2r the two peaks had a positive value of d (d = 0.06r).

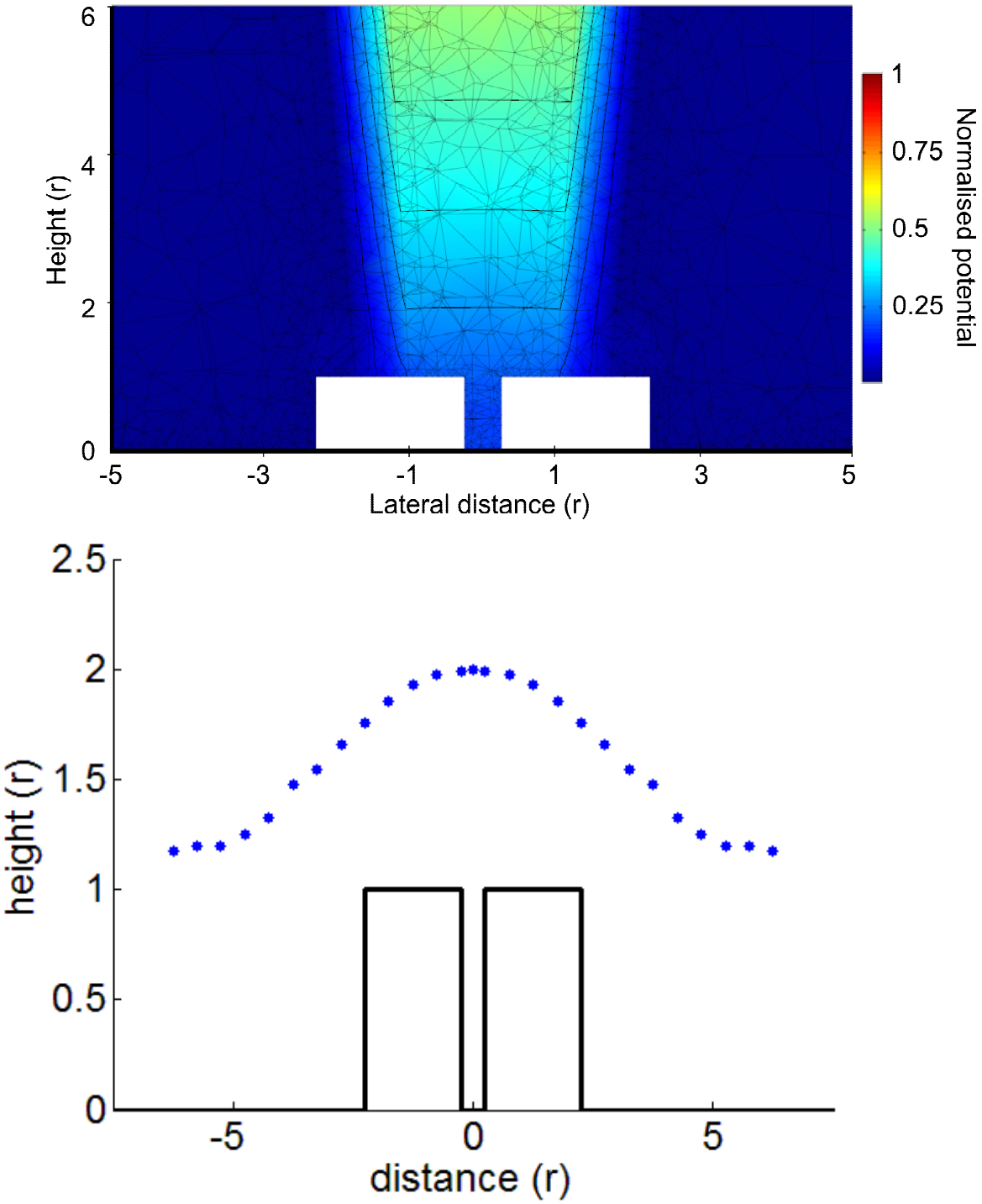

Figure 4.6: Two pedestals of height 1r and spacing 0.5r
The upper panel shows the calculated potentials in a region close to the pipette tip for a surface-tip separation of 0.1r. The pipette is centred on the centre between pedestals. Normalised potential is shown in pseudo-colour, equi-potential lines are shown as mid-weight lines and the mesh is shown as light-weight lines. The lower panel shows the height profile returned with a set point of 1 % (blue circles). The position of the pedestals is also indicated (heavy black line). For this spacing d = -0.07r.

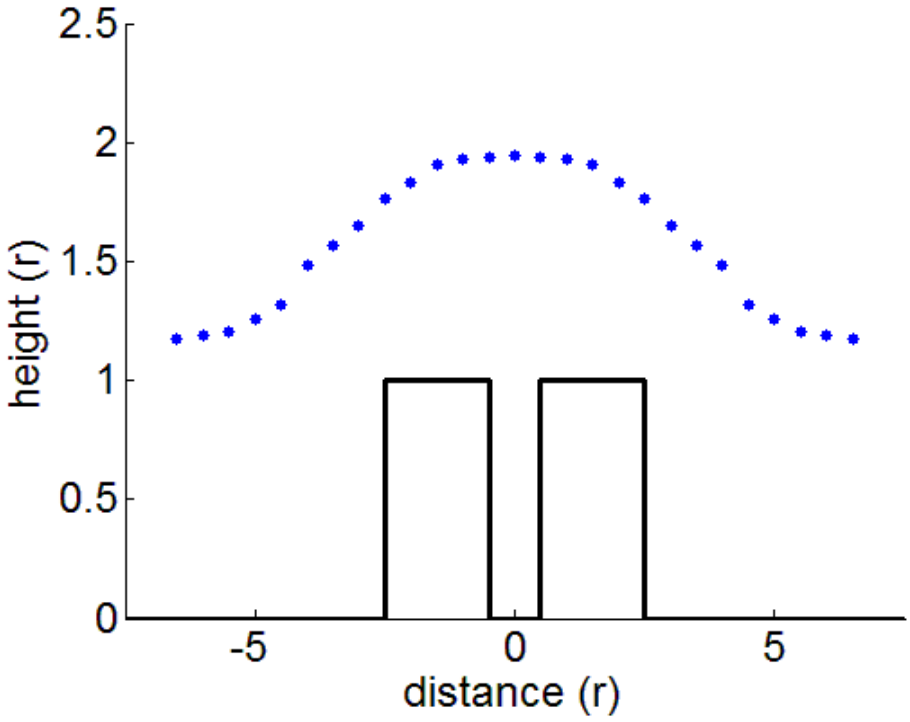

Figure 4.7 Two pedestals of height 1r and spacing 1r
The height profile returned with a set point of 1 % (blue circles) is shown. The position of the pedestals is also indicated (heavy black line). For this spacing d = -0.04r.

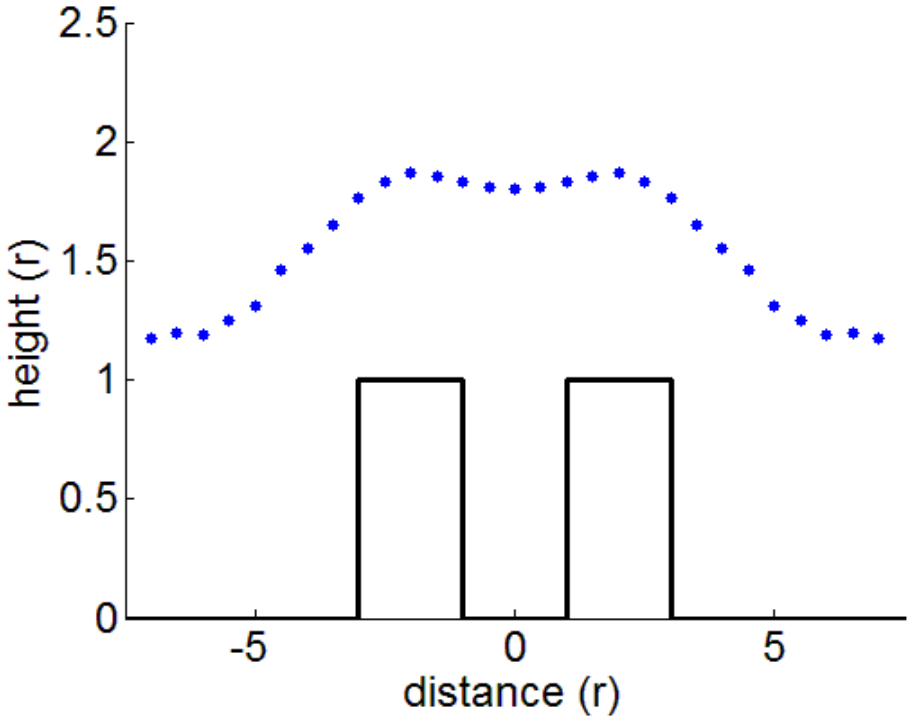

Figure 4.8 Two pedestals of height 1r and spacing 2r
The height profile returned with a set point of 1 % (blue circles) is shown. The position of the pedestals is also indicated (heavy black line). For this spacing d = 0.07r.

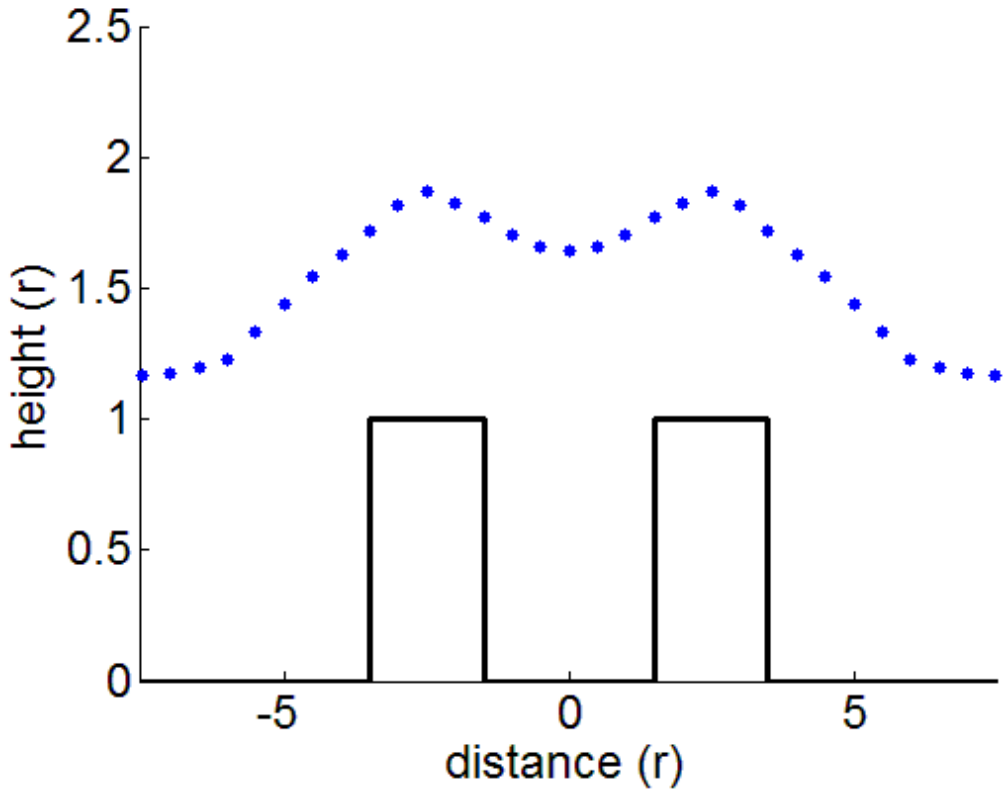

Figure 4.9 Two pedestals of height 1r and spacing 3r
The height profile returned with a set point of 1 % (blue circles) is shown. The position of the pedestals is also indicated (heavy black line). For this spacing d = 0.22r.

For pedestals of height 5r, at a spacing of 0.5r the features were not distinguishable as separate peaks but appeared instead as a single peak, d = -0.07r. However, for a spacing of 1r, two peaks were just evident as a very small deflection, with d = 0.01 and δ = 0.3%. For a spacing of 2r d = 0.22r and δ = 4.9 %. Finally, at a spacing of 3r d = 0.47r and δ = 10.3%.

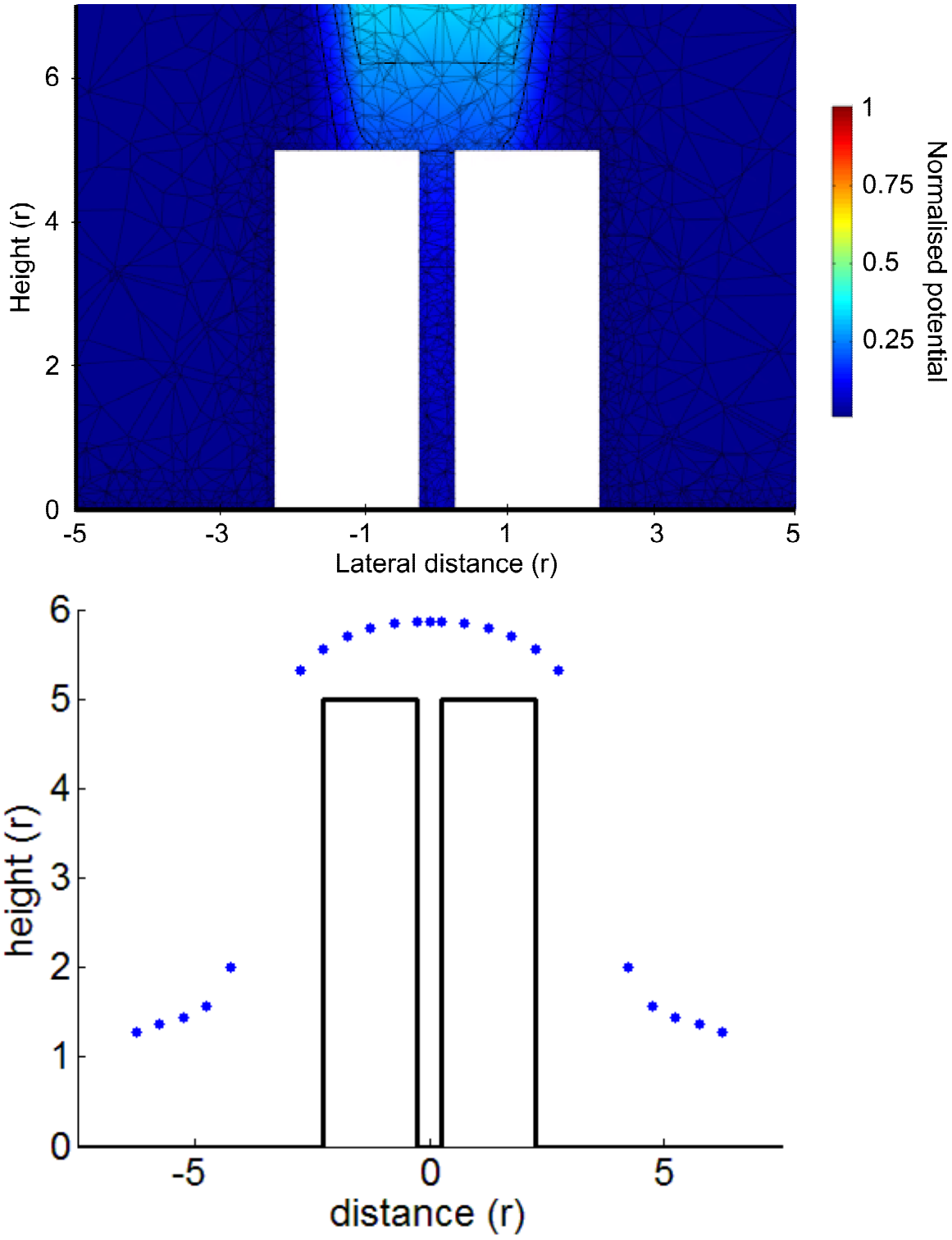

Figure 4.10 Two pedestals of height 5r and spacing 0.5r
The upper panel shows the calculated potentials in a region close to the pipette tip with a surface-tip separation of 0.1r. The pipette is centred between the two pedestals. Normalised potential is shown in pseudo-colour, equi-potential lines are shown as mid-weight lines and the mesh is shown as light-weight lines. The lower panel shows the height profile returned with a set point of 1 % (blue circles). The position of the pedestals is also indicated (heavy black line). For this spacing d = -0.07r.

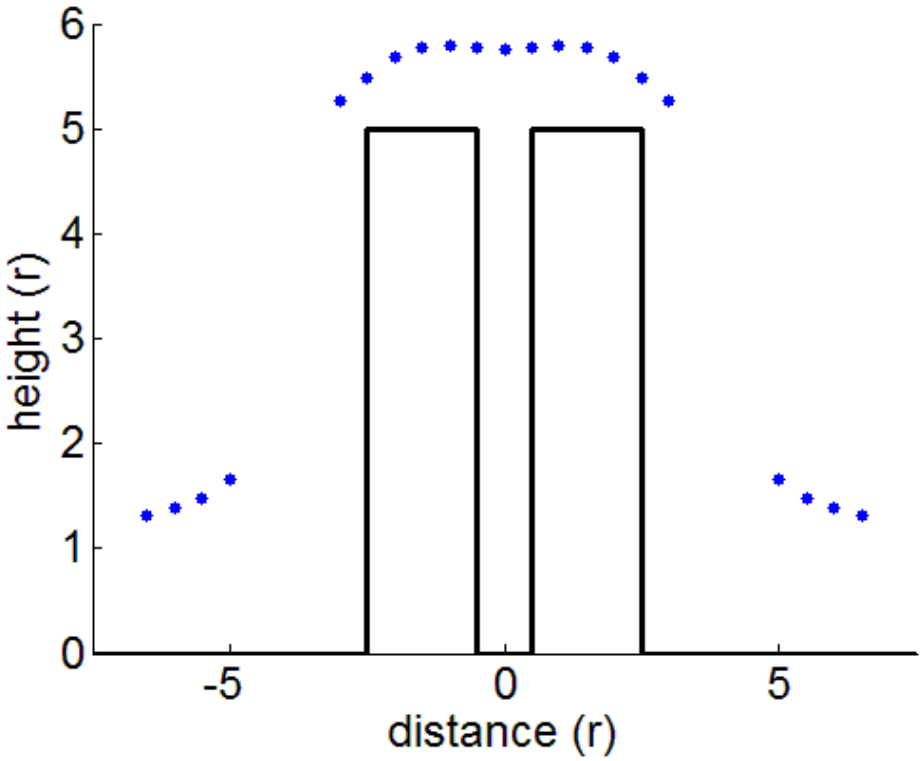

Figure 4.11 Two pedestals of height 5r and spacing 1r
The height profile returned with a set point of 1 % (blue circles) is shown. The position of the pedestals is also indicated (heavy black line). For this spacing d = 0.01r.

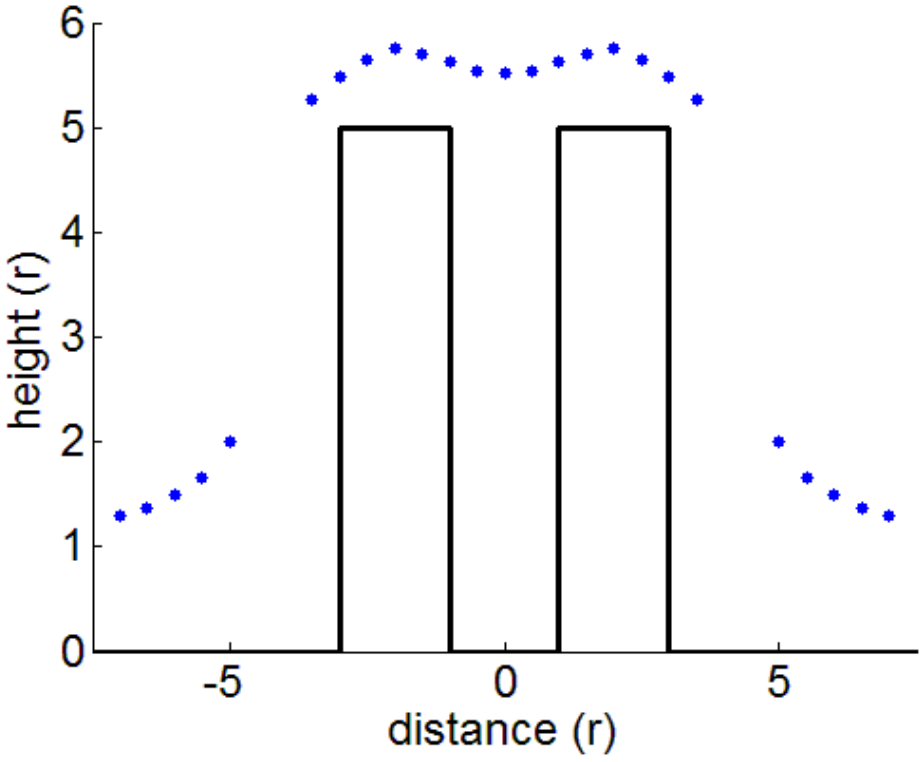

Figure 4.12 Two pedestals of height 5r and spacing 2r
The height profile returned with a set point of 1 % (blue circles) is shown. The position of the pedestals is also indicated (heavy black line). For this spacing d = 0.22r.

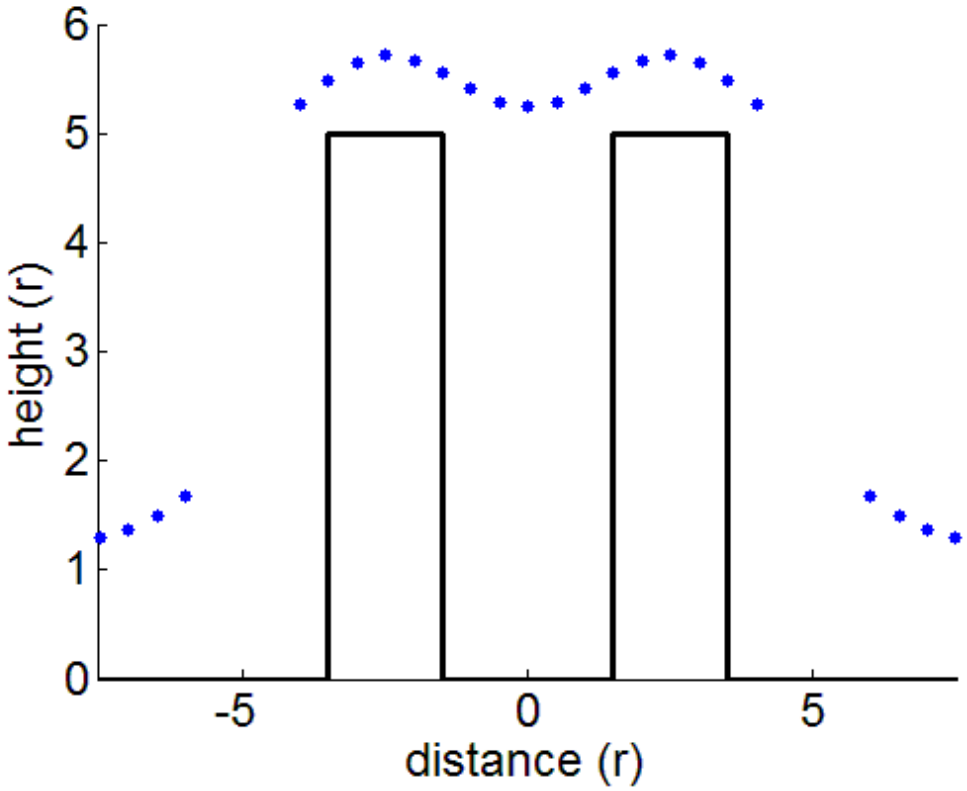

Figure 4.13 Two pedestals of height 5r and spacing 3r
The height profile returned with a set point of 1 % (blue circles) is shown. The position of the pedestals is also indicated (heavy black line). For this spacing d = 0.47.

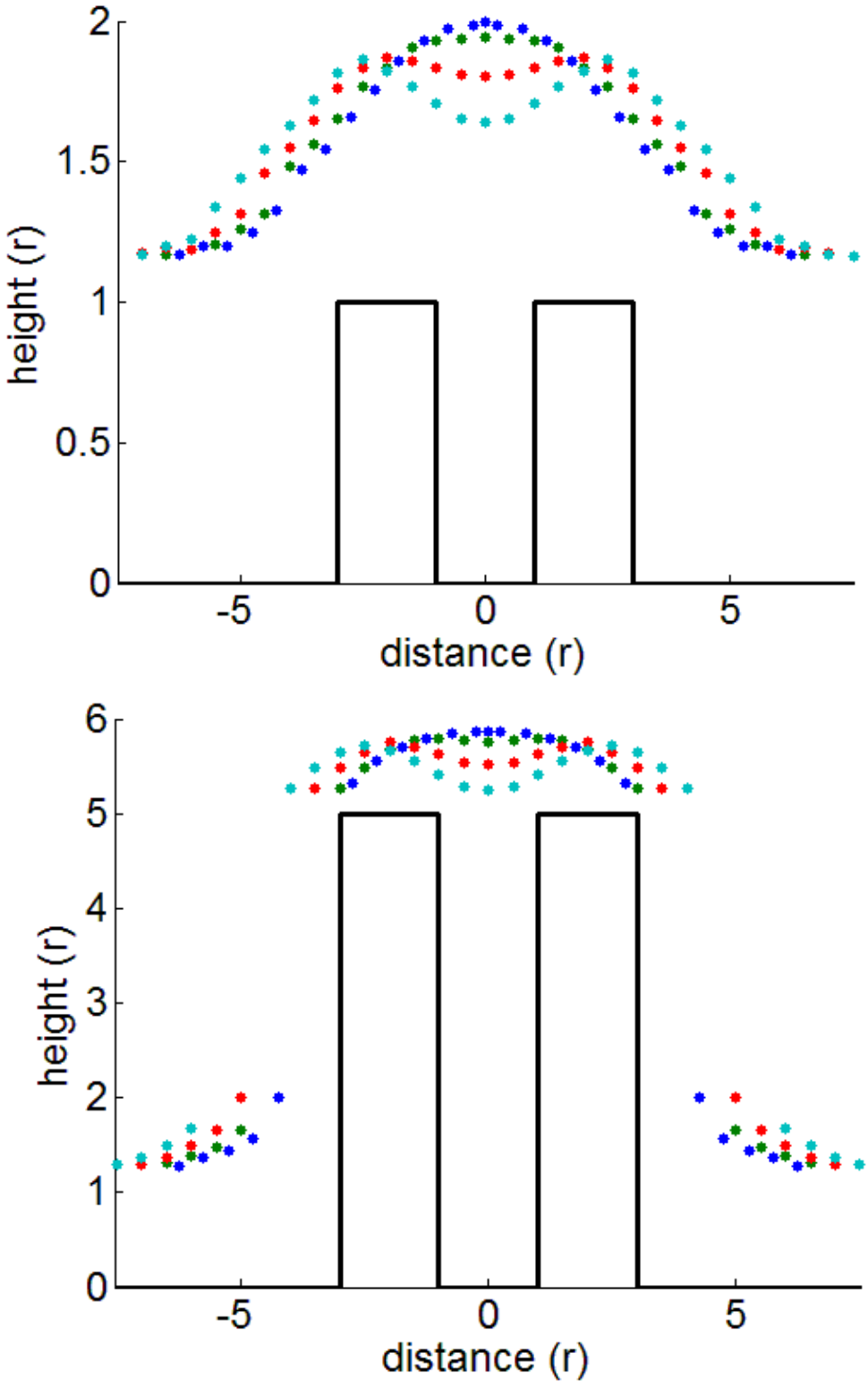

Figure 4.14 Comparison of the height profiles of two pedestals with different spacing between them

The upper panel shows the responses to a set of peaks of height 1r and the lower panel shows responses to peaks of height 5r. In both panels data for peak spacings of 0.5r (blue circles), 1r (green circles), 2r (red circles) and 3r (cyan circles), analysed at a set point of 1 % are presented. In both panels the heavy black line represents a set of peaks with spacing 2r between them, to represent the height of the features imaged.

4.2 The ability to scan slopes in a sample

As illustrated in the early simulations, when the SICM probe encounters a vertical edge of height >1r it is not possible to obtain a 1% shutdown of current without colliding. This raises a very important consideration for scanning samples in general. Specifically, what is the maximum slope that can be scanned at a given set point? To investigate this issue approach curves to a set of surfaces with a uniform gradient of known angle were calculated. The geometry tested is shown in Fig. 4.15. An example of the simulated potentials is shown in Fig. 4.16.

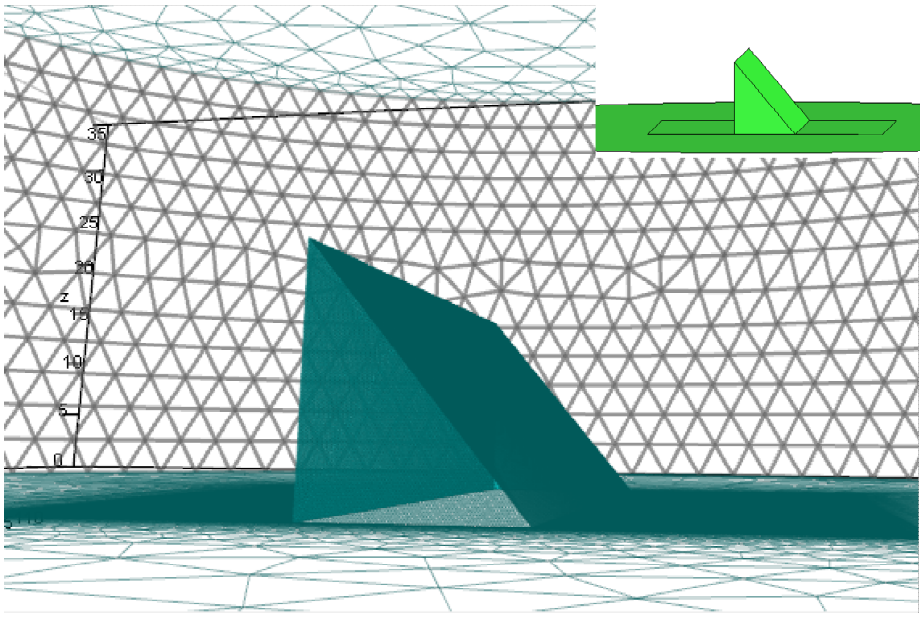

Figure 4.15 Mesh profile of the surface used to investigate the ability to scan over slopes in a sample without contact
An elongated slope of uniform angles was used in these simulations and the angle was varied to generate a number of approach curves. A view of an example surface mesh for this object, with a slope angle of 45 ° is shown along with the surface as specified in GiD (inset).

It is not possible to create a mesh for FEM analysis at the exact point of contact between the surface and the probe. Therefore, for each slope, the probe current was calculated up to a point at which the probe was situated at a height of 0.01r above the surface. This current was then converted into a set point by fitting the full approach curve. A plot of the maximum slope angle that can be scanned at a particular set point is shown in Figure 4.17. Because this type of calculation could be very dependent on the exact geometry of the probe glass, the entire procedure was repeated for three values of pipette outer:inner diameters (OD:ID). The three pairs of values chosen all correspond to commercially available glass types and were i), the glass thickness used experimentally in this laboratory (and therefore the value used in the other simulations

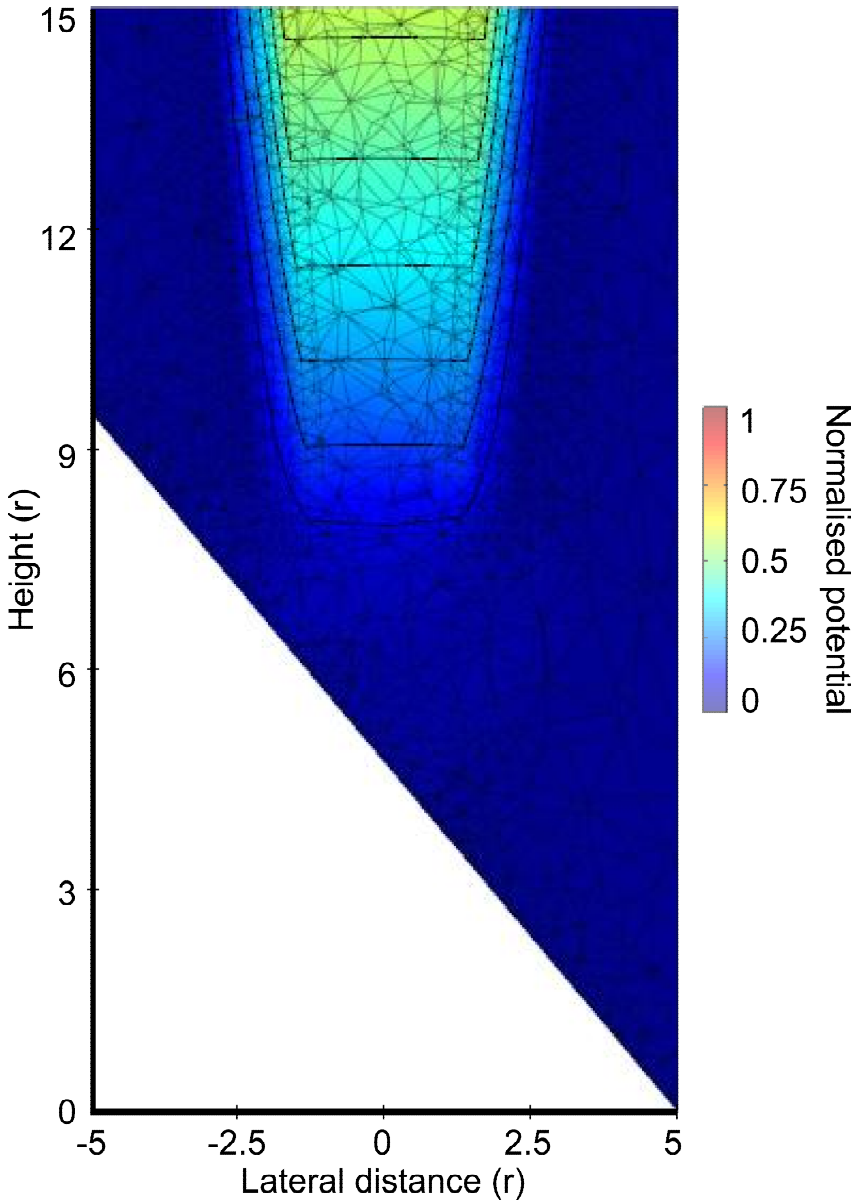

Figure 4.16 FEM-calculated potentials as a probe approaches a 45 º slope.
This image shows the potential in the region close to the pipette tip for a single simulation position with a surface-tip separation of 1r. The slope angle is 45 º. A continuous solution with no singularities can be seen. Normalised potential is shown in pseudo-colour, equipotential lines are shown as mid-weight lines and the mesh is shown as light-weight lines.

presented in this thesis) of 1:0.58, ii) an alternative experimentally used thick-walled glass of 1:0.50, and iii) a typical

thin-walled glass of 1:0.78. The resulting data sets were each found to be well-fitted by a double exponential function $y = y_0 + A_1 e^{-x/t_1} + A_2 e^{-x/t_2}$ with fitting parameters as shown in the table in Figure 4.17.

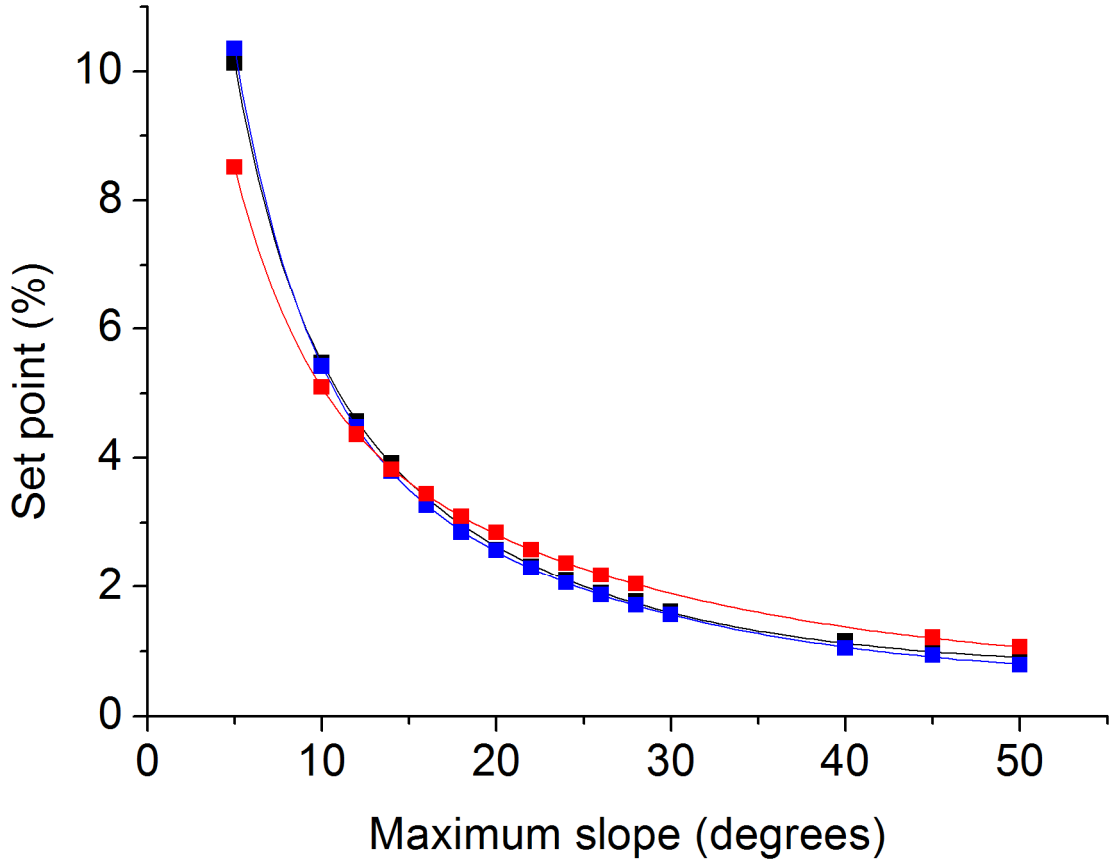

Glass thickness OD:ID	Fitted parameters (value ± standard error)				
	y_0	A_1	t_1	A_2	t_2
1 : 0.58	0.71±0.05	8.7±0.7	13.1±0.8	17.1±1.3	3.1±0.3
1 : 0.50	0.48±0.04	6.8±0.3	16.3±0.7	18.8±0.3	3.7±0.1
1 : 0.78	0.60±0.06	12.0±0.2	3.9±0.2	6.0±0.3	19.5±1.2

Figure 4.17 The maximum slope that can be scanned successfully at a given set point
The upper panel shows the maximum slope angle at which it is possible to scan with a pipette of the simulated OD:ID ratio before contact with the surface is made when the data is analysed at different set points. Three OD:ID ratios were simulated corresponding to the glass thickness used experimentally in this laboratory, 1:0.58 (black), an alternative experimentally used glass, 1:0.50 (blue), and a typical thin-walled glass, 1:0.78 (red). Over this range of slopes the relationship between maximum slope angle and set point was found to be well fitted by a double exponential function $y = y_0 + A_1 e^{-x/t_1} + A_2 e^{-x/t_2}$ with decay constants as shown in the table in the lower panel.

4.3 Imaging features smaller than the tip

A narrow, elongated pit

In this section the imaging fidelity for objects smaller than the pipette inner radius is investigated. The first tests were on a simulated, elongated pit of width ≤ 1r. Figure 4.18 illustrates the geometry.

Starting with a pit of fixed width 1r, simulations were performed as the pit depth was varied between 1r and 5r (Fig. 4.19-22). Next, a pit of fixed depth 5r, was examined as the width was varied between 0.2r and 1r (Fig. 4.23-25).

In all of these cases the presence of the pit is detectable at a high set point (the data shown are for 4.75 %). Importantly, the probe begins to respond to the object at the pipette outer radius and the pit is not accurately imaged. Despite this, a pit of greater depth does produce a slightly larger dip (Fig.4.22), so scans can provide some indication as to whether or not the pit is very shallow.

When the width of the pit was varied between 0.2r and 1r for a pit of fixed depth 5r (Fig. 4.21 and 4.23-24), the feature always remained detectable. As with shallower pits the height and width were inaccurately imaged. As the pit width becomes much smaller than the pipette inner radius the magnitude of the pit depth reported by the probe is reduced (Fig 4.25), indicating an interaction between height and width in these scans. Generally speaking, since the probe response to these features begins at the pipette outer radius the pit features presented here produce a profile image that can be seen as a convolution of the feature and the probe tip. This observation is interesting because it may allow the dimensions of the probe tip to be estimated through scanning with a 'live' tip rather than by using electron microscopy to determine the tip size. Apart from the additional convenience that this may offer in terms of cost and preparation, it should also be noted that the process of pipette pulling still produces considerable variation. This means that measurements as made using electron microscopy can only provide a guide to tip size and can say nothing about a specific probe.

In order to investigate this possibility further a scan across a pit of width 0.5r and depth 5r was simulated for a probe with a doubled outer glass radius (Fig. 4.26, 4.27). It was thought that this would indicate if the response was related to the pipette outer radius or a particular distance from the feature. These data suggest the response is

dependent on the pipette outer diameter because the pit becomes broadened. However, this effect becomes very small at the outer edges of the probe.

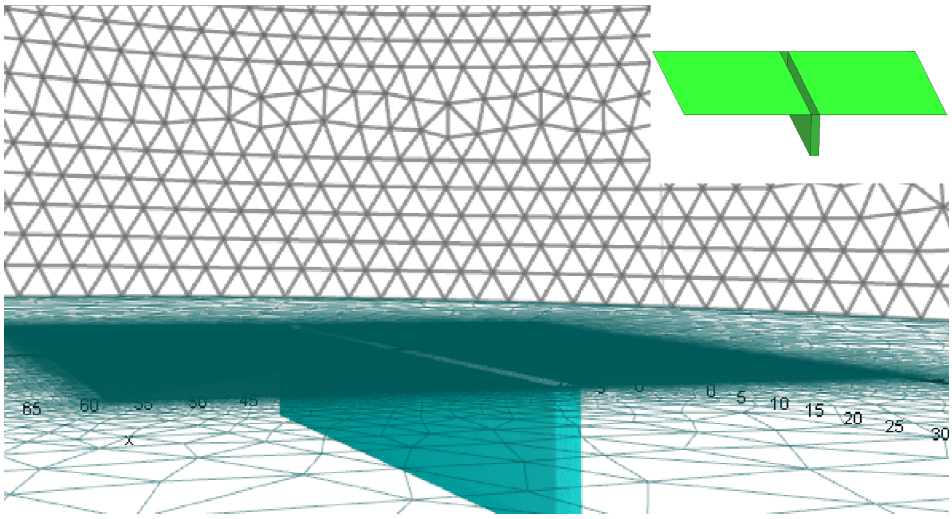

Figure 4.18 Mesh profile of the surface used to investigate the response to an elongated pit of width ≤ r
Both the width and the depth of the pit were varied. A view of an example surface mesh for this object is shown along with the surface as specified in GiD (inset).

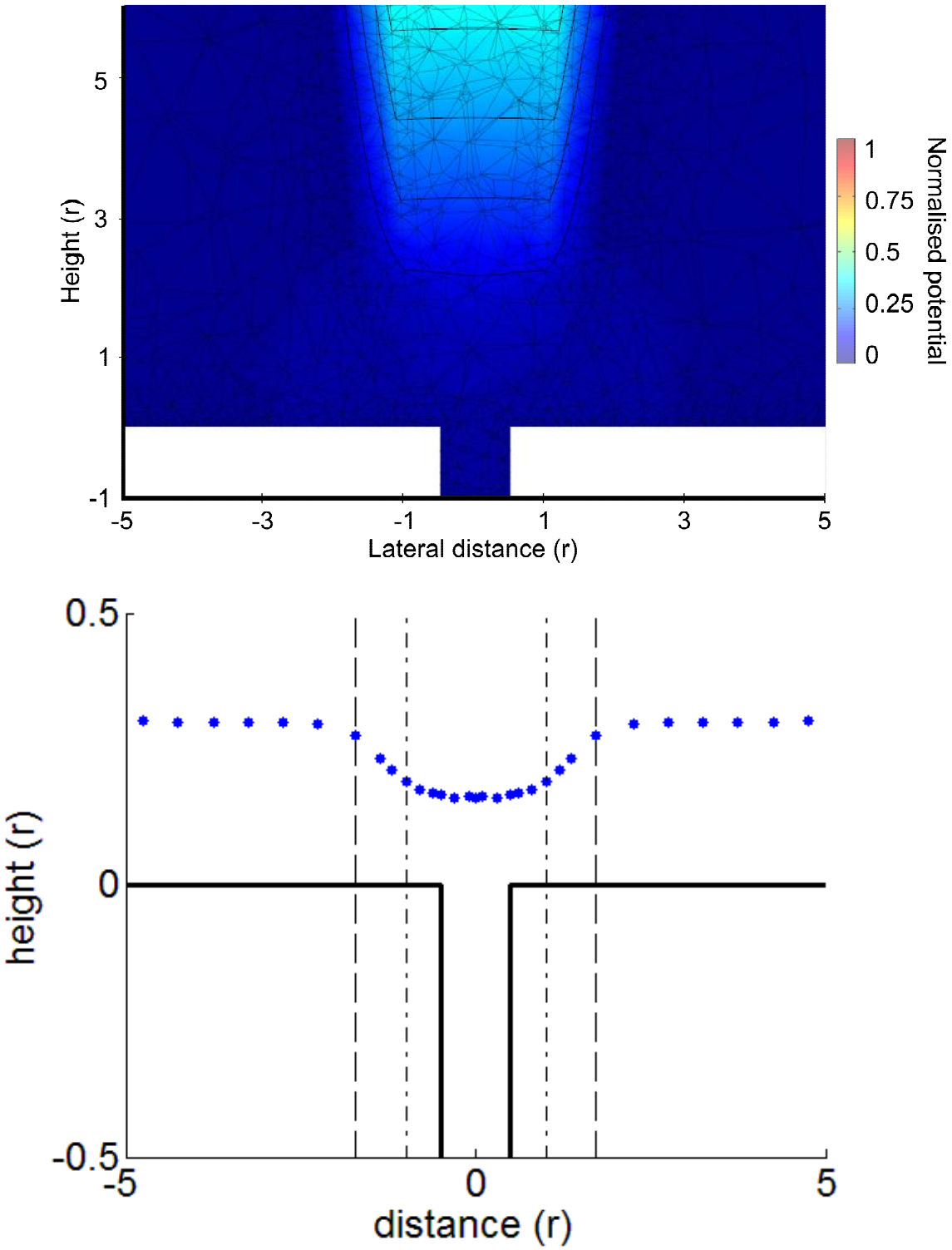

Figure 4.19 Pit of width 1r and depth 1r

The upper panel shows the potential in the region close to the pipette tip for a single simulation for a pit of width 1r and depth 1r with a surface-tip separation of 2r and the pipette centred on the pit centre. Normalised potential is shown in pseudo-colour, equipotential lines are shown as mid-weight lines and the mesh is shown as light-weight lines. The lower panel shows the height profile returned with a set point of 4.75 % (blue circles), the dimensions of the pit are indicated (solid black line), with the pipette outer (dashed line) and inner radius (dotted line) also shown relative to the pit centre.

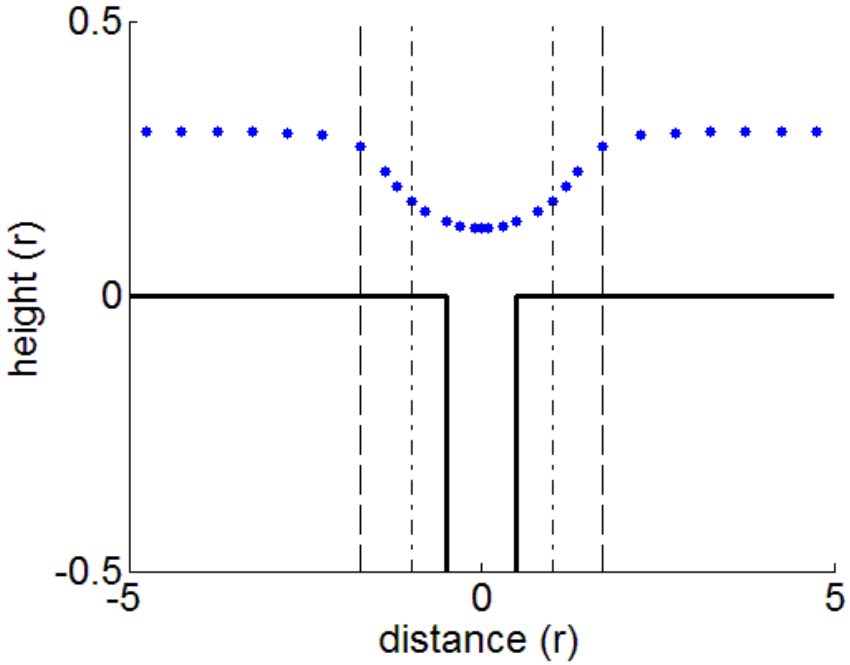

Figure 4.20 Pit of width 1r and depth 2r
The height profile returned with a set point of 4.75 % (blue circles) is shown. The dimensions of the pit are indicated by solid black lines, with the pipette outer (dashed line) and inner radius (dotted line) also shown relative to the pit centre. It should be noted that the vertical scale does not show the full depth of the pit to make the scan profile more clearly visible.

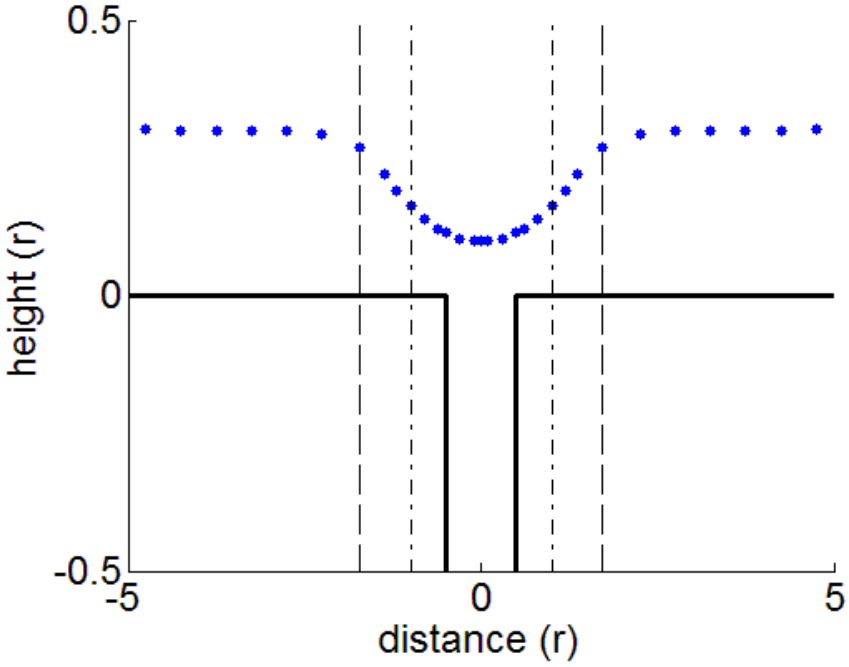

Figure 4.21 Pit of width 1r and depth 5r
The height profile returned with a set point of 4.75 % (blue circles) is shown. The dimensions of the pit are indicated by solid black lines, with the pipette outer (dashed line) and inner radius (dotted line) also shown relative to the pit centre. It should be noted that the vertical scale does not show the full depth of the pit to make the scan profile more clearly visible.

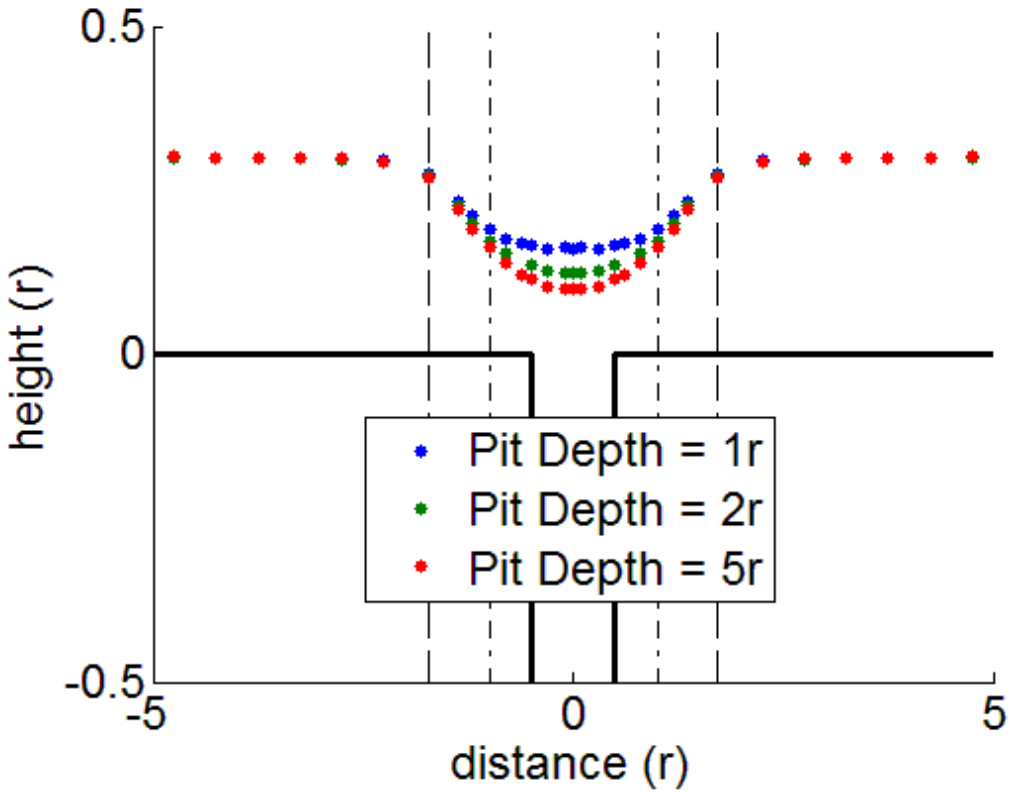

Figure 4.22 Comparison of height profiles for different pit depths
The scan profile produced as the depth, of a pit of a fixed diameter of 1r, was varied from -1r to -5r is shown. The width of the pit is shown (solid black line), with the pipette outer (dashed line) and inner radius (dotted line) also shown relative to the pit centre. The data shown were analysed with a 4.75 % set point. It should be noted that the vertical scale does not show the full depth of the pit to make the scan profile more clearly visible.

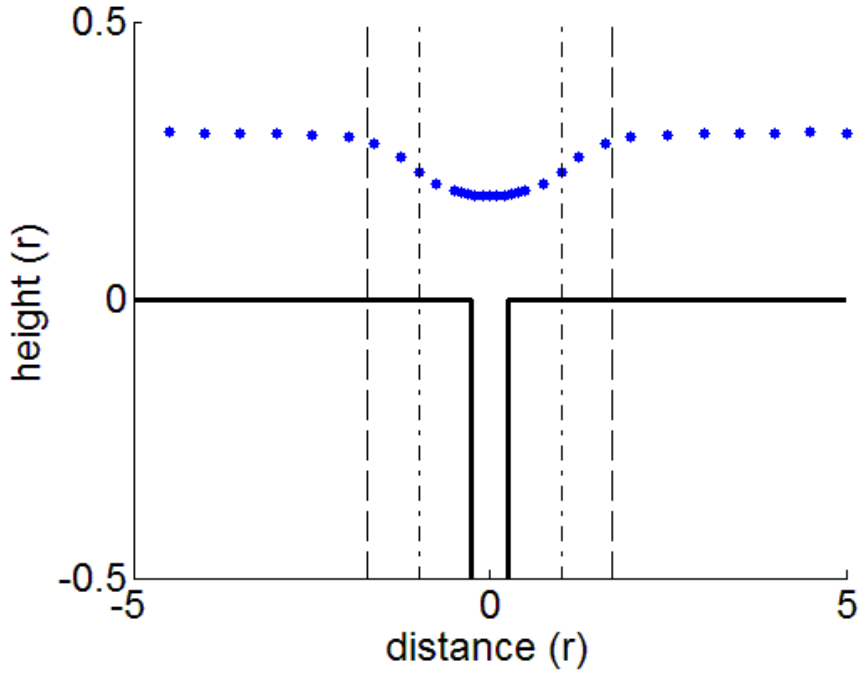

Figure 4.23 Pit of width 0.5r and depth 5r

The height profile returned with a set point of 4.75 % (blue circles) is shown. The dimensions of the pit are indicated by solid black lines, with the pipette outer (dashed line) and inner radius (dotted line) also shown relative to the pit centre. It should be noted that the vertical scale does not show the full depth of the pit to make the scan profile more clearly visible.

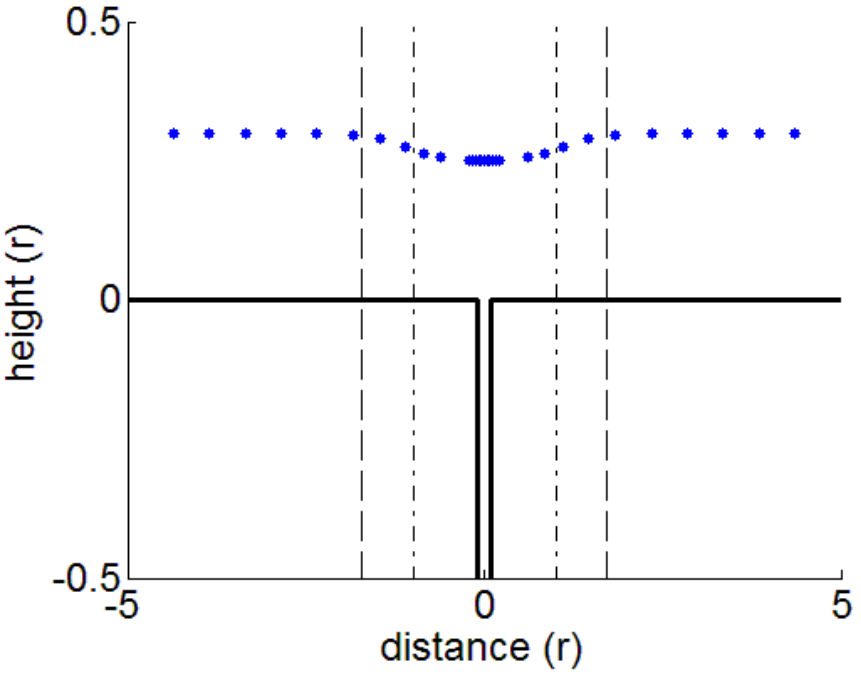

Figure 4.24 Pit of width 0.2r and depth 5r

The height profile returned with a set point of 4.75 % (blue circles) is shown. The dimensions of the pit are indicated by solid black lines, with the pipette outer (dashed line) and inner radius (dotted line) also shown relative to the pit centre. It should be noted that the vertical scale does not show the full depth of the pit to make the scan profile more clearly visible.

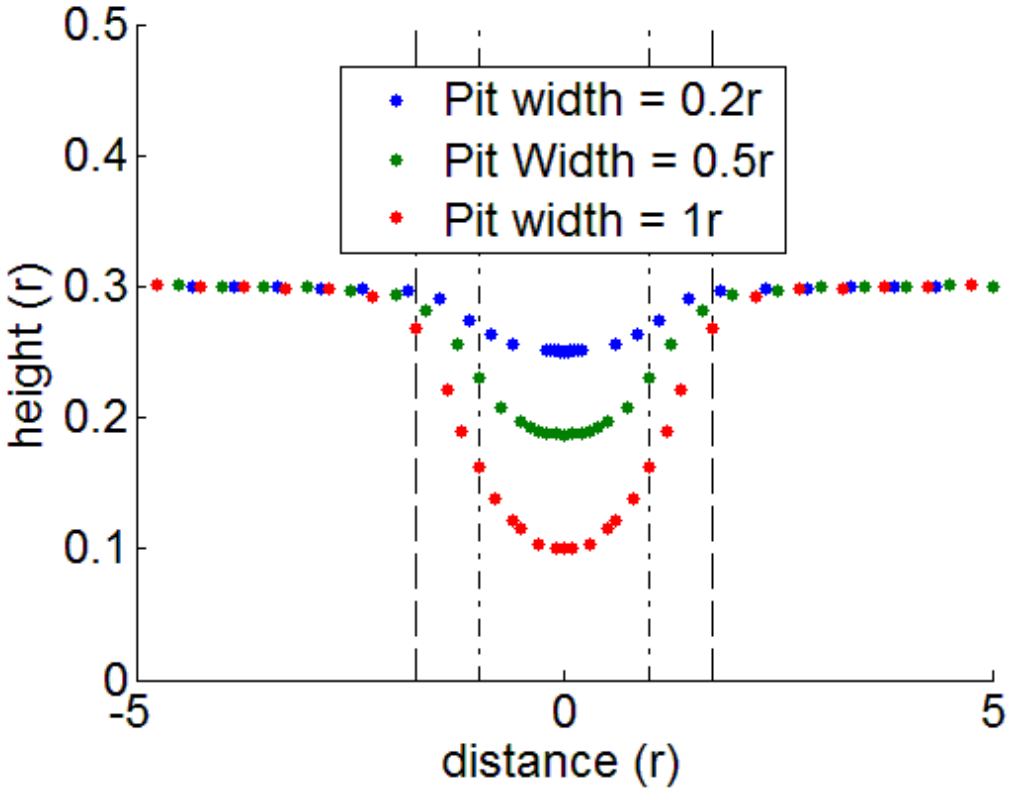

.

Figure 4.25 Comparison of pits of different widths ≤ 1r

For a pit of depth 5r the width was varied from 0.2r - 1r. The scan profiles produced are shown. The pipette outer (dashed line) and inner radius (dotted line) are also indicated relative to the pit centre. The data shown were analysed with a 4.75 % set point.

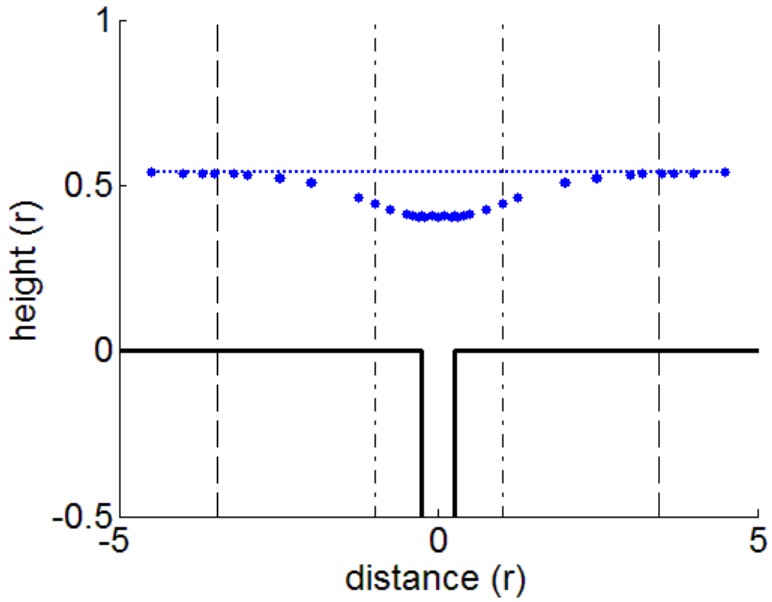

Figure 4.26 A pit of width 0.5r and depth 5r scanned with a probe of large outer radius
The height profile returned with a set point of 4.75 % (blue circles) is shown. The dimensions of the pit are indicated by solid black lines, with the pipette outer (dashed line) and inner radius (dotted line) also shown relative to the pit centre. It should be noted that the vertical scale does not show the full depth of the pit to make the scan profile more clearly visible.

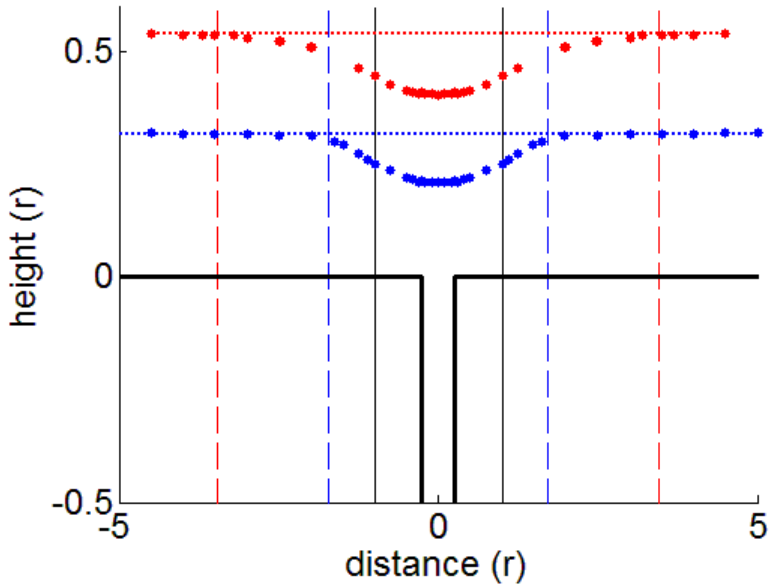

Figure 4.27 Comparison of pits of width 0.5r and depth 5r scanned with probes of different outer diameters
The height profiles returned with a set point of 4.5 % are shown whilst scanning with a pipette of the normal outer diameter (blue circles) and an outer diameter of double this value (red circles). The detected height of the flat surface surrounding the pit is indicated by the dotted lines. The pipette inner diameter (black line) and the outer diameters used (dashed coloured lines) are also shown relative to the pit centre. The dimensions of the pit are indicated by the solid black lines. It should be noted that the vertical scale does not show the full depth of the pit.

A wide elongated pit

To put these findings on the probe response to narrow elongated features into context simulations of much wider elongated pits were also undertaken. For this purpose an elongated pit of width 7r was simulated with three different pit depths 1r (Fig. 4.28) 2r (Fig. 4.29) and 5r (Fig. 4.30). At a 1 % set point a shallow pit of depth 1r has the profile shown in Fig. 4.28. It is essentially the image obtained when scanning a vertical step of similar proportions (Fig. 4.3) but inverted. However, at the greater depths of 2r and 5r the profiles change and a more rapid deflection is observed at a certain distance from the edge of the pit. In both these cases the depth of the pit is fairly accurately reported with an image depth at a 1 % set point of 1.78r (2r object depth) and 4.76r (5r object depth). However the width of the pit is underestimated by approximately 1r.

When considering the way the height profile varies with the depth of an elongated pit, height profiles at two different set points of 1% (Fig 4.31 upper panel) and 2 % (Fig. 4.31 lower panel) were examined. The accuracy of the imaged depth is increased on increasing the set point from 1 % to 2 %. For a depth of 1r the error in the image depth decreases from 0.07r to 0.03r. For a pit of depth 2r the error decreases from 0.22r to 0.07r and for a pit of depth 5r the error decreases from 0.24r to 0.08r. As may also be seen in the lower panel of Fig. 4.31, the height profile at a 2 % set point is more accurate in that it reflects a straight-edged pit with a flat, rather than rounded, bottom. it should also be noted that for the pit of depth 5r, at many points near the edge of the pit the probe would contact the surface before the set point was reached.

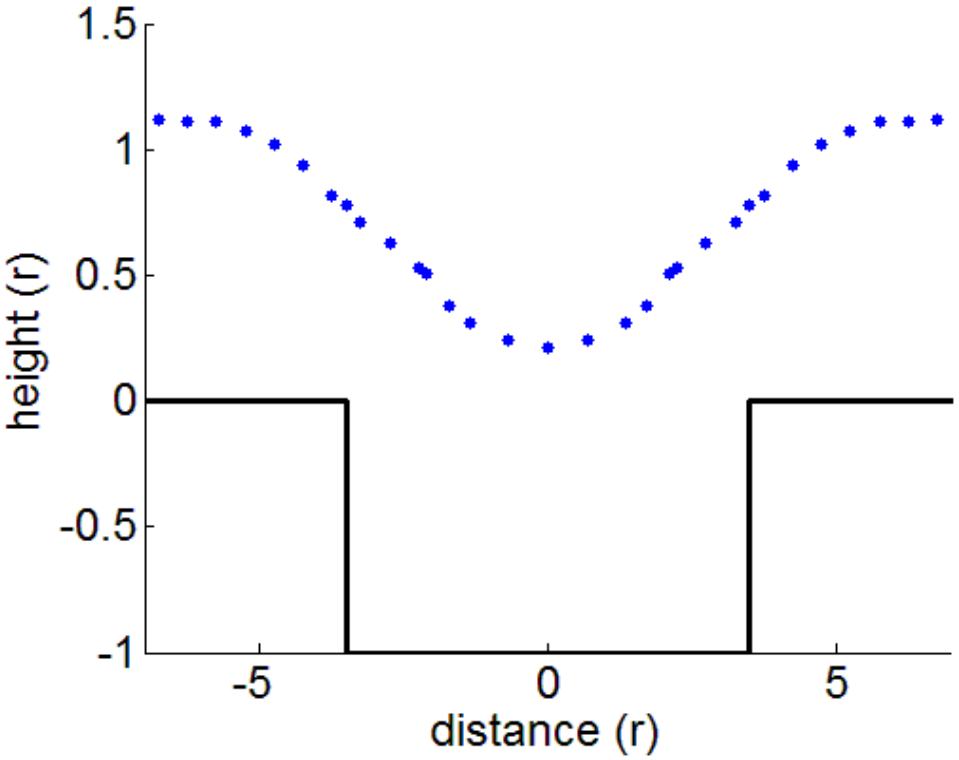

Figure 4.28 Image profile for an elongated pit of width 7r and depth 1r
The height profile returned with a set point of 1 % (blue circles) is shown with the dimensions of the pit also indicated (solid black line).

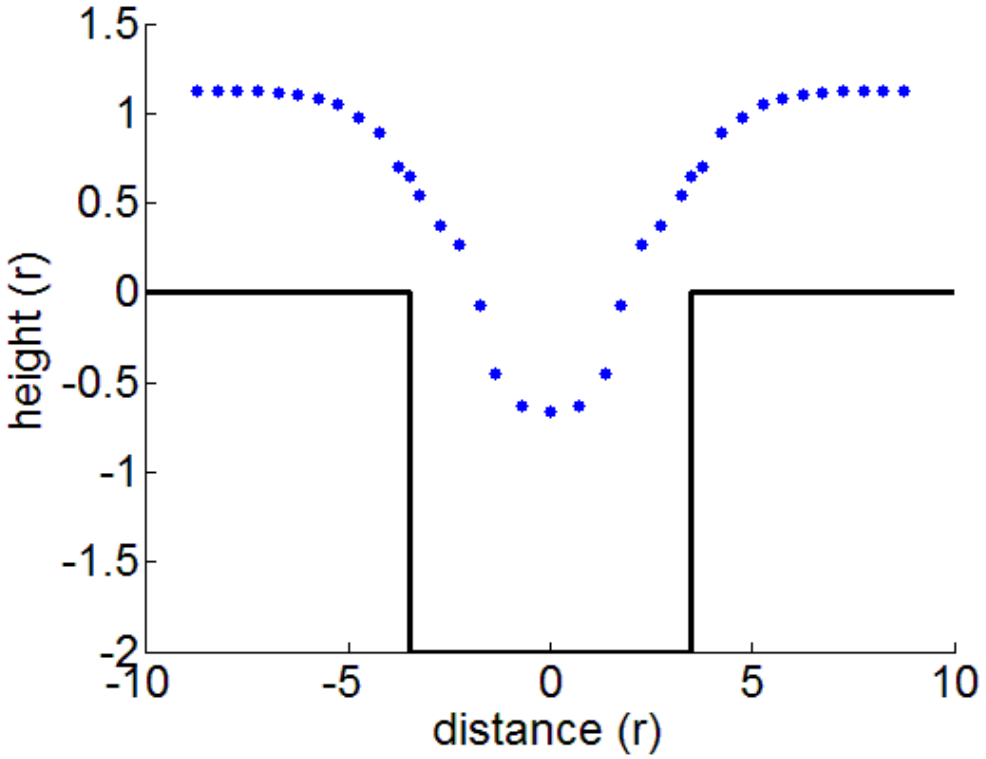

Figure 4.29 Height profile for an elongated pit of width 7r and depth 2r
The height profile returned with a set point of 1 % (blue circles) is shown with the dimensions of the pit also indicated (solid black line).

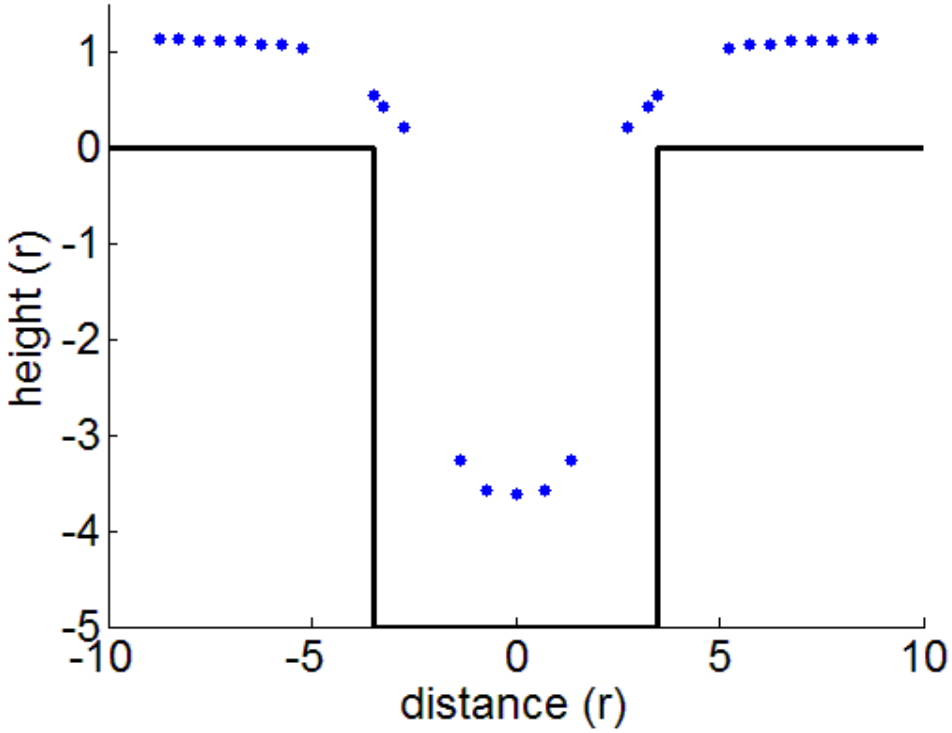

Figure 4.30 Height profile for an elongated pit of width 7r and depth 5r
The height profile returned with a set point of 1 % (blue circles) is shown with the dimensions of the pit also indicated (solid black line).

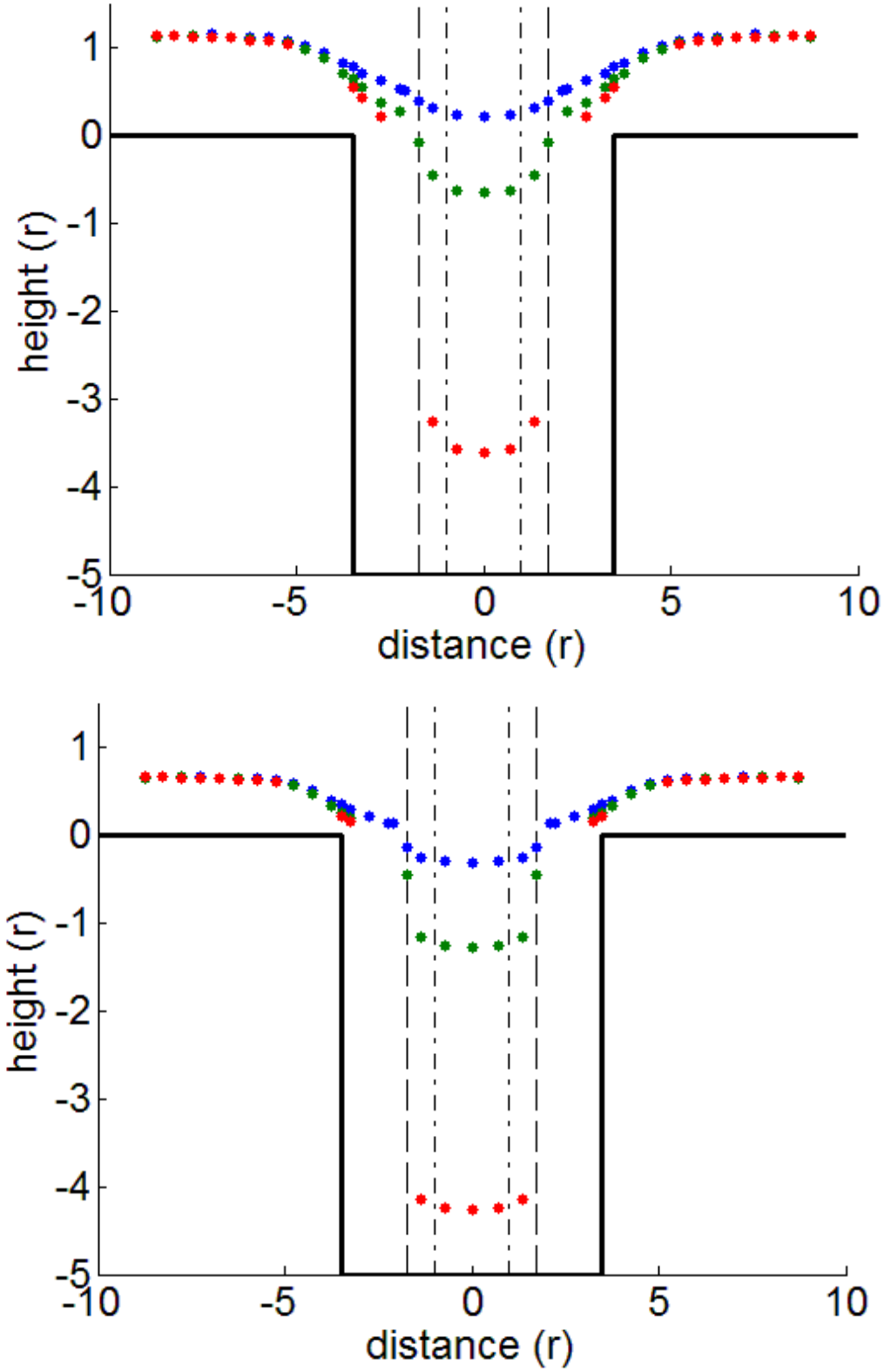

Figure 4.31 Comparison of image profiles for pits of width 7r and differing depths
The scan profiles produced as the depth was varied of a pit of width 7r are shown. The upper panel show the profile returned for a 1 % set point and the lower panel for a 2 % set point. Depths of 1r (blue circles), 2r (green circles) and 5r (red circles) were investigated. The pipette outer (dashed line) and inner radius (dotted line) are also indicated relative to the pit centre.

A pit of equal width and breadth

From the above simulations it is evident that some information about the probe can be obtained by scanning an appropriate sample. To examine this idea more closely scans across pits of equal width and breadth were simulated (Fig.4.32). Widths and breadths of 1r (i.e. less than the pipette diameter) and depths of 1r (Fig.4.33) and 5r (Fig.4.34) were simulated.

The first such simulation is shown in Figure 4.33. The FEM simulations suggest no change in apparent height when the probe is directly above the pit but a small dip when the probe is situated on each side. This profile does not vary substantially when the pit depth is altered (Fig. 4.35). Interestingly, when the pit width is increased to equal the pipette inner diameter (2r) this profile becomes exaggerated (Fig 4.36-37 and Fig. 4.39) and still appears independent of depth (Fig. 4.38). In three dimensions this creates an image of the pipette convoluted with the probe tip.

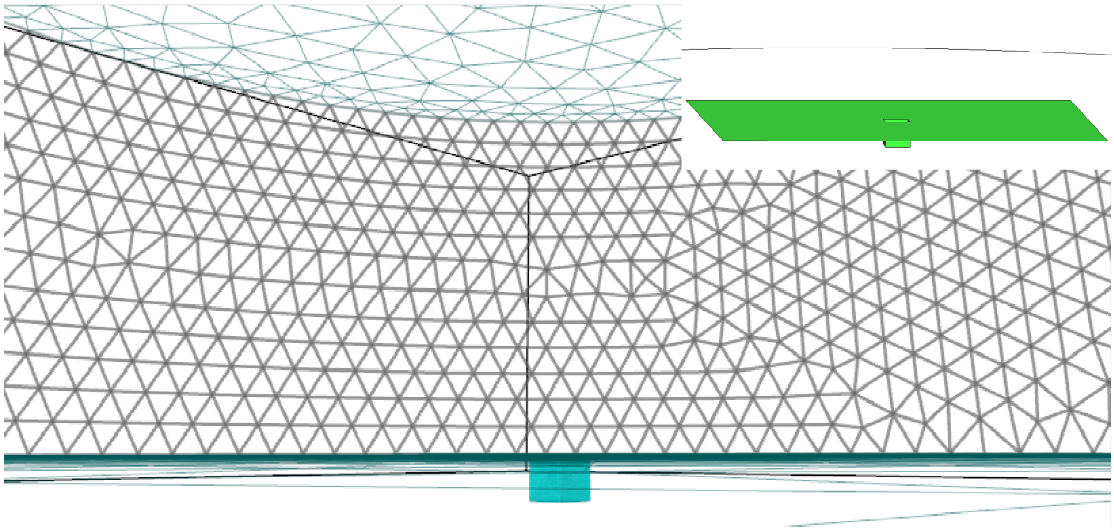

Figure 4.32 Mesh profile of the surface used to investigate the response to a pit of equal width and breadth
Both the width and the depth of the pit were varied. A view of an example surface mesh for this object is shown with the surface as specified in GiD shown inset.

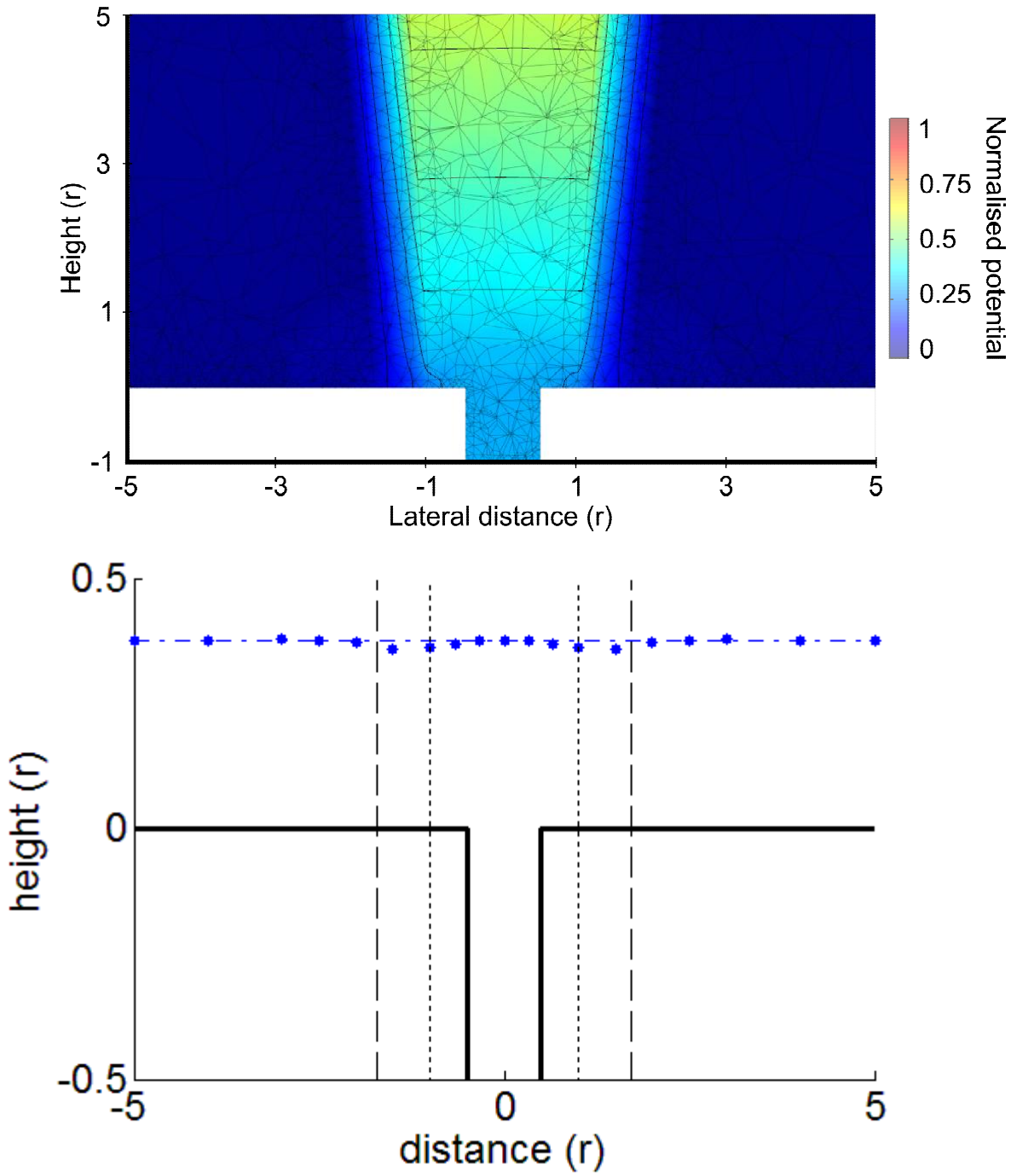

Figure 4.33 Simulations for a pit of equal width and breadth of 1r and depth 1r
The upper panel shows calculated potentials in the region close to the pipette tip with a surface-tip separation of 0.1r and the pipette centred on the pit centre. Normalised potential is shown in pseudo-colour, equipotential lines are shown as mid-weight lines and the mesh is shown as light-weight lines. The lower panel shows the height profile returned with a set point of 3.75 % (blue circles), the detected height of the flat surface surrounding the pit is indicated by the dashed blue line, the dimensions of the pit are indicated (solid black line), with the pipette outer (dashed line) and inner radius (dotted line) also shown relative to the pit centre. It should be noted that the vertical scale does not show the full depth of the pit to make the scan profile more clearly visible.

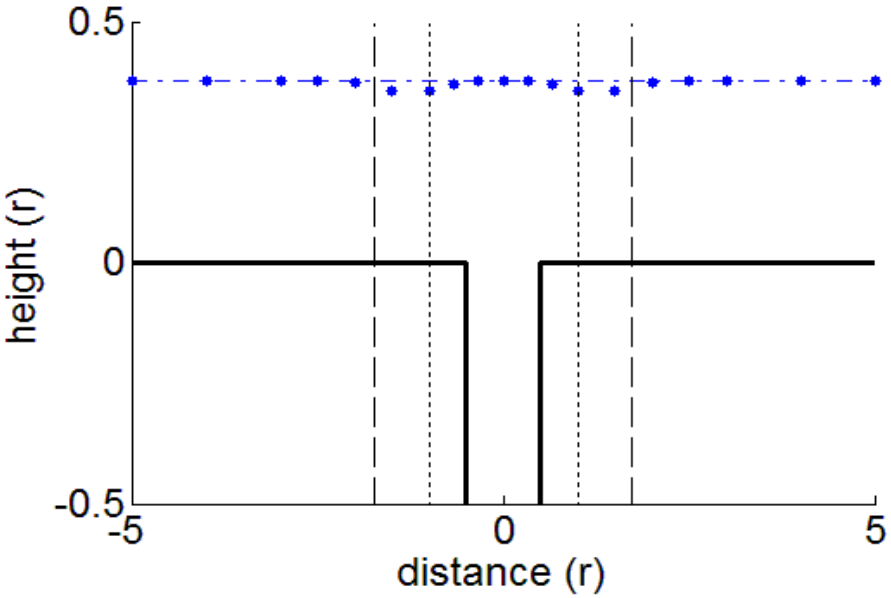

Figure 4.34 A pit of equal width and breadth of 1r and depth 5r

The height profile returned with a set point of 3.75 % (blue circles) is shown. The detected height of the flat surface surrounding the pit is indicated by the dashed blue line. The dimensions of the pit are indicated by solid black lines, with the pipette outer (dashed line) and inner radius (dotted line) also shown relative to the pit centre. It should be noted that the vertical scale does not show the full depth of the pit to make the scan profile more clearly visible.

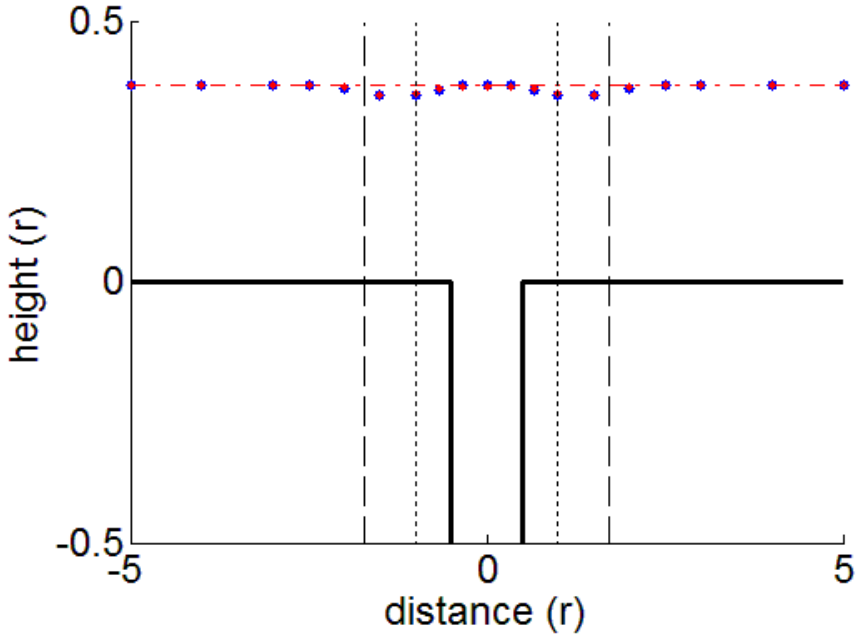

Figure 4.35 Comparison of profiles obtained using pits of different depths for a fixed width and breadth of 1r

The height profile produced for pits of depth 1r (blue circle) and 5r (red circles) is shown for a 3.75 % set point. The detected height of the flat surface surrounding the pit is indicated by the dashed coloured lines (1r, blue; 5r, red). The pipette outer (dashed line) and inner radius (dotted line) are shown relative to the pit centre. It should be noted that the vertical scale does not show the full depth of the pit to make the scan profile more clearly visible.

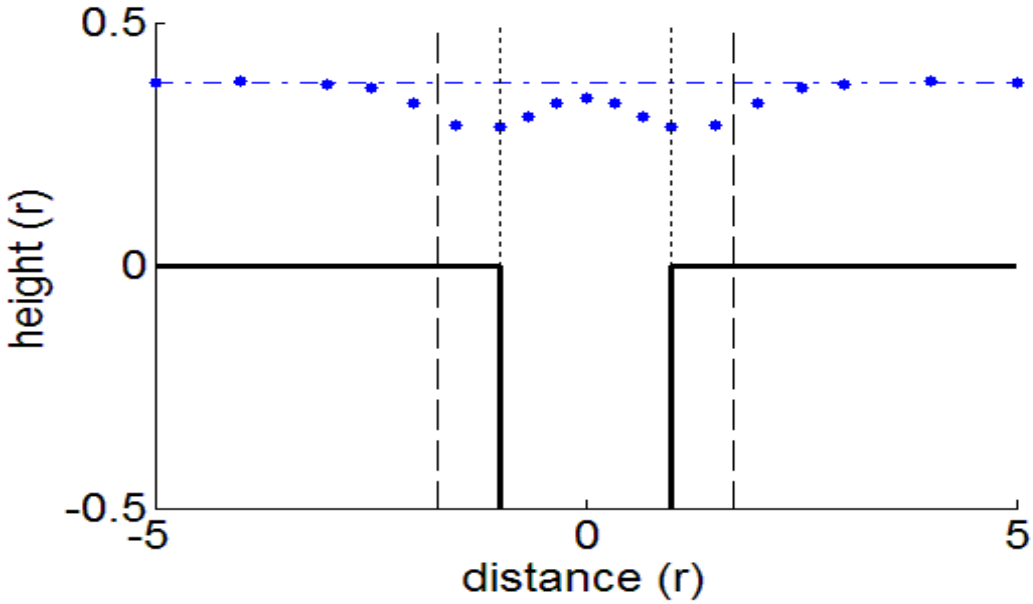

Figure 4.36 A pit of equal width and breadth of 2r and depth 2r
The height profile returned with a set point of 3.75 % (blue circles) is shown. The detected height of the flat surface surrounding the pit is indicated by the dashed blue line. The dimensions of the pit are indicated by solid black lines, with the pipette outer (dashed line) and inner radius (dotted line) also shown relative to the pit centre. It should be noted that the vertical scale does not show the full depth of the pit to make the scan profile more clearly visible.

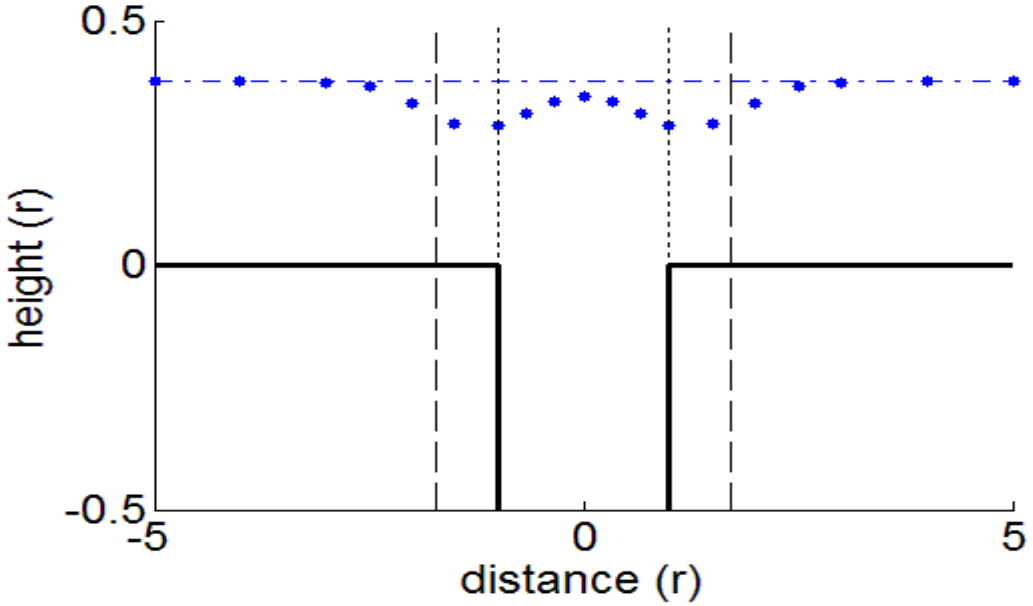

Figure 4.37 A pit of equal width and breadth of 2r and depth 5r
The height profile returned with a set point of 3.75 % (blue circles) is shown. The detected height of the flat surface surrounding the pit is indicated by the dashed blue line. The dimensions of the pit are indicated by solid black lines, with the pipette outer (dashed line) and inner radius (dotted line) also shown relative to the pit centre. It should be noted that the vertical scale does not show the full depth of the pit to make the scan profile more clearly visible.

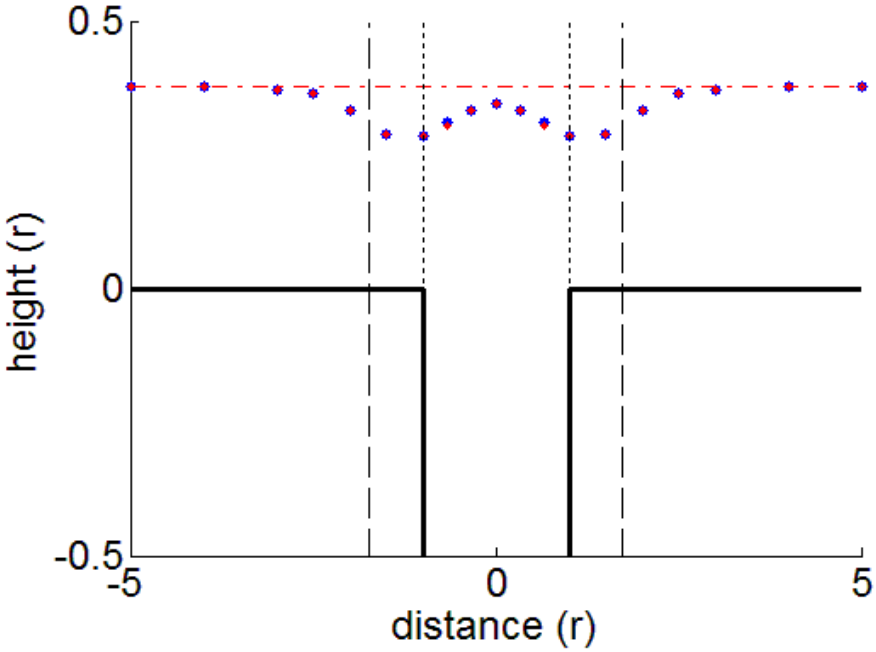

Figure 4.38 Comparison of pits of different depths for a fixed width and breadth of 2r
The height profile produced for pits of depth 2r (blue circle) and 5r (red circles) is shown for a 3.75 % set point. The detected height of the flat surface surrounding the pit is indicated by the dashed coloured lines (2r, blue; 5r, red). The pipette outer (dashed line) and inner radius (dotted line) are shown relative to the pit centre. It should be noted that the vertical scale does not show the full depth of the pit to make the scan profile more clearly visible.

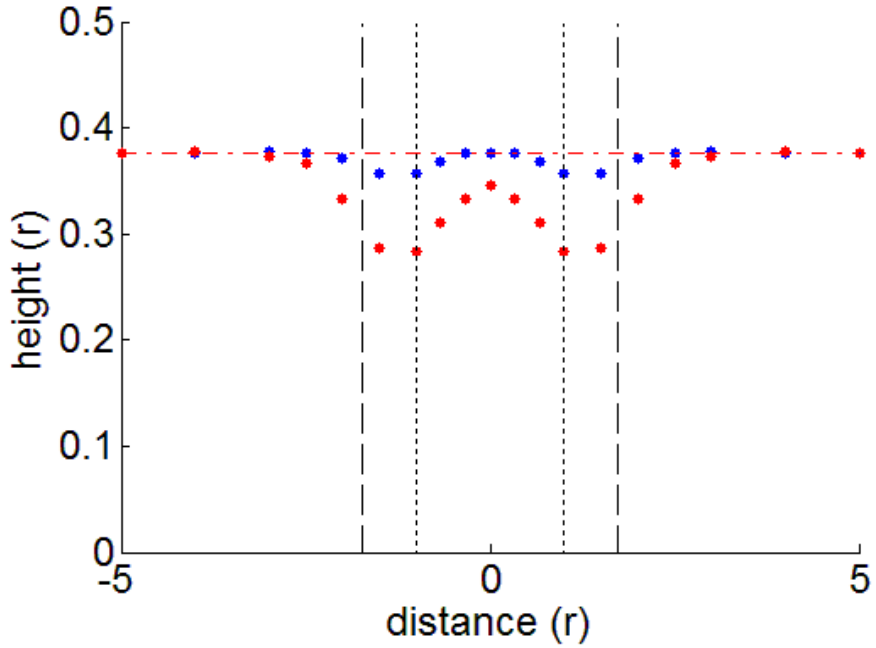

Figure 4.39 Comparison of pits of different width/breadth for a fixed depth of 5r
The height profile produced for pits of width/breadth 1r (blue circle) and 2r (red circles) is shown for a 3.75 % set point. The detected height of the flat surface surrounding the pit is indicated by the dashed coloured lines (1r, blue; 2r, red). The pipette outer (dashed line) and inner radius (dotted line) are shown relative to the pit centre.

4.4 Simulation of scanning profiles across biologically realistic surface shapes

Omega shape

Often in scanning biological samples the probe will encounter rounded objects such as cell bodies, dendrites or axons. In order to examine how images of these objects may appear an "omega shaped cylinder" with 15 % of the radius submerged below the surface (Fig. 4.40) was simulated. The omega shape used for these studies had a diameter of 3r (Fig. 4.41).

One point to note immediately from the simulations is that it is not possible to scan over the entire surface using a 1% setpoint without colliding, so some of the points are missing from the lower panel of Fig. 4.41. This is perhaps to be expected because the edge of the omega becomes increasingly upright and thus, as far as the pipette is concerned, approaches a profile somewhat resembling that of a square step. From the remaining points it can be seen that the object has a rounded profile that is slightly broadened by the pipette.

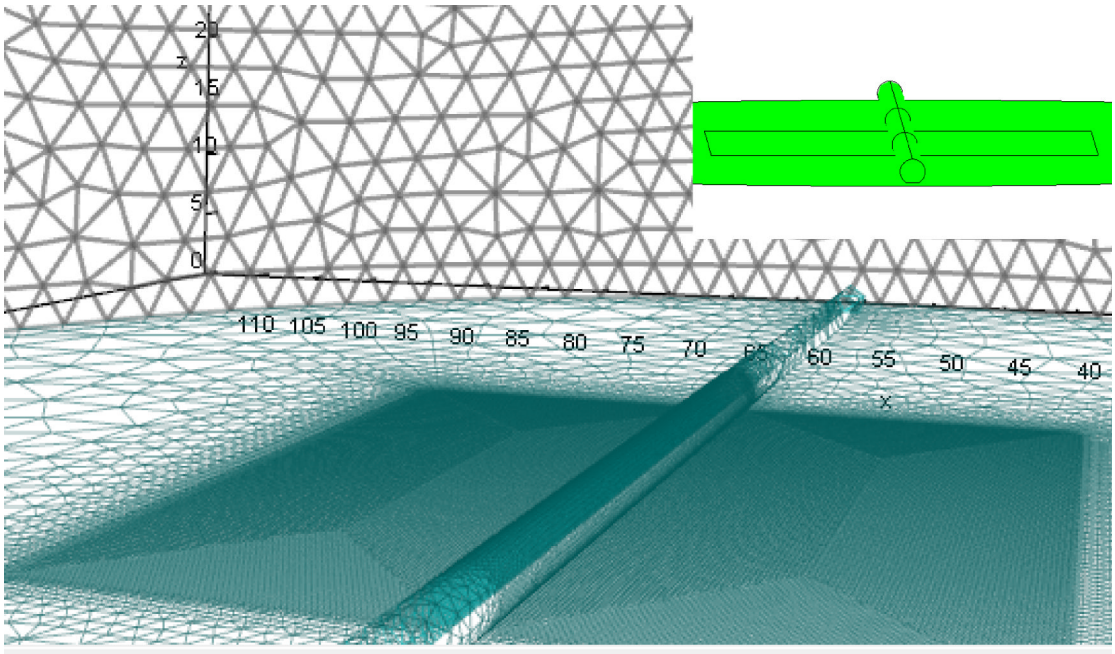

Figure 4.40 Mesh profile of the surface used to investigate the response to a rounded omega feature
A view of an example surface mesh for this object is shown with the surface as specified in GiD shown inset.

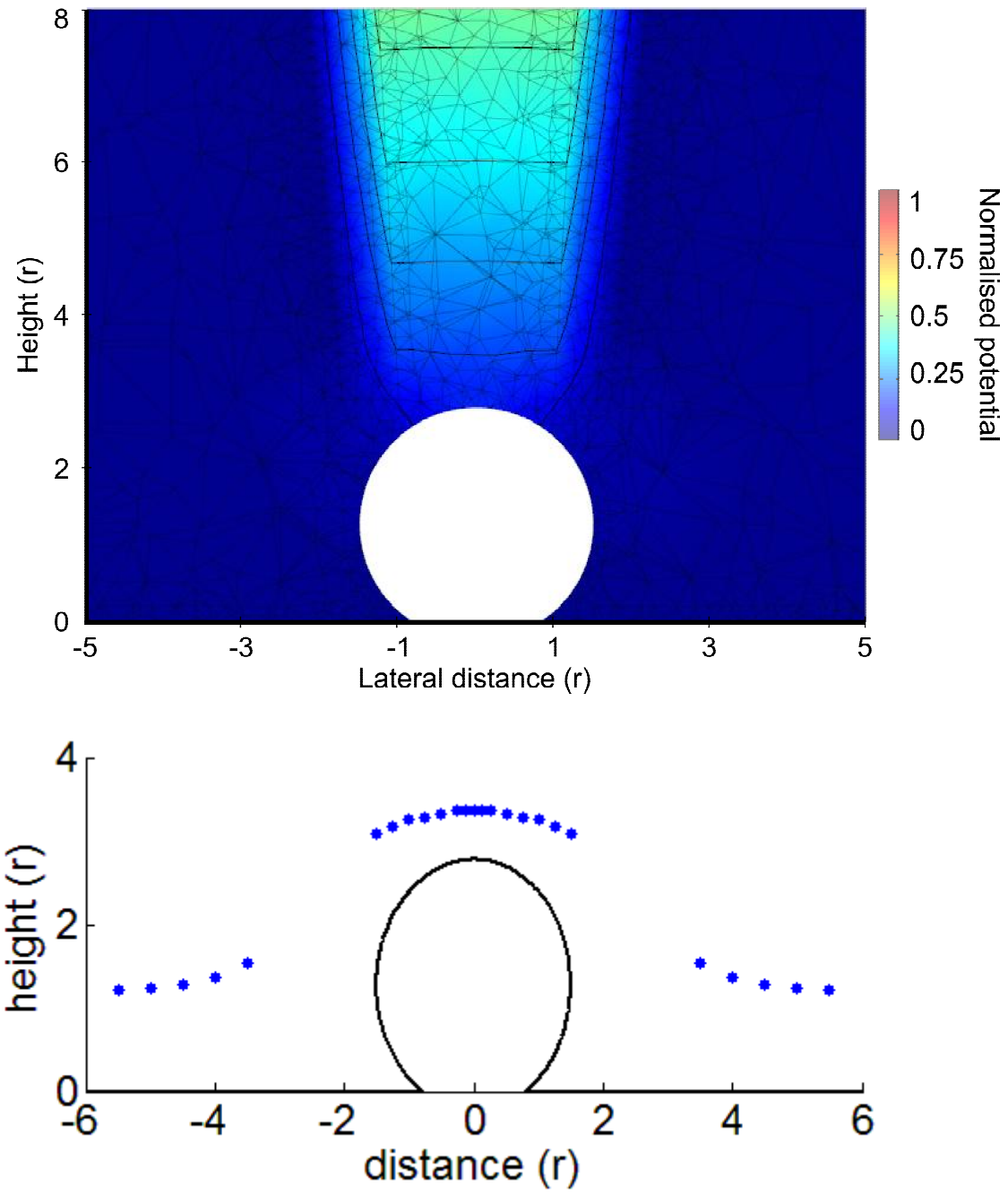

Figure 4.41 Simulations for the scan of an omega shape of diameter 3r
The upper panel shows the potential in the region close to the pipette tip for a surface-tip separation of 0.1r and the pipette centred on the pit centre. Normalised potential is shown in pseudo-colour, equipotential lines are shown as mid-weight lines and the mesh is shown as light-weight lines. The lower panel shows the height profile returned with a set point of 1 % (blue circles), the dimensions of the omega is also indicated (solid black line). It should be noted that the vertical and horizontal scaling are not equal in order to show the scan profile more clearly.

Double omegas

A pair of omega features was also investigated (Fig. 4.42). The purpose of this simulation was to provide an estimated measure of 'biological resolution' and to obtain data that could then be compared with the double pedestal simulations presented earlier. With this in mind, pairs of extended omega features of maximum diameter 2r (and maximum height 1.85r) were created and the separation between the inner-most edges of these omegas was varied from 1r – 5r (Fig. 4.43-46).

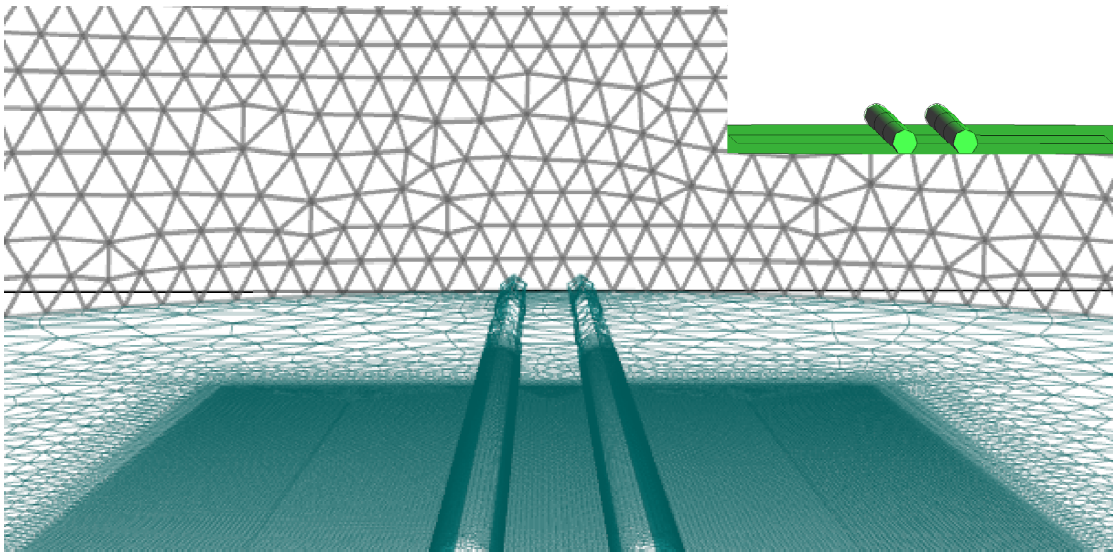

Figure 4.42 Mesh profile of the surface used to investigate the response to a pair of extended omega features
A view of an example surface mesh for this object is shown along with the surface as specified in GiD (inset).

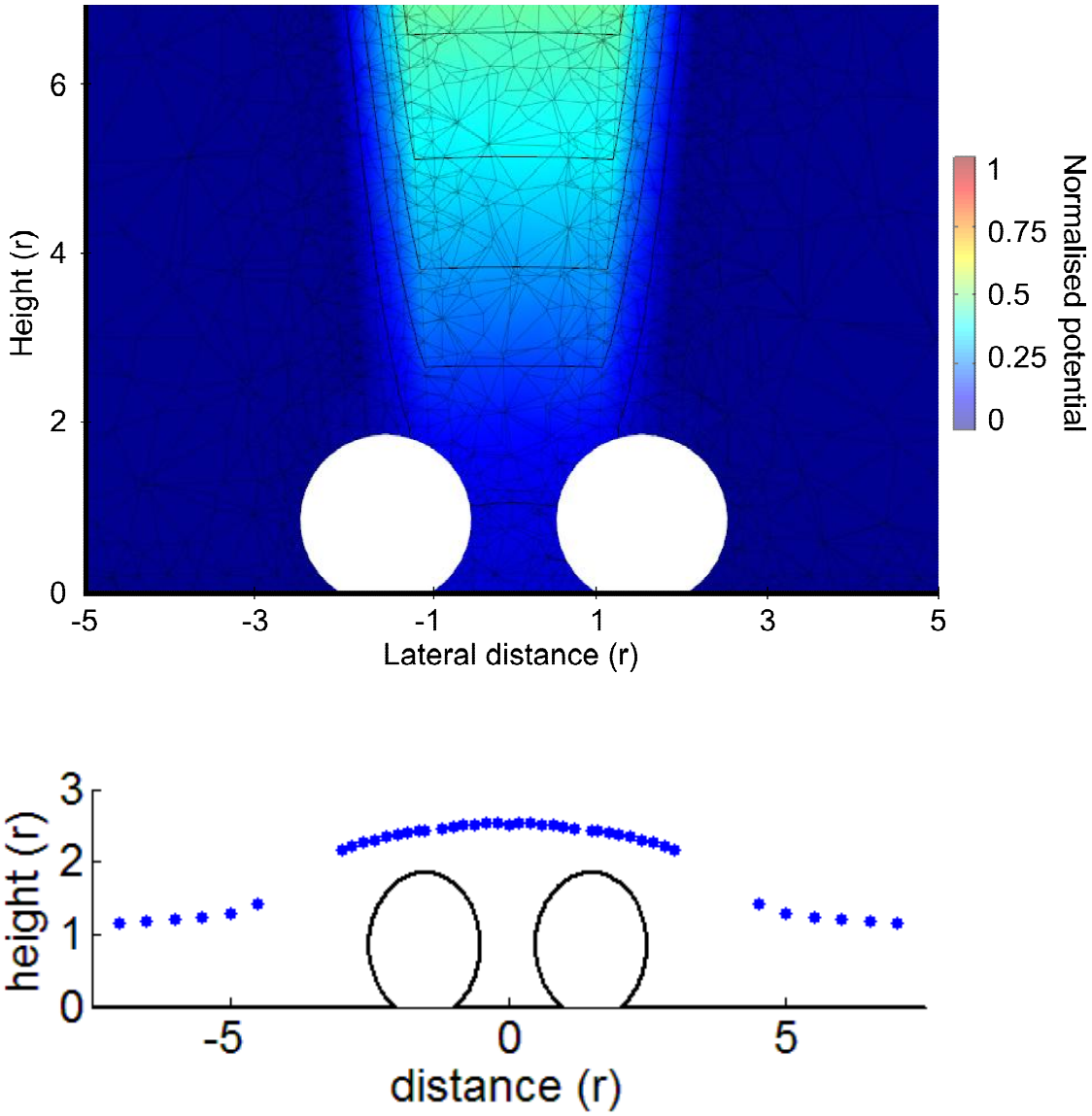

Figure 4.43 Double omega of diameter 2r and separation 1r
The upper panel shows the potential in the region close to the pipette tip for a surface-tip separation of 0.1r and the pipette centred on the pit centre. Normalised potential is shown in pseudo-colour, equipotential lines are shown as mid-weight lines and the mesh is shown as light-weight lines. The lower panel shows the height profile returned with a set point of 1 % (blue circles), d = -0.08r. The dimensions of the omegas are indicated (solid black line). It should be noted that the vertical and horizontal scaling are not equal in order to show the scan profile more clearly.

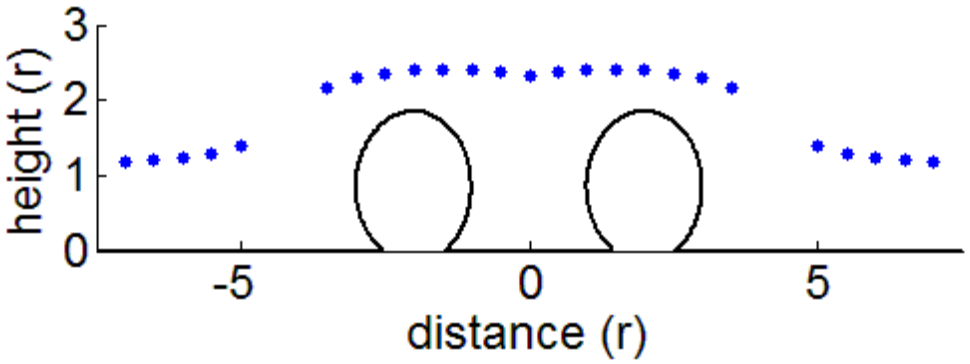

Figure 4.44 Double omega of diameter 2r and separation 2r
The height profile returned with a set point of 1 % (blue circles) is shown. These data give d = 0.06r. The dimensions of the omegas are indicated (solid black line). It should be noted that the vertical and horizontal scaling are not equal in order to show the scan profile more clearly.

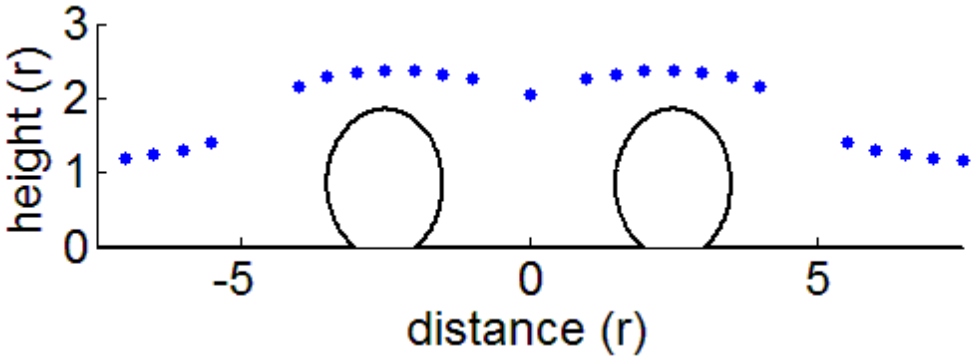

Figure 4.45 Double omega of diameter 2r and separation 3r
The height profile returned with a set point of 1 % (blue circles) is shown. These data give d = 0.31r. The dimensions of the omegas are indicated (solid black line). It should be noted that the vertical and horizontal scaling are not equal in order to show the scan profile more clearly.

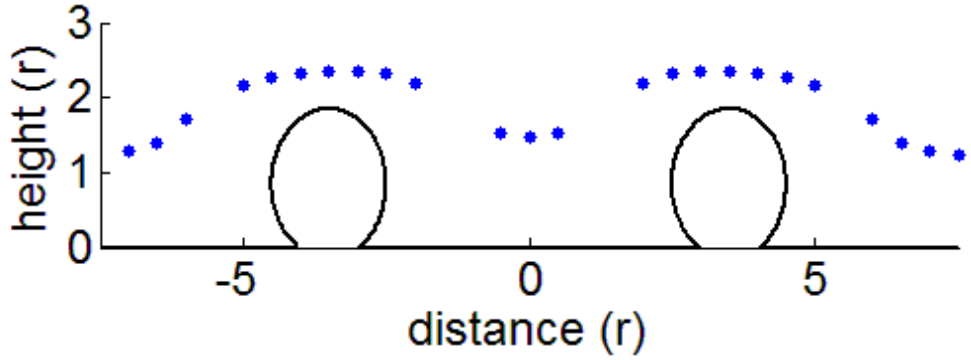

Figure 4.46 Double omega of diameter 2r and separation 5r
The height profile returned with a set point of 1 % (blue circles) is shown. These data give d = 0.87r. The dimensions of the omegas are indicated (solid black line). It should be noted that the vertical and horizontal scaling are not equal in order to show the scan profile more clearly.

Omegas with spacing 1r were not distinguishable, producing a deflection of d = -0.08r, and δ = -6.6% which suggests that the omega shapes are slightly less "resolvable" than their pedestal counterparts where the value found for two pedestals of height 1r and spacing 1r was d = -0.04r. Indeed this finding also proved to be true with other spacings. For example, omegas of spacing 2r gave d = 0.06r while square pedestals of height 1r and 5r with this spacing both produced larger d values of 0.07 (1r) and 0.22 (5r) reflecting bigger dips between adjacent objects. The omegas were more readily distinguishable as a pair with spacings of 3r (d = 0.31r and δ = 26.0%) and at 5r (d = 0.87r and δ = 74.2%). Overall these results suggest that more curved surfaces may tend to be imaged with a slightly lower working resolution.

When both square pedestals and round omegas are close together they cannot be resolved and appear as a single peak. It is interesting to note that the closer the spacing the better the height of this peak reflects the true height of the underlying objects. In contrast, when the objects are widely spaced and apparently well resolved they have a reduced height (Fig. 4.47and Fig. 4.48).

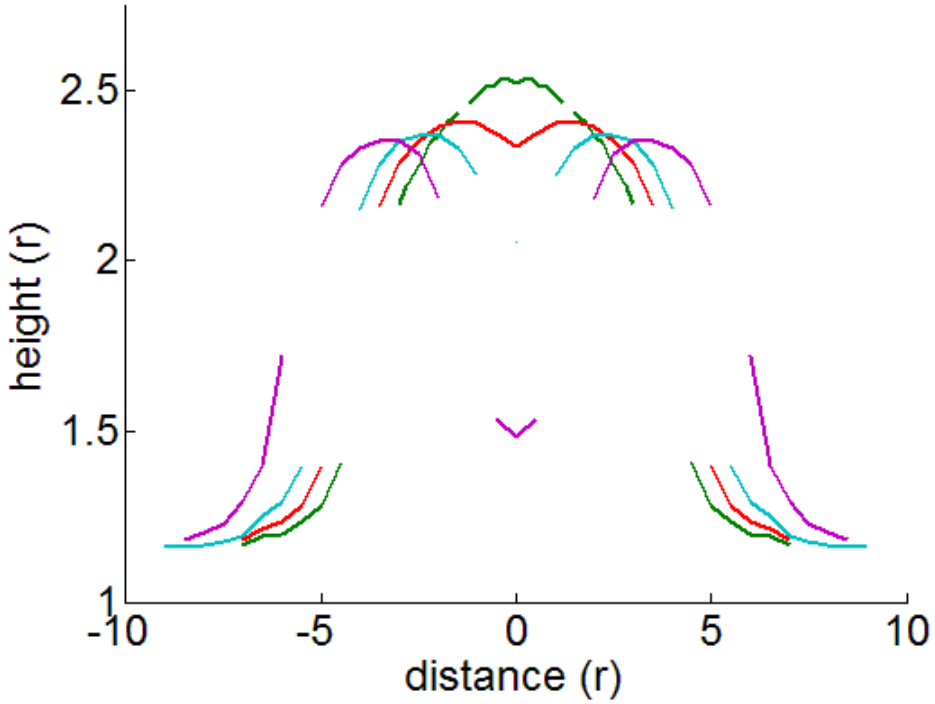

Figure 4.47 Comparison of double omegas at different separations
The height profiles returned with a 1 % set point from simulated line scans across a pair of omega features at different spacings is shown. Data is shown as line plots where breaks in these lines indicate data missing due to points where the probe would contact the surface. The spacings between centres of the omega shapes investigated were 1r (green), 2r (red), 3r (cyan), 5r (purple). It should be noted that the vertical and horizontal scaling is not equal in order to show the scan profiles more clearly.

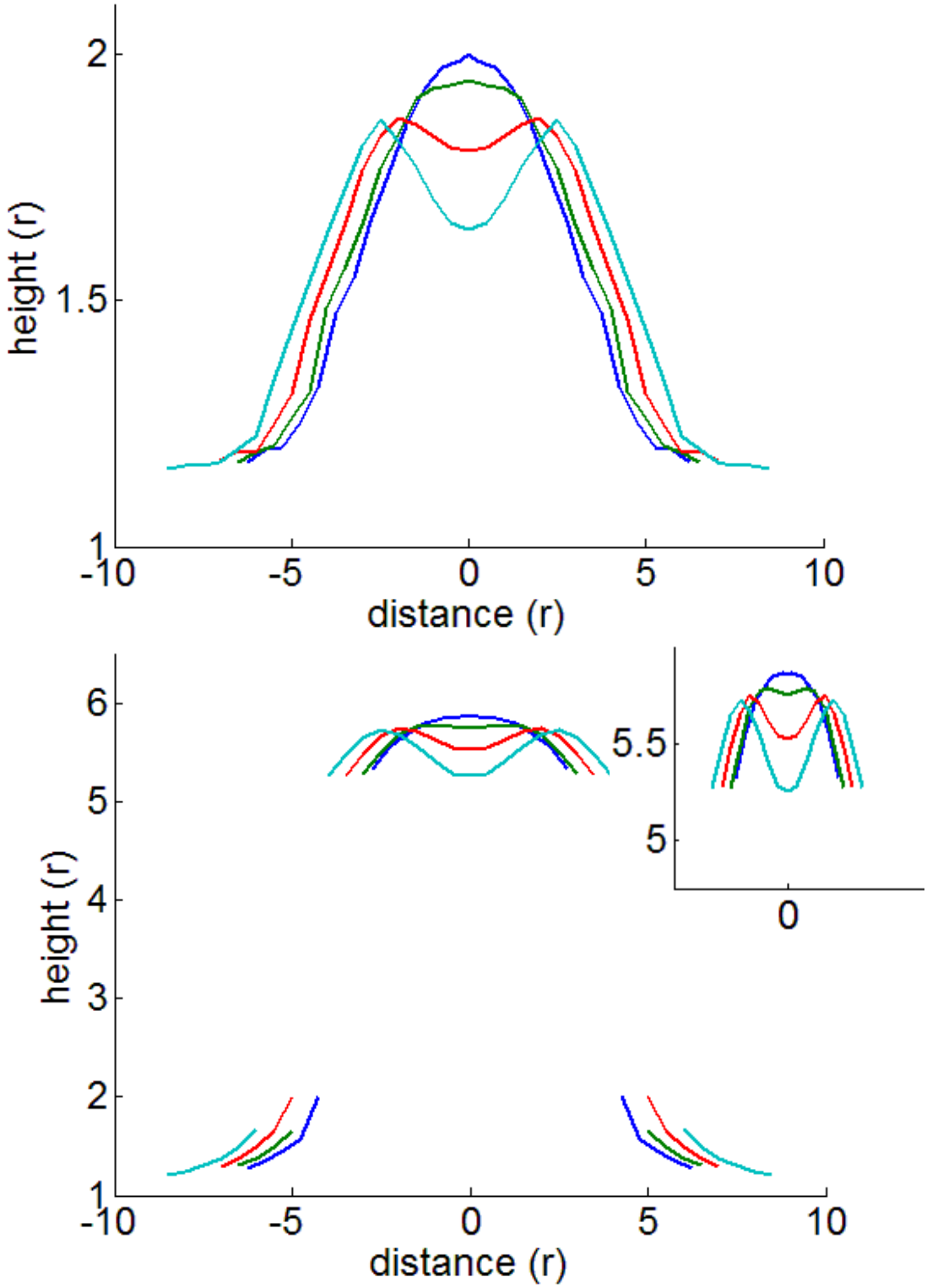

Figure 4.48 Comparison of double peaks at different separations
The height profiles returned with a 1 % set point from simulated line scans across a pair of pedestal profiles at different spacings is shown (as presented in section 4.1). Data is shown as line plots where breaks in these lines indicate data missing due to points where the probe would contact the surface. The spacings between centres of the peaks investigated were 0.5r (blue), 1r (green), 2r (red) and 3r (cyan). The upper panel shows data for peaks of height 1r. The lower panel shows data for peaks of height 5r with the line-scans in the region directly above the peaks on the same scale as the upper panel shown inset.

A single, very small hemisphere

Small structures such as microvilli can appear as small protrusions on the surface of a cell. Similarly, it has been suggested that dense core granules may deposit cargo on the surface of the cell without it dispersing (de Wit et al., 2009). Finally, viral particles attaching to a cell surface and subsequently entering have been imaged by SICM (Shevchuk et al., 2008b). Objects such as these are very small and are often comparable to, or even smaller than, the inner radius of the SICM probe. To determine how objects such as these might appear in SICM images, a positive hemisphere was simulated (Fig. 4.49). Small hemispheres of radii 0.25r (Fig. 4.50), 0.5r (Fig. 4.51) and 1.5r (Fig. 4.52) were all investigated (Fig. 4.53).

The scan appears insensitive to the smallest hemisphere of 0.25r radius, even at a set point of 2.25 %. However an image is obtained for hemispheres of radius 0.5r and 0.75r. In both these cases a pair of raised features is observed each centred at the pipette inner wall (Fig. 4.53). This suggests the produced image represents a convolution between the probe tip and the surface.

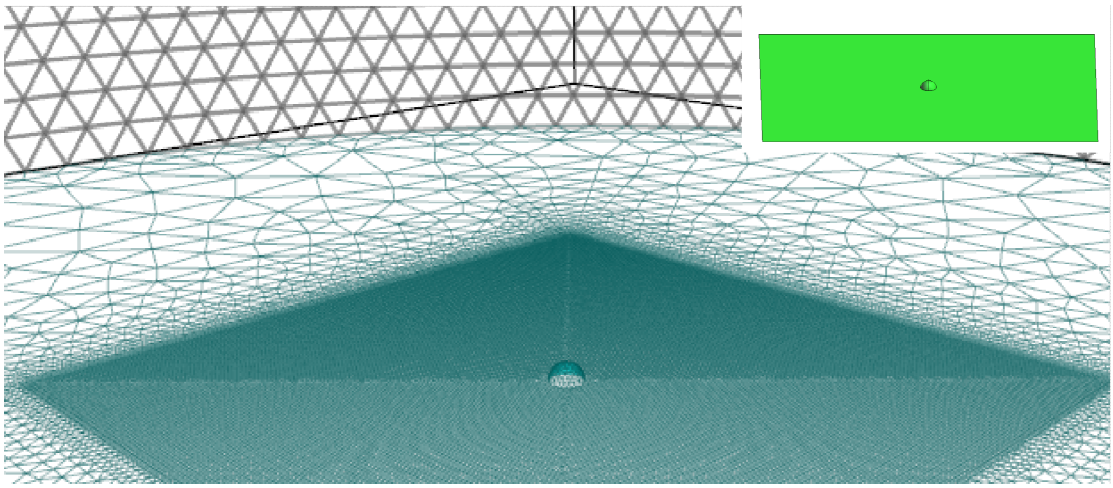

Figure 4.49 Mesh profile of the surface used to investigate the response to a raised hemisphere
A view of an example surface mesh for this object is shown along with the surface as specified in GiD (inset).

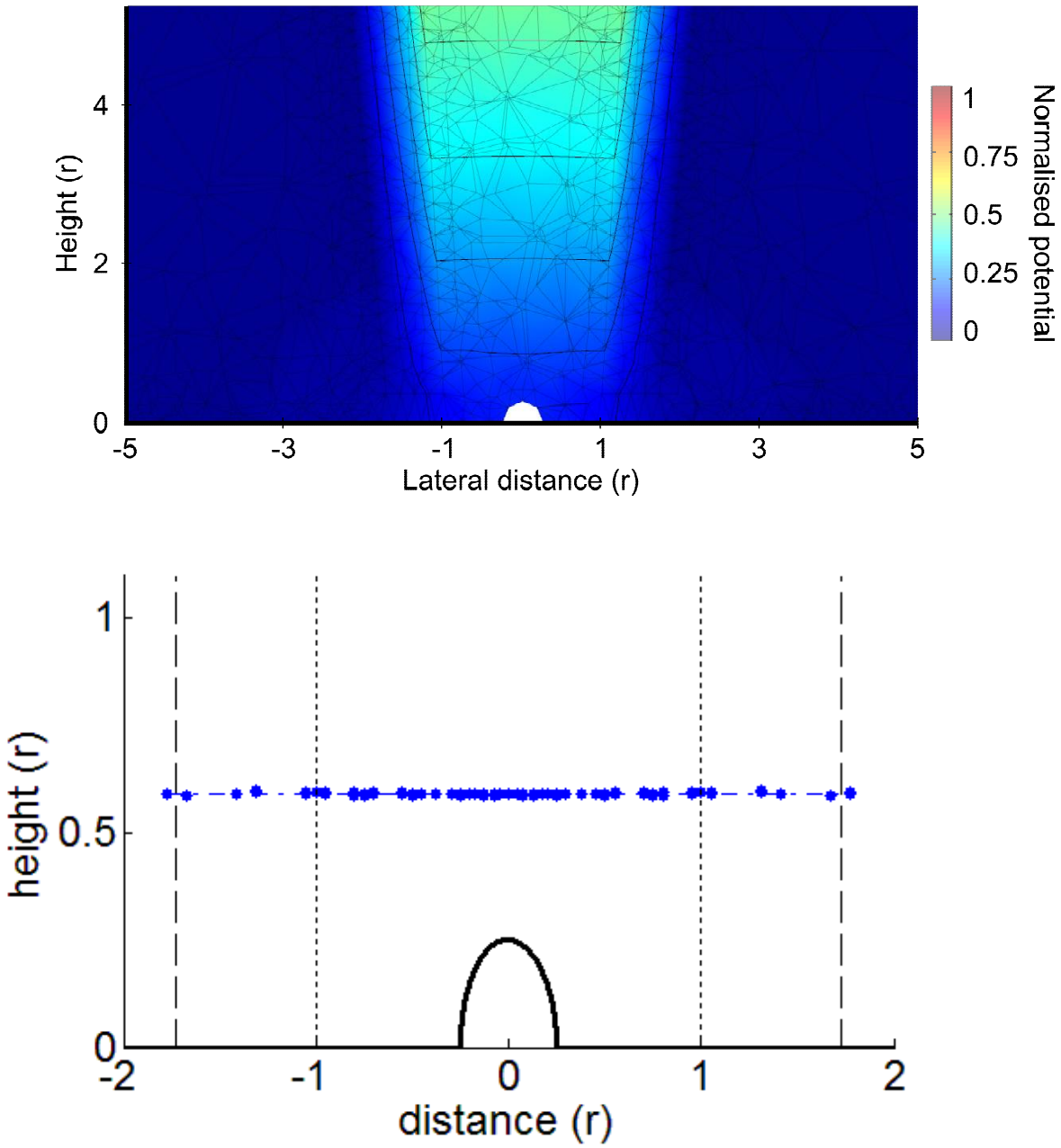

Figure 4.50 Hemisphere of radius 0.25r

The upper panel shows the potential in the region close to the pipette tip for a single position with a surface-tip separation of 0.1r and the pipette centred on the hemisphere centre. Normalised potential is shown in pseudo-colour, equipotential lines are shown as mid-weight lines and the mesh is shown as light-weight lines. The lower panel shows the height profile returned with a set point of 2.25 % (blue circles), the detected height of the flat surface surrounding the hemisphere is indicated by the dashed blue line, the dimensions of the hemisphere are indicated (solid black line), with the pipette outer (dashed line) and inner radius (dotted line) also shown relative to the hemisphere centre. It should be noted that the vertical and horizontal scaling are not equal in order to show the scan profile more clearly.

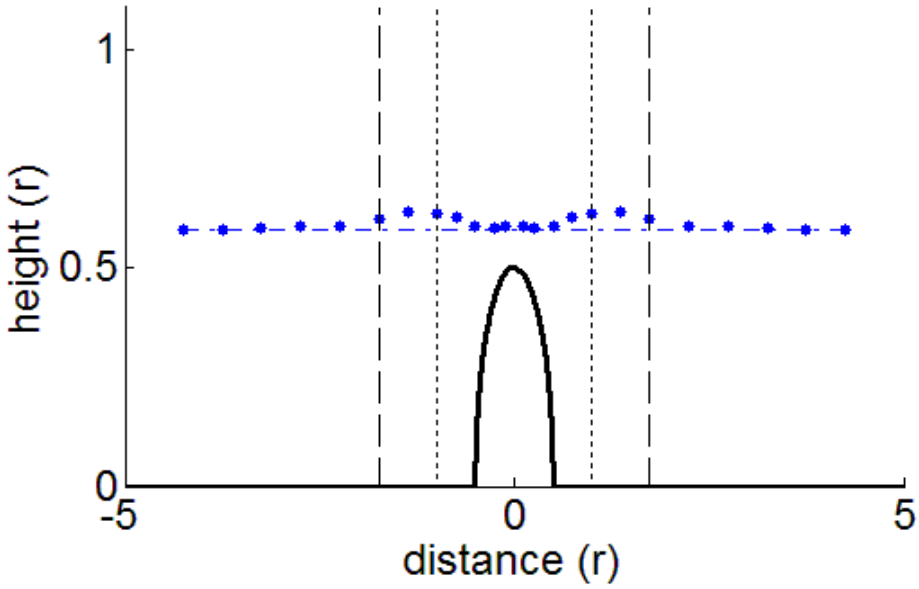

Figure 4.51 Hemisphere of radius 0.5r

The height profile returned with a set point of 2.25 % (blue circles) is shown. The detected height of the flat surface surrounding the hemisphere is indicated by the dashed blue line. The dimensions of the hemisphere are indicated by a solid black line, with the pipette outer (dashed line) and inner radius (dotted line) also shown relative to the hemisphere centre. It should be noted that the vertical and horizontal scaling are not equal in order to show the scan profile more clearly.

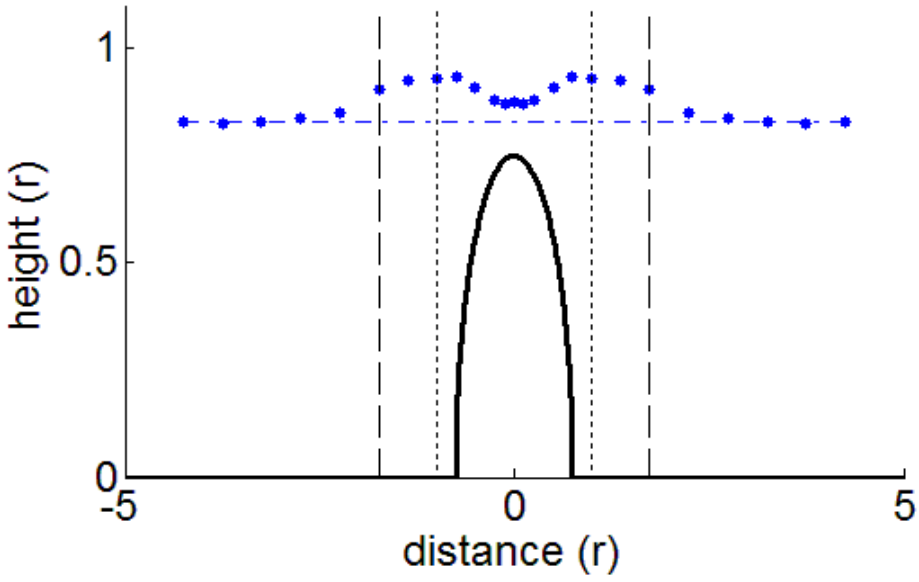

Figure 4.52 Hemisphere of radius 0.75r

The height profile returned with a set point of 2.25 % (blue circles) is shown. The detected height of the flat surface surrounding the hemisphere is indicated by the dashed blue line. The dimensions of the hemisphere are indicated by a solid black line, with the pipette outer (dashed line) and inner radius (dotted line) also shown relative to the hemisphere centre. It should be noted that the vertical and horizontal scaling are not equal in order to show the scan profile more clearly.

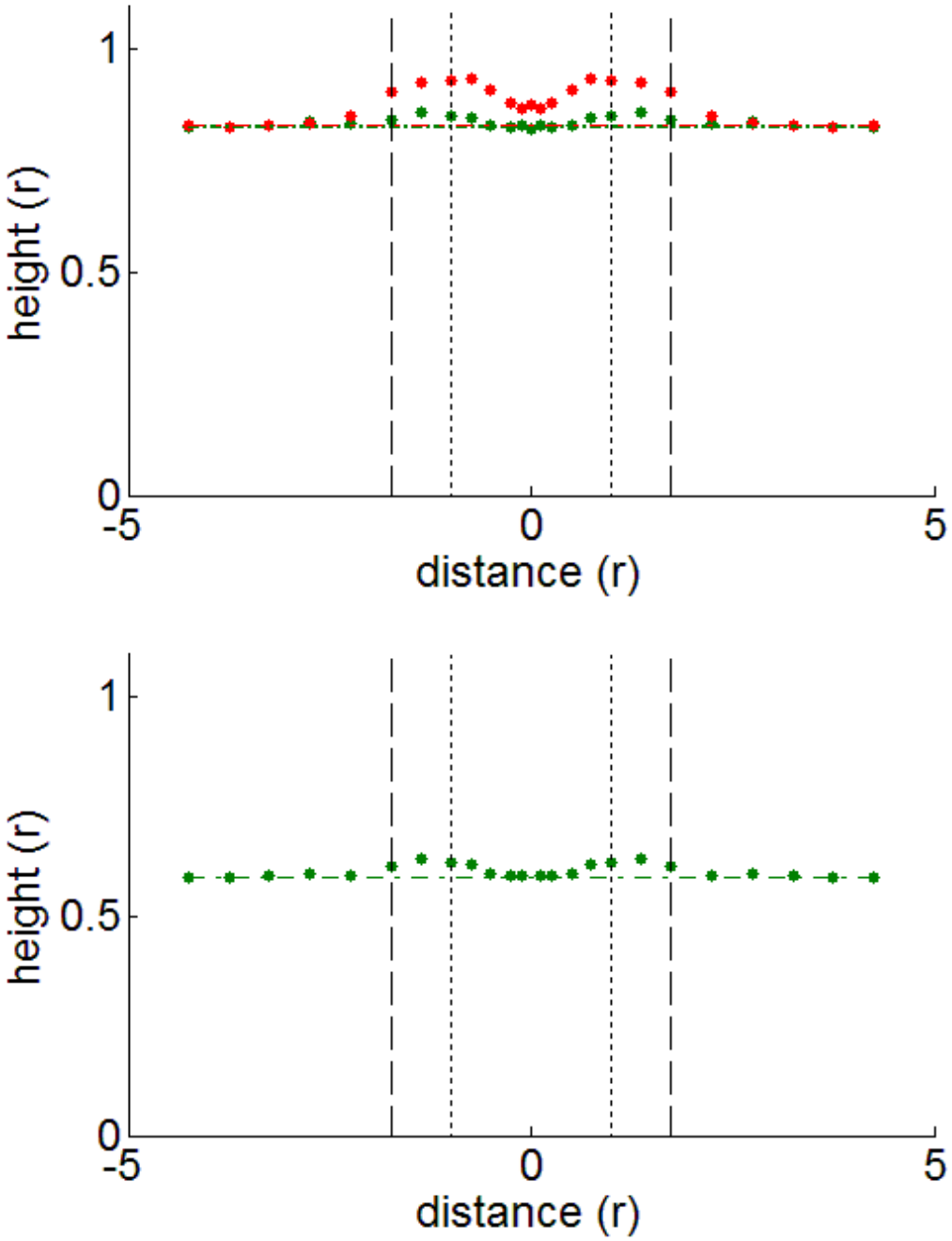

Figure 4.53 Comparison of hemispheres of different radii
The upper panel shows the height profile produced for a hemisphere of radius 0.5r (green circles) and 0.75r (red circles) for a 1.5 % set point. The lower panel shows the height profile produced for hemispheres of 0.5r (green circles), analysed at the higher set point of 2.25 %. In both panels the detected height of the flat surface surrounding the hemisphere is indicated by the dashed coloured lines (0.25r, blue; 0.5r, green). The pipette outer (dashed line) and inner radius (dotted line) are also shown relative to the hemisphere centre. It should be noted that the vertical and horizontal scaling are not equal in order to show the scan profile more clearly.

Inverted hemisphere

In addition to the types of small positive protrusion sometimes found in biology and discussed above, small infolds on the surface of cells or tissues are also possible. The most common example of this is probably the forming of pits during cycles of exo- and endo- cytosis. To examine how these might appear, the scanning of a fused secretory granule was simulated using an inverted hemisphere (Fig. 4.54). Granule radii of 1r (Fig. 4.55), 1.5r (Fig. 4.56) and 2r (Fig. 4.57) were investigated in this way.

For both 1r and 1.5r radii granules, the image produced resembles that of the narrow square pits simulated earlier, in that a probe tip image is observed (Fig. 4.58). Once the granule becomes equal to the size of the pipette inner radius (a granule radius of 2r) the feature dimensions are more accurately reflected in the image and it appears more clearly as a depression in the cell surface. However the apparent depth of the granule is significantly reduced and the lateral dimensions are also extended by convolution with the tip.

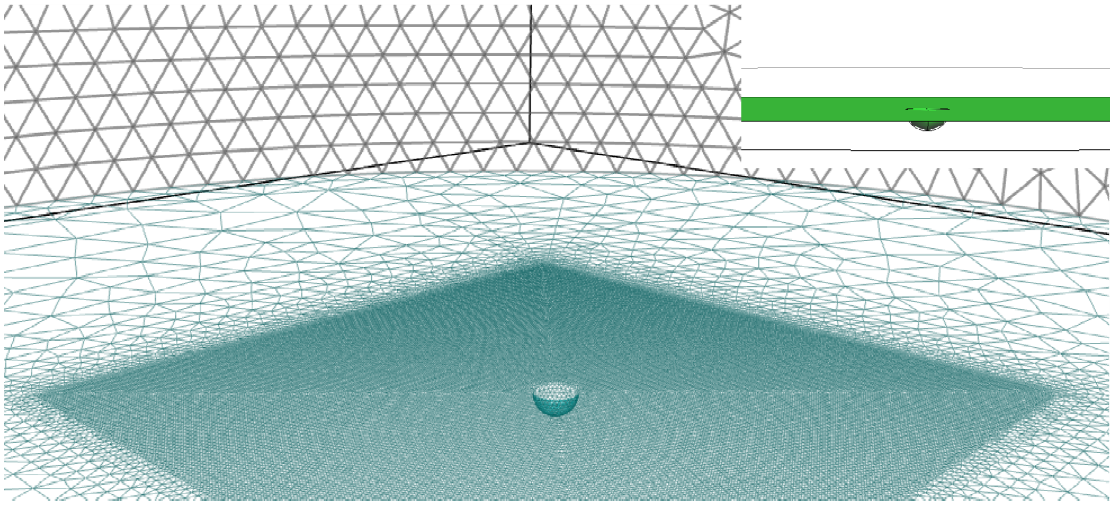

Figure 4.54 Mesh profile of the surface used to investigate the response to an inverted hemisphere
A view of an example surface mesh for this object is shown along with the surface as specified in GiD (inset).

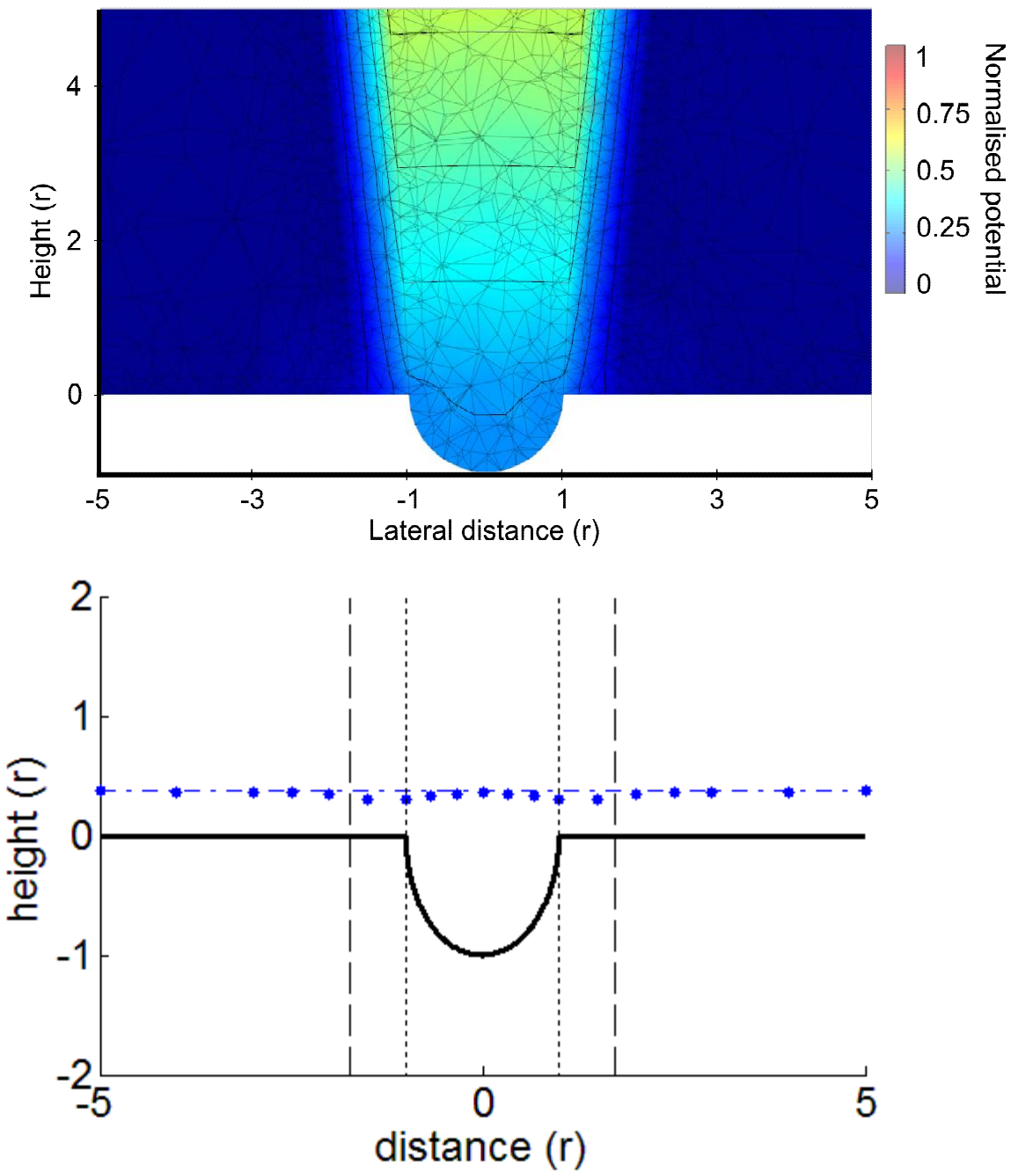

Figure 4.55 Granule of radius 1r

The upper panel shows the potential in the region close to the pipette tip for a single position with a surface-tip separation of 0.1r and the pipette centred on the granule centre. Normalised potential is shown in pseudo-colour, equipotential lines are shown as mid-weight lines and the mesh is shown as light-weight lines. The lower panel shows the height profile returned with a set point of 3.75 % (blue circles), the detected height of the flat surface surrounding the feature is indicated by the dashed blue line, the dimensions of the granule are indicated (solid black line), with the pipette outer (dashed line) and inner radius (dotted line) also shown relative to the granule centre. It should be noted that the vertical and horizontal scaling are not equal in order to show the scan profile more clearly.

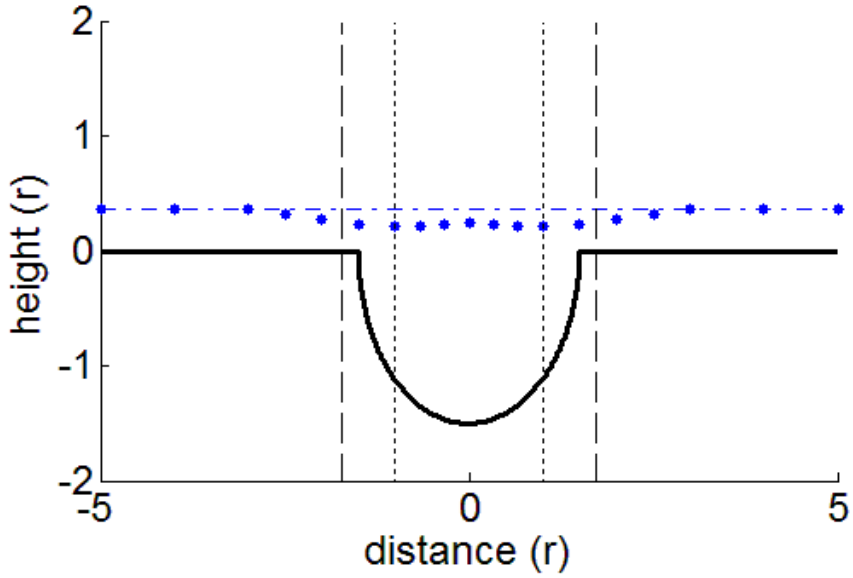

Figure 4.56 Granule of radius 1.5r

The height profile returned with a set point of 3.75 % (blue circles) is shown. The detected height of the flat surface surrounding the feature is indicated by the dashed blue line. The dimensions of the granule are indicated by the solid black line, with the pipette outer (dashed line) and inner radius (dotted line) also shown relative to the granule centre. It should be noted that the vertical and horizontal scaling are not equal in order to show the scan profile more clearly.

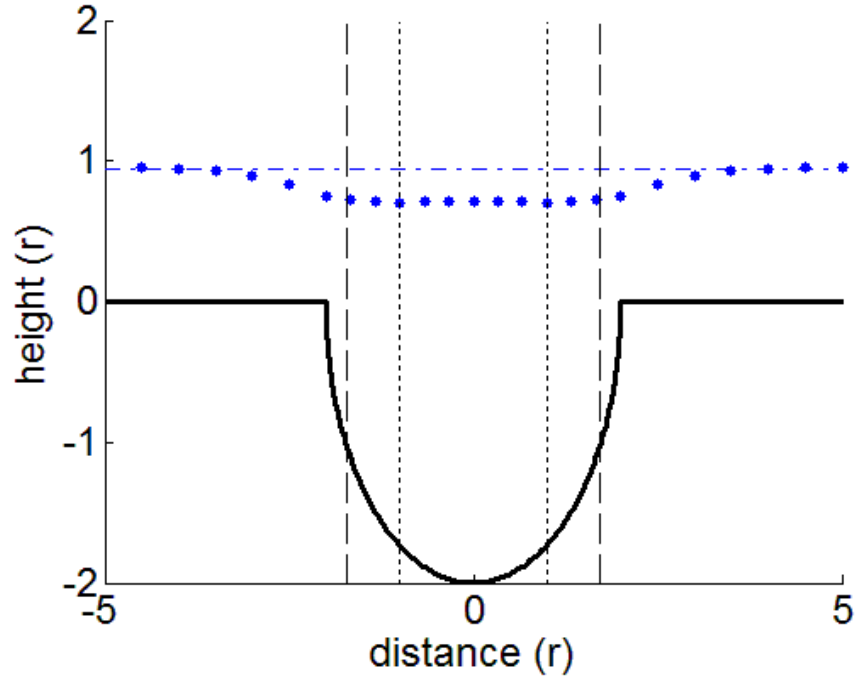

Figure 4.57 Granule of radius 2r

The height profile returned with a set point of 3.75 % (blue circles) is shown. The detected height of the flat surface surrounding the feature is indicated by the dashed blue line. The dimensions of the granule are indicated by the solid black line, with the pipette outer (dashed line) and inner radius (dotted line) also shown relative to the granule centre. It should be noted that the vertical and horizontal scaling are not equal in order to show the scan profile more clearly.

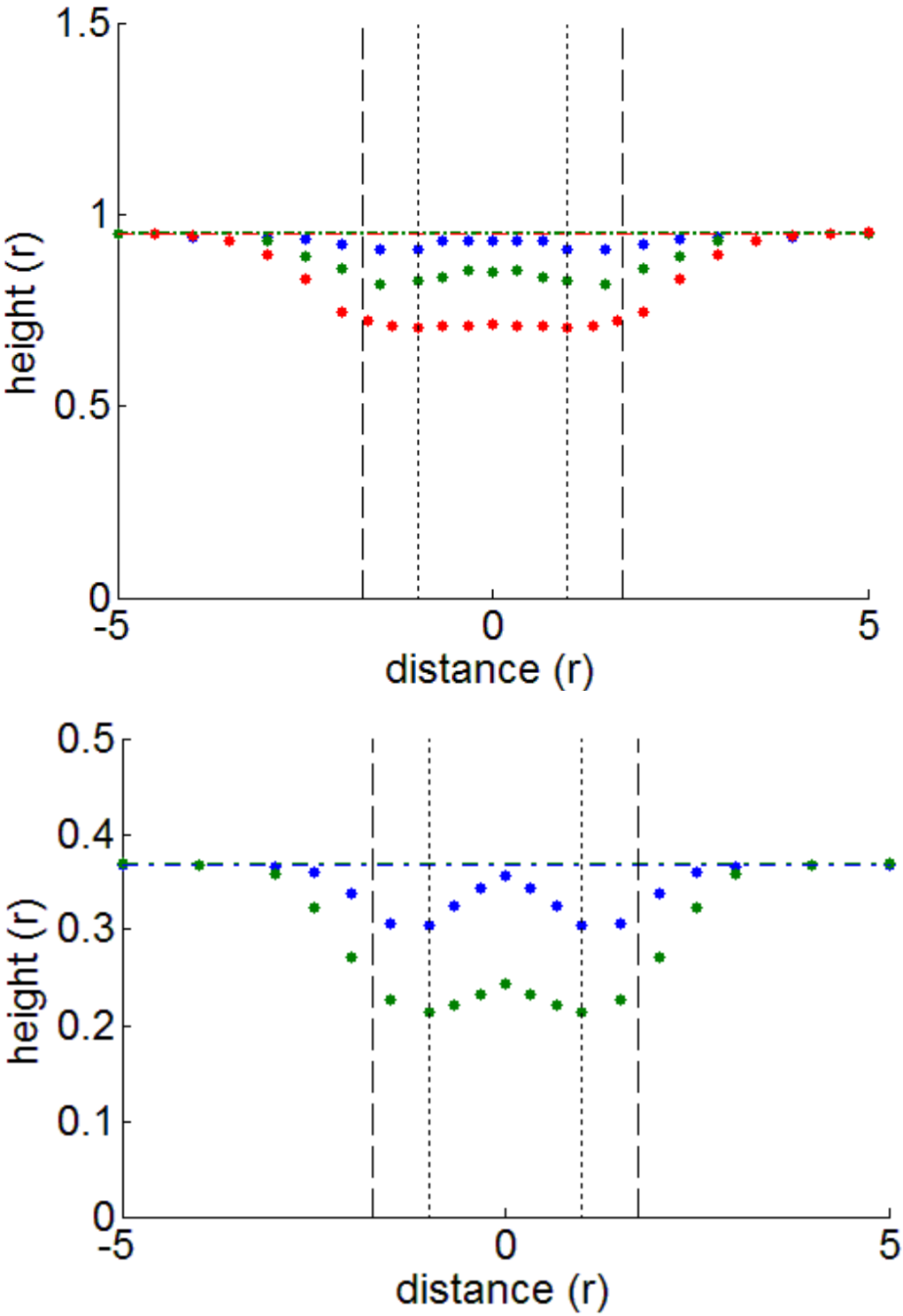

Figure 4.58 Comparison of simulations for granules of different radii
The upper panel shows the height profile produced for a granule of radius 1r (blue circles), 1.5r (green circles) and 2r (red circles) is shown for a 1.25 % set point. The lower panel shows the height profile produced for granules of 1r (blue circles) and 1.5r (green circles), analysed at the higher set point of 3.75 %. In both panels the detected height of the flat surface surrounding the feature is indicated by the dashed coloured lines (1r, blue; 1.5r, green). The pipette outer (dashed line) and inner radius (dotted line) are also shown relative to the granule centre. It should be noted that the vertical and horizontal scaling are not equal in order to show the scan profile more clearly.

4.5 Discussion

Previously, there has been only limited work in an effort to define the resolution and imaging capability of scanning ion conductance microscopy. Based on some early theoretical work Korchev and colleagues estimated the resolution to be less than one pipette radius (Korchev et al., 1997b; Ying et al., 2004), a figure which seemed consistent with comparisons of images obtained by SICM and electron microscopy (Novak et al., 2009). However, it is always difficult to be certain about the dimensions of a probe while scanning. (Experience in this laboratory suggests that even two halves of the same capillary may have unequal tips). Further, while the work in this thesis was ongoing two other FEM studies were published, each of which focused on particular aspects of SICM scanning (Edward et al., 2009; Rheinlaender and Schäffer 2009). I will therefore discuss my findings in relation to these papers.

Lateral resolution

The work of Edwards and co-workers touched upon lateral resolution by considering an object which was equivalent to the single elongated step presented in Fig. 4.3 - 4.4. However, no precise quantitative value of step response was given. Rheinlaender and Schäffer addressed this problem in a more detailed way, both by studying a single thin vertical cylinder (equivalent to the square pedestals presented earlier but with rounded sides). They also considered the ability to resolve a pair of such features. They examined objects of two heights: 1r and 0.5r. They found the full width at half maximum (FWHM) response to a single feature of width 1r (and height 1r) was 3.2r. In my model the half maximal response for a feature of the same height (1r) but of the greater width 7r, corresponds to FWHM = 8.25r. This represents a smaller broadening (1.25r) than that produced in the model of Rheinlaender and Schäffer (~2.2r). This difference appears to reflect the interaction between height, width and breadth for small objects. Further, evidence for this interaction can be seen in the simulations of a peak of width 7r and of height 5r (Fig. 4.4). This produces a FWHM of 9.38r, (an increase of 2.38r compared to the actual feature width) and thus represents a greater image broadening for this taller object. (This greater broadening occurs even though for taller pedestals the scan response to the feature is more rapid (as measured by $X_{25\text{-}75}$).) Thus, the likely explanation for any difference between the results presented here and those of Rheinlaender and Schäffer lies in the combination of dimensions

chosen for the object to be imaged. I have examined the lateral resolution independently of the interactions caused by having narrow objects.

Rheinlaender and Schäffer also examined resolution in terms of the ability to resolve pairs of adjacent objects. They found that at a spacing of 2r between paired cylindrical features no dip in apparent height is seen as the probe passes between the objects, i.e. the profile is flat. The two objects thus appear as a single feature. In optics, one measure of resolution is defined as this point, i.e. the point at which the intensity profile between two adjacent objects is flat. This is known as Sparrow's criterion. This result agrees with the data shown above for a pair of square peaks of height 1r. However, the results for a taller peak do not show a flat profile at the same separation but instead show an inflection (Fig. 4.12). Further the separation at which Sparrow's criterion is met is the lower object spacing of 1r. This suggests that taller pairs of objects are more easily resolved. Further work was undertaken to examine pairs of "omega" features, which may represent a more relevant definition of resolution when scanning biological samples. For these objects the ability to detect two separate objects was poorer for a given spacing than either of the square-edged peaks of 1r or 5r heights. This suggests that for features with more rounded edges, which perhaps represents a more practical measure of biological resolution, the resolution may be lower.

Whilst the minimum spacing needed to see the scan profile showing an inflection between closely spaced objects gives a theoretical minimum value at which it may be possible to distinguish paired features it is also worth considering whether this would be experimentally detectable. One reasonable measure of this is to consider the signal/noise ratio and that when S/N > 3 the signal is detectable. Several factors influence the experimental noise and as such this will vary depending on the material of the probe, the depth of the probe in the bath (which affects the capacitive noise) and the vibrational noise (which will increase with decreasing probe-sample separation, although this variation would only be significant at very high set points). However, in this laboratory our working practice is to reject pipettes if the current noise is > ± 0.1 % of the total current. Considering this as a standard level of “experimental” noise (n_e), it was possible to calculate the maximal error introduced into the detected heights. The simulated approach curves were then reanalysed at the specified set point, s, perturbed by this "experimental" noise. The maximal difference between the measured surface height at $s \pm n_e$ and the measured height at s was then used as a measure of the noise, the pseudo-experimental noise (n_{pe}). Using this definition of the noise the deflection signal,

d, is detectable for omegas at a minimum spacing of 3r d = 3.2 × n_{pe}. For square edged peaks of height 5r, they can be separated at spacing of 2r d = 2.9 × n_{pe} which would be at the limit of experimental detectability. (At spacing 3r d = 7.5 × n_{pe} and so this would easily be detectable.) However for, square edged peaks of height 1r, even at spacing 3r d = 2.3 × n_{pe}, suggesting that such features may be difficult to detect experimentally without averaging. This is of course just one estimate of resolution and, as discussed above, depends on specific experimental configurations. Using a definition of detectability which is equivalent to the Rayleigh criterion in optics would require a deflection between peaks of ≥ 18.9 %. Square edged peaks of height 1r at a spacing of 3r have δ = 31.5±9.6 % (quoted as δ ± δ(n_{pe})) and therefore meet this criterion. It therefore seems reasonable to consider these features resolved in a noiseless system.

Treatment of a pit

The work of Edwards et al., also examined the SICM response to a small cylindrical pit. This was investigated in two ways. The first method used a 2D simulation and considered a single approach curve to the pit centre. They found that for a pit of width much greater than 2r the depth of the pit was accurately estimated. In contrast, for a pit of width ~2r, the depth was only accurately measured for a very shallow pit (of depth 0.1r). Edwards and co-workers next used a 3D FEM model to simulate a line scan across cylindrical pits of fixed depth 5r and widths of either 2.2r (equal to the outer pipette width in their model) or 4r. Their 2.2r case shows a profile very similar to those shown in this thesis in Fig. 4.28 – 4.30 for a range of elongated pits. My work shows additionally that the qualitative shape of the detected height profile is independent of the pit depth. Further, the exact amplitude of this deflection depends on the pit width, for pits of width ≤ 2r. In both my work and that of Edwards et al, (their Figure 7) a pit of small breadth and width is shown to produce two negative deflections (centred on the pipette walls). This arises from decreased current shut-down as the probe walls pass over the pit centre. The shape of this profile is again qualitatively independent of pit depth and width/breadth (in the regime when the width/breadth is ≤ 2r).

The work presented in this thesis extends the previous work on pit imaging by examining how elongated pits should appear during SICM scans. In these cases the SICM profile will underestimate the depth of the pit for small pit widths. The measured depth does however increase with increasing pit depth and also with increasing pit

width (for pits of width ≤ 1r). Interestingly the dip in scan profile seemed to begin at approximately the outer pipette radius when simulating a standard glass geometry and this was confirmed by simulating a pipette of doubled outer diameter. As mentioned earlier, this raises the possibility of imaging a live probe tip, by scanning across an appropriate target.

Treatment of hopping-mode SICM

Hopping-mode SICM offers many advantages over previous scan modes and has therefore been adopted by several different groups (e.g. Novak et al., 2009, Takahashi et al., 2010, Happel and Dietzel, 2009). Consequently it is important that theoretical work on SICM incorporates the use of this scan mode, as the work outlined in this thesis has done. It is worth noting that neither the work of Edwards and co-workers nor that of Rheinlaender and Schäffer simulated the SICM hopping mode. The model of Edwards et al. simulated tip-modulated constant current mode. Details of precisely how this was done are a little unclear in their report but it seems likely they would have to simulate an entire approach curve for each x,y position and therefore it would not be difficult to reanalyse these data to examine hopping mode. Conversely Rheinlaender and Schäffer simulated constant-height currents and then used an extrapolation of their data to create a profile that would be equivalent to a constant-current scan. Consequently, they only simulated a single probe height at each x,y position and would have to undertake many more simulations to fully address hopping-mode. Further, their extrapolation procedure assumes a constant form of the approach curve. From my simulations this assumption does not appear to be valid. If this were the case it would be possible to fit each approach curve with the same parameters (once the heights are adjusted to the probe-surface separation, a procedure routinely done before fitting my simulated approach curves). This was not the case with my data.

Work not covered in previous SICM models

The work presented in this chapter also examines features of SICM that have not been addressed by any previous models. This includes the imaging of sloped features, a more comprehensive analysis of the imaging of small objects and the imaging of more biologically realistic feature profiles.

Treatment of slopes in the sample

The limited ability of SICM to scan across the edge of a square step raised an important issue about the maximum possible slope that could be scanned without colliding. In simulations to address this issue using set points of 1-10%, it is estimated that the maximum angle that can be safely negotiated for a pipette with glass outer diameter:inner diameter (OD:ID) of 1:0.58 is 45 º (at 1 %) and just 5 º (at 10 %). This has important implications for scanning biological samples. In particular, when scanning over a spherical object, the angle between the probe and the sample surface will become increasingly acute. Eventually, a point will be reached at which the slope is too steep and it is likely that contact will be made. This situation is illustrated in schematic fashion in Figure 4.59.

Assuming a particular set point and glass geometry, it is possible to estimate the point at which contact will be made. If the cell is perfectly spherical and a 1% set point is used with a glass OD:ID of 1:0.58, then collisions will begin to occur at a slope angle (shown as θ in Fig. 4.59) of 45˚. Therefore, referring to Figure 4.59, the proportion, x_1, of the cell diameter, h, which may be sampled before contact is made is 0.71 × h. In other words, contact will be made over approximately one third of the cell surface. Fortunately, most cells do not really assume a spherical configuration in culture. Nonetheless, this highlights a very important consideration if it is really essential to use a noncontact scan.

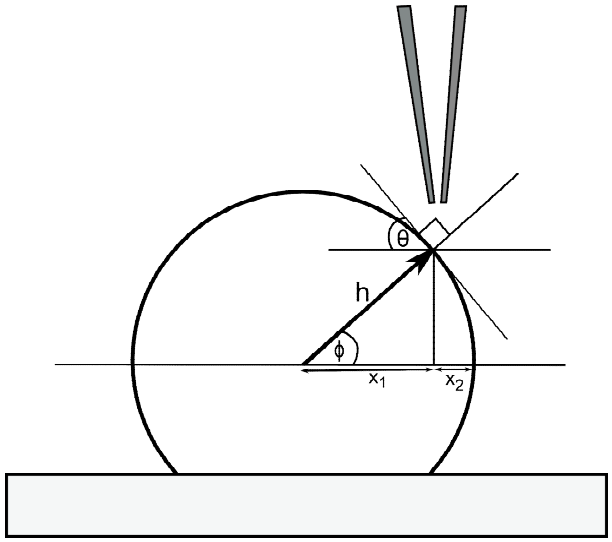

Figure 4.59 Possible contact between the probe walls and a curved surface
For a spherical cell of radius h, the proportion of the radius which may be scanned without contact with the probe wall x_1 is given by $x_1 = h\cos(\phi)$. The angle ϕ may be calculated from the slope angle θ, as $\phi = 90 - \theta$ degrees.

Finally, the ability to scan over slopes could potentially mean that some glass OD:ID ratios would provide better scanning than others. With this in mind, three different experimentally used glass thicknesses (at a fixed half angle of 6 º) were simulated. The results suggest that thin-walled borosilicate glass may allow slopes of up to 50 º to be imaged without contact at a 1 % set point (and in this case $x_1 = 0.77 \times h$), however, perhaps surprisingly for high set point scans ($> \approx 4$ %) thick-walled glass is better. Experimentally, probes should therefore be optimised for different uses. For example, a probe with thick glass and a large half-cone angle would be appropriate for scanning samples with low slope angles, whereas this would be inappropriate for imaging highly convoluted and sloped samples such as neuronal cultures.

Treatment of a very small hemisphere and a small an inverted hemisphere

As seen when simulating a 3D pit the study of very small positive hemispheres showed that such scans essentially produced an image of the probe tip. In this way a single hemisphere appears as two positive bumps each centred at one pipette wall. However, the image of the probe is convolved with the object. This work also suggested a minimum size of object which would be at all detectable at the maximum set point used in this investigation of 2.25 %, of a 0.5r diameter hemisphere.

The study of an inverted small hemisphere was envisaged to address the question of whether a fused dense core granule would be visible in an SICM scan. The results shown in Fig. 4.44 -4.47 suggest that granules of diameter 1r will effectively image the probe tip again and therefore appear as a pair of deflections in a line scan. The size of this effect is reduced with increasing granule radius such that a granule of width 4r appears as a single object, although the depth of the granule is still significantly underestimated. For a typical experimental probe with an internal radius of 50 - 100 nm this would imply that it may be possible to detect a fused granule of 200 - 400 nm diameter, although the depth of the fused granule might be underestimated.

Implications of imaging small objects

Finally, the work I have presented here provides a basic understanding of what happens when the SICM probe encounters objects that are comparable to, or smaller than, the probe tip in all dimensions. Edwards et al., (2009) provided a very brief examination of a similar issue whilst Rheinlaender and Schäffer examined small positive cylinders, both singly and in pairs. All of this work shows that the imaging of

such objects may essentially be thought of as imaging the probe with the sample. This is a common finding in scanning probe methods but it may particularly useful in SICM as a means of calibrating an individual probe non-destructively.

Biological implications of the simulations

Several features relevant to the imaging of biological samples were investigated. The investigation of sloped samples implies that, for the typical pipette geometry modelled, there are limitations on the proportion of a curved cell surface which may be imaged in a truly non-contact manner, which in an idealised worse case would imply contact was made over 30 % of the cell surface. This work also suggests, however, that using a more thin-walled glass will reduce this problem and implies that the investigation of further pipette features in the model, such as pipette angle, may allow an improved pipette geometry to be proposed. In addition the treatment of the rounded 'omega' surfaces aimed to directly estimate the properties of imaging biological features such as neuronal processes. This suggested that rounded features have a lower resolution than square edged features of a similar height. The resolution found for these objects was still however 2r – 3r, which for a 50 nm radius pipette suggests a lateral resolution of 100 nm – 150 nm, which could be improved by the use of smaller imaging pipettes. A further investigation was made to address the detectability of small indentations in the cell surface, such as clathrin pits, or partially fused/collapsed vesicles. This work suggests that it is possible to detect small, rounded, indented features so long as they are 4r or greater in size, although the depth may not be accurately imaged. Thus for these indented features, with a 50 nm radius pipette the minimum size of feature which we expect to reliably detect is 200 nm.

Chapter 5: Development and initial use of an experimental system to follow neuropeptide secretion via SICM topographic scanning

This chapter presents results from two types of experiments. First, experiments designed to create and test an optical detection method for peptide secretion. Second, experiments designed to test the ability of SICM to follow secretory events (including those simultaneously identified by optical detection). As demonstrated in earlier chapters the resolution of a typical SICM probe of ~100 nm radius is close to the limit for resolving dense core granule pits or granule cargo. However, similar SICM scans should be able to readily resolve secretion from larger granules such as the Weibel-Palade bodies in epithelial cells. In this chapter attempts are made to compare theory to practice.

5.1 Neuropeptide release

The molecular processes regulating peptide secretion and degranulation are still not well understood. While delays between cell stimulation and peptide release are well known, more recent work has also highlighted delays between the formation of the fusion pore and peptide release (e.g. Barg et al., 2002a, Obermüller et al., 2005). Interestingly, there may be a number of steps involved in fusion pore opening with at least one study suggesting that the fusion pore may begin as a passage with very tiny dimensions (allowing only proton transport) before widening sufficiently to allow small molecules such as HEPES to traverse it (Barg et al., 2002a, Vardjan et al., 2007a). Furthermore, following "release" degranulation may not always proceed instantaneously as it is often thought to. For example, de Wit et al., (2009) imaged granule cargo at the cell surface which was available for antibody binding but did not degranulate. This is surprising because the accessibility of the cargo for antibody binding would appear to rule out the existence of a very narrow fusion pore and under these circumstances one would expect rapid degranulation. The development of SICM may be a way to confirm and extend these findings.

One approach to following peptide secretion and the process of release is via optical tagging of LDCVs. This usually takes the form of engineering a fluorescent protein sequence into a peptide preprohormone. Several groups have used this approach (e.g. Barg et al., 2002a; Vardjan et al., 2007a). One interesting fluorophore to use in this

type of approach is the pH-sensitive GFP super ecliptic pHluorin (seGFP), which undergoes an increase in fluorescence intensity when the pH is increased in the range pH 5 to pH 8 (Miesenböck et al., 1998). Therefore, if seGFP is located inside a mammalian LDCV, which has an internal pH of ~ 5.2, then on fusion the pH will rise to the extracellular pH of ~ 7.4 and give a resultant brightening in the fluorescence of seGFP. pH-sensitive GFPs have previously been used in ways such as this to give information about the pH environment of vesicles (Sturman et al., 2006) and to follow the kinetics of synaptic vesicle retrieval (Balaji and Ryan, 2007; Gandhi and Stevens, 2003; Granseth et al., 2006; Zhu et al., 2009). In one study Sturman and co-workers were able to determine that the LDCVs in drosophila were less acidic than previously thought by using seGFP targeted to the granule interior (Sturman et al., 2006). SeGFP has also been used to study release from mammalian LDCVs (e.g. Vardjan et al., 2007a). This body of work suggests that seGFP is a useful tool for studying vesicle secretion and it was therefore decided to incorporate seGFP into the neuropeptide tyrosine (NPY) preprohormone as the fluorophore for following secretory events in this project.

FMRFamide tagging is an additional method for following peptide secretion previously developed in this laboratory (Whim and Moss, 2001). This method utilises the ionotropic FMRFamide receptor derived from Helix aspersa (Lingueglia et al., 1995). This is a sodium-permeable ion channel which is a member of the ASIC/ENaC family (Lingueglia et al., 2006). In brief, the FMRFamide sequence was added to the NPY preprohormone sequence. A dibasic cleavage site was included such that the FMRFamide was expressed as a free neuropeptide, which, as it is generated from the same prohormone, co-localises with NPY in LDCVs. On vesicle fusion FMRFamide is co-released with NPY. When both this artificial preprohormone and the FMRFamide receptor are expressed in the same cell an inward current is evoked upon vesicle fusion which can be monitored electrophysiologically (Whim and Moss, 2001). This approach allows neuropeptide release to be measured with a fast time resolution. The difficulty with this approach however is that it cannot give information about which part of the cell release occurs from. If we are to start to address questions of peptide release using SICM, we need to scan in regions of the cell where release happens or is happening. The problem of identifying such positions lends itself to an optical technique, where cell-wide images can be assessed by either confocal microscopy or by using widefield

fluorescence. However, the introduction of fluorescent proteins has been reported to disrupt release kinetics in some cases (e.g. Michael et al., 2004, Felmy, 2007). For this reason it is sensible to introduce seGFP into a FMRFamide-tagged NPY prohormone so that release kinetics can be easily measured using the FMRFamide technique. Our system was therefore designed to combine optical labelling of dense core granules with FMRFamide-tagging.

5.2 Structure of an seGFP-NPY construct

Our preprohormone construct differed from many of those discussed above in that seGFP is designed to be processed into a free protein (rather than a fusion protein) within the LDCV (Fig. 5.1). This strategy was chosen as it potentially allows the distinction between kiss-and-run fusion, full vesicle fusion events and even surface deposition of granule cargo, via distinct optical signals. For example, the inclusion of seGFP in the prohormone should ensure brightening on the formation of a partial fusion pore. This pore would only have to be of sufficient diameter to allow the passage of H^+ ions for this brightening to occur; it could thus be of dimensions which are much narrower than those necessary for the release of seGFP. In contrast, in the event of full fusion (and degranulation) a bright spot would be observed which would rapidly vanish as seGFP diffuses away from the cell membrane. As a further alternative, in the case of kiss-and-run fusion, cycles of brightening and dimming of fluorescence should be seen as the vesicle is re-acidified between partial fusion events (so long as the rate of this process was slow enough for re-acidification to occur). In summary, the seGFP-NPY construct shown in figure 5.1 may allow detection of multiple modes and multiple stages of peptide secretion. (The NPY-seGFP construct was made in a previous project in this laboratory by the author, but was untested.)

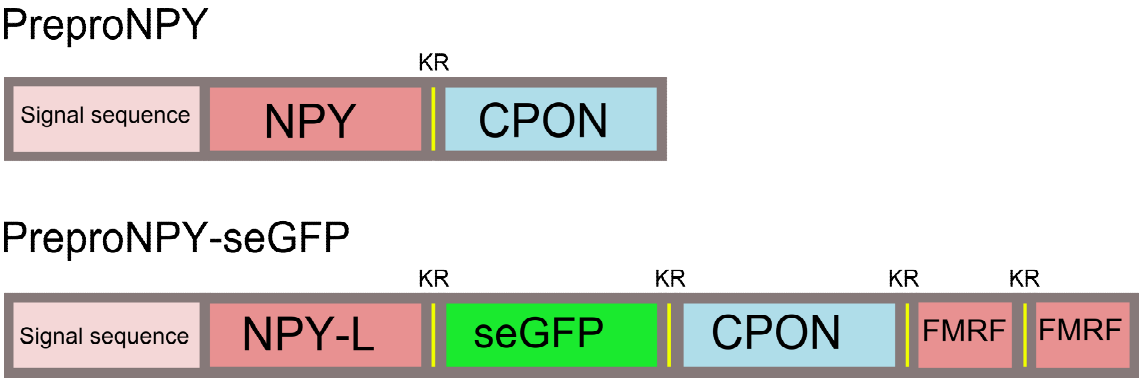

Figure 5.1 Schematic of an NPY reporter pre-prohormone construct used for these studies

Two reporting methods are added to the normal NPY pre-prohormone. The first reporter is the pHluorin, seGFP, the sequence of which is inserted into the pre-prohormone sequence between dibasic prohormone convertase cleavage signals (KR). It is therefore expected to be processed to a free fluorescent protein, rather than a fusion product, before secretion. It should also be noted that in order to introduce a restriction enzyme recognition site at the 3' end of NPY that the amidation signal was destroyed, implying the NPY expressed may not be functional. The second of the reporting signals is a double FMRFamide tag, added at the 3' end of CPON. Each FMRFamide sequence is followed by an amidation signal and is preceded by a cleavage signal such that FRMRFamide should be processed as an active, amidated free peptide.

5.3 Localisation of NPY-EGFP to dense core granules

In order to confirm that the addition of a fluorescent protein to the NPY-FMRFamide construct did not interfere with the localisation to dense core granules an immunohistochemical study was undertaken. In this study seGFP in the construct illustrated in Figure 5.1 was replaced with EGFP to simplify and enhance detection. The colocalisation of the EGFP expressed from pNPY-EGFP with the endogenously expressed peptide ACTH was then investigated in AtT20s Fig. 5.2-3.

A punctate red signal due to ACTH was observed for both transfected and untransfected cells but a green punctate signal due to GFP was only observed in transfected cells. Examination of the transfected cells in detail (Figure 5.3) showed a marked overlap of red and green puncta. Line profiles (Fig. 5.3 lower panel) across four regions of interest (shown as white lines in Fig. 5.3 upper panel right-most image) also showed that red and green fluorescence mostly varied in consort. However, in a very small number of areas the normalised levels of the two signals are very different and in very few puncta only one signal is raised. This is perhaps not entirely unexpected. Granules may be of very different ages and therefore not all will have formed during the expression of EGFP. Furthermore, since our NPY construct is over-expressed those formed at peak expression may be dominated by NPY-GFP, with little room for ACTH.

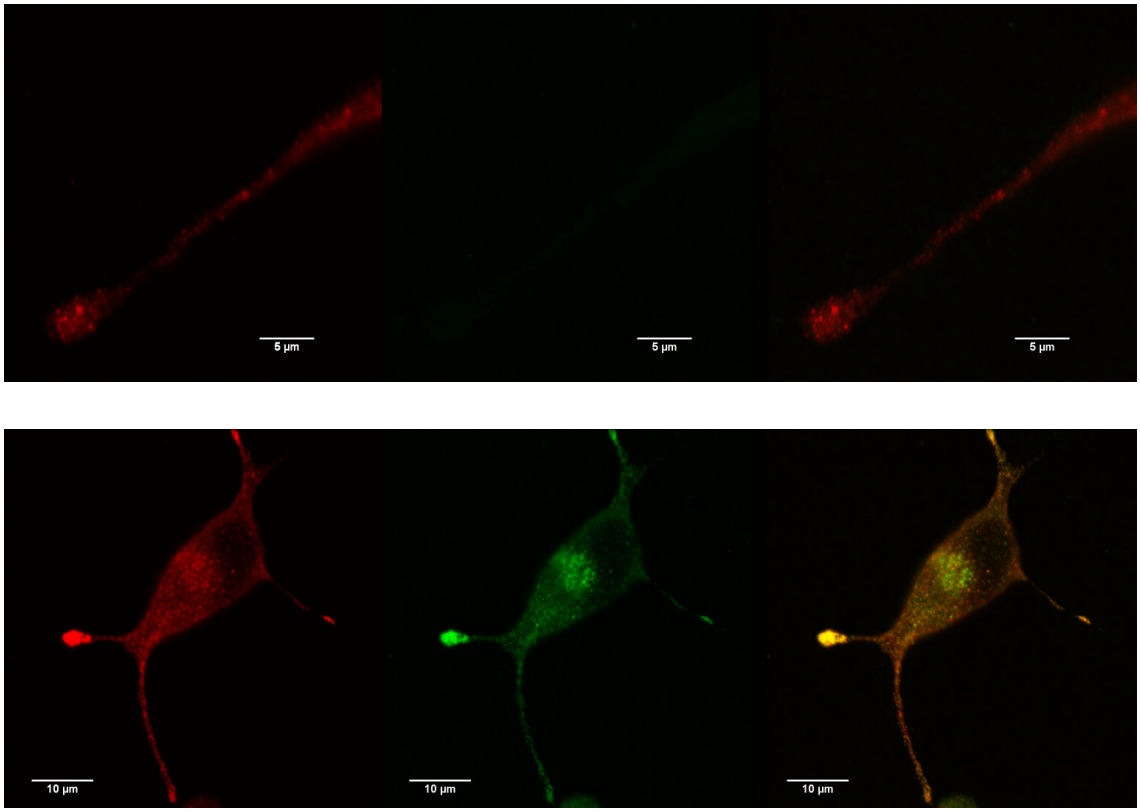

Figure 5.2 Localisation of GFP-NPY constructs to dense core granules
Both untransfected cells (upper panel) and cells transfected with pNPY-EGFP (lower panel) were investigated. Only in images of AtT-20 cells expressing the pNPY-EGFP (green, central column) and stained for the endogenous peptide ACTH (red, left-hand column) are both signals evident. The ACTH and EGFP signals in these transfected cells co-localise as revealed by an overlay of the red and green signals (right-hand column).

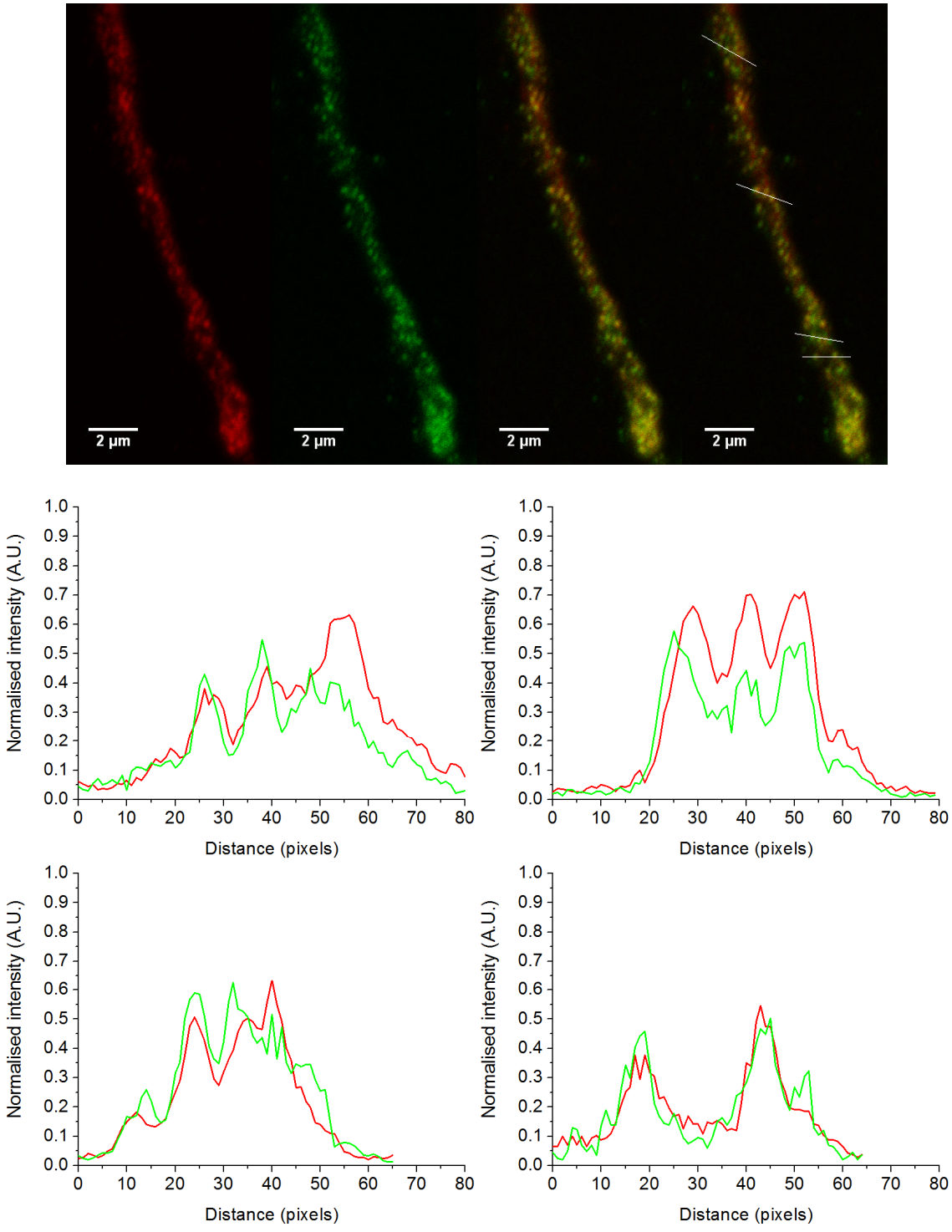

Figure 5.3 NPY-EGFP and ACTH are co-localised in the dense core granules
The upper panel shows an enlargement of a single process of the transfected cell shown in Fig. 5.2. Four regions of interest (ROIs) were chosen and are shown as white lines in the overlaid image. The lower panel shows the fluorescence intensity profiles in these ROIs. The red (red line) and green (green line) intensity profiles are plotted on a single graph for each ROI. The fluorescence intensity in each channel was normalised to the highest intensity value found in the whole image for that channel.

5.4 Response of pNPY-seGFP Transfected Cells to pH Change

To confirm that an optical signal could be readily detected from the NPY-seGFP construct, pNPY-seGFP was transfected into AtT20cells which were challenged with a pH change. Figures 5.4 and 5.5 shows results obtained from these cells before, during and after challenge with an NH_4Cl solution (pH 8.0) designed to collapse internal pH gradients. Within a LDCV this should represent a transition from ~ pH 5.4 to pH 8.0, similar to (although slightly greater than) the change expected on granule fusion with the plasma membrane.

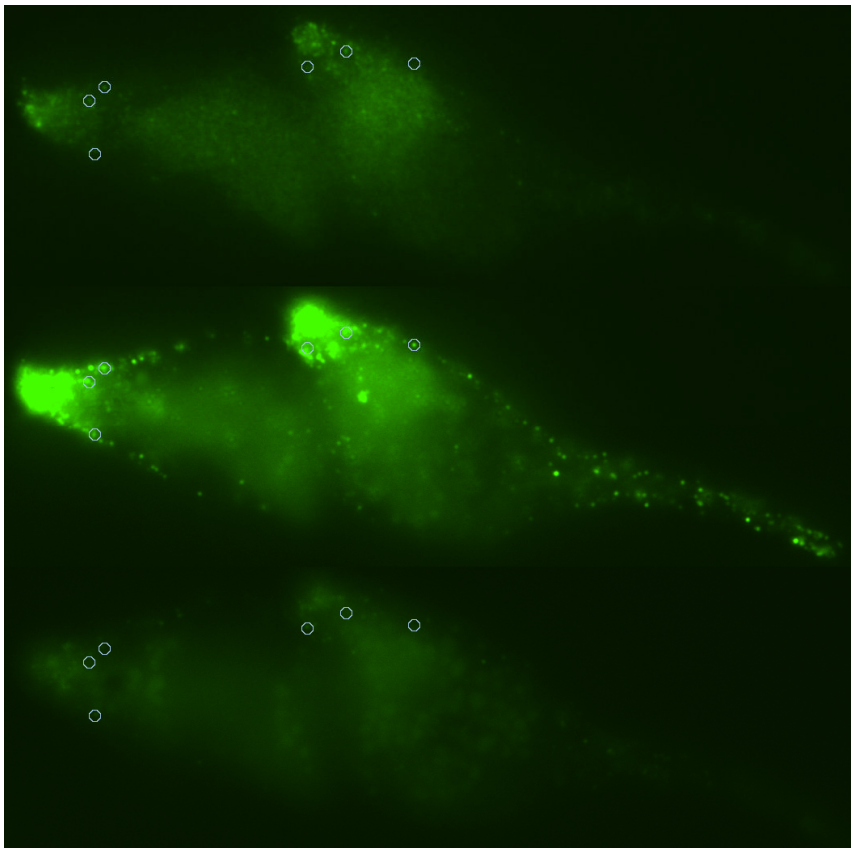

Figure 5.4 The NPY-seGFP-FMRFamide construct shows large fluorescence changes in response to changes in pH
Widefield epifluorescence images of a pair of AtT-20 cells transfected with pNPY-seGFP-FMRF (as outlined in Chapter 2) are shown. The upper image shows the cells in standard buffer, the middle image is 30 s after the solution was changed to an NH_4Cl solution (standard buffer where 50 mM of NaCl was replaced with NH_4Cl) titrated to pH 8.0, while the lower image shows the cells 30 s after the return to standard buffer. In the middle image some saturation of the signal was observed in the brightest parts of the image. This occurred as the camera gain and integration time were chosen based on the initial image.

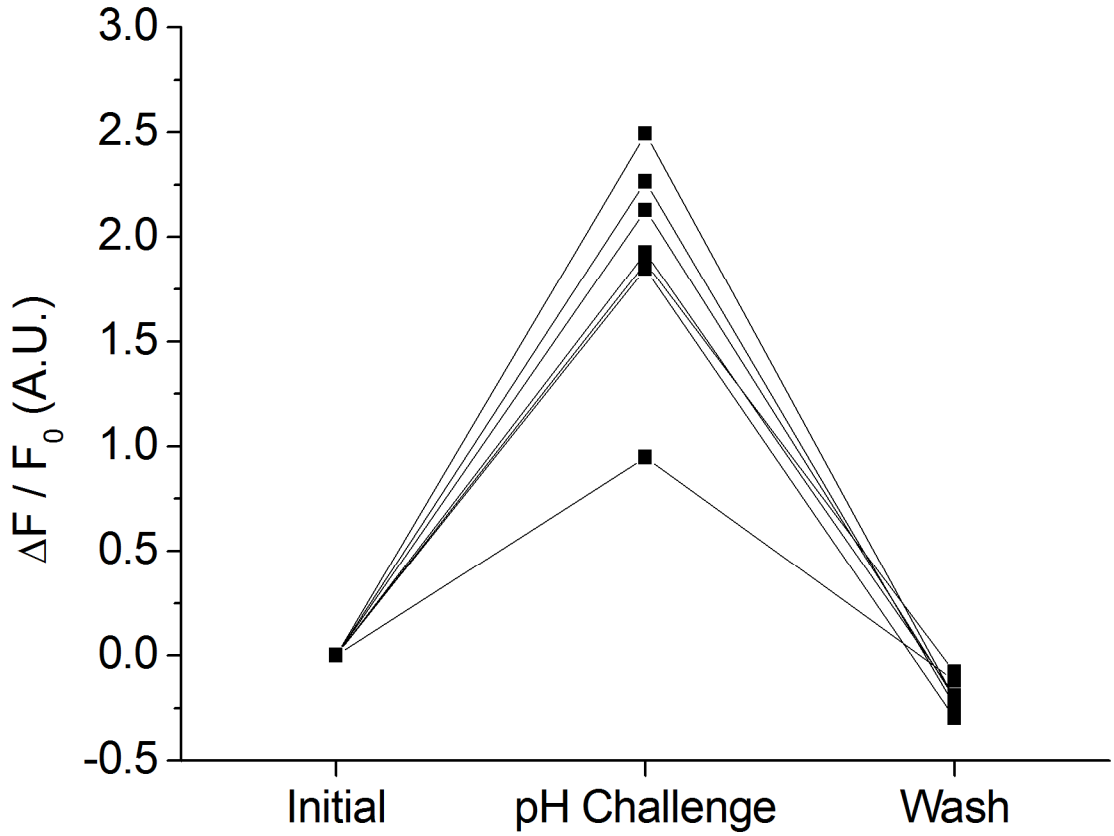

Figure 5.5 Quantified fluorescence changes show that the signal from granules expressing pNPY-seGFP can be readily detected

Fluorescence changes measured at six circular regions of interest (ROIs), chosen outside the most saturated fluorescent areas, as marked by the blue circles in Fig. 5.4. The fluorescence change with respect to the ROI fluorescence in the first image $\Delta F/F_0$, is shown for each condition and expressed in arbitrary units.

5.5 Production and testing of mCherry-tagged FaNaCh FMRFamide channel

A fluorescently tagged version of FaNaCh (mCherry-FaNaCh) was made as outlined in Chapter 2, with two purposes in mind. First, it was developed for examining the kinetics of granule release. (By patching cells with the brightest red fluorescence it should be possible to maximize signals in response to FMRFamide secretion.) Second, co-expression of this channel with pNPY-EGFP makes it possible to see whether the FMRFamide channel enters the regulated secretory pathway by examining fluorescence from granules. (If it were to enter regulated secretory granules this could confuse the interpretation of kinetic release events.) Therefore, localisation of this mCherry-tagged FaNaCh was examined in AtT20s cotransfected with pNPY-EGFP.

These cells were plated on glass-bottomed dishes and imaged on a confocal microscope. Figure 5.6 shows a single z-slice from a confocal stack of these cells (upper panel). The red channel reflects red fluorescence from the mCherry-tagged channel. This fluorescence shows a pronounced signal at, or close to, the plasma membrane. On the other hand, the green channel, which reflects fluorescence from the pNPY-EGFP construct reveals a number of puncta, as might be expected from secretory granules when pNPY-EGFP-FMRFamide is expressed. Six linear regions of interest were chosen and the fluorescence intensity profiles along these lines were plotted (Fig. 5.6 lower panel). These profiles show that red and green fluorescence vary independently suggesting no colocalisation. Additionally the red signal appears to be evenly distributed over the plasma membrane in both this z-plane and others, indicating that there is no obvious clustering of the receptor

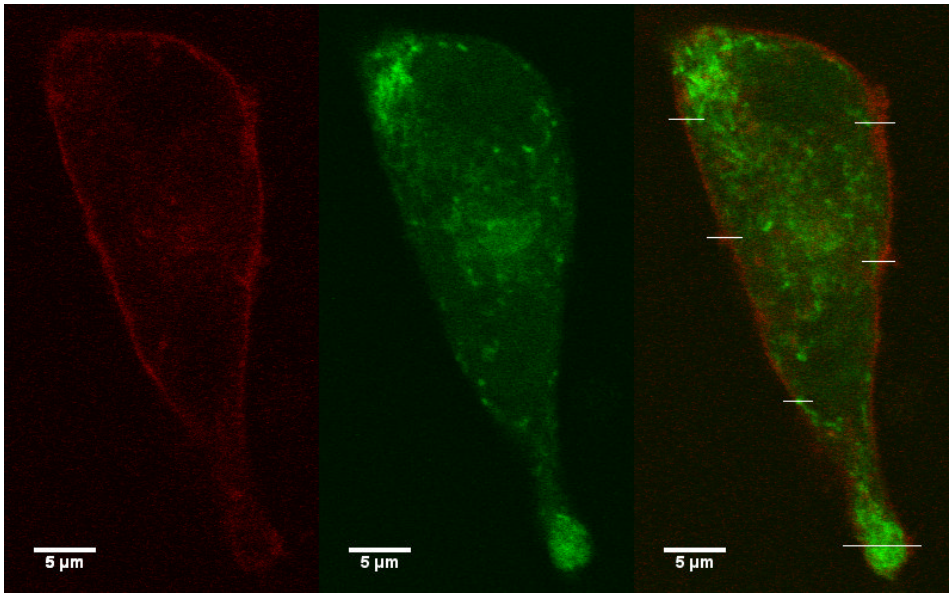

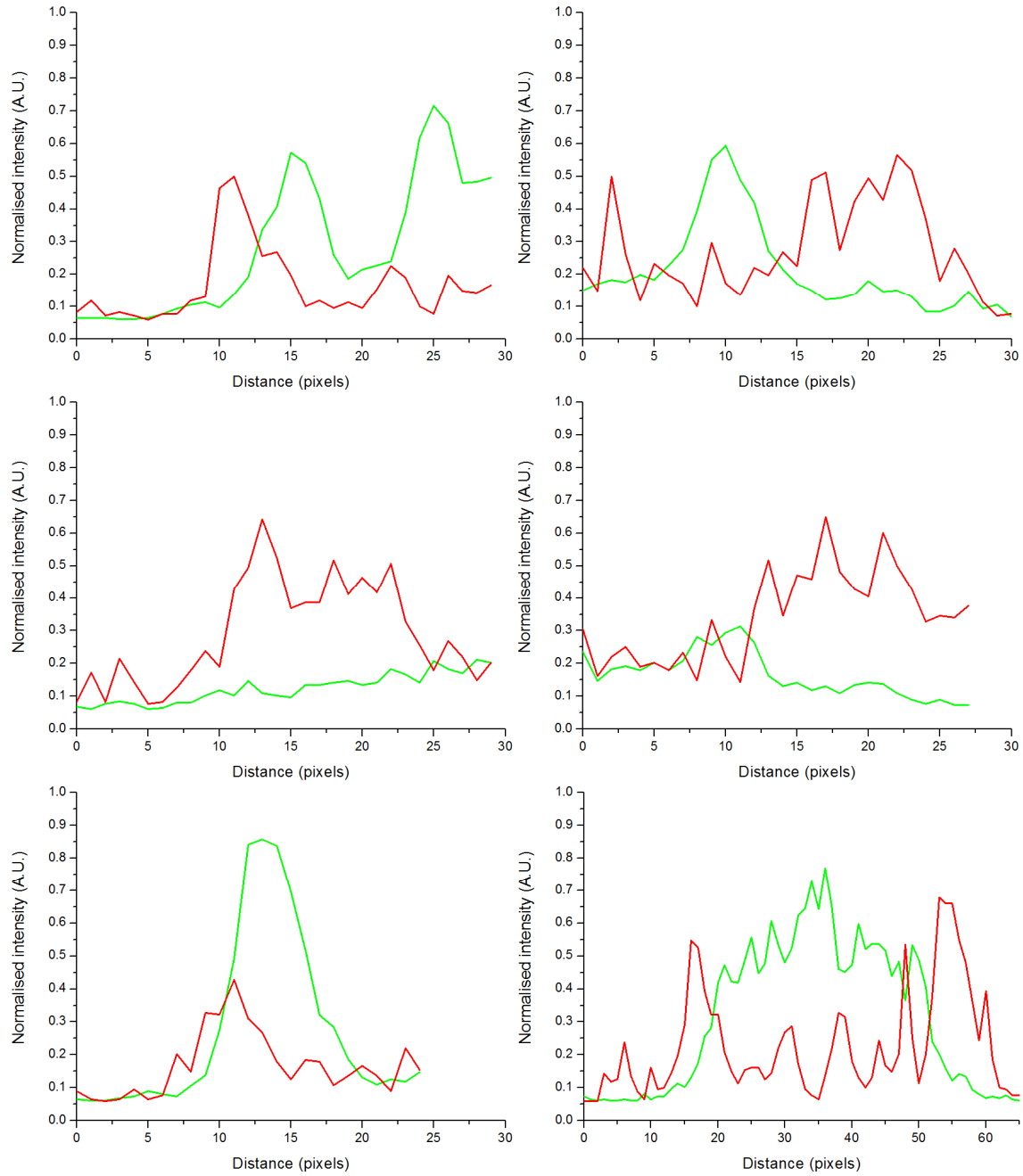

Figure 5.6 Fluorescence measurements demonstrate that the FMRFamide channel does not enter the secretory granules

Simultaneous expression of mCherry-FaNaCH, and pNPY-EFGP suggest that the mCherry-FaNaCH revealed no colocalisation.

The upper panel (previous page) shows fluorescent images from a single confocal slice. From left to right the red, green and an overlay of these two channels are shown. Six linear regions of interest were chosen and are shown as white lines in the overlaid image. The lower panel shows the fluorescence intensity profiles in these ROIs. The red (red line) and green (green line) intensity profiles are plotted on a single graph for each ROI. The fluorescence intensity in each channel was normalised to the highest intensity value found in the whole image for that channel. Note that the *x* scale in the final plot covers approximately twice the range of the other plots.

5.6 Electrophysiological Response of a Fluorescently Labelled NPY-FMRFamide Construct

As mentioned earlier in this chapter, the artificial addition of a fluorescent protein into the peptide prohormone has been reported to alter release in some constructs (e.g. Michael et al., 2004, Felmy, 2007). Therefore, experiments were performed to use FMRFamide tagging to compare release kinetics from cells transfected with the seGFP fluorescently labelled NPY-FMRFamide construct (and a fluorescent-NPY fusion prohormone) with the kinetics of release recorded from cells transfected with a similar construct that has no fluorescent protein sequence inserted. Recordings were made in which dense core granule release was stimulated using a depolarising pulse in the whole cell patch configuration. An example trace showing the response to 100 stimulation pulses is show in Figure 5.7. Following the depolarising pulse, many events, appearing as rounded downward deflections on the current trace can be seen to occur. Figure 5.8 shows histograms of the amplitude, rise time and decay time of detected events for the unlabelled construct (NPY-FMRFamide, Fig. 5.8 top row), a construct labelled with the yellow fluorescent protein Venus expressed as a fusion product with NPY (NPY-Venus, Fig. 5.8 second row) or the construct labelled with seGFP (NPY-seGFP, Fig. 5.8 third row). All three constructs appear to give similar distributions of event kinetics (rise time and decay time). However there may be a slight reduction in event amplitude with an added fluorescent protein.

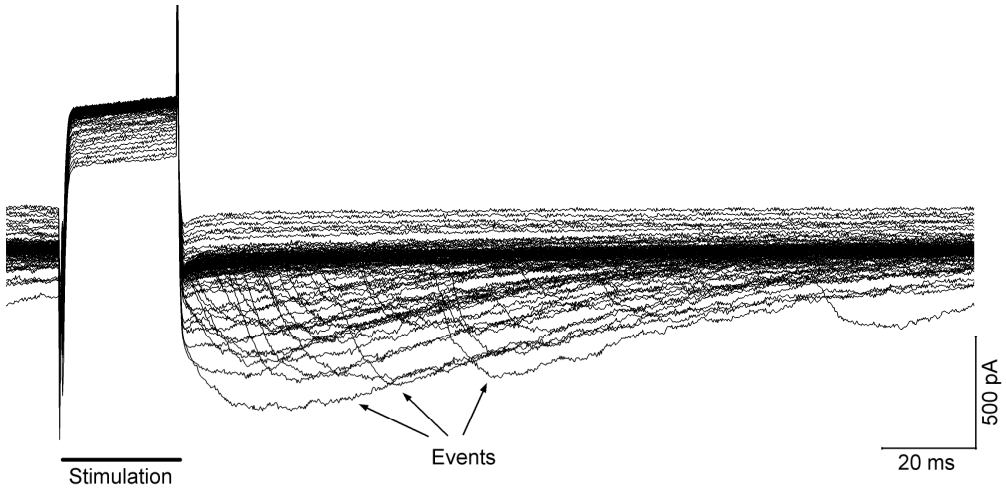

Figure 5.7 Example of stimulated FMRFamide currents from the unlabelled NPY-FMRFamide construct
The whole cell current recorded on depolarising the cell from -70 mV to 0 mV, with a 25 ms pulse at 5 Hz for 100 sweeps is shown. FMRFamide-generated events following release appear as downward deflections on the current record.

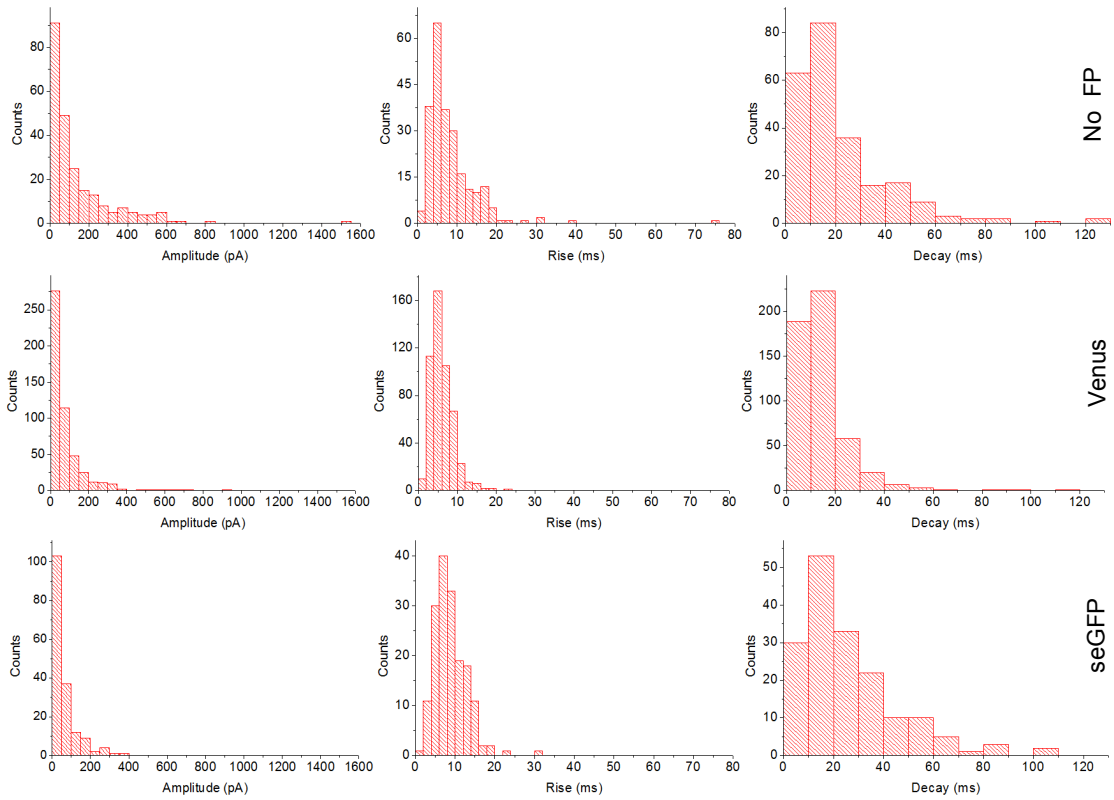

Figure 5.8 Similar event characteristics are generated by different forms of the NPY-FMRFamide preprohormone

Only events that could be fully characterised in the interval between stimulation pulses were included. Similarly, double peaks, where events overlapped were excluded. Data from different cells were pooled for each condition and histograms produced of the distributions of amplitude, rise time and decay time. The top row shows these distributions for the unlabelled NPY-FMRFamide construct (shown as No FP, n = 4), the middle row from the NPY-FMRFamide construct tagged with the yellow fluorescent protein Venus as a C-terminal fusion product with NPY (NPY-Venus (Mitchell et al., 2008)) (shown as Venus, n = 4), and the bottom row shows the distributions for NPY-seGFP (shown as seGFP, n = 3). It should be noted that these experiments were carried out both in the laboratory of Dr Matthew Whim (Penn. State University, PA, USA) and at UCL and data from all experiments were pooled.

5.7 Simultaneous optical imaging and electrophysiological recording

Since the NPY-seGFP construct was localised to dense core granules and did not appear to substantially alter FMRFamide release, it was deemed suitable for examining secretory events by SICM. However, in initial tests it proved difficult to stimulate secretion from the cells plated on glass (see results in Fig. 5.13). Therefore, additional tests were performed utilising optical imaging and FMRFamide detection to examine this problem. Thus, transfected cells were patched in the whole cell configuration and stimulated by depolarisation whilst simultaneously acquiring widefield epifluorescence

images. Recordings were obtained from a large number of cells (n = 51) but no FMRFamide currents were observed (Fig. 5.9). For a minority of cells (n = 8) fluorescent puncta were observed to appear or increase in brightness but without subsequent loss of fluorescence (Fig.5.10-12).

These observations suggested that granules may have fused without releasing their contents. As mentioned above, since most transfected cells had produced a FMRFamide current in the previous (solely electrophysiological) experiments where cells were plated on plastic rather than glass, it was thought that the substrate may be promoting the retention of granule cargo. In the initial experiments described, cells were plated on commercially available glass bottomed dishes (Matek) where the glass was pre-coated with poly-D-lysine. Several different coatings for glass on our in-house-fashioned glass bottomed dishes were therefore tried (poly-L-lysine, poly-D-lysine, gelatin, poly-L-ornithine). With these substrates there was still no observation of FMRFamide currents (n = 51, so a total n = 102).

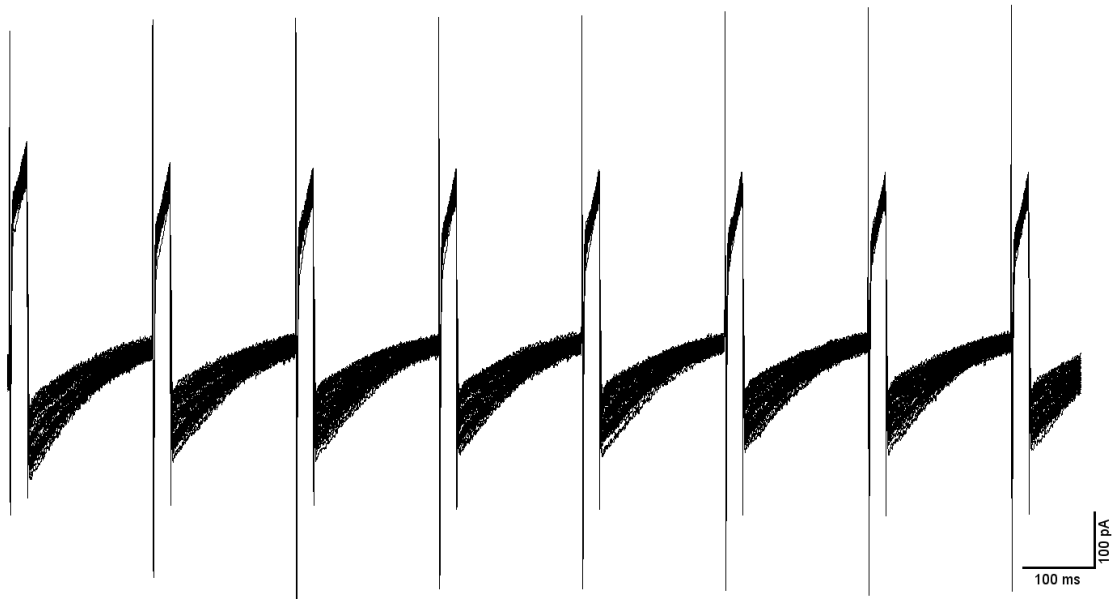

Figure 5.9 Whole cell recording showing lack of stimulated FMRFamide currents
Cells co-transfected with NPY-seGFP and mCherry-FaNaCh or untagged-FaNaCh showed no inward currents on stimulation by a depolarising pulse. An example trace is shown of one cell, stimulated with a 25 ms step from the holding potential of -70 mV to 0 mV at 5Hz. The current response to 414 pulse is shown overlaid. This experiment was conducted at the laboratory of Dr Tom Carter (National Institute for Medical Research, UK).

On two substrates no confirmed granule brightening was observed, poly-D-lysine (n = 8), poly-L-ornithine (n = 6) and poly-L-ornithine was found to be detrimental to cell health. However stable granule brightening was observed on gelatin in 3/13 cells, on poly-L-lysine in 9/24 cells compared to a total of 8/51 cells on Matek dishes.

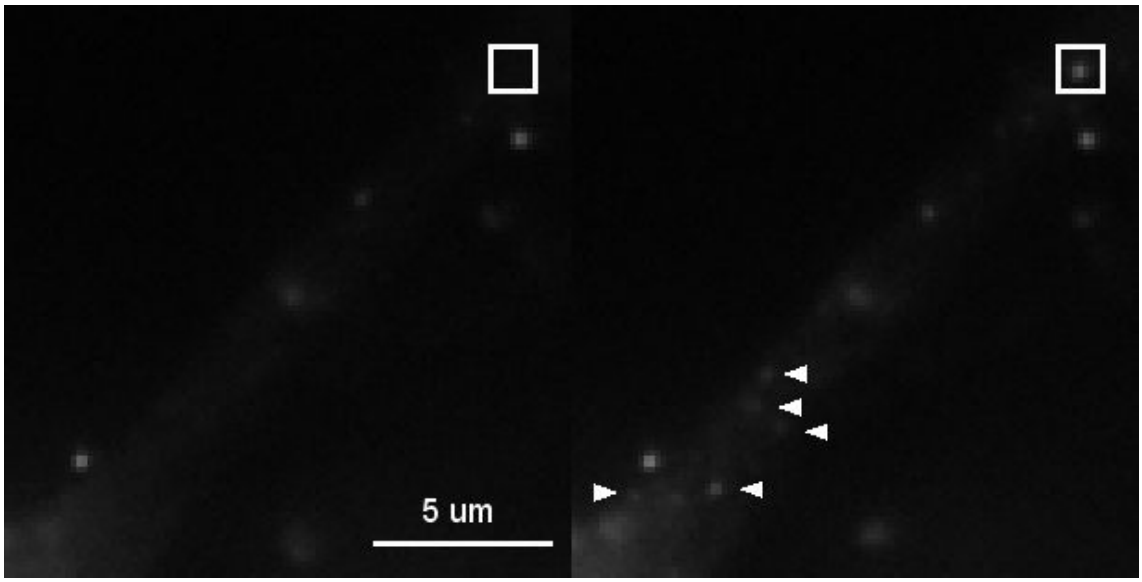

Figure 5.10 Bright puncta appear during stimulation
Images of a single process of an AtT20 cell at the start of stimulation (left hand image) and 63 s later at the end of stimulation (right hand image) are shown in gray scale. Several new puncta were present at the end of stimulation. Some examples of these are indicated by arrowheads, whilst the square shows the region of interest examined in Fig. 5.11.

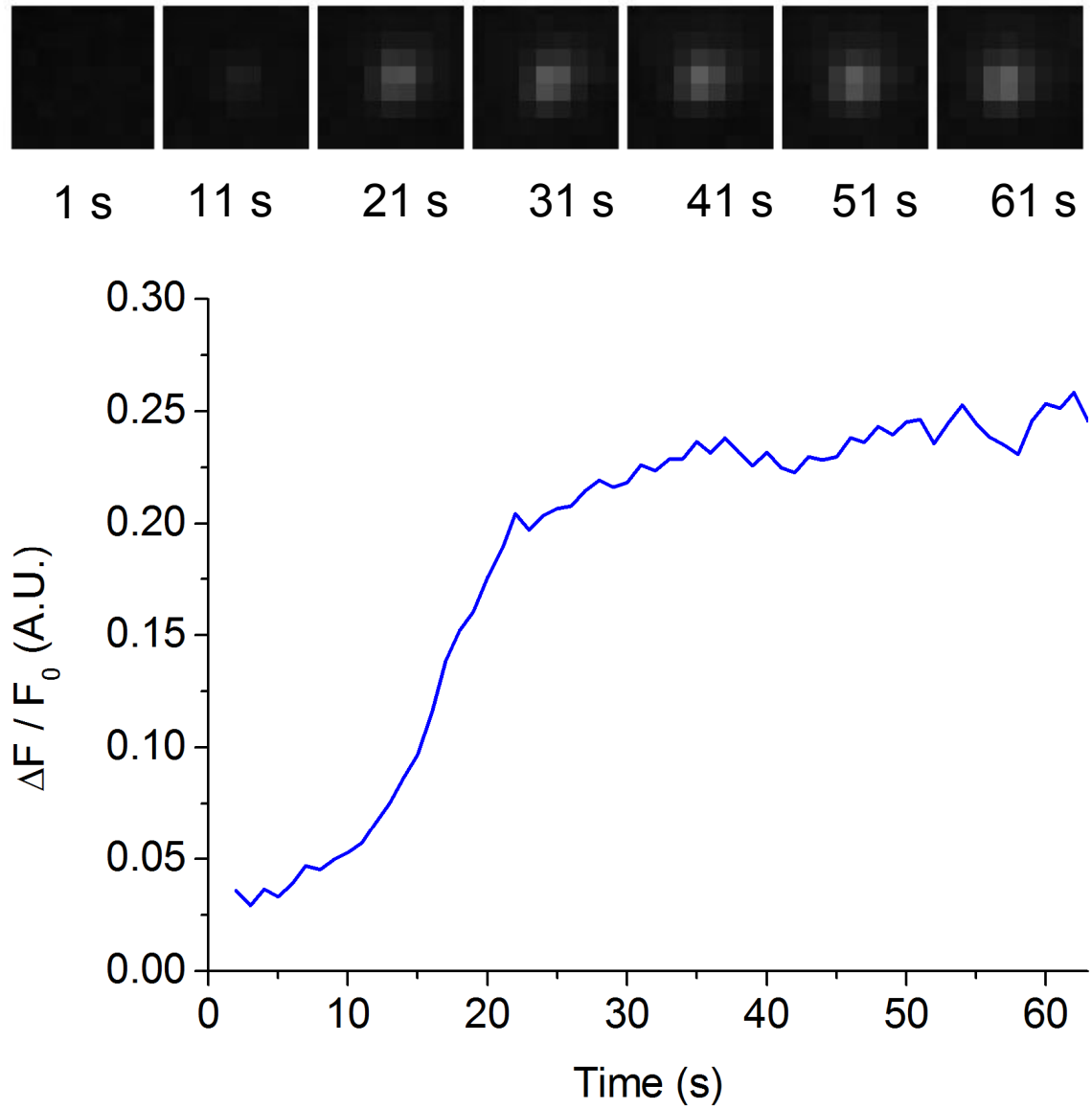

Figure 5.11 Puncta brighten stably

The upper panel shows fluorescence data from the square ROI shown in Fig. 5.10. Images were acquired at 100 ms intervals and averaged over 10 frames (1 s final interval). Averaged frames at the times indicated are shown. The lower panel shows the change in fluorescence intensity as a proportion of the initial intensity ($\Delta F / F_0$) of these averaged data. In both panels t=0 s is taken at the start of stimulation and image acquisition.

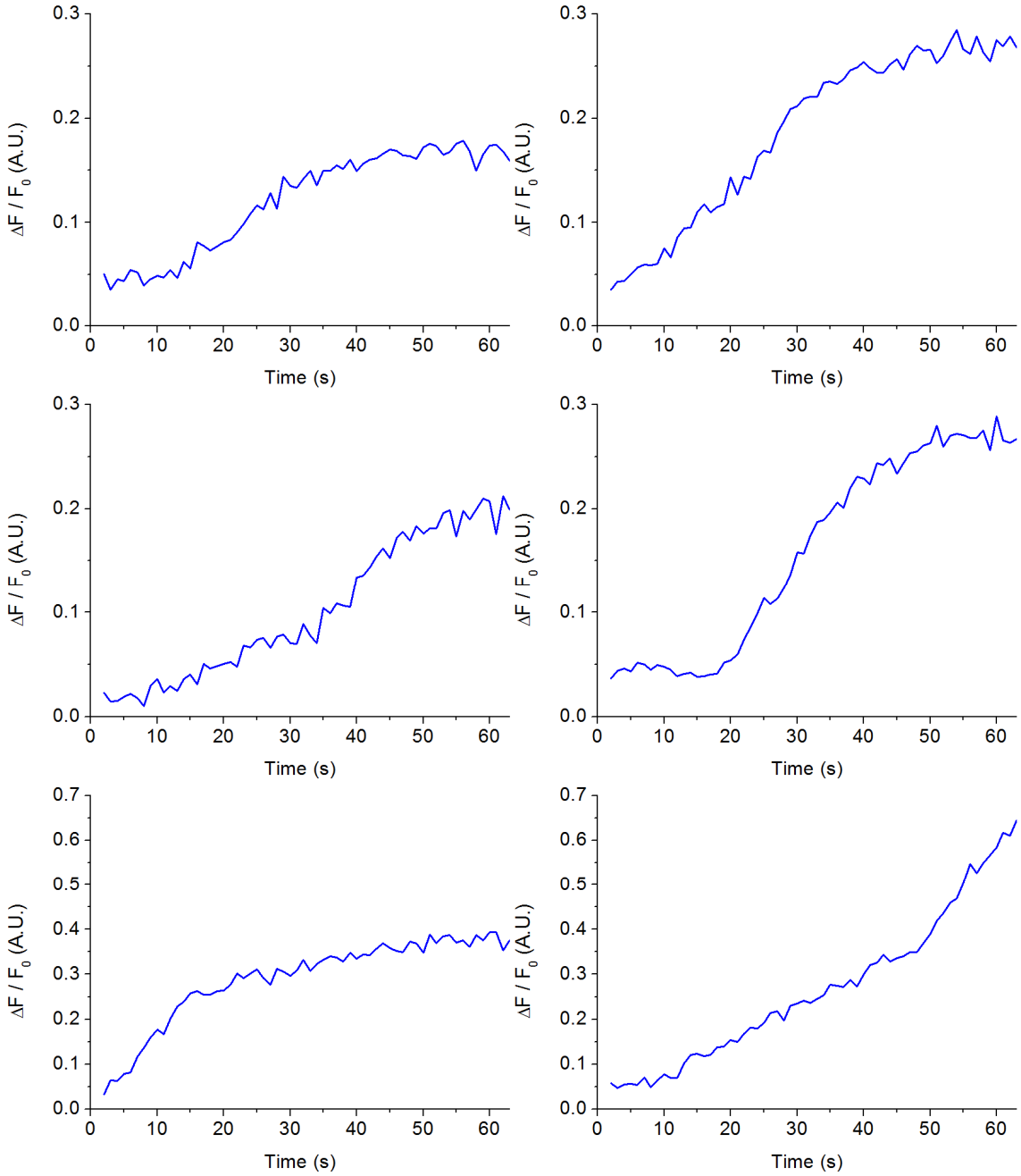

Figure 5.12 The time course and amplitude of fluorescence change is variable
Several circular ROIs were chosen on both the process shown in Fig. 5.10 and the lower process of the same cell. The time course of fluorescence change is shown above. The initial fluorescence F_0 is the average fluorescence for that ROI at the first time point. Frame averaging was undertaken as for Fig. 5.11. Note that the vertical scale on the lowest two plots is different from the others.

On an unpredictable basis FMRFamide events were very occasionally seen on glass coated with poly-D-lysine (although these events were not seen whilst simultaneously imaging). These events could not be reliably evoked but Figure 5.13 compares event characteristics recorded using the NPY construct that did not contain any fluorescent protein for comparison between plastic (Fig. 5.13 top row) and glass (Fig. 5.13 bottom row). The amplitude and rise time distributions seem similar for both substrates but the decay time distribution may be shifted slightly to the right for cells plated on glass, although this effect is quite small. If either the rise time or decay time distributions had been significantly altered between substrates then this may have been further evidence for some substrate specific interaction which slowed the release of FMRFamide from the LDCV. However the kinetics of those FMRFamide events which were observed on glass seem to be largely unaltered. Despite these difficulties in evoking granule release on glass, some SICM data were obtained on both glass and plastic. These results are presented in section 5.8.

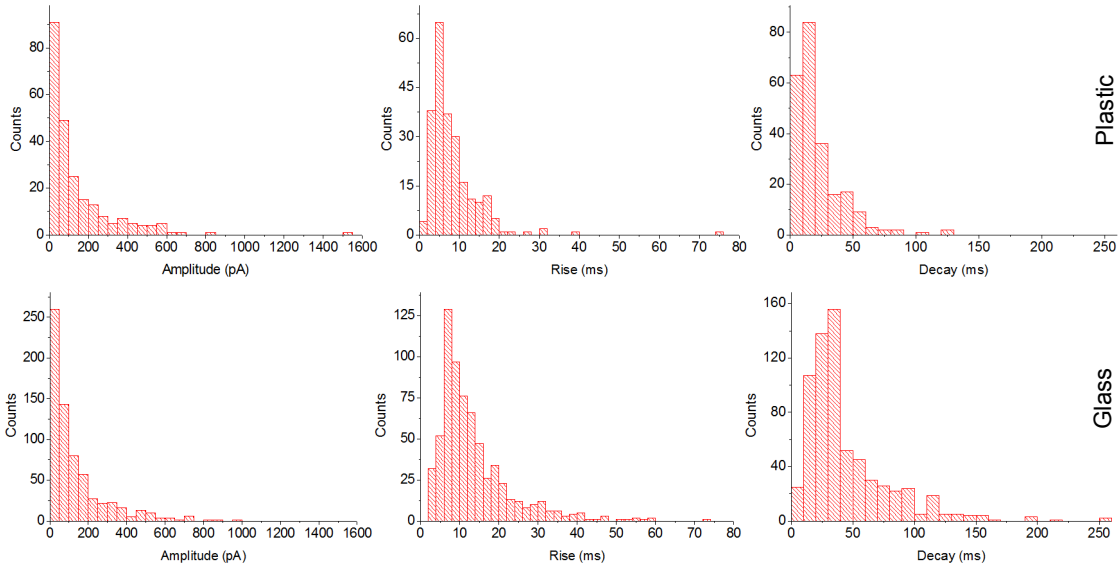

Figure 5.13 Comparison of events evoked from cells plated on plastic and cells plated on glass using the FMRFamide construct that contained no fluorescent protein
The top row shows amplitude, rise time and decay distributions for cells plated on plastic (n = 4) whilst the bottom row shows cells plated on glass-bottomed dishes coated with poly-D-lysine (n = 2).

5.8 Investigation of secretory events from Weibel-Palade bodies via SICM

Setting aside issues relating to the limits of resolution of SICM, one additional question arises when it comes to studying degranulation. Specifically, given that the SICM probe images via conductance, what is to be expected when the probe scans over the dense protein core of a granule? In order to address this issue test scans were performed on secreting Weibel-Palade bodies (WPBs). Studying secretion from Weibel-Palade bodies has two advantages. First, these granules secrete (amongst other cargo) a large quantity of the pro-coagulant protein von Willebrand factor (VWF) which is known to disperse quite slowly. Second, the large size (up to 4 μm long (Hannah et al., 2002)) of these specialised secretory organelles means that the protein core should be easily visible, thus eliminating possible complications arising from SICM resolution.

Exocytosis from WPBs was studied by taking SICM scans before and after stimulation of the cells with ionomycin. For this purpose human umbilical vein endothelial cells (HUVECs) were nucleofected with EGFP-labelled VWF to allow WPBs to be identified and exocytosis to be observed (these cells were prepared by Dr Laura Knipe in the laboratory of Dr Tom Carter, NIMR, UK). Several SICM scans of different parts of the cell were performed both before and after stimulation. Prior to stimulation the cells were extremely flat with only very modest features visible on the surface (Fig. 5.13). Indeed the height variation across even the most ruffled parts of the surface, close to the edge of the cell, was ~100 nm, while the width of these features was ~500-800 nm. The dimensions of these protrusions are similar to those reported by George et al., (2002), when scanning unstimulated HUVECs by AFM. However, after stimulation large raised features appeared on the cell surface (Figure 5.13), which had a much greater height than the height variation observed anywhere on the cell surface prior to stimulation. The dimensions of these raised features were ~ 1.5 × 3.0 μm. This seems congruent with the dimensions of VWF secreted from a WPB; with the length consistent with the length of the WPB as given by electron microscopy (Hannah et al., 2002) and the width consistent with fluorescence images of secreted VWF-EGFP (Hannah et al., 2005). These features gradually flattened over time. Figure 5.14 shows repeated scans of one such feature that appeared after stimulation with ionomycin. Closer examination of the tip of the raised feature, shown in the first scan, indicates that over time the height of this feature reduces towards the level of the surrounding area (Fig. 5.14). This may indicate the dispersal of surface localised secreted protein.

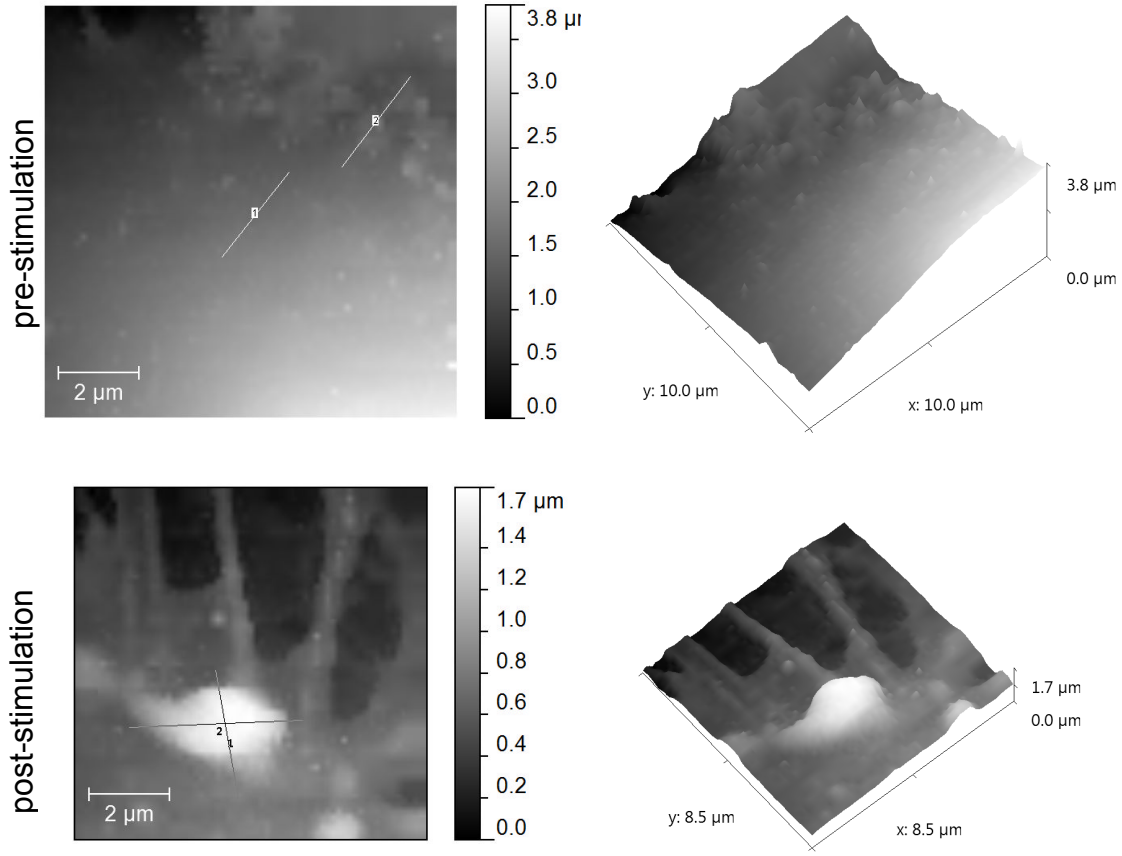
pre-stimulation
2 µm
3.8 µm
3.0
2.5
2.0
1.5
1.0
0.5
0.0
3.8 µm
0.0 µm
y: 10.0 µm
x: 10.0 µm
post-stimulation
2 µm
1.7 µm
1.4
1.2
1.0
0.8
0.6
0.4
0.2
0.0
1.7 µm
0.0 µm
y: 8.5 µm
x: 8.5 µm

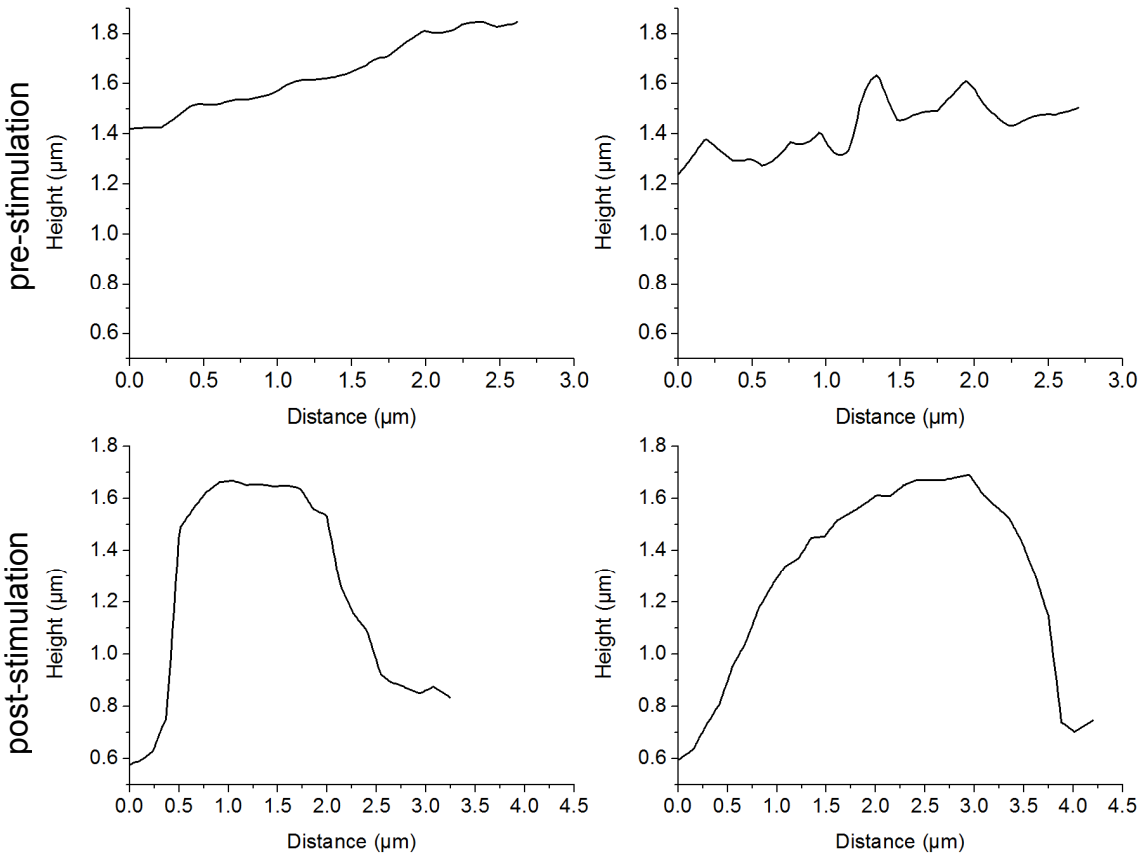
pre-stimulation
Height (µm)
Distance (µm)
post-stimulation
Height (µm)
Distance (µm)

Figure 5.13 (Previous page) Stimulated secretion from HUVECs
SICM scans, at 1 % set point, of different areas of a single HUVEC before and after stimulation with 2 μM ionomycin. In the upper two panels the left hand images show the detected surface topography with heights shown in greyscale, while the right hand images show a 3D rendering of each scan (it should be noted that in these images the greyscale values are on a different scale in each 3D panel, but the z-height displayed is on the same scale in both panels). In the lower two panels the height profiles along the lines of interest indicated in the grayscale images are shown. In the pre-stimulation image the height variation in both the smooth area far from the edge of the cell and the more ruffled edge of the cell is significantly less than the height of the raised feature seen in the post stimulation image.

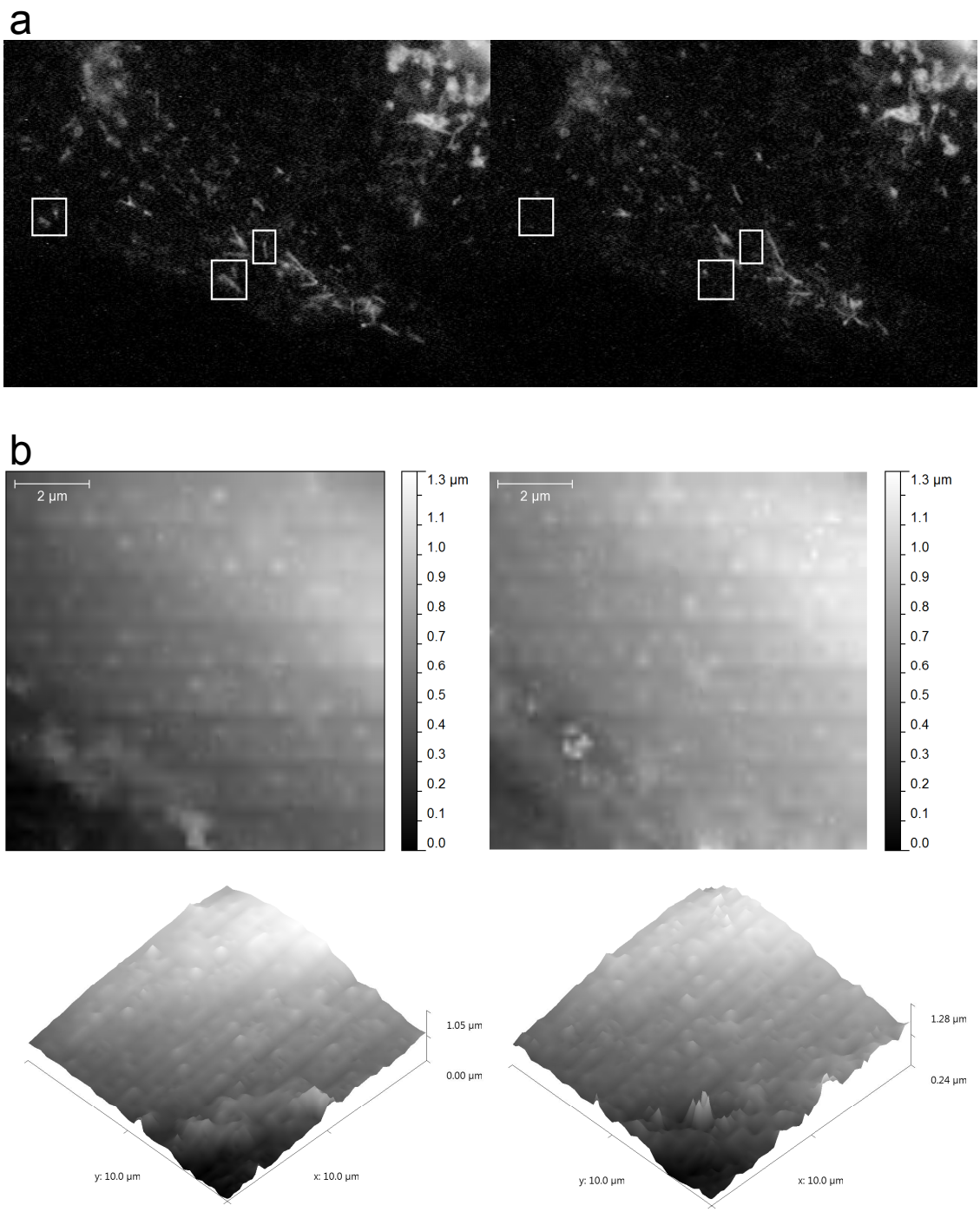

Figure 5.14 Sequential scans of the same area before and after stimulation of HUVECs a) Widefield epifluorescence images of the green signal before (left hand image) and after (right hand image) stimulation with 2 µM ionomycin. A loss of some VWF fluorescence is observed following stimulation (marked regions). b) SICM scans, at a 1% set point with the detected surface topography shown in grayscale (upper panels) and a 3D rendering of this topography (lower panels). A raised spot may be observed in the post-stimulation images (right hand images) which was not present in the pre-stimulation images (left hand images). Sequential scans of this area are shown in Figure 5.15.

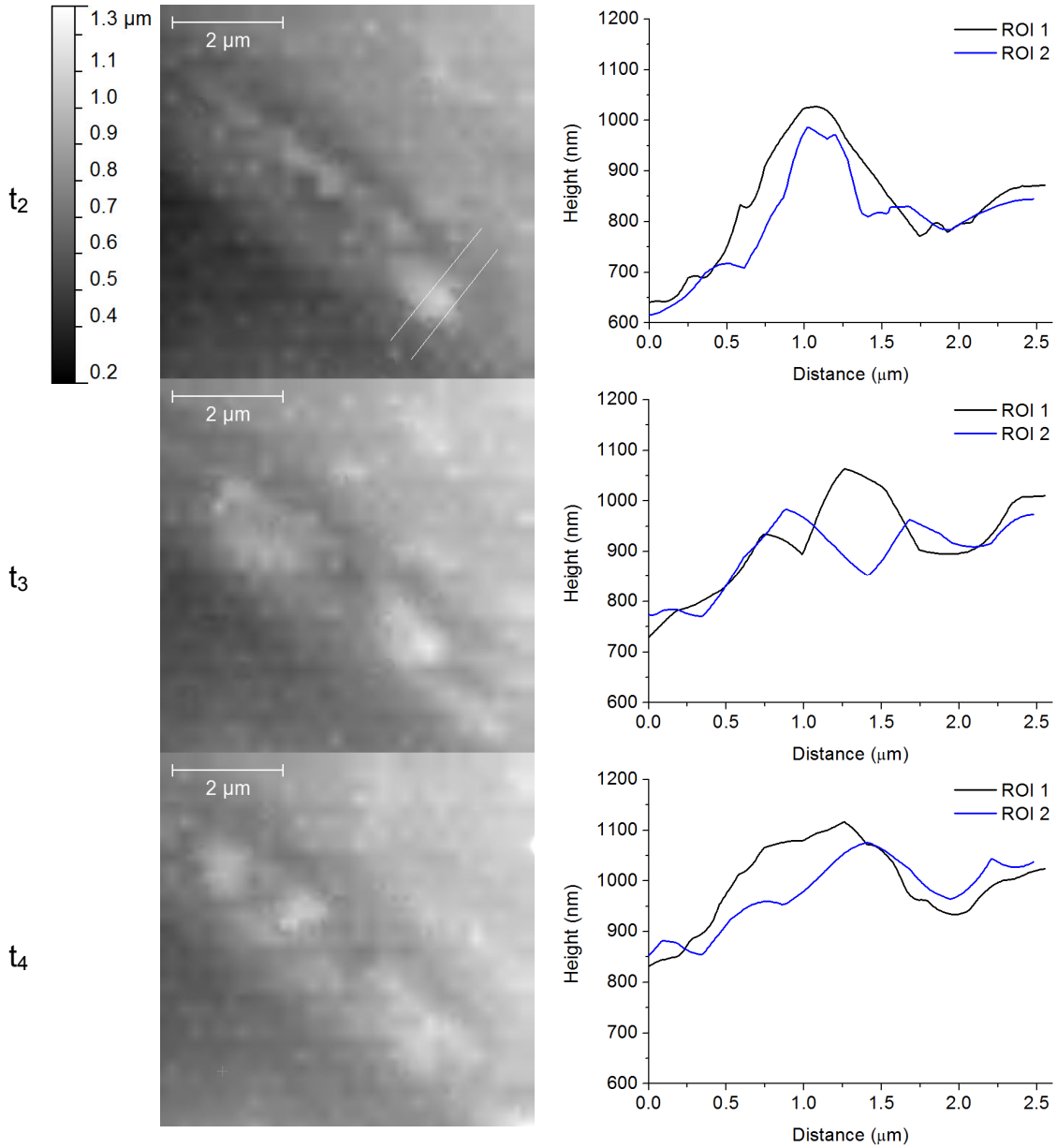

Figure 5.15 Sequential scans across the raised feature shown in Fig. 5.14b
Scans were recorded at times (in min post-stimulation) t_2 = +5, t_3 = +9, t_4 = +12. Grayscale topography images (left hand column) and the height profiles along two regions of interest (shown in the first grayscale image) are also shown. Over time the relief flattens as a result of protein dispersion

5.9 Investigation of secretory events via SICM using the NPY-seGFP construct

With the knowledge that adherent secreted protein cargo can be detected via SICM from WPBs, secretion from the smaller LDCVs of AtT20 cells was investigated via SICM. AtT20 cells transfected with the NPY-seGFP constructs were plated on both glass and on plastic. As may be seen in fluorescent images, LDCVs cluster in the processes of AtT20 cells, so sequential SICM scans were taken of a single process of a transfected cell before and after stimulation with ionomycin. The initial experiments, performed using cells plated on glass coverslips, revealed surprisingly large changes in the cell topography with many raised features appearing on the cell surface after stimulation both on glass (Figure 5.16-5.17) and on plastic (Figure 5.18). These changes were transient (Figure 5.16-5.17, on glass) but persisted for a long time (~ 15 min) compared to the probable time course of individual exocytotic events.

There are several possible causes of these raised features. One possible identity is stable deposits of granule cargo (which may be promoted by the experimental conditions of a standing, rather than perfused, solution). Alternatively these raised features may represent (some average of (since the duration of each scan was ~ 3 – 4 min)) the changes due to many exocytotic events (due to the large stimulus used, 10 μM ionomycin) such as large amounts of secreted protein appearing under the SICM probe or a transient increase in the cell membrane due to a difference in rates between exo- and endo- cytosis under these conditions, or some combination of these two. Both semi-stable cargo deposits and a prolonged period of many exocytotic events could therefore explain both the observed SICM data and the fact that some stable seGFP fluorescence was observed after the scanning period (Figure 5.17-5.18).

Figure 5.16 (Following page) Stimulated secretion from AtT20 cells plated on glass
Sequential SICM scans, at 1 % set point, of a single process of a transfected AtT20 cell before (t_{-1}) and after (at times (in min post-stimulation) t_1 = +1, t_2 = +5, t_3 = +10, t_4 = +14.5) stimulation with 10 μM ionomycin. The left hand images show the detected surface topography with heights shown in greyscale, while the right hand images show a 3D rendering of each scan (it should be noted that in these images the greyscale values are on a different scale in each 3D panel, but the z-height displayed is on the same scale in all panels).

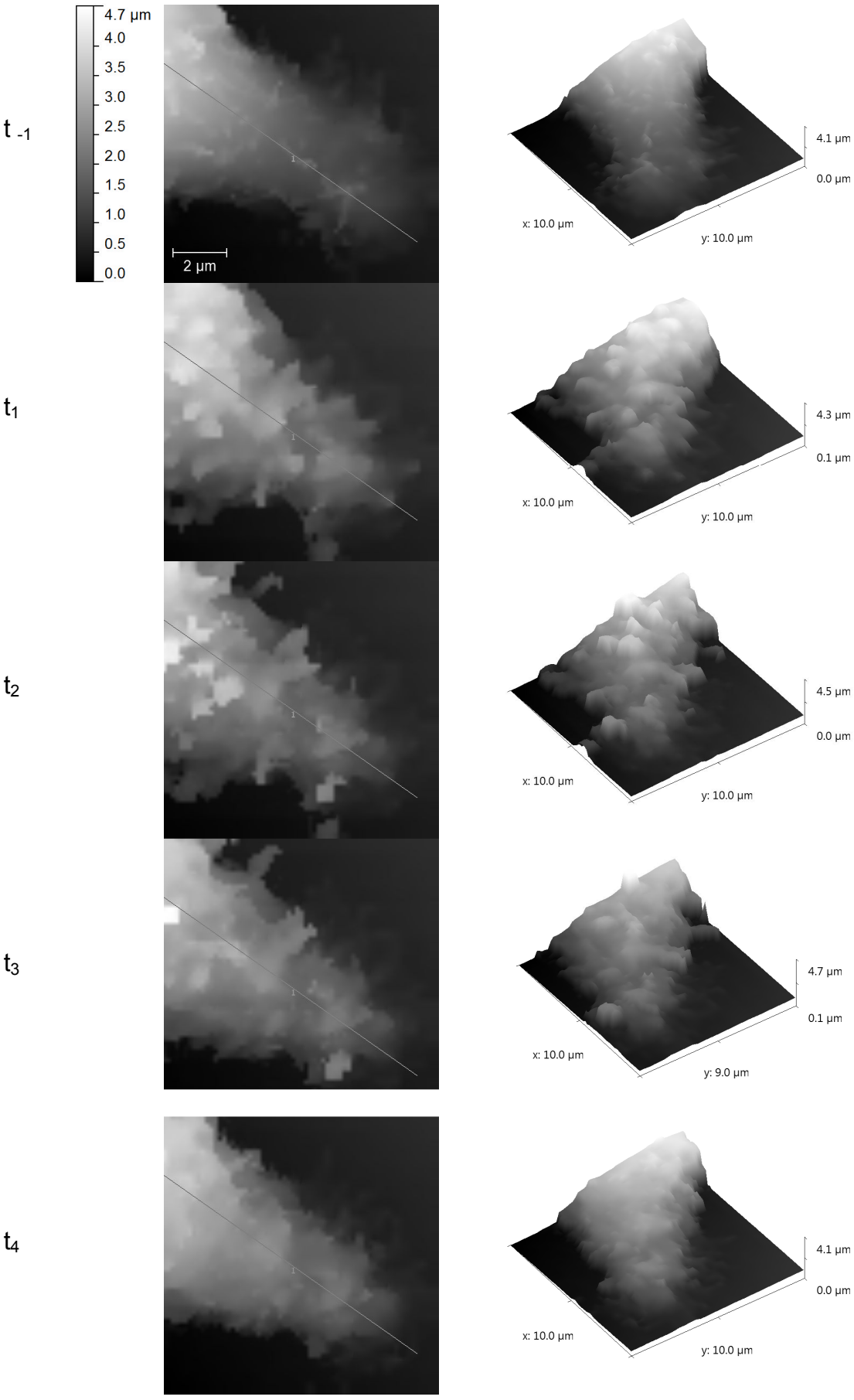
t -1
4.7 µm
4.0
3.5
3.0
2.5
2.0
1.5
1.0
0.5
0.0
2 µm
4.1 µm
0.0 µm
x: 10.0 µm
y: 10.0 µm
t1
4.3 µm
0.1 µm
x: 10.0 µm
y: 10.0 µm
t2
4.5 µm
0.0 µm
x: 10.0 µm
y: 10.0 µm
t3
4.7 µm
0.1 µm
x: 10.0 µm
y: 9.0 µm
t4
4.1 µm
0.0 µm
x: 10.0 µm
y: 10.0 µm

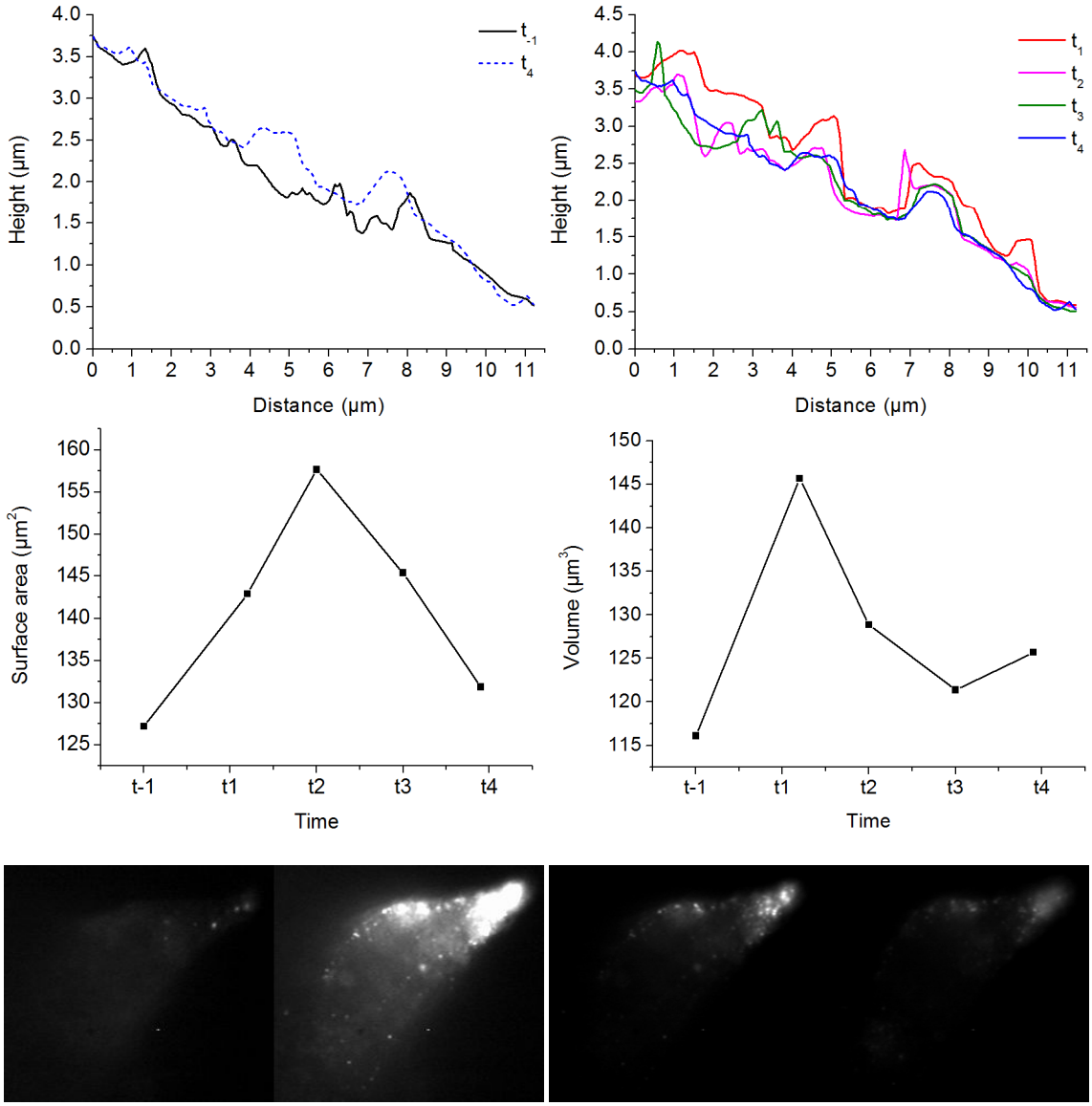

Figure 5.17 Detected changes in cell properties during sequential imaging
The upper panel (this page) shows the height profile of the detected surface along the line shown as 1 in the greyscale images above (previous page). The right hand image shows the height variation along the cell process before stimulation (solid black line) and in the last scan taken after stimulation (dotted blue line). The left hand image shows the height variation along this line in four sequential post-stimulation scans. Measurements of the total surface area (middle panel, right-hand image) and total volume (middle panel, left-hand image) recorded in each scan are also shown. The lowest panel shows epifluorescence images of the green signal, the left-hand pair of images show the cell before (at t_{-1} left-most image) and after (at t_1 right hand image) stimulation. A marked increase in fluorescence may be observed. The left-hand image pair shows images of the post-stimulation cell acquired with a lower camera gain than in the previous pair, at times t_1 (right-hand image) and t_5 after all the post stimulation SICM scans were taken (left-hand image). It may be observed that there is some persistent punctate fluorescence. In this experiment all post stimulation scans were completed within 19 minutes of stimulation and each scan took approximately 4 min to complete.

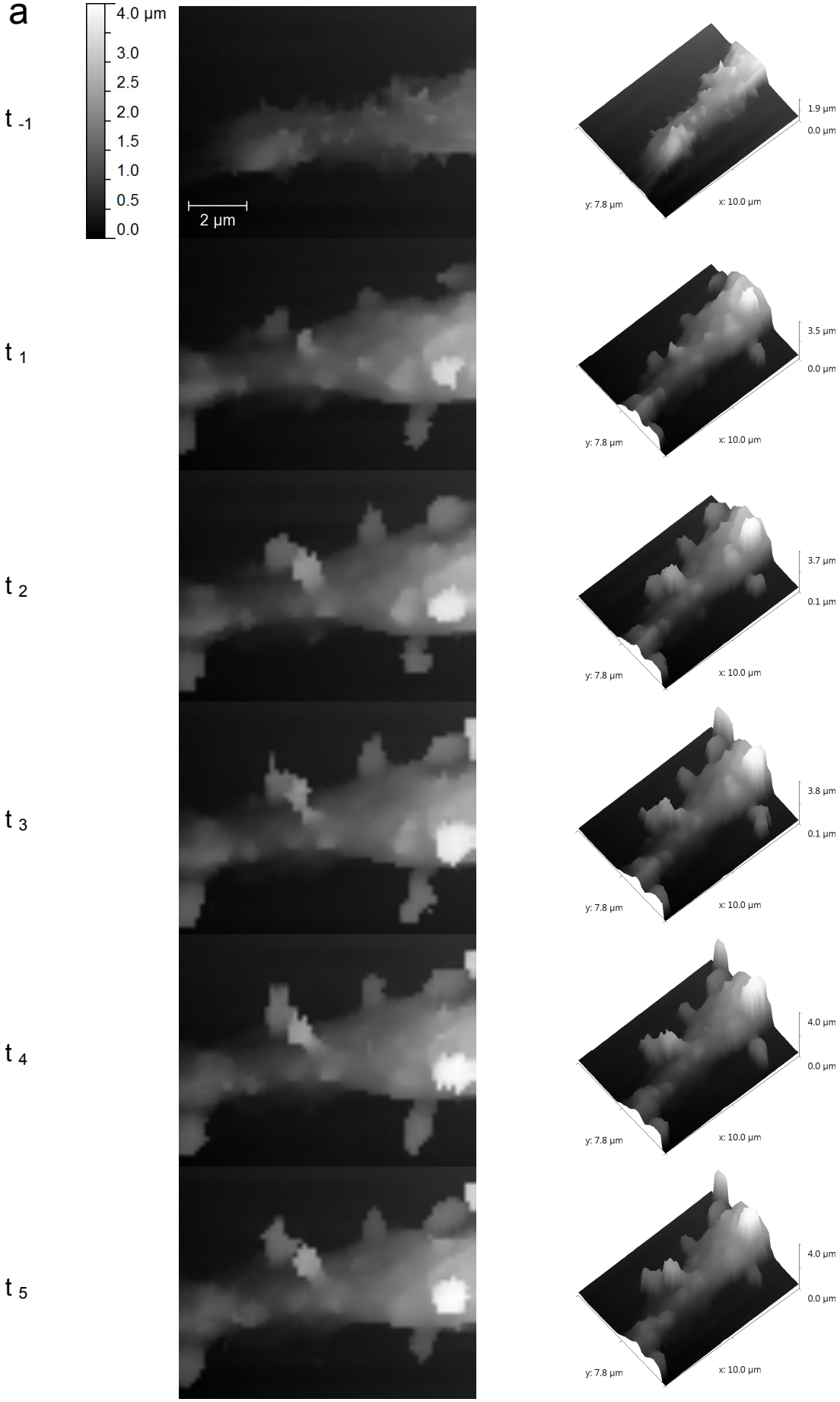
a
4.0 µm
3.0
2.5
2.0
1.5
1.0
0.5
0.0
2 µm
t -1
t 1
t 2
t 3
t 4
t 5
1.9 µm
0.0 µm
y: 7.8 µm
x: 10.0 µm
3.5 µm
0.0 µm
y: 7.8 µm
x: 10.0 µm
3.7 µm
0.1 µm
y: 7.8 µm
x: 10.0 µm
3.8 µm
0.1 µm
y: 7.8 µm
x: 10.0 µm
4.0 µm
0.0 µm
y: 7.8 µm
x: 10.0 µm
4.0 µm
0.0 µm
y: 7.8 µm
x: 10.0 µm

b

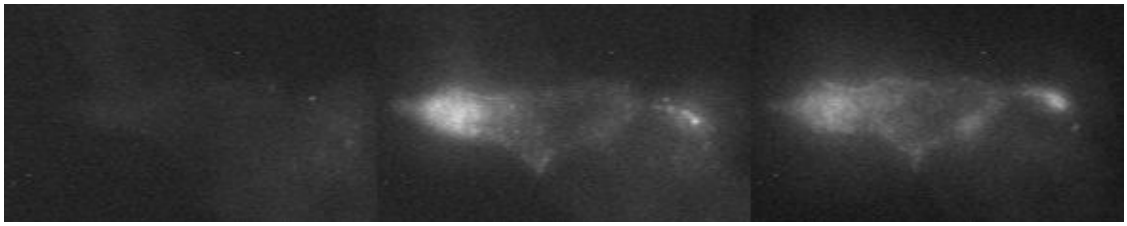

Figure 5.18 Stimulated secretion from AtT20 cells plated on plastic
a) (Previous page) Sequential SICM scans, at a 1 % set point, of a single process of a transfected AtT20 cell before (t_{-1}) and after (at times (in min post-stimulation) t_1 = +1, t_2 = +4, t_3 = +8, t4 = +11.5, t5 = +15.5) stimulation with 10 μM ionomycin. The left hand images show the detected surface topography with heights shown in greyscale, while the right hand images show a 3D rendering of each scan (it should be noted that in these images the greyscale values are on a different scale in each 3D panel, but the z-height displayed is on the same scale in all panels).
b) The image sequence (this page) shows widefield epifluorescence images of the green signal before (left hand image), after (middle image) stimulation and after the last SICM scan was taken (right hand image). A marked increase in post stimulation fluorescence may be observed and there is some persistent fluorescence after the scan period. These images also show that the sample may have been moved slightly laterally during stimulation. In this experiment all post stimulation scans were completed within 19 minutes of stimulation and each scan took approximately 3.5 min to complete.

5.10 Discussion

In this chapter an NPY construct containing seGFP is described and a number of control experiments are presented which demonstrate that this construct is suitable for following secretion optically. First, the data shown in Figure 5.2-3 support the localisation of labelled-NPY-fluorescent protein-FMRFamide constructs to dense core granules, since there is much colocalisation with endogenously expressed ACTH. Although there are slight differences in the levels of fluorescence observed in each granule it is not expected that all dense core granules in these cells will express both cargoes at the same level. A second control experiment is presented in Fig. 5.4-5 which shows that the pHluorin seGFP brightens on alkalinisation when localised to these compartments. The NPY-FMRFamide construct thus appears to be robust to the addition of fluorescent labels in the position indicated in Fig. 5.1. The electrophysiological experiments presented in Fig 5.7-9 show that the NPY constructs containing a fluorescent protein tended to produce smaller amplitude events than the "backbone" construct from which they were made (Fig. 5.8). This result is of some interest with regard to models of peptide sorting. If, as is often suggested, large dense core granules fill by bulk flow then the addition of a fluorescent protein in the prohormone would be expected to leave a smaller fraction of the granule space available for FMRFamide and this, in turn, could provide smaller amplitude events. Despite possible changes in amplitude, the kinetics of FMRFamide currents appeared largely unaffected by the presence of the fluorescent label either as a fusion product with NPY or as a free protein. These data taken together suggest that the NPY-seGFP construct functions as expected and should be viable as a detector of dense core granule fusion.

Attempts to use the NPY-seGFP construct to detect peptide secretion during SICM scans, as envisaged during its design, gave surprising results: cells plated on glass coverslips showed much less reliable secretion. Extensive experiments recording from cells plated on glass did show very occasional full secretion but more often there was only brightening of seGFP and this suggests that some form of fusion or partial fusion of the granule occurs. However the stability of this brightening is inconsistent with the formation of a single transient fusion pore as the most conservative estimate of vesicle reacidification time reported by other groups of a first order decay constant of 4-5 s (Atluri and Ryan, 2006), would indicate that the fluorescent intensity shown in Fig. 5.11 should have dropped in the recording period if a single transient fusion pore opening

had occurred. This result is therefore more consistent with either the presence of a flickering or stable fusion pore, or the stable deposition of granule cargo on the plasma membrane. The lack of FMRFamide response cannot easily distinguish between these possibilities; no response would be expected if the fusion pore diameter was too small to allow the passage of FMRFamide, or if the diffusion of secreted FMRFamide was disrupted by the formation of stable deposits of granule cargo on the cell surface.

The SICM images of HUVECs after stimulation shown in Fig. 5.13-5.15 indicate that it is possible to detect secreted protein cargoes and to follow their dispersal via SICM, at least for large secretory organelles. Although previous studies have looked at secretion in fixed HUVECs, this work represents the first scanning probe images of secretion obtained from live cells. It is interesting to note that WPB release does not produce surface cargo in the shape of a WPB (~200 nm x 3 μm). This is in keeping with other data, such as fluorescence imaging (Hannah et al., 2005), that supports a model of WPB secretion akin to the squeezing of a tube of toothpaste.

Examining the secretion of NPY-seGFP from AtT20s via SICM topographic scanning provided surprising results and further experimentation will be needed before they can be clearly interpreted (Fig. 5.16-5.18). Transient large scale changes in apparent cell surface area and volume were observed (Fig. 5.16) and appeared to peak at different points in time and to return to some value close to the pre-stimulation level (at least on glass). It is perhaps not surprising that surface area appears to increase during secretion while endocytosis and exocytosis struggle to keep in balance. However, the difference in time course between cell surface area and volume changes could be due to errors in the volume estimation since SICM is a 2.5 D rather than a true 3D measurement (i.e. it cannot see under overhanging surfaces). Nevertheless, the striking appearance of relatively long-lived raised features remains an interesting finding. One possible interpretation is that these features are due to the stable deposition of secreted cargo proteins under strong stimulation. Alternatively, as suggested above, these features may simply reflect a lag in the rate of exocytosis under these conditions. Due to the time taken to perform each scan (~ 3-5 min, although it should be possible to reduce this to ~ 1-2 min without reducing sampling, with improvements to the experimental apparatus) changes in topography due to individual exocytotic events may have been obscured. Thus while these data do support the interpretation of stable granule cargo deposition (as was also suggested for the previous FMRFamide data) this experiment

was limited by the fact that it would not have been possible to detect rapidly diffusing cargoes or the fusion pore.

Overall, the work presented in this chapter suggests that it may be possible to use SICM to investigate peptide secretion by measuring surface topography. However, several practical modifications would be useful in further employing this technique, such as increasing scan-speed and finding an appropriate stimulus to give physiologically relevant levels of secretion whilst allowing the sample to remain unmoved. Additionally, the combination of SICM topographic imaging with improved optical imaging, such as confocal microscopy, may aid in the interpretation of topographic data.

Chapter 6: Discussion

In this chapter the main findings of this thesis are summarised and discussed in a wider context. The implications for future work are also considered.

6.1 Finite element method model of SICM

Scanning ion conductance microscopy is a relatively new technology, with many possible applications in biology. There are two main reasons for this. First, it allows very precise topographical imaging under physiologically realistic conditions. Second, it can be easily coupled to other measurements such as confocal microscopy or patch clamp recording. Despite the promise of SICM, at the start of this thesis the theory of SICM imaging had not been explored within a rigorous and generalisable framework. Thus, for example, the lateral resolution of SICM had not been clearly defined. Other important aspects of the technique, in particular the likely effects of probe geometry on the imaging process, were also under-studied. For these reasons a finite element method model of SICM was developed (Chapter 3). The fidelity of this model was examined by comparison with both experimental data and existing theory in cases where analytically tractable solutions are possible. For example, the probe resistance R_p and its dependence on probe half-cone angle were calculated by FEM modelling and compared to theoretically calculated values. Simulations using a variety of half-cone angles gave values in exact accord with the values of R_p expected analytically. In a second similar test, the pipette access resistance was calculated. In this case there was a small difference (6%) observed between the theoretical access resistance R_{ac} that can be calculated for a circular pore in an infinitely resistive medium and the simulated asymptotic value of R_{ac} calculated as the glass thickness of a straight-walled pipette (far from the surface) was increased. However, such a small but significant difference is perhaps not entirely unexpected. One explanation for this difference is that in Hall's theoretical approach (Hall, 1975) the pore mouth is treated as an equipotential surface. It is clear from the simulation that this is not true because there is clear variation in the potential across the pipette mouth. It thus seems likely that the FEM simulation more accurately reflects the experimental situation. Finally, the model appears to be capable of estimating the experimental approach curve with good accuracy. In the experiment presented in Fig. 3.13 the simulated and experimental approach curves would be in agreement for a pipette of radius 150 nm, which is typical of values estimated in this

laboratory using electron microscopy. Taken together these findings support the argument that the FEM model of SICM presented in this thesis accurately reflects SICM electrostatics and may therefore be used to investigate features of scanning.

Lateral resolution in SICM

Two definitions of lateral resolution were examined in this thesis (Chapter 4). The first of these was the lateral distance taken to respond to a square step (with the response defined as a change in estimated height of one half of the step size). The second measure of resolution examined was that of the minimum separation at which two objects could be discriminated (see Fig. 4.1 for definitions). It was found that both of these definitions gave similar values of lateral resolution as discussed below.

The estimate of resolution made by examining a step response was addressed using an elongated object of much greater width than the probe diameter. This object was chosen in order to avoid possible artefacts caused by interactions between height and width/breadth. The lateral resolution thus found was seen to be dependent on the height of the feature. For a short feature of height 1r, an apparent broadening in FWHM of 1.25±0.12r was observed and for taller features of height 5r, a broadening of 2.38±0.09r was seen. A similar object was investigated by Edwards et al. (2009) who addressed a step of height << 1r and a step of height = 1r. They also found that the taller step gave a larger value of lateral response distance although this was not addressed quantitatively.

The second measure of lateral resolution examined in this thesis is the separation between a pair of objects at which they become distinguishable as two objects. This was investigated first by using a pair of square peaks of height 1r or 5r whilst varying the separation between peaks. The calculation here was of a minimum separation, at which a positive value of deflection (d) would be seen between the peaks at the point equidistant between them (as described in Figure 4.1). As also noted in examining the response to a square step, there was an interaction between sample height and lateral resolution. Thus, for objects of height 5r at a 1% set point, it was possible to distinguish them at a separation of 1r but for objects of height 1r, the resolution drops to ~2r. It was also observed that for the taller peaks there was a larger dip (d) for a given spacing, although this represented a smaller percentage (δ) of the detected object height. Leaving aside the issue of small numerical errors (such as rounding errors), these simulations represent a “noiseless” system. Therefore, it is worth considering whether these

deflections would be detectable experimentally. This is not an entirely straightforward issue because experimental noise will be contributed from a number of sources, such as the quality of vibration isolation, capacitive coupling due to the depth of solution in which the pipette is submerged and capacitive noise from the type of glass used. However, in this laboratory our working practice is to reject pipettes if the current rms noise is > 0.1 % of the total current. Considering this as a standard level of "experimental" noise simulations were re-examined and for peaks of height 5r, scanned using a 1 % set point, a spacing of 2r is close to the likely limit of resolution. However for peaks of height 1r, using the same 1 % set point, even at a spacing of 3r they would be difficult to detect experimentally without averaging (but see below). This is interesting because the size of deflection expected in a noiseless system in this case would be approximately equivalent to the Rayleigh criterion used in optical imaging. The Rayleigh criterion corresponds to $\delta = 18.9$ % and for a 3r spacing $\delta = 31.5$ %, thus exceeding the Rayleigh value. Indeed, comparisons to other measures of resolution commonly used in optics, e.g. Sparrow's limit, (the point at which a "dip" between objects just vanishes) peaks of height 5r would be said to be resolvable at a spacing of 1r and peaks of height 1r at a spacing of 2r.

As a final measure of resolution, the ability of SICM to resolve more biologically realistic, rounded "omega" features has also been examined. Results from these simulations suggested that rounded objects are imaged with a similar lateral resolution to features with sharper edges although there was, generally speaking, a small reduction in the expected "dip" between objects. Considering the Sparrow criterion, rounded features of maximum height 1.85r (and the same width as the square pedestals of 2r) were resolvable at a spacing of 2r. However, considering resolution as subject to pseudo-experimental noise at a spacing of 3r $d = 3.2 \times n_{pe}$ and so this would be more likely to represent an experimentally reasonable detection limit.

Rheinlaender and Schäffer (2009) also investigated pairs of objects in an attempt to define SICM's lateral resolution. They also used FEM but assumed that all approach curves were the same as the curve obtained when the probe approaches a flat surface (rather than attempting to fit individual approach curves as presented in this thesis). Their investigation of a pair of small cylindrical pillars of diameter 1r and maximum height 1r gave a lateral resolution of approximately 2r (when using the definition of spacing which has been used in this thesis). My findings for sharp-edged objects are

broadly in agreement with these results and do not suffer as much from possible ambiguity caused by interactions between object height and width/breadth since I used elongated objects. Also the results presented in this thesis using rounded objects give additional information which may be useful in interpreting scan data for biological samples.

Reassuringly for experimental scanning, it may be observed from the data presented here that so long as two objects are separated by the minimal lateral distance (of 1-2 r for sharp-edged and 2r for rounded objects) then the separation between the centres of paired objects in the image appears to be accurately represented (Fig. 4.47-4.48).

Interestingly, as illustrated in Figure 6.1, these conclusions about resolution are, if anything, slightly exceeded by estimates that might be inferred from SICM data obtained when scanning HUVEC cells. This figure shows a scan over a pair of small raised features that are just resolvable at a separation of ~300 nm. By comparison with the model and assuming a probe of 100 nm radius this would be like resolving peaks of just over ~1r at a separation of ~3r.

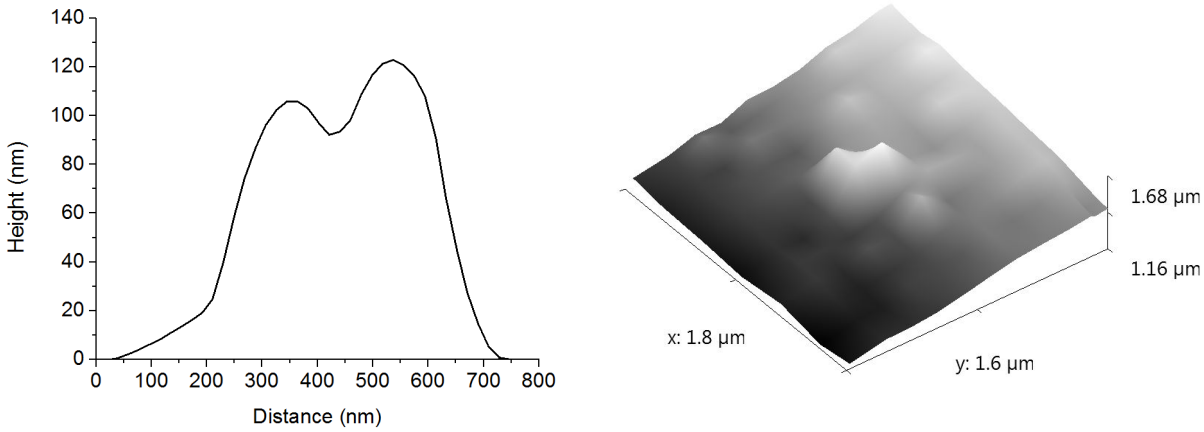

Figure 6.1The ability to separate a pair of small closely spaced features is broadly in keeping with theory

Two closely separated peaks are resolved at a distance of ~ 300 nm apart with a pipette of radius ~100 nm (line profile left-hand panel). This feature was observed during a HUVEC cell scan with a 1 % set point. The plot has been corrected for a background slope due to the curvature of the cell, by subtracting a linear offset found by fitting the data at the edges of the profile. The right-hand panel shows a 3D rendering of a small area surrounding this feature.

The treatment of slopes in the sample

One feature of SICM addressed uniquely in this thesis is the ability to retain non-contact scanning when imaging steeply sloping samples (Chapter 4.2). From a practical point of view this is extremely important. The results from slope/scan simulations in this situation suggest that for high set point scans and samples which contain steep (>45 degree) slopes, such as cells, it is likely that some contact will be made with the surface and this should be taken into account when true non-contact imaging is a particular requirement. Indeed, at a 1 % set point, the SICM probe will be some way from the edge of a perfectly round object when it makes contact. So that the information could provide the most useful practical advice for scanning, three different, experimentally used, glass thicknesses were simulated. Results from these simulations showed that thin-walled glass gives a probe which may access a more angled surface without contact, even though the investigation into increasing glass thickness presented in Chapter 3.4 suggested that a thicker glass could give a more sensitive probe in some sense (i.e. one with an increased access resistance). It therefore seems that there is scope to optimise the choice of probe glass thickness and set point at which to scan for different applications.

The imaging of objects of dimension similar to the probe inner diameter

Several different objects were simulated in order to investigate the imaging of objects of a similar size to the probe (Chapter 4). One such was an elongated pit of width $\leq$ 1r. In this case it was seen that a single qualitative line scan profile was observed independent of pit width and depth. The exact amplitude of the negative deflection did not accurately reflect the pit depth and increased both with increasing depth and with increasing width (for widths $\leq$ 1r). There is however evidence that the lateral distance at which this deflection begins to be observed has some dependence of the outer probe diameter, as was seen by examining a probe of doubled outer diameter (and fixed inner diameter). A similar investigation was carried out using a pit of equal width and breadth ($\leq$ 2r). In this situation the line scan profile showed two negative deflections, each centred on the probe walls. In other words the 3D relief created reflects the geometry of the probe rather than the pit. Indeed, the qualitative shape of the profile was again invariant on pit depth and width. Interestingly in this case the depth of the pit did not appear to affect the deflection amplitude, even though a greater pit

width/breadth did increase the deflection amplitude. However, the profile of the deflection did appear to reflect the value of r, thus providing useful information about the probe. Indeed the results overall suggested that in future work it may be possible to develop a calibration target for SICM which would allow both the inner and outer pipette radii of an experimental probe to be determined. For example, sets of elongated pits of varying known width could be used to give information about the outer probe radius whilst pits of varying, known, equal width and breadth could be used to determine the inner probe radius. This could potentially be useful as it is not currently possible to investigate the probe properties in a non-destructive way. There is significant variation in tip geometry between probes and there may be variation even between probes formed from the two halves of a single pulled capillary tube (electron microscopy data from this laboratory, unpublished). Thus, the development of a simple, non-destructive way of examining probes before imaging seems feasible and could be very useful in defining likely image resolution as well as providing a means to examine the quality of pipettes.

6.2 The testing of a combined FMRFamide-tagged and pHluorin-tagged construct for the detection of neuropeptide secretory events

In order to study neuropeptide secretion via SICM topographic scanning it is necessary to identify likely secretion sites on the cell surface. Additionally, fluorescent labelling of granule cargo allows a second way of following granule fusion and peptide release and may help in the interpretation of topographic data. It was therefore decided to use a fluorescent protein to label LDCVs by inserting a fluorescent protein sequence into the preprohormone for NPY that was already tagged with FMRFamide. The fluorescent label chosen was a pH-sensitive version of the green fluorescent protein called super-ecliptic pHluorin (seGFP). With this system a large increase in fluorescence intensity was observed in fusing LDCVs as a result of the change in its pH environment from ~ pH 5.4 – 7.3. It was thought that this scheme would allow different secretory modes to be identified with full vesicle fusion leading to transient brightening and subsequent rapid loss of fluorescence as the cargo diffused away, whilst kiss-and-run fusion would be shown as cycles of brightening and dimming. Additionally, since the construct was built from the FMRFamide-tagged NPY, it allowed secretion to be followed by the FMRFamide tagging method (Whim and Moss, 2001). This dual

labelling allowed an investigation to be made into whether the seGFP label altered the kinetics of secretory events.

Experiments were performed to confirm that expression of NPY-seGFP creates seGFP that is localised to dense core granules (Chapter 5). These experiments confirmed the co-localisation of the fluorescent label with the endogenously expressed peptide ACTH in AtT20 cells, suggesting that the fluorescent protein from the NPY-construct was localised to LDCVs. Further seGFP expressed from NPY-seGFP in AtT20 cells was also seen to give the expected increase in fluorescence intensity when exposed to pH change. Next, since there have been some few reports in the literature that labelling granule cargo with GFP may affect the kinetics of secretion (e.g. Michael et al., 2004; Felmy, 2007) it was decided to investigate the kinetics of secretory events from cells expressing the NPY-construct labelled with a variety of fluorescent proteins and also without a fluorescent label. These kinetics were studied by the FMRFamide-tagging method.

The kinetics of FMRFamide events showed that there did not appear to be major variations in the amplitude, onset or decay time of events between the unlabelled construct, NPY-seGFP and NPY-Venus (where the fluorescent protein was expressed as a fusion product with NPY). In keeping with other studies of dense core granule release however, there was considerable variation in the amplitude and time course of events recorded from an individual cell. Notably in some cases an extended onset state was observed which had a form qualitatively similar to the ‘feet’ seen in amperometric recordings (Fig. 6.2). These feet were observed for all constructs. Given their similarity to amperometric ‘feet’, it is possible that these might represent partial granule fusion events which later develop into full fusion release.

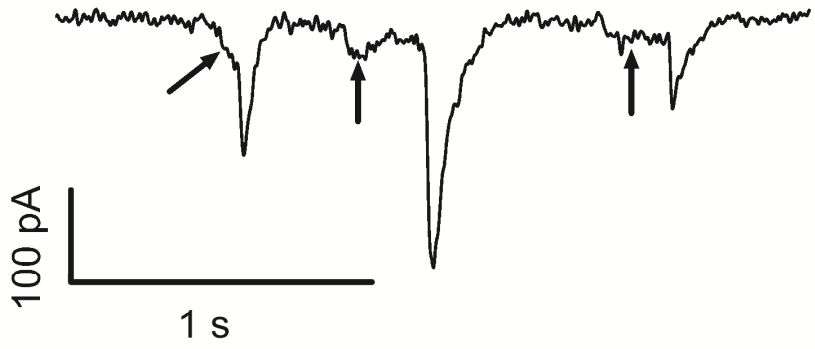

Figure 6.2. Some FMRFamide secretory events show a time course that is reminiscent of the "feet" seen in amperometric recordings
Arrows in the above trace indicate these portions of the events. (This trace was obtained for AtT20s transfected with NPY-seGFP and was recorded by Dr. David C. H. Benton, UCL).

This is very interesting because the fusion pore is generally thought not to allow peptides to traverse it (Salio et al., 2006). The obvious way to test this is to look for coincident feet with seGFP brightening. Unfortunately, experiments which may have shed light on this relationship did not work because FMRFamide secretion proved to be highly unreliable when the cells were plated on glass. Thus, although a number of experiments were performed in which high-resolution fast optical imaging and electrophysiology, (FMRFamide tagging) were combined (in collaboration with Dr Tom Carter, NIMR, UK), no FMRFamide events were seen (n = 102). However, in several cases persistent increases in seGFP fluorescence were observed, without FMRFamide currents (n = 20 from a total of n = 102 cells). This suggests that under the conditions used in this experiment the secretion of FMRFamide from LDCVs was impeded. One possible cause would be if only partial fusion events occurred (with a fusion pore of insufficient diameter to allow the release of FMRFamide). Alternatively this could occur if the granule contents (including seGFP and FMRFamide) were deposited on the cell surface in a stable manner. Further, if we are to reconcile this with the escape of FMRFamide causing feet signals, then we would probably require a two-stage pore dilation as suggested by Vardjan et al. (2007b). Thus, more work will be needed in order to determine whether the fusion pore can really enter a state in which small peptides such as FMRFamide might be released.

6.3 Detection of fused secretory granules or stable cargo deposits via SICM topographic imaging

Simulations of inverted hemispheres suggested that partially fused secretory granules may be recognisable for granules of diameter ≥ 3 to 4r. Therefore, for a probe of internal radius ~100 nm (close to a typical value used experimentally in this laboratory) a granule of ~ 300 to 400 nm diameter should be detectable in an SICM topographic scan. This diameter is at the large end of the scale for most dense core granules, which are ~150 to 300 nm, prior to fusion. However, following fusion, granules might be expected to form a pit of slightly larger diameter, depending on the exact mechanism of the fusion process. Thus, depending on the exact combination of the size of probe and size of the granule it may be possible to see either individual granules, or possible multiple fusing granules. Similarly, stable deposits of protein cargo are close to the limit of detection. However, prior to the work presented here it was not known how SICM detection would respond to surface cargo deposits. Therefore, an experimental investigation was undertaken using a large secretory organelle, the Weibel-Palade body (WPB), which may be up to 4 μm long (Hannah et al., 2002). SICM scans of HUVEC cells prior to and just after stimulation revealed large surface features emerging only after the stimulus. Simultaneous optical monitoring showed that exocytosis had occurred. This is the first time that exocytotic events from Weibel-Palade bodies have been imaged in live cells using a scanning probe approach (although previous studies have been made using AFM on fixed cells). The fact that mounds of secretory protein appear to be imaged suggests that surface deposits of secreted protein can be detected via SICM topographic scanning and that it may also be possible to monitor the dispersal of these deposits over time.

Due to the success of these initial experiments a study of secretion from LDCVs in AtT20 cells, using our previously validated NPY-seGFP construct, was performed. It was thought that this might allow the distinction between two possible interpretations of the observations in the previous combined electrophysiological and optical experiments. These experiments had shown an increase of seGFP fluorescence (indicating an increase in the pH of its environment), which was persistent (for the duration of the recording ~ 5 min). However, this was observed without any detection of peptide secretion via the FMRFamide signal. The topographic imaging of AtT20 cells showed that on both glass and plastic substrates large changes in the cell surface topography appeared after

stimulation only whilst an increase in seGFP fluorescence was also observed. Therefore, it seems that the structural changes observed in these scans should be attributed to the secretory processes. Interestingly, these raised features were observed in several sequential scans before the cell geometry returned towards its initial form over time (~ 20 min) and some fluorescence was also observed over this time (although it decreases, it does not completely vanish). Perhaps therefore, these findings are in better agreement with the stable deposition of at least some granule cargoes on the cell surface rather than the formation of either a stable or flickering fusion pore which has too small a diameter to allow the passage of FMRFamide (and would presumably be initially undetectable). If there are stable deposits of cargo these could perhaps be caused by the cell releasing unprocessed cargo, given the very strong stimulation used. This unprocessed cargo could then perhaps form a sufficiently tangled deposit to remain stable.

There are however several other factors to consider in relation to these observations. From these data it is not possible to distinguish between deposits of secreted protein cargo and rearrangements of the cell membrane. Therefore the raised features observed may also be due to temporary increases in the cell surface area due to a lag between exocytosis and compensatory endocytosis during high-levels of exocytosis.

Finally, the temporal resolution of these scans was unlikely to be sufficient to capture the full dynamics of vesicle fusion, although it should be possible to identify a smaller region of interest and then to follow this at a high temporal resolution in subsequent scans.

6.4 Future work

Extension of the model

One possible avenue for future work would be to extend the model to include partially conductive surfaces, thus making a more realistic representation of the cell surface. This may be possible to achieve simply by adding an extra volume to the simulation which had a third specified conductivity. This type of approach could be used to investigate more realistic cell membranes and to assess the effect of ion channel openings under the scanning pipette, which has thus far been thought to be negligible (at standard scanning set points).

Other applications of SICM to investigate neuropeptide secretion

Simple topographical scanning is not the only possible application of SICM to studying peptide secretion. Other potential ways in which SICM could be used to study peptide secretion rely more on using SICM as a tool for small scale manipulation rather than solely for imaging. One promising application may be to use the SICM probe to iontophoretically deliver drugs to highly localised parts of the cell. Such local dosing has previously been achieved with K^+ ions (Piper et al., 2008), which could be used as a localised secretagogue. If the problems with secretion of NPY-seGFP on glass are resolved, this could be an ideal system to use with local dosing via SICM. Release could be followed optically while stimulants (such as high K^+, caffeine, ionomycin etc) or potential secretion modifiers (e.g. Ca^{2+}/ Ca^{2+} buffers, dynamin inhibitors, etc) were delivered to particular compartments such as the cell processes in AtT20s. Finally, SICM could be used to patch small cellular compartments seen to be containing high concentrations of granules, thereby allowing such questions as whether particular ion channels are clustered close to dense core granule release sites to be investigated, as has been suggested in pancreatic β cells (Barg et al., 2002b).

Appendix 1: Guide to Appendix 2

The code used in the finite element method simulation of SICM can be found on the attached cd (Appendix 2). For each surface simulated a command script (i*.m) was run in Matlab. The flow of the program within the command script is shown in figure A.1. Further details are also given of the meshing (Fig. A.2) and solving (Fig. A.3) routines. In these figures, scripts marked † were written by Dr. Eero Willman, Department of Electrical Engineering, UCL, and are indicated with the exact name of the file. In Appendix 2, the files used in all simulations are in the "common" directory. There is also a directory for each type of surface modelled in this thesis, which contains examples of the files used to simulate this surface.

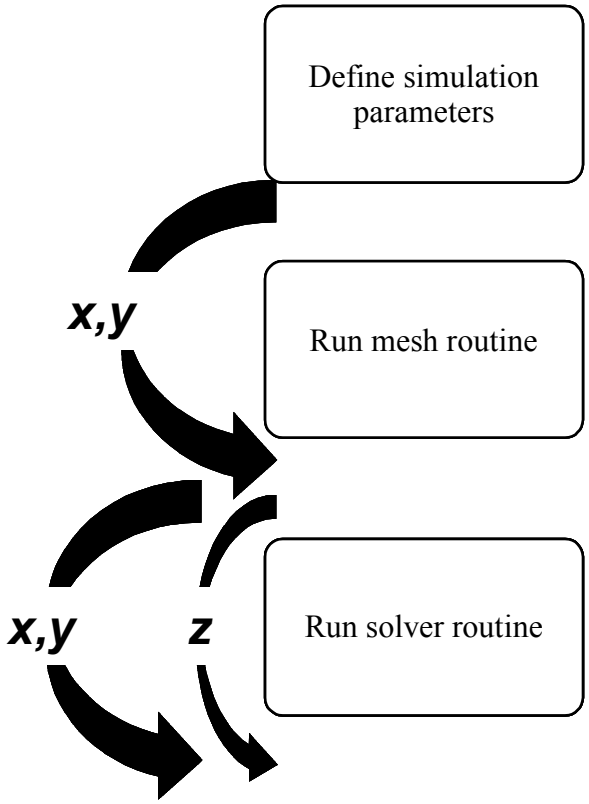

Figure A.1 Flow of the program within each command script
In each command script the parameters such as simulation volume and the maximum size of mesh elements was specified. Next the meshing routine was iterated to give a mesh for each *z* and *x,y* pipette position studied. Finally the solver routine was run on all these meshes. In the diagram above the bold arrows indicate for loops.

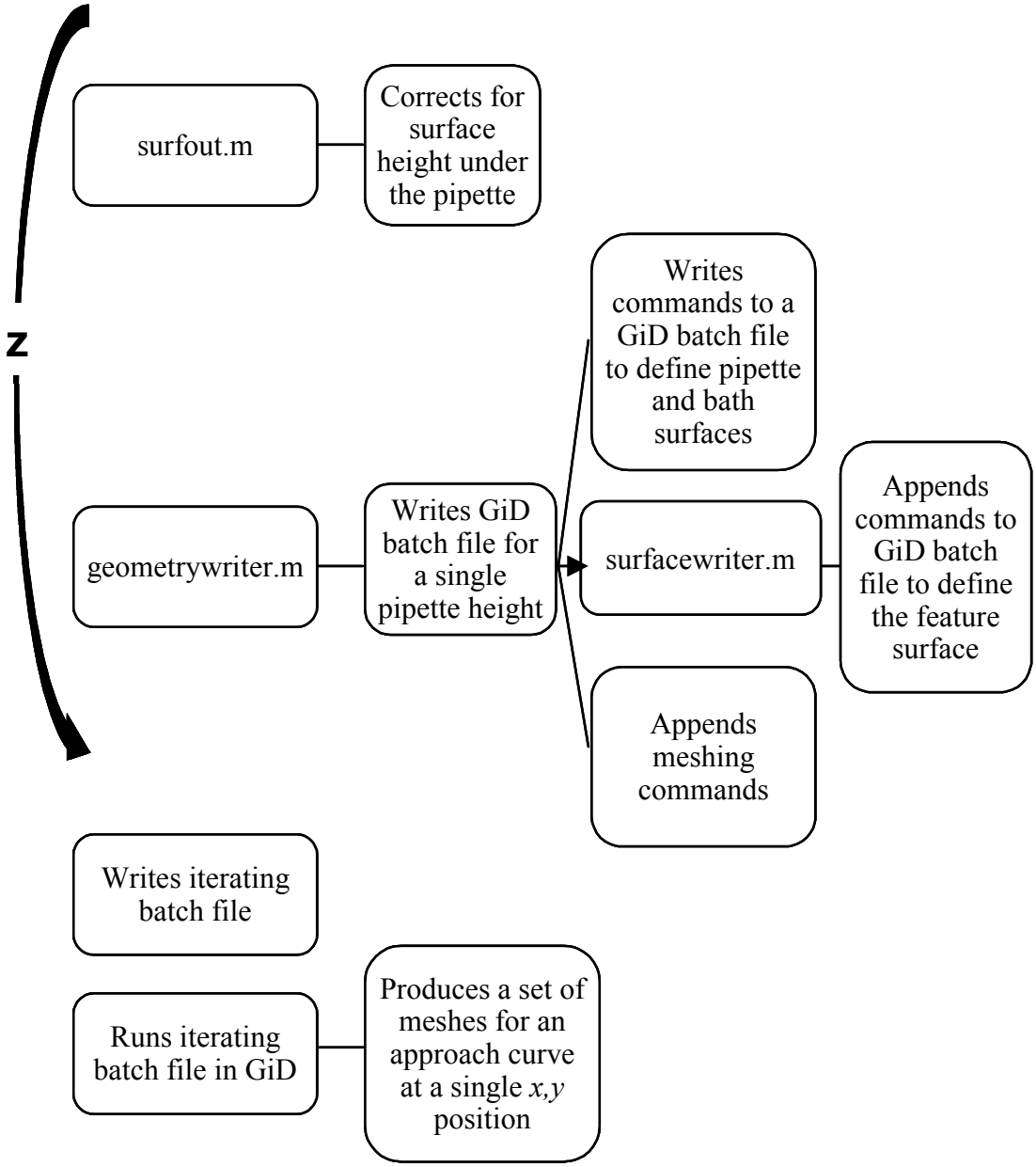

Figure A.2 Flow of the program within the meshing routine
Lines linking the different elements indicate the function of the element to the left. Arrows linking elements indicate a call to a function. The bold arrow indicates an iterating loop.

Figure A.3 (Following page) Flow of the program within the solving routine
Lines linking the different elements indicate the function of the element to the left. Arrows linking elements indicate a call to a function. The bold arrow indicates an iterating loop. Elements marked † were written by Dr. Eero Willman and may be found in the common directory (Appendix 2).

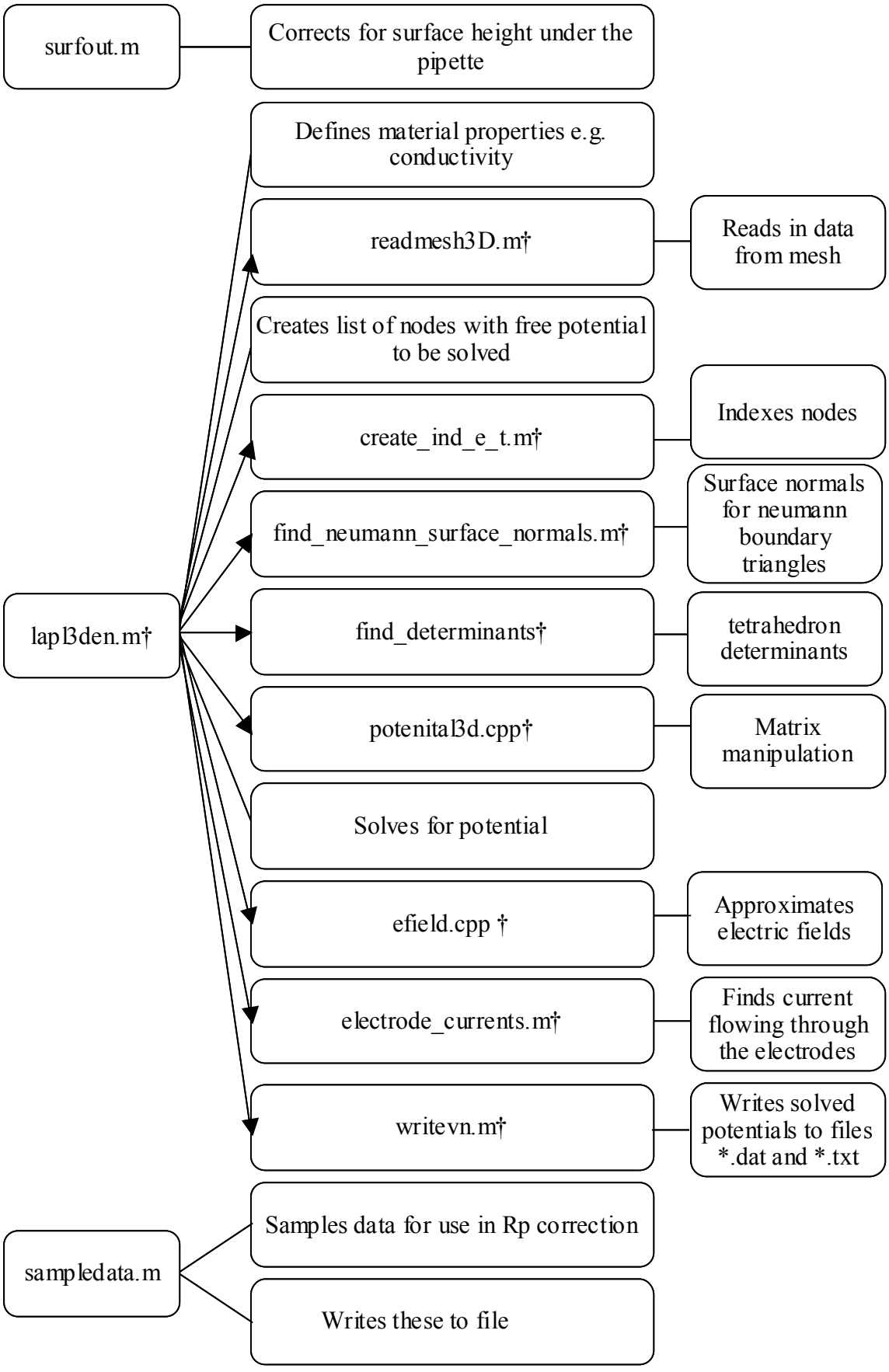
surfout.m
Corrects for surface height under the pipette
lapl3den.m†
Defines material properties e.g. conductivity
readmesh3D.m†
Reads in data from mesh
Creates list of nodes with free potential to be solved
create_ind_e_t.m†
Indexes nodes
find_neumann_surface_normals.m†
Surface normals for neumann boundary triangles
find_determinants†
tetrahedron determinants
potenital3d.cpp†
Matrix manipulation
Solves for potential
efield.cpp †
Approximates electric fields
electrode_currents.m†
Finds current flowing through the electrodes
writevn.m†
Writes solved potentials to files *.dat and *.txt
sampledata.m
Samples data for use in Rp correction
Writes these to file

References

1. Abramoff, M. D., P. J. Magelhaes, and S. J. Ram. 2004. Image Processing with ImageJ. Biophotonics International 11: 36-42.

2. Adenle, O., and W. Fitzgerald. 2005. Simulating imaging with the scanning ion-conductance microscope. Conf. Proc. IEEE Eng Med. Biol. Soc. 4: 3410-3413.

3. Albillos, A., G. Dernick, H. Horstmann, W. Almers, T. G. Alvarez de, and M. Lindau. 1997. The exocytotic event in chromaffin cells revealed by patch amperometry. Nature 389: 509-512.

4. Albillos, A., E. Neher, and T. Moser. 2000. R-Type Ca2+ channels are coupled to the rapid component of secretion in mouse adrenal slice chromaffin cells. J. Neurosci. 20: 8323-8330.

5. Ales, E., L. Tabares, J. M. Poyato, V. Valero, M. Lindau, and T. G. Alvarez de. 1999. High calcium concentrations shift the mode of exocytosis to the kiss-and-run mechanism. Nat. Cell Biol. 1: 40-44.

6. Amemiya, S., J. Guo, H. Xiong, and D. A. Gross. 2006. Biological applications of scanning electrochemical microscopy: chemical imaging of single living cells and beyond. Anal. Bioanal. Chem. 386: 458-471.

7. Andersson, P. O., S. R. Bloom, A. V. Edwards, and J. Jarhult. 1982. Effects of stimulation of the chorda tympani in bursts on submaxillary responses in the cat. J. Physiol 322: 469-483.

8. Artalejo, C. R., M. E. Adams, and A. P. Fox. 1994. Three types of Ca2+ channel trigger secretion with different efficacies in chromaffin cells. Nature 367: 72-76.

9. Atluri, P. P., and T. A. Ryan. 2006. The kinetics of synaptic vesicle reacidification at hippocampal nerve terminals. J. Neurosci. 26: 2313-2320.

10. Bae, C., and P. J. Butler. 2008. Finite element analysis of microelectrotension of cell membranes. Biomech. Model. Mechanobiol. 7: 379-386.

11. Balaji, J., and T. A. Ryan. 2007. Single-vesicle imaging reveals that synaptic vesicle exocytosis and endocytosis are coupled by a single stochastic mode. Proc. Natl. Acad. Sci. U. S. A 104: 20576-20581.

12. Bard, A. J., F. R. Fan, J. Kwak, and O. Lev. 1989. Scanning electrochemical microscopy. Introduction and principles. Analytical Chemistry 61: 132-138.

13. Barg, S., L. Eliasson, E. Renstrom, and P. Rorsman. 2002. A subset of 50 secretory granules in close contact with L-type Ca2+ channels accounts for first-phase insulin secretion in mouse beta-cells. Diabetes 51 Suppl 1: S74-S82.

14. Barg, S., C. S. Olofsson, J. Schriever-Abeln, A. Wendt, S. Gebre-Medhin, E. Renstrom, and P. Rorsman. 2002. Delay between fusion pore opening and peptide release from large dense-core vesicles in neuroendocrine cells. Neuron 33: 287-299.

15. Bauer, C. S., R. J. Woolley, A. G. Teschemacher, and E. P. Seward. 2007. Potentiation of exocytosis by phospholipase C-coupled G-protein-coupled receptors requires the priming protein Munc13-1. J. Neurosci. 27: 212-219.

16. Berglund, M. M., P. A. Hipskind, and D. R. Gehlert. 2003. Recent developments in our understanding of the physiological role of PP-fold peptide receptor subtypes. Exp. Biol. Med. (Maywood.) 228: 217-244.

17. Bicknell, R. J. 1988. Optimizing release from peptide hormone secretory nerve terminals. J. Exp. Biol. 139: 51-65.

18. Binnig, G., C. F. Quate, and C. Gerber. 1986. Atomic force microscope. Phys. Rev. Lett. 56: 930-933.

19. Bond, A. M., K. B. Oldham, and C. G. Zoski. 1988. Theory of electrochemical processes at an inlaid disc microelectrode under steady-state conditions. Journal of Electroanalytical Chemistry and Interfacial Electrochemistry 245: 71-104.

20. Burgoyne, R. D., and A. Morgan. 2003. Secretory granule exocytosis. Physiol Rev 83: 581-632.

21. Camacho, M., J. D. Machado, M. S. Montesinos, M. Criado, and R. Borges. 2006. Intragranular pH rapidly modulates exocytosis in adrenal chromaffin cells. J. Neurochem. 96: 324-334.

22. Casuso, I., and S. Scheuring. 2010. Automated setpoint adjustment for biological contact mode atomic force microscopy imaging. Nanotechnology 21: 035104.

23. Chen, X. K., L. C. Wang, Y. Zhou, Q. Cai, M. Prakriya, K. L. Duan, Z. H. Sheng, C. Lingle, and Z. Zhou. 2005. Activation of GPCRs modulates quantal size in chromaffin cells through G(betagamma) and PKC. Nat. Neurosci. 8: 1160-1168.

24. Chow, R. H., R. L. von, and E. Neher. 1992. Delay in vesicle fusion revealed by electrochemical monitoring of single secretory events in adrenal chromaffin cells. Nature 356: 60-63.

25. Clark, J. T., P. S. Kalra, W. R. Crowley, and S. P. Kalra. 1984. Neuropeptide Y and human pancreatic polypeptide stimulate feeding behavior in rats. Endocrinology 115: 427-429.

26. Cool, D. R., M. Fenger, C. R. Snell, and Y. P. Loh. 1995. Identification of the sorting signal motif within pro-opiomelanocortin for the regulated secretory pathway. J. Biol. Chem. 270: 8723-8729.

27. Czajkowsky, D. M., and Z. Shao. 2002. Supported lipid bilayers as effective substrates for atomic force microscopy. Methods Cell Biol. 68: 231-241.

28. Dannies, P. S. 1999. Protein hormone storage in secretory granules: mechanisms for concentration and sorting. Endocr. Rev. 20: 3-21.

29. de Wit, J., R. F. Toonen, and M. Verhage. 2009. Matrix-dependent local retention of secretory vesicle cargo in cortical neurons. J. Neurosci. 29: 23-37.

30. Dufrêne, Y. F., and P. Hinterdorfer. 2008. Recent progress in AFM molecular recognition studies. Pflugers Arch. 456: 237-245.

31. Duncan, R. R., J. Greaves, U. K. Wiegand, I. Matskevich, G. Bodammer, D. K. Apps, M. J. Shipston, and R. H. Chow. 2003. Functional and spatial segregation of secretory vesicle pools according to vesicle age. Nature 422: 176-180.

32. Edwards, M. A., C. G. Williams, A. L. Whitworth, and P. R. Unwin. 2009. Scanning ion conductance microscopy: a model for experimentally realistic conditions and image interpretation. Anal. Chem. 81: 4482-4492.

33. El Meskini, R., L. Jin, R. Marx, A. Bruzzaniti, J. Lee, R. Emeson, and R. Mains. 2001. A signal sequence is sufficient for green fluorescent protein to be routed to regulated secretory granules. Endocrinology 142: 864-873.

34. Elhamdani, A., F. Azizi, and C. R. Artalejo. 2006. Double patch clamp reveals that transient fusion (kiss-and-run) is a major mechanism of secretion in calf adrenal chromaffin cells: high calcium shifts the mechanism from kiss-and-run to complete fusion. J. Neurosci. 26: 3030-3036.

35. Eliasson, L., E. Renstrom, W. G. Ding, P. Proks, and P. Rorsman. 1997. Rapid ATP-dependent priming of secretory granules precedes Ca(2+)-induced exocytosis in mouse pancreatic B-cells. J. Physiol 503 (Pt 2): 399-412.

36. Eliasson, L., F. Abdulkader, M. Braun, J. Galvanovskis, M. B. Hoppa, and P. Rorsman. 2008. Novel aspects of the molecular mechanisms controlling insulin secretion. J. Physiol 586: 3313-3324.

37. Evans, E. 1998. Energy landscapes of biomolecular adhesion and receptor anchoring at interfaces explored with dynamic force spectroscopy. Faraday Discuss. 1-16.

38. Fan, F. R., and A. J. Bard. 1999. Imaging of biological macromolecules on mica in humid air by scanning electrochemical microscopy. Proc. Natl. Acad. Sci. U. S. A 96: 14222-14227.

39. Felmy, F. 2007. Modulation of cargo release from dense core granules by size and actin network. Traffic. 8: 983-997.

40. Feng, W., S. A. Rotenberg, and M. V. Mirkin. 2003. Scanning electrochemical microscopy of living cells. 5. Imaging of fields of normal and metastatic human breast cells. Anal. Chem. 75: 4148-4154.

41. Francis, L. W., P. D. Lewis, C. J. Wright, and R. S. Conlan. 2010. Atomic force microscopy comes of age. Biol. Cell 102: 133-143.

42. Frederix, P. L. T. M., M. R. Gullo, T. Akiyama, A. Tonin, N. F. de Rooij, U. Staufer, and A. Engel. 2005. Assessment of insulated conductive cantilevers for biology and electrochemistry. 997.

43. Fulop, T., and C. Smith. 2006. Physiological stimulation regulates the exocytic mode through calcium activation of protein kinase C in mouse chromaffin cells. Biochem. J. 399: 111-119.

44. Gainer, H., S. A. Wolfe, Jr., A. L. Obaid, and B. M. Salzberg. 1986. Action potentials and frequency-dependent secretion in the mouse neurohypophysis. Neuroendocrinology 43: 557-563.

45. Ganchev, D. N., D. T. Rijkers, M. M. Snel, J. A. Killian, and K. B. de. 2004. Strength of integration of transmembrane alpha-helical peptides in lipid bilayers as determined by atomic force spectroscopy. Biochemistry 43: 14987-14993.

46. Gandhi, S. P., and C. F. Stevens. 2003. Three modes of synaptic vesicular recycling revealed by single-vesicle imaging. Nature 423: 607-613.

47. Ge, Q., Y. M. Dong, Z. T. Hu, Z. X. Wu, and T. Xu. 2006. Characteristics of Ca2+-exocytosis coupling in isolated mouse pancreatic beta cells. Acta Pharmacol. Sin. 27: 933-938.

48. Gerber, C., and H. P. Lang. 2006. How the doors to the nanoworld were opened. Nat. Nanotechnol. 1: 3-5.

49. Goerge, T., A. Niemeyer, P. Rogge, R. Ossig, H. Oberleithner, and S. W. Schneider. 2002. Secretion pores in human endothelial cells during acute hypoxia. J. Membr. Biol. 187: 203-211.

50. Gorelik, J., A. Shevchuk, M. Ramalho, M. Elliott, C. Lei, C. F. Higgins, M. J. Lab, D. Klenerman, N. Krauzewicz, and Y. Korchev. 2002. Scanning surface confocal microscopy for simultaneous topographical and fluorescence imaging: application to single virus-like particle entry into a cell. Proc. Natl. Acad. Sci. U. S. A 99: 16018-16023.

51. Granseth, B., B. Odermatt, S. J. Royle, and L. Lagnado. 2006. Clathrin-mediated endocytosis is the dominant mechanism of vesicle retrieval at hippocampal synapses. Neuron 51: 773-786.

52. Green, K. A., and G. A. Cottrell. 1999. Block of the helix FMRFamide-gated Na+ channel by FMRFamide and its analogues. J. Physiol 519 Pt 1: 47-56.

53. Gruber, B., S. Greber, E. Rupp, and G. Sperk. 1994. Differential NPY mRNA expression in granule cells and interneurons of the rat dentate gyrus after kainic acid injection. Hippocampus 4: 474-482.

54. Gustavsson, N., and W. Han. 2009. Calcium-sensing beyond neurotransmitters: functions of synaptotagmins in neuroendocrine and endocrine secretion. Biosci. Rep. 29: 245-259.

55. Hall, J. E. 1975. Access resistance of a small circular pore. J. Gen. Physiol 66: 531-532.

56. Hannah, M. J., R. Williams, J. Kaur, L. J. Hewlett, and D. F. Cutler. 2002. Biogenesis of Weibel-Palade bodies. Semin. Cell Dev. Biol. 13: 313-324.

57. Hannah, M. J., P. Skehel, M. Erent, L. Knipe, D. Ogden, and T. Carter. 2005. Differential kinetics of cell surface loss of von Willebrand factor and its propolypeptide after secretion from Weibel-Palade bodies in living human endothelial cells. J. Biol. Chem. 280: 22827-22830.

58. Hansma, P. K., B. Drake, O. Marti, S. A. Gould, and C. B. Prater. 1989. The scanning ion-conductance microscope. Science 243: 641-643.

59. Hansma, P. K., J. P. Cleveland, M. Radmacher, D. A. Walters, P. E. Hillner, M. Bezanilla, M. Fritz, D. Vie, H. G. Hansma, C. B. Prater, J. Massie, L. Fukunaga, J. Gurley, and V. Elings. 1994. Tapping mode atomic force microscopy in liquids. Applied Physics Letters 64: 1738-1740.

60. Happel, P., and I. D. Dietzel. 2009. Backstep scanning ion conductance microscopy as a tool for long term investigation of single living cells. J. Nanobiotechnology. 7: 7.

61. Heinemann, C., R. L. von, R. H. Chow, and E. Neher. 1993. A two-step model of secretion control in neuroendocrine cells. Pflugers Arch. 424: 105-112.

62. Heinemann, C., R. H. Chow, E. Neher, and R. S. Zucker. 1994. Kinetics of the secretory response in bovine chromaffin cells following flash photolysis of caged Ca2+. Biophys. J. 67: 2546-2557.

63. Hille, B. 1968. Pharmacological modifications of the sodium channels of frog nerve. J. Gen. Physiol 51: 199-219.

64. Hinterdorfer, P., W. Baumgartner, H. J. Gruber, K. Schilcher, and H. Schindler. 1996. Detection and localization of individual antibody-antigen recognition events by atomic force microscopy. Proc. Natl. Acad. Sci. U. S. A 93: 3477-3481.

65. Hökfelt, T., C. Broberger, X. Zhang, M. Diez, J. Kopp, Z. Xu, M. Landry, L. Bao, M. Schalling, J. Koistinaho, S. J. DeArmond, S. Prusiner, J. Gong, and J. H. Walsh. 1998. Neuropeptide Y: some viewpoints on a multifaceted peptide in the normal and diseased nervous system. Brain Res. Brain Res. Rev. 26: 154-166.

66. Holt, K. B., and A. J. Bard. 2005. Interaction of silver(I) ions with the respiratory chain of Escherichia coli: an electrochemical and scanning electrochemical microscopy study of the antimicrobial mechanism of micromolar Ag+. Biochemistry 44: 13214-13223.

67. Horrigan, F. T., and R. J. Bookman. 1994. Releasable pools and the kinetics of exocytosis in adrenal chromaffin cells. Neuron 13: 1119-1129.

68. Jackson, M. B., A. Konnerth, and G. J. Augustine. 1991. Action potential broadening and frequency-dependent facilitation of calcium signals in pituitary nerve terminals. Proc. Natl. Acad. Sci. U. S. A 88: 380-384.

69. Janovjak, H., M. Kessler, D. Oesterhelt, H. Gaub, and D. J. Müller. 2003. Unfolding pathways of native bacteriorhodopsin depend on temperature. EMBO J. 22: 5220-5229.

70. Jorgacevski, J., M. Fosnaric, N. Vardjan, M. Stenovec, M. Potokar, M. Kreft, V. Kralj-Iglic, A. Iglic, and R. Zorec. 2010. Fusion pore stability of peptidergic vesicles. Mol. Membr. Biol. 27: 65-80.

71. Kalra, S. P., M. G. Dube, S. Pu, B. Xu, T. L. Horvath, and P. S. Kalra. 1999. Interacting Appetite-Regulating Pathways in the Hypothalamic Regulation of Body Weight. Endocr Rev 20: 68-100.

72. Kedrov, A., M. Krieg, C. Ziegler, W. Kuhlbrandt, and D. J. Müller. 2005. Locating ligand binding and activation of a single antiporter. EMBO Rep. 6: 668-674.

73. Kedrov, A., M. Appel, H. Baumann, C. Ziegler, and D. J. Müller. 2008. Examining the dynamic energy landscape of an antiporter upon inhibitor binding. J. Mol. Biol. 375: 1258-1266.

74. Klenerman, D., and Y. Korchev. 2006. Potential biomedical applications of the scanned nanopipette. Nanomed. 1: 107-114.

75. Korchev, Y. E., M. Milovanovic, C. L. Bashford, D. C. Bennett, E. V. Sviderskaya, I. Vodyanoy, and M. J. Lab. 1997. Specialized scanning ion-conductance microscope for imaging of living cells. J. Microsc. 188: 17-23.

76. Korchev, Y. E., C. L. Bashford, M. Milovanovic, I. Vodyanoy, and M. J. Lab. 1997. Scanning ion conductance microscopy of living cells. Biophys. J. 73: 653-658.

77. Korchev, Y. E., Y. A. Negulyaev, C. R. Edwards, I. Vodyanoy, and M. J. Lab. 2000. Functional localization of single active ion channels on the surface of a living cell. Nat. Cell Biol. 2: 616-619.

78. Laforge, F. O., J. Velmurugan, Y. Wang, and M. V. Mirkin. 2009. Nanoscale imaging of surface topography and reactivity with the scanning electrochemical microscope. Anal. Chem. 81: 3143-3150.

79. Lee, C., J. Kwak, and A. J. Bard. 1990. Application of scanning electrochemical microscopy to biological samples. Proc. Natl. Acad. Sci. U. S. A 87: 1740-1743.

80. Liebetrau, J. M., H. M. Miller, J. E. Baur, S. A. Takacs, V. Anupunpisit, P. A. Garris, and D. O. Wipf. 2003. Scanning electrochemical microscopy of model neurons: imaging and real-time detection of morphological changes. Anal. Chem. 75: 563-571.

81. Lindner, D., J. Stichel, and A. G. Beck-Sickinger. 2008. Molecular recognition of the NPY hormone family by their receptors. Nutrition 24: 907-917.

82. Lingueglia, E., G. Champigny, M. Lazdunski, and P. Barbry. 1995. Cloning of the amiloride-sensitive FMRFamide peptide-gated sodium channel. Nature 378: 730-733.

83. Lingueglia, E., E. Deval, and M. Lazdunski. 2006. FMRFamide-gated sodium channel and ASIC channels: a new class of ionotropic receptors for FMRFamide and related peptides. Peptides 27: 1138-1152.

84. Loh, Y. P., C. R. Snell, and D. R. Cool. 1997. Receptor-mediated targeting of hormones to secretory granules: role of carboxypeptidase E. Trends Endocrinol. Metab 8: 130-137.

85. Ludwig, M., and G. Leng. 2006. Dendritic peptide release and peptide-dependent behaviours. Nat. Rev. Neurosci. 7: 126-136.

86. Lundberg, J. M., and L. Stjarne. 1984. Neuropeptide Y (NPY) depresses the secretion of 3H-noradrenaline and the contractile response evoked by field stimulation, in rat vas deferens. Acta Physiol Scand. 120: 477-479.

87. Lundberg, J. M., A. Rudehill, A. Sollevi, E. Theodorsson-Norheim, and B. Hamberger. 1986. Frequency- and reserpine-dependent chemical coding of sympathetic transmission: differential release of noradrenaline and neuropeptide Y from pig spleen. Neurosci. Lett. 63: 96-100.

88. Lundberg, J. M., A. Rudehill, A. Sollevi, G. Fried, and G. Wallin. 1989. Co-release of neuropeptide Y and noradrenaline from pig spleen in vivo: importance of

subcellular storage, nerve impulse frequency and pattern, feedback regulation and resupply by axonal transport. Neuroscience 28: 475-486.

89. Lundberg, J. M., A. Franco-Cereceda, J. S. Lacroix, and J. Pernow. 1990. Neuropeptide Y and sympathetic neurotransmission. Ann. N. Y. Acad. Sci. 611: 166-174.

90. MacDonald, P. E., M. Braun, J. Galvanovskis, and P. Rorsman. 2006. Release of small transmitters through kiss-and-run fusion pores in rat pancreatic beta cells. Cell Metab 4: 283-290.

91. Marengo, F. D. 2005. Calcium gradients and exocytosis in bovine adrenal chromaffin cells. Cell Calcium 38: 87-99.

92. Marsh, D. J., S. C. Baraban, G. Hollopeter, and R. D. Palmiter. 1999. Role of the Y5 neuropeptide Y receptor in limbic seizures. Proc. Natl. Acad. Sci. U. S. A 96: 13518-13523.

93. Michael, D. J., X. Geng, N. X. Cawley, Y. P. Loh, C. J. Rhodes, P. Drain, and R. H. Chow. 2004. Fluorescent cargo proteins in pancreatic beta-cells: design determines secretion kinetics at exocytosis. Biophys. J. 87: L03-L05.

94. Miesenböck, G., D. A. De Angelis, and J. E. Rothman. 1998. Visualizing secretion and synaptic transmission with pH-sensitive green fluorescent proteins. Nature 394: 192-195.

95. Mitchell, G. C., Q. Wang, P. Ramamoorthy, and M. D. Whim. 2008. A common single nucleotide polymorphism alters the synthesis and secretion of neuropeptide Y. J. Neurosci. 28: 14428-14434.

96. Möller, C., M. Allen, V. Elings, A. Engel, and D. J. Müller. 1999. Tapping-mode atomic force microscopy produces faithful high-resolution images of protein surfaces. Biophys. J. 77: 1150-1158.

97. Mosharov, E. V., L. W. Gong, B. Khanna, D. Sulzer, and M. Lindau. 2003. Intracellular patch electrochemistry: regulation of cytosolic catecholamines in chromaffin cells. J. Neurosci. 23: 5835-5845.

98. Moy, V. T., E. L. Florin, and H. E. Gaub. 1994. Intermolecular forces and energies between ligands and receptors. Science 266: 257-259.

99. Müller, D. J., W. Baumeister, and A. Engel. 1999. Controlled unzipping of a bacterial surface layer with atomic force microscopy. Proc. Natl. Acad. Sci. U. S. A 96: 13170-13174.

100. Müller, D. J., and A. Engel. 2007. Atomic force microscopy and spectroscopy of native membrane proteins. Nat. Protoc. 2: 2191-2197.

101. Müller, D. J. 2008. AFM: a nanotool in membrane biology. Biochemistry 47: 7986-7998.

102. Müller, D. J., and A. Engel. 2008. Strategies to prepare and characterize native membrane proteins and protein membranes by AFM. Current Opinion in Colloid & Interface Science 13: 338-350.

103. Müller, D. J., and Y. F. Dufrêne. 2008. Atomic force microscopy as a multifunctional molecular toolbox in nanobiotechnology. Nat. Nanotechnol. 3: 261-269.

104. Muschol, M., and B. M. Salzberg. 2000. Dependence of transient and residual calcium dynamics on action-potential patterning during neuropeptide secretion. J. Neurosci. 20: 6773-6780.

105. Neher, E., and R. S. Zucker. 1993. Multiple calcium-dependent processes related to secretion in bovine chromaffin cells. Neuron 10: 21-30.

106. Novak, P., C. Li, A. I. Shevchuk, R. Stepanyan, M. Caldwell, S. Hughes, T. G. Smart, J. Gorelik, V. P. Ostanin, M. J. Lab, G. W. J. Moss, G. I. Frolenkov, D. Klenerman, and Y. E. Korchev. 2009. Nanoscale live-cell imaging using hopping probe ion conductance microscopy. Nat. Methods 6: 279-281.

107. Obermüller, S., A. Lindqvist, J. Karanauskaite, J. Galvanovskis, P. Rorsman, and S. Barg. 2005. Selective nucleotide-release from dense-core granules in insulin-secreting cells. J. Cell Sci. 118: 4271-4282.

108. Oesterhelt, F., D. Oesterhelt, M. Pfeiffer, A. Engel, H. E. Gaub, and D. J. Müller. 2000. Unfolding pathways of individual bacteriorhodopsins. Science 288: 143-146.

109. Orci, L., J. D. Vassalli, and A. Perrelet. 1988. The insulin factory. Sci. Am. 259: 85-94.

110. Pang, Z. P., and T. C. Sudhof. 2010. Cell biology of Ca2+-triggered exocytosis. Curr. Opin. Cell Biol. 22: 496-505.

111. Park, P. S., K. T. Sapra, M. Kolinski, S. Filipek, K. Palczewski, and D. J. Müller. 2007. Stabilizing effect of Zn2+ in native bovine rhodopsin. J. Biol. Chem. 282: 11377-11385.

112. Parsons, T. D., J. R. Coorssen, H. Horstmann, and W. Almers. 1995. Docked granules, the exocytic burst, and the need for ATP hydrolysis in endocrine cells. Neuron 15: 1085-1096.

113. Payza, K. 1987. FMRFamide receptors in Helix aspersa. Peptides 8: 1065-1074.

114. Peng, Y. Y., and J. P. Horn. 1991. Continuous repetitive stimuli are more effective than bursts for evoking LHRH release in bullfrog sympathetic ganglia. J. Neurosci. 11: 85-95.

115. Perrais, D., I. C. Kleppe, J. W. Taraska, and W. Almers. 2004. Recapture after exocytosis causes differential retention of protein in granules of bovine chromaffin cells. J. Physiol 560: 413-428.

116. Piper, J. D., C. Li, C. J. Lo, R. Berry, Y. Korchev, L. Ying, and D. Klenerman. 2008. Characterization and application of controllable local chemical changes produced by reagent delivery from a nanopipet. J. Am. Chem. Soc. 130: 10386-10393.

117. Pitta Bauermann, L., W. Schuhmann, and A. Schulte. 2004. An advanced biological scanning electrochemical microscope (Bio-SECM) for studying individual living cells. Phys. Chem. Chem. Phys. 6: 4003-4008.

118. Putman, C. A. J., K. O. Van Der Werf, B. G. De Grooth, N. F. Van Hulst, and J. Greve. 1994. Tapping mode atomic force microscopy in liquid. Applied Physics Letters 64: 2454-2456.

119. Rheinlaender, J., and T. E. Schäffer. 2009. Image formation, resolution, and height measurement in scanning ion conductance microscopy. Journal of Applied Physics 105

120. Rief, M., F. Oesterhelt, B. Heymann, and H. E. Gaub. 1997. Single Molecule Force Spectroscopy on Polysaccharides by Atomic Force Microscopy. Science 275: 1295-1297.

121. Rief, M., M. Gautel, F. Oesterhelt, J. M. Fernandez, and H. E. Gaub. 1997. Reversible unfolding of individual titin immunoglobulin domains by AFM. Science 276: 1109-1112.

122. Rief, M., H. Clausen-Schaumann, and H. E. Gaub. 1999. Sequence-dependent mechanics of single DNA molecules. Nat. Struct. Biol. 6: 346-349.

123. Rizo, J., X. Chen, and D. Arac. 2006. Unraveling the mechanisms of synaptotagmin and SNARE function in neurotransmitter release. Trends Cell Biol. 16: 339-350.

124. Salio, C., L. Lossi, F. Ferrini, and A. Merighi. 2006. Neuropeptides as synaptic transmitters. Cell Tissue Res. 326: 583-598.

125. Sapra, K. T., H. Besir, D. Oesterhelt, and D. J. Müller. 2006. Characterizing molecular interactions in different bacteriorhodopsin assemblies by single-molecule force spectroscopy. J. Mol. Biol. 355: 640-650.

126. Sánchez, D., N. Johnson, C. Li, P. Novak, J. Rheinlaender, Y. Zhang, U. Anand, P. Anand, J. Gorelik, G. I. Frolenkov, C. Benham, M. Lab, V. P. Ostanin, T. E.

Schaffer, D. Klenerman, and Y. E. Korchev. 2008. Noncontact measurement of the local mechanical properties of living cells using pressure applied via a pipette. Biophys. J. 95: 3017-3027.

127. Scalettar, B. A. 2006. How neurosecretory vesicles release their cargo. Neuroscientist. 12: 164-176.

128. Schroeder, T. J., J. A. Jankowski, K. T. Kawagoe, R. M. Wightman, C. Lefrou, and C. Amatore. 1992. Analysis of diffusional broadening of vesicular packets of catecholamines released from biological cells during exocytosis. Anal. Chem. 64: 3077-3083.

129. Shevchuk, A. I., J. Gorelik, S. E. Harding, M. J. Lab, D. Klenerman, and Y. E. Korchev. 2001. Simultaneous measurement of Ca2+ and cellular dynamics: combined scanning ion conductance and optical microscopy to study contracting cardiac myocytes. Biophys. J. 81: 1759-1764.

130. Shevchuk, A. I., P. Hobson, M. J. Lab, D. Klenerman, N. Krauzewicz, and Y. E. Korchev. 2008. Endocytic pathways: combined scanning ion conductance and surface confocal microscopy study. Pflugers Arch. 456: 227-235.

131. Shevchuk, A. I., P. Hobson, M. J. Lab, D. Klenerman, N. Krauzewicz, and Y. E. Korchev. 2008. Imaging single virus particles on the surface of cell membranes by high-resolution scanning surface confocal microscopy. Biophys. J. 94: 4089-4094.

132. Shin, W., and K. D. Gillis. 2006. Measurement of changes in membrane surface morphology associated with exocytosis using scanning ion conductance microscopy. Biophys. J. 91: L63-L65.

133. Shu, X., N. C. Shaner, C. A. Yarbrough, R. Y. Tsien, and S. J. Remington. 2006. Novel chromophores and buried charges control color in mFruits. Biochemistry 45: 9639-9647.

134. Sobota, J. A., F. Ferraro, N. Back, B. A. Eipper, and R. E. Mains. 2006. Not all secretory granules are created equal: Partitioning of soluble content proteins. Mol. Biol. Cell 17: 5038-5052.

135. Sorensen, J. B. 2004. Formation, stabilisation and fusion of the readily releasable pool of secretory vesicles. Pflugers Arch. 448: 347-362.

136. Sorensen, J. B. 2009. Conflicting views on the membrane fusion machinery and the fusion pore. Annu. Rev Cell Dev. Biol. 25: 513-537.

137. Stanley, B. G., and S. F. Leibowitz. 1985. Neuropeptide Y injected in the paraventricular hypothalamus: a powerful stimulant of feeding behavior. Proc. Natl. Acad. Sci. U. S. A 82: 3940-3943.

138. Stenovec, M., M. Kreft, I. Poberaj, W. J. Betz, and R. Zorec. 2004. Slow spontaneous secretion from single large dense-core vesicles monitored in neuroendocrine cells. FASEB J. 18: 1270-1272.

139. Stuenkel, E. L., and J. J. Nordmann. 1993. Intracellular calcium and vasopressin release of rat isolated neurohypophysial nerve endings. J. Physiol 468: 335-355.

140. Sturman, D. A., D. Shakiryanova, R. S. Hewes, D. L. Deitcher, and E. S. Levitan. 2006. Nearly neutral secretory vesicles in Drosophila nerve terminals. Biophys. J. 90: L45-L47.

141. Sudhof, T. C. 2004. The synaptic vesicle cycle. Annu. Rev Neurosci. 27: 509-547.

142. Sudhof, T. C., and J. E. Rothman. 2009. Membrane fusion: grappling with SNARE and SM proteins. Science 323: 474-477.

143. Takahashi, Y., A. I. Shevchuk, P. Novak, Y. Murakami, H. Shiku, Y. E. Korchev, and T. Matsue. 2010. Simultaneous noncontact topography and electrochemical imaging by SECM/SICM featuring ion current feedback regulation. J. Am. Chem. Soc. 132: 10118-10126.

144. Tatemoto, K., M. Carlquist, and V. Mutt. 1982. Neuropeptide Y--a novel brain peptide with structural similarities to peptide YY and pancreatic polypeptide. Nature 296: 659-660.

145. Teschemacher, A. G., and E. P. Seward. 2000. Bidirectional modulation of exocytosis by angiotensin II involves multiple G-protein-regulated transduction pathways in chromaffin cells. J. Neurosci. 20: 4776-4785.

146. Tsuboi, T., C. Zhao, S. Terakawa, and G. A. Rutter. 2000. Simultaneous evanescent wave imaging of insulin vesicle membrane and cargo during a single exocytotic event. Curr. Biol. 10: 1307-1310.

147. Tsuboi, T., and G. A. Rutter. 2003. Multiple forms of "kiss-and-run" exocytosis revealed by evanescent wave microscopy. Curr. Biol. 13: 563-567.

148. Tsujino, N., and T. Sakurai. 2009. Orexin/hypocretin: a neuropeptide at the interface of sleep, energy homeostasis, and reward system. Pharmacol. Rev 61: 162-176.

149. Vardjan, N., M. Stenovec, J. Jorgacevski, M. Kreft, and R. Zorec. 2007. Subnanometer fusion pores in spontaneous exocytosis of peptidergic vesicles. J. Neurosci. 27: 4737-4746.

150. Vardjan, N., M. Stenovec, J. Jorgacevski, M. Kreft, and R. Zorec. 2007. Elementary properties of spontaneous fusion of peptidergic vesicles: fusion pore gating. J. Physiol 585: 655-661.

151. Voets, T., E. Neher, and T. Moser. 1999. Mechanisms underlying phasic and sustained secretion in chromaffin cells from mouse adrenal slices. Neuron 23: 607-615.

152. Wahlestedt, C., L. Edvinsson, E. Ekblad, and R. Hakanson. 1985. Neuropeptide Y potentiates noradrenaline-evoked vasoconstriction: Mode of action. Journal of Pharmacology and Experimental Therapeutics 234: 735-741.

153. Wang, W., S. H. Zhang, L. M. Li, Z. L. Wang, J. K. Cheng, and W. H. Huang. 2009. Monitoring of vesicular exocytosis from single cells using micrometer and nanometer-sized electrochemical sensors. Anal. Bioanal. Chem. 394: 17-32.

154. Whim, M. D., and G. W. J. Moss. 2001. A novel technique that measures peptide secretion on a millisecond timescale reveals rapid changes in release. Neuron 30: 37-50.

155. Whim, M. D. 2006. Near simultaneous release of classical and peptide cotransmitters from chromaffin cells. J. Neurosci. 26: 6637-6642.

156. Wiegand, U. K., R. R. Duncan, J. Greaves, R. H. Chow, M. J. Shipston, and D. K. Apps. 2003. Red, yellow, green go!--A novel tool for microscopic segregation of secretory vesicle pools according to their age. Biochem. Soc. Trans. 31: 851-856.

157. Wipf, D. O., and A. J. Bard. 1992. Scanning electrochemical microscopy. 15. Improvements in imaging via tip-position modulation and lock-in detection. Analytical Chemistry 64: 1362-1367.

158. Xia, X., V. Lessmann, and T. F. Martin. 2009. Imaging of evoked dense-core-vesicle exocytosis in hippocampal neurons reveals long latencies and kiss-and-run fusion events. J. Cell Sci. 122: 75-82.

159. Xu, T., U. Ashery, R. D. Burgoyne, and E. Neher. 1999. Early requirement for alpha-SNAP and NSF in the secretory cascade in chromaffin cells. EMBO J. 18: 3293-3304.

160. Yannielli, P. C., and M. E. Harrington. 2001. Neuropeptide Y in the mammalian circadian system: effects on light-induced circadian responses. Peptides 22: 547-556.

161. Ying, L., A. Bruckbauer, A. M. Rothery, Y. E. Korchev, and D. Klenerman. 2002. Programmable delivery of DNA through a nanopipet. Anal. Chem. 74: 1380-1385.

162. Ying, L., S. S. White, A. Bruckbauer, L. Meadows, Y. E. Korchev, and D. Klenerman. 2004. Frequency and voltage dependence of the dielectrophoretic trapping of short lengths of DNA and dCTP in a nanopipette. Biophys. J. 86: 1018-1027.

163. Zhou, Z., S. Misler, and R. H. Chow. 1996. Rapid fluctuations in transmitter release from single vesicles in bovine adrenal chromaffin cells. Biophys. J. 70: 1543-1552.

164. Zhu, Y., J. Xu, and S. F. Heinemann. 2009. Two pathways of synaptic vesicle retrieval revealed by single-vesicle imaging. Neuron 61: 397-411.